Carnegie Mellon University

CARNEGIE INSTITUTE OF TECHNOLOGY

THESIS

SUBMITTED IN PARTIAL FULFILLMENT OF THE REQUIREMENTS

FOR THE DEGREE OF Doctor of Philosophy

TITLE Characterization and Modeling of Macromolecules on Nanoparticles and their Effects of Nanoparticle Aggregation

PRESENTED BY Stacey Marie Louie

ACCEPTED BY THE DEPARTMENTS OF

Civil and Environmental Engineering

Gregory Lowry CO-ADVISOR, MAJOR PROFESSOR	August 14, 2014 DATE
Robert Tilton CO-ADVISOR, MAJOR PROFESSOR	August 14, 2014 DATE
David A. Dzombak DEPARTMENT HEAD	August 19, 2014 DATE

APPROVED BY THE COLLEGE COUNCIL

Vijayakumar Bhagavatula DEAN	August 28, 2014 DATE

Characterization and modeling of macromolecules on nanoparticles and their effects on nanoparticle aggregation

Submitted in partial fulfillment of the requirements for

the degree of

Doctor of Philosophy

in

Civil and Environmental Engineering

Stacey Marie Louie

B.S., Chemical Engineering, The University of Texas at Austin

M.S., Civil and Environmental Engineering, Carnegie Mellon University

Carnegie Mellon University

Pittsburgh, PA

July, 2014

Acknowledgments

The research presented in this dissertation and my journey through the Ph.D. program at Carnegie Mellon University would not have been possible without the support of a great many professors, colleagues, and friends. I am grateful for the time, energy, and care they have extended to train me as a researcher, encourage me in everything I do, and create a positive working environment throughout my time here.

I sincerely thank my primary advisor, Greg Lowry, for his constantly positive outlook on my work and for always advocating on my behalf. Greg's forward-thinking approach to research, desire to ask and answer the most relevant research questions, and ability to see the big picture all inspire me to become a better scientist. I am also grateful for his willingness to prioritize the needs of his students among his busy work schedule and feel incredibly fortunate to have had Greg as my advisor. I also thank my co-advisor, Bob Tilton, for his great enthusiasm for science and the excellent advice he has given me throughout my studies. I am grateful for his willingness to share his endless wealth of knowledge and ideas to help me improve my research. Greg and Bob have been the best advisors I could ever ask for.

I would also like to thank my committee members, Mitch Small and Peter Vikesland, for their interest in my research and the time and effort they have spent in providing comments to improve the quality of my work. Mitch has provided essential advice on my research, particularly in pointing me toward the correct statistical approaches to apply in the electrokinetic modeling project, as well as improving the statistical analyses used in the natural organic matter project. Peter provided excellent feedback on my proposal and brought new ideas to the table, particularly regarding the kinetics and tranformations of natural organic matter coatings; his feedback has helped me expand my perspective and has inpired my ideas for future work.

Many collaborators and colleagues have provided helpful feedback and friendly encouragement. I especially thank the CEINT group and the Tilton group at Carnegie Mellon for both their feedback on my work, as well as for sharing their own expertise during group meetings. I have learned something new from all of them and appreciate the opportunity to have been exposed to their variety of research topics and skill sets. I thank Prof. Liz Casman for her kind words and sharing a policy-oriented perspective. I am also thankful to have been part of the larger CEINT community, through which I was able to learn about the research of colleagues at other universities and discuss my research in a supportive and collaborative environment.

I thank many researchers for providing advice, resources, and laboratory assistance. For the electrokinetic modeling project: Prof. Reghan Hill, who provided his MPEK program for the numerical model; Prof. Craig Maloney, who provided computing resources; Dr. Ya-Mei (Cheryl) Yang, who provided invaluable encouragement and statistics advice during the early stages of the project; and Dr. Zhiqiang (Eric) Li, who provided advice on coding and numerical methods. For the natural organic matter (NOM) project: Dr. Stella Marinakos, who provided the citrate-stabilized gold nanoparticles; Chuanjia (C.J.) Jiang, Prof. Heileen Hsu-Kim, and Dr. George Aiken, who provided the Pacific Ocean fulvic acid sample; Dr. Gayathri Withers, who performed ^{1}H NMR measurements; Dr. Tom Nuhfer, who provided assistance with the TEM imaging; and John Riley, who set up and helped analyze QCM-D measurements. I especially thank Eleanor Spielman-Sun, who contributed a significant amount of work for the NOM project as an REU student. I was impressed by her ability to learn quickly and work independently, and I am excited that she will be joining the Lowry group for her graduate studies.

I thank Ron Ripper for his support in the lab and cheerful presence in the office. I am especially grateful to Pom Phenrat, Trish Golas, and Matt Hotze, who trained me in the lab and

shared a great deal of knowledge to get me started, before I knew anything about nanoparticles or polymers. Finally, I am thankful for all of my colleagues: Hye-Jin Kim, Teresa Kirschling, Jee Eun Song, Sherry Peng, Yan Xu, Mei Sun, Eric Li, Brian Reinsch, Stacy Wirth, Rui Ma, Arvind Murali-Mohan, Jess Wilson, Linchen Han, Jeremy Gernand, Alan Masinter, Amy Dale, Zenille Saunders, Djuna Gulliver, Yuxin Wang, Kai Chucherdwatanasak, Ke Gai, Hari Parthasarathy, Megan Leitch, Aniela Burant, Joe Moore, John Stegemeier, Clint Noack, Lauren Strahs, Eric McGivney, Nizette Edwards, and Alex Bertuccio. Each one of them has contributed something meaningful during my time at CMU, whether knowledge and technical assistance; moral support, generosity, humor, and acts of kindness; or friendship inside and outside of the lab. I wish the best to all those continuing in their doctoral programs at CMU and know they will have great futures ahead of them.

Outside of CMU, I am grateful to my parents, Howard and Ruth, for their love and for giving me the freedom to pursue any opportunity I desired; my sister, Stephanie, for always looking out for me; and my friends in Pittsburgh and at home for their encouragement and prayers and for always lending an ear.

Funding for this work was provided by the National Science Foundation Center for Environmental Implications of Nanotechnology (CEINT) (EF-0830093), U.S. Environmental Protection Agency (EPA) R833326, and U.S. EPA STAR Graduate Fellowship Assistance Agreement FP-91714101 the Prem Narain Srivastava Legacy Fellowship, Carnegie Institute of Technology Dean's Fellowship, and the Steinbrenner Institute for Environmental Education and Research (SEER) through the Jared and Maureen Cohon Graduate Fellowship.. This work has not been formally reviewed by EPA. The views expressed in this publication are solely those of the authors; EPA does not endorse any products or commercial services mentioned.

Abstract

The increasing production and usage of engineered nanoparticles has raised concerns about potential ecological and human exposures and the risks these novel materials may pose. Nanoparticles are often manufactured with an organic macromolecular coating, and they will attain further coatings of adsorbed natural organic matter (NOM) in the environment. The overall objective of this thesis is to improve our ability to quantify the effects of adsorbed coatings on nanoparticle fate in the environment. The physicochemical properties of the coating or the adsorbing macromolecule are expected to strongly mediate the surface interactions, and hence the environmental fate, of coated nanoparticles. To this end, this research focuses on assessing a coating characterization method and applying extensive characterization of NOM coatings to enable the development of correlations to predict nanoparticle deposition onto model environmental surfaces and aggregation.

The first objective is to assess the applicability of a soft particle electrokinetic modeling approach to characterize adsorbed layer thickness, which contributes to repulsive steric forces that will affect nanoparticle deposition. A statistical analysis determined that high uncertainty in fitted layer thicknesses will limit this approach to thin, low-charged coatings (for which it may be advantageous to typical sizing methods such as dynamic light scattering). Application of this method in experimental studies further confirmed the model limitations in estimating layer thicknesses and the inability of this measurement (and other commonly measured properties) to fully explain nanoparticle deposition behavior. These results demonstrated the need for improved detail and accuracy in coating characterization.

The second objective is to correlate the properties of NOM to its effects on gold nanoparticle aggregation, with particular focus on the role of heterogeneity or polydispersity of

the NOM molecular weight. Multiple types of NOM collected from representative water bodies and soils were used, both in whole and separated into molecular weight (MW) fractions, and characterized for chemical composition and MW distribution. While average MW of the NOM provided good correlation with aggregation rate, the highest MW components were found to contribute disproportionately in stabilizing nanoparticles against aggregation, highlighting the importance of measuring and accounting for high MW components to explain nanoparticle aggregation. However, an outlier from the MW trend was identified, emphasizing the need for additional characterization (e.g. of reduced sulfur content or the conformation of the adsorbed NOM) to fully explain the effects of NOM on nanoparticle aggregation. Altogether, this research provides novel knowledge that will guide future application of characterization methods to predict attachment processes for coated nanoparticles in the environment.

Table of Contents

List of Tables

List of Figures

Chapter 1. Introduction

The increasing production of nanomaterials and their use in commercial products have led to concerns over the potential release of these materials into the natural environment (e.g., via release from products into waste or disposal streams) and the environmental, health, and safety risks that these materials may pose.[1,2] Nanoparticles are of particular interest compared to their bulk analogs because novel properties, such as increased reactivity, can exist at the nanoscale, resulting in distinct impacts on ecological or biological systems.

Novel nanomaterials with no prior natural analog will require new risk assessments. Even for nanomaterials with conventional analogs (i.e., bulk solids or dissolved materials), the environmental transport behavior and biouptake of nanoparticles can differ from that of the conventional material, resulting in differences in their mobility and distribution among environmental and biological compartments. If the nanoparticle persists in its nanoscale form or otherwise exhibits different physical, chemical, or biological behavior compared to its conventional natural analog, new environmental fate and transport models and risk assessments will be required to predict the distribution of nanomaterials released into the environment and their exposure and hazard risks.

Although significant progress has been accomplished over the past ten years to assess nanoparticle transport behavior in environmental media and toxic effects in various model organisms and model ecosystems, overarching models to assess nanoparticle risk are not yet available. To develop these models, challenges must be overcome in the characterization of nanoparticles and correlation of these properties to their fate and transport behavior of nanoparticles. These challenges are first summarized broadly for nanoparticles in comparison to

conventional organic chemicals. Then, research priorities are introduced more specifically for macromolecule-coated nanoparticles, which are the focus of this thesis.

1.1 Challenges in risk assessments for nanoparticles

Prediction of the behavior of nanoparticles will be more difficult than for dissolved chemicals because of the added physical complexity of the nanoparticle; that is, important particle-specific parameters are introduced that are not relevant or defined for bulk or dissolved species. These parameters include the properties of the nanoparticle core (e.g., size and crystallinity), as well as surface features such as roughness, surface charge, and the adsorption of small organic molecules or large macromolecules that will affect the interactions of a nanoparticle with its surrounding environment.[3] Furthermore, nanoparticle behavior is sensitive to variability in system properties, such as pH and ionic strength, within the typical range of natural environmental systems, whereas dissolved, nonionic organic molecules are typically less sensitive to these properties. Fate and effects models for nanoparticles must be able to accommodate these system properties. Finally, nanoparticles are likely to undergo physicochemical transformations in environmental and biological systems, such as oxidation-reduction reactions or adsorption of organic matter.[4-8] These transformations may only partially transform the surface of the nanoparticle, resulting in significant modification of its behavior without complete removal or degradation of the nanoparticle. Therefore, these transformations cannot be disregarded when assessing the risks of engineered nanoparticles released into natural environments.

This thesis focuses on elucidating and predicting the effects of adsorbed macromolecular coatings on nanoparticle fate and transport. Adsorbed macromolecules will be ubiquitous on

nanoparticle surfaces. Organic coatings are often applied during the manufacture of nanoparticles to provide various functions (e.g., colloidal stability or biocompatibility); furthermore, incidental coatings of natural organic matter (NOM) and proteins or other biological materials will be attained in the natural environment or upon interaction with an organism.[4,5,7,9-11] Many studies have qualitatively demonstrated that adsorbed coatings significantly change the transport, biouptake, and toxicity of nanoparticles. However, the behavior of macromolecule-coated nanoparticles is currently poorly predictable compared to that of uncoated nanoparticles, both because of the additional complexity imparted by the adsorbed layer, as well as the wide variety of macromolecules that can be encountered and must be accommodated.

1.2 Research priorities for risk assessment of macromolecule-coated nanoaprticles

Recent review articles and research strategies published under the National Nanotechnology Initiative and the National Research Council[1,2] have emphasized the assessment of the transformations of nanoparticles (including interactions with macromolecules) and the effects of these transformations on nanoparticle risk as a salient research priority. The existing knowledge gap is attributable in part to the need for better methods to measure fundamental properties of the adsorbed layer. From colloid theory, the physicochemical properties of the adsorbed layer, such as layer thickness, charge, and the volume fraction or adsorbed mass of macromolecule around the nanoparticle, are expected to significantly affect the behavior of the coated nanoparticle.[12,13] A recent correlation of nanoparticle deposition behavior has confirmed the need to include adsorbed layer properties to accurately predict the environmental transport of nanoparticles.[14] However, environmental studies assessing coated nanoparticles often lack

sufficient characterization to fully describe the adsorbed layer (e.g., its layer thickness) because simple and reliable characterization methods are not available. These characterization data will be essential to parameterize models of coated nanoparticle behavior.

A second research priority is the need for thorough and systematic studies that are designed to correlate the properties of the adsorbed macromolecular layer to the behavior of the coated nanoparticle. To establish quantitative correlations, studies that cover a broader data set (e.g., assessing more than two or three common coating types) are required. Further challenges are introduced when the nanoparticle encounters a complex mixture of macromolecules, as is present in natural organic matter or in biological media. Recent studies have demonstrated that specific proteins can adsorb preferentially to a nanoparticle from a complex serum mixture, and that the type of protein adsorbed will determine the pharmacokinetic behavior of the coated nanoparticle.[10,11] Similar studies are required to assess the interactions of specific components of natural organic matter with nanoparticles and their effects on nanoparticle behavior.

1.3 Objectives and overview of this thesis

The overarching motivation of this thesis is to further our knowledge of the effects of adsorbed macromolecules on nanoparticle fate and transport in the environment and our ability to measure the adsorbed layer properties contributing to these effects. This thesis encompasses two major projects that contribute to addressing the research needs for risk assessment of coated nanoparticles introduced in Section 1.2.

1.3.1 Part 1: Assessment of soft particle electrokinetic modeling approaches to characterize adsorbed layers on nanoparticles

The first part of this thesis (Chapters 3 and 4) addresses the need for new or improved methods to characterize adsorbed macromolecules on nanoparticles. The main objective of this research is to assess and apply an electrokinetic modeling method to estimate the physical properties of the adsorbed layer on nanoparticles. Specifically, this study (1) determines the types of coated nanoparticles for which this method can be applied to obtain layer properties with good confidence; (2) identifies feasible methods for uncertainty analysis and demonstrates their application for the electrokinetic modeling method; and (3) assesses the application of the method to explain nanoparticle transport behavior. This research identifies advantages and limitations in the electrokinetic modeling approach and future needs for characterization methods that will enable the prediction of the environmental transport behavior of coated NPs. This work has resulted in peer-reviewed publications in *Langmuir* (first author S. Louie)[15] and *Environmental Chemistry* (co-author S. Louie, first author E. Hotze).[16]

1.3.2 Part 2: Effects of the heterogeneity and variability of natural organic matter on nanoparticle aggregation

The second project (Chapters 5, 6, and 7) addresses the need for a more thorough and mechanistic understanding of the effects of NOM on nanoparticle fate and transport. The main objectives are to assess the impact of the heterogeneity and physicochemical properties of natural organic matter on gold nanoparticle of aggregation, and to correlate these properties to aggregation across several NOM samples. In particular, the role of the heterogeneity and polydispersity of the NOM is investigated by fractionating the NOM, characterizing these

fractions, and assessing how specific components of NOM interact with nanoparticles. Then, important properties of the NOM that correlate to its effects on nanoparticle aggregation behavior are identified across fractionated and unfractionated samples of several NOM sources. This research provides a more detailed and mechanistic basis for understanding the interactions between NPs and NOM, which will inform broader assessments of NP fate and transport behavior in environmental systems. This work has resulted in one published article in *Environmental Science & Technology* (first author S. Louie)[17] and a second article (first author S. Louie) to be submitted shortly after submission of this thesis.

References for Chapter 1

(1) National Research Council (NRC). *A research strategy for environmental, health and safety aspects of nanomaterials.* National Acadamies Press, 2012.
(2) National Science and Technology Council. *NNI environmental, health, and safety (EHS) research strategy*, 2011.
(3) Pettitt, M. E.; Lead, J. R. Minimum physicochemical characterisation requirements for nanomaterial regulation. *Environ. Int.* **2013**, *52*, 41-50.
(4) Christian, P.; Von der Kammer, F.; Baalousha, M.; Hofmann, T. Nanoparticles: Structure, properties, preparation and behaviour in environmental media. *Ecotoxicology* **2008**, *17* (5), 326-343.
(5) Klaine, S. J.; Alvarez, P. J. J.; Batley, G. E.; Fernandes, T. F.; Handy, R. D.; Lyon, D. Y.; Mahendra, S.; McLaughlin, M. J.; Lead, J. R. Nanomaterials in the environment: Behavior, fate, bioavailability, and effects. *Environ. Toxicol. Chem.* **2008**, *27* (9), 1825-1851.
(6) Levard, C.; Hotze, E. M.; Lowry, G. V.; Brown, G. E. Environmental transformations of silver nanoparticles: Impact on stability and toxicity. *Environ. Sci. Technol.* **2012**, *46* (13), 6900-6914.
(7) Lowry, G. V.; Gregory, K. B.; Apte, S. C.; Lead, J. R. Transformations of nanomaterials in the environment. *Environ. Sci. Technol.* **2012**, *46* (13), 6893-6899.
(8) Nowack, B.; Ranville, J. F.; Diamond, S.; Gallego-Urrea, J. A.; Metcalfe, C.; Rose, J.; Horne, N.; Koelmans, A. A.; Klaine, S. J. Potential scenarios for nanomaterial release and subsequent alteration in the environment. *Environ. Toxicol. Chem.* **2012**, *31* (1), 50-59.
(9) Ju-Nam, Y.; Lead, J. R. Manufactured nanoparticles: An overview of their chemistry, interactions and potential environmental implications. *Sci. Total Environ.* **2008**, *400* (1-3), 396-414.

(10) Lynch, I.; Cedervall, T.; Lundqvist, M.; Cabaleiro-Lago, C.; Linse, S.; Dawson, K. A. The nanoparticle - protein complex as a biological entity; a complex fluids and surface science challenge for the 21st century. *Adv. Colloid Interface Sci.* **2007**, *134-35*, 167-174.
(11) Nel, A. E.; Madler, L.; Velegol, D.; Xia, T.; Hoek, E. M. V.; Somasundaran, P.; Klaessig, F.; Castranova, V.; Thompson, M. Understanding biophysicochemical interactions at the nano-bio interface. *Nat. Mater.* **2009**, *8* (7), 543-557.
(12) Israelachvili, J. N. *Intermolecular and surface forces*; 3rd ed.; Academic Press: Amsterdam, **2011**.
(13) Vincent, B.; Edwards, J.; Emmett, S.; Jones, A. Depletion flocculation in dispersions of sterically-stabilized particles (soft spheres). *Colloids and Surfaces* **1986**, *18* (2-4), 261-281.
(14) Phenrat, T.; Song, J. E.; Cisneros, C. M.; Schoenfelder, D. P.; Tilton, R. D.; Lowry, G. V. Estimating attachment of nano- and submicrometer-particles coated with organic macromolecules in porous media: Development of an empirical model. *Environ. Sci. Technol.* **2010**, *44* (12), 4531-4538.
(15) Louie, S. M.; Phenrat, T.; Small, M. J.; Tilton, R. D.; Lowry, G. V. Parameter identifiability in application of soft particle electrokinetic theory to determine polymer and polyelectrolyte coating thicknesses on colloids. *Langmuir* **2012**, *28* (28), 10334-10347.
(16) Hotze, E. M.; Louie, S. M.; Lin, S.; Wiesner, M. R.; Lowry, G. V. Nanoparticle core properties affect attachment of macromolecule-coated nanoparticles to silica surfaces. *Environ. Chem.* **2014**, *11* (3), 257-267.
(17) Louie, S. M.; Tilton, R. D.; Lowry, G. V. Effects of molecular weight distribution and chemical properties of natural organic matter on gold nanoparticle aggregation. *Environ. Sci. Technol.* **2013**, *47* (9), 4245-4254.

Chapter 2. Background

Elucidating the interactions of engineered nanomaterials (ENMs) with macromolecules is fundamental to understanding their fate and effects. Many ENMs are designed with macromolecular coatings, such as polymers, proteins, and DNA, that will determine their environmental behavior and fate. All ENMs, coated or uncoated, will also interact with natural macromolecules, such as natural organic matter, proteins, or biological exudates, when introduced into a natural aqueous environment or an organism.[1-10] Myriad studies have demonstrated the often dramatic effects of macromolecular coatings on aggregation, deposition, removal in water and wastewater treatment plants, and reactivity.[1-6,11-14] The important role of macromolecular coatings on the biological uptake, pharmacokinetics, and toxicity potential is well-recognized, and reviews of these effects have been published in the biomedical literature,[7-10,15] as well as the ecotoxicological literature for silver nanoparticles.[16] To our knowledge, there has not yet been a review of the environmental fate literature that synthesizes the breadth of mechanisms by which macromolecules affect the environmental fate of ENMs. Here, we review the relevant literature from a broad range of systems that have been studied, and determine trends, and well as inconsistencies, in the available data. We place these recent results in the context of what is already known in this area from decades of colloid science research.

This chapter will (1) review relevant theory from related fields (colloid science) that can be used to describe ENM environmental behaviors (Section 2.1); (2) introduce classes of macromolecules of interest in the field of environmental nanotechnology (Section 2.2); (3) describe methods to characterize adsorbed macromolecules on ENMs and their limitations (Section 2.3); (4) review the current state of knowledge regarding the effects of attached organic macromolecules, both engineered and incidental, on the environmental fate and potential

environmental effects of ENMs (Section 2.4); and (5) identify the fundamental gaps in understanding and metrology that must be addressed to improve our mechanistic understanding of the effects of organic macromolecules on ENM environmental fate (Section 2.5).

2.1 Prior Knowledge from Colloid Science

This section (Section 2.1) presents a brief overview of the theory describing the adsorption of macromolecules onto colloids and ENMs and the surface forces they impart, which will affect ENM behavior in the environment. This is addressed only briefly to orient the reader because these forces have been reviewed recently.[14]

2.1.1. Adsorption of macromolecules to solid surfaces

Adsorption of a macromolecule to a particle surface will occur if it reduces the overall energy of the system, i.e. if the adsorption energy of a segment of the macromolecule onto the particle surface is more favorable than the sum of the adsorption energy of the solvent and the loss of entropy of the macromolecule upon adsorption. Adsorption can be classified as chemisorption (in which a chemical bond is formed) or physisorption (in which only non-specific forces are involved).

The conformation of a macromolecular layer is generally depicted as in Figure 2.1(a) and includes trains, loops, and tails, where trains are segments adsorbed to the substrate, loops are non-adsorbed segments between trains, and tails are the non-adsorbed ends of the macromolecule.[17] These conformations are produced by linear homopolymers (i.e., polymers composed of only one type of monomer) where no particular section of the polymer will have a higher or lower affinity to adsorb to the ENM. The flatness or extension of the layer will depend

on the strength of interaction between the monomer and the particle surface and the charge density for polyelectrolytes (charged polymers). It will also depend on the solvent quality for that particular polymer, especially with respect to the ionic strength and composition of counter ions for polyelectrolytes.

Alternatively, synthetic polymers can be attached to a surface in more ordered conformations,[18] e.g., by grafting *from* the surface using polymerization from initiators bound to the NP surface, or grafting *to* the surface by designing polymers with segments that have a stronger affinity to attach to the ENM, such as block copolymers or polymers with terminal functional groups. The conformation of these grafted layers will depend on the grafting density: at low grafting density, "mushroom" or "pancake" conformations are attained (depending on the solvent quality and interaction with the surface); at high grafting density, relatively uniform "brush" coatings are formed (Figure 2.1(b)).[19]

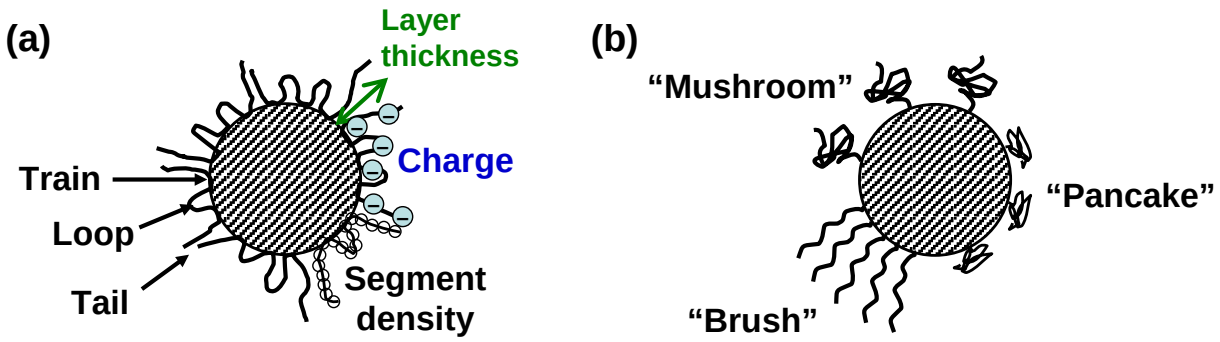

Figure 2.1. Basic conformations of an adsorbed macromolecule on an engineered nanomaterial (ENM). Physisorbed macromolecules can form trains, loops, and tails (a); end-grafted polymers can form "mushroom" or "pancake" layers at low grafting density, or "brush" layers at high grafting density (b). Adsorbed layer properties of interest include the adsorbed mass (not labeled), layer thickness, charge (or charge density), and segment density or permeability of the adsorbed layer to the solvent. The effect of nanoparticle size (i.e., high surface curvature) on the adsorbed layer conformation is illustrated in Figure 2.3.

Models for polymer adsorption have been developed using conformational statistics, e.g., Monte Carlo simulation, in which chain conformations are sampled; and self-consistent field (SCF) methods, in which mean properties such as the volume fraction of polymer are modeled. In both cases, the contributions of trains, loops, and tails can be determined. These models have been described by Fleer et al. for adsorption onto flat surfaces.[17]

It is emphasized that the standard models depicted in Figure 2.1 can deviate significantly from reality. For example, nonlinear (branched) macromolecules, such as humic acids and dendrimers, can exhibit other conformations than depicted in Figure 2.1. Most notably, the simple adsorption of macromolecules onto a particle surface does not typically cover the surface fully without a specific chemical interaction with the surface. Furthermore, the conformation of the adsorbed layer will depend on the particle's surface curvature (or size) when the particle radius is small compared to the radius of gyration of the macromolecule or the layer thickness it produces on a flat surface. These considerations are discussed in Section 2.1.3

2.1.2. Interactions of coated particles

Fundamental colloid science informs much of our understanding of the surface properties and forces that dictate ENM interactions in the environment. Reviews of these forces for *uncoated* particles in an environmental context have been provided elsewhere.[14,20,21] Briefly, Derjaguin-Landau-Verwey-Overbeek (DLVO) theory is typically used to estimate the energy of interaction between a particle and another surface (V_{DLVO}) by summing the van der Waals (V_{vdw}) and electrostatic forces (V_{el}):

$$V_{DLVO} = V_{vdw} + V_{el} \quad (2.1)$$

Expressions for the van der Waals and electrostatic energies for sphere-sphere interactions (e.g., aggregation) and sphere-plate interactions (e.g., deposition) for *uncoated particles* are provided elsewhere.[14,22] The strength of these interactions will depend on the properties of the ENM (size, Hamaker constant, and charge or zeta-potential) and the dispersion medium (ionic strength and composition). Analytical expressions have also been developed for deposition interactions of nanoparticles where assumptions for larger colloids do not apply.[23]

Adsorbed macromolecules will change the DLVO forces and impart additional forces of interaction between two particles or between a particle and a surface. These "extended DLVO" forces have also been reviewed.[14] These forces include steric and electrosteric forces and Lewis acid-base interactions (including hydrophilic/hydrophobic forces).[22,24] We focus on steric forces, which become important for thick macromolecular layers and have a strong impact on ENM stability against aggregation, particularly at higher ionic strengths where purely electrostatic interactions are screened. Electrosteric forces can also be produced by charged polyelectrolyte coatings, for which the electrostatic and steric forces may not be independent or additive.[25,26]

For the homoaggregation of two identical spherical particles with the unrealistic assumption of a uniform adsorbed layer (i.e., uniform volume fraction of macromolecule around the particle), steric interactions can be incorporated into DLVO theory using the following equations by Vincent et al. (Equations 2.2-2.4).[27] These expressions account for the entropy loss and osmotic pressure upon overlap or mixing of the adsorbed layers ($V_{s,mix}$) and the elastic repulsion when the layers are compressed between the particles ($V_{s,el}$). The particle and adsorbed layer properties required to calculate these forces are the particle radius (a) and the macromolecule's molecular weight (M_2^a), Flory-Huggins parameter (χ), density (ρ_2), volume fraction (ϕ_2^a), and layer thickness (δ).

$$V_{s,mix} = \frac{4\pi a k T}{v_1}\left(\bar{\phi}_2^a\right)^2\left(\frac{1}{2}-\chi\right)\left(\delta-\frac{h}{2}\right)^2 \; ; \qquad \delta < h < 2\delta \qquad (2.2)$$

$$V_{s,mix} = \frac{4\pi a \delta^2 k T}{v_1}\left(\bar{\phi}_2^a\right)^2\left(\frac{1}{2}-\chi\right)\left(\frac{h}{2\delta}-\frac{1}{4}-\ln\frac{h}{\delta}\right) \; ; \qquad 0 < h < \delta \qquad (2.3)$$

$$V_{s,el} = \frac{2\pi a k T \delta^2 \rho_2 \bar{\phi}_2^a}{M_2^a}\left\{\frac{h}{\delta}\ln\left[\frac{h}{\delta}\left(\frac{3-h/\delta}{2}\right)^2\right]-6\ln\left(\frac{3-h/\delta}{2}\right)+3\left(1-h/\delta\right)\right\}; \quad 0 < h < \delta \qquad (2.4)$$

where h is the separation distance between the hard particle surfaces, k is the Boltzmann constant, T is the temperature, and v_1 is the molar volume of the solvent. The magnitude of the steric force increases with the segment density or volume fraction (ϕ_2^a) of macromolecule around the particle surface. The layer thickness determines the volume of overlap of the adsorbed layers, as well as the extent of the repulsive interaction; coatings that are thick relative to the length scale of the attractive van der Waals interaction can prevent close approach and attachment of surfaces in the primary energy minimum (Figure 2.2). Finally, the solvency of the macromolecule in the dispersion medium of interest (e.g., water) will determine the sign and affect the magnitude of the energy of mixing for the overlapping adsorbed layers: layer overlap is unfavorable in "good" solvents for the macromolecule (i.e., χ < ½) but favorable in "poor" solvents (i.e., χ > ½).

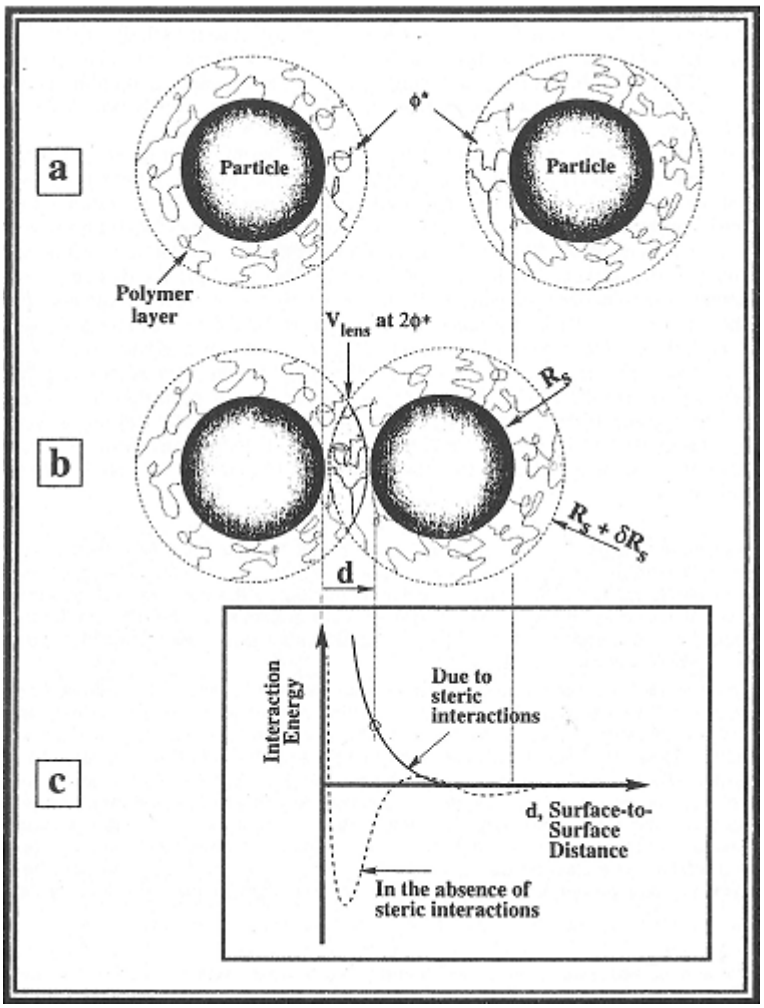

Figure 2.2. Interaction (a) and close approach (b) of macromolecule-coated particles, and the effect of steric interactions on the interaction energy between their surfaces (c). Steric interactions, included in extended DLVO models, (solid line) produce strong repulsive forces that exceed the attractive van der Waals forces. Therefore, the primary energy minimum that exists when only van der Waals and electrostatic forces are included (dashed line) may not exist when steric interactions are present. Reproduced from Hiemenz, P. C.; Rajagopalan, R. (1997). *Principles of colloid and surface chemistry*,[28] with permission of Marcel Dekker Inc.

2.1.3. Unique considerations for nanoparticles, and limitations of extended DLVO models

The small size and high surface curvature of nanoparticles present additional challenges to typical models for macromolecule adsorption and coated particle interactions. First, the

conformation of the coating (e.g., the layer thickness and segment density profile around the particle) will depend on the surface curvature. For brushes, "blob" models for neutral polymers and polyelectrolytes at high ionic strength (where charges are screened) predict a decrease in layer thickness with surface curvature (Figure 2.3(a)); furthermore, the segment density decreases with radial distance (i.e., the segment density is *non-uniform* and Equations 2.2 – 2.4 no longer apply).[29,30] It is noted that polyelectrolyte brushes at low ionic strength (not depicted) can behave differently, e.g. due to the osmotic effects of the counterions in the charged layer.[30]

The effect of surface curvature has also been explored for polymers that adsorb in train-loop-tail configurations. Assuming the adsorbed mass and volume occupied per macromolecule as on a flat surface, simple geometric scaling suggests that a thinner layer will be produced as surface curvature increases[31] (Figure 2.3(b)). Experimental studies have demonstrated that further conformational changes on a high curvature surface can result in an even greater effect on layer thickness than geometrically expected.[32] In addition, edge effects for nanocrystals can result in disorder in coatings of even small molecules that typically produce self-assembled monolayers on flat surfaces.[33] For large adsorbed polymers, non-uniform radial segment distributions are expected even on flat surfaces, as described by de Gennes.[34] Aubouy et al. extended the work of de Gennes for curved surfaces and identified a "self-similar" region (within distance R of the surface, where R is the particle radius) where the loop density is similar to the profile obtained on a flat surface; at further distances, a "mushroom" region consisting of a sparse number of extended loops or tails is observed[35] (Figure 2.3(c)).

Macromolecules that are not flexible, linear homopolymers can exhibit significantly different behavior. Experimental studies have demonstrated that globular proteins unfold more when adsorbing to larger particles but maintain a more globular structure when adsorbing to

small (high curvature) particles[36-38] (Figure 2.3(d)). These studies emphasize that fundamental theory for synthetic homopolymers or block copolymers may not be appropriate for more complex macromolecules, such as humic substances or proteins, which will violate many of the assumptions of available models.

More extreme asymmetries may be attained when the nanoparticle is smaller than the macromolecule. In this scenario, the conceptual model of an organic coating surrounding the particle may be inaccurate, and other morphologies should be considered, e.g., a "nanoparticle-decorated macromolecule" or a "nanoparticle-macromolecule complex." The stiffness of the macromolecule will affect its ability to unfold on or wrap around the nanoparticle. Bridging of multiple nanoparticles by stiff polyelectrolytes[39] or polysaccharides[40] is possible (Figure 2.3(e)).

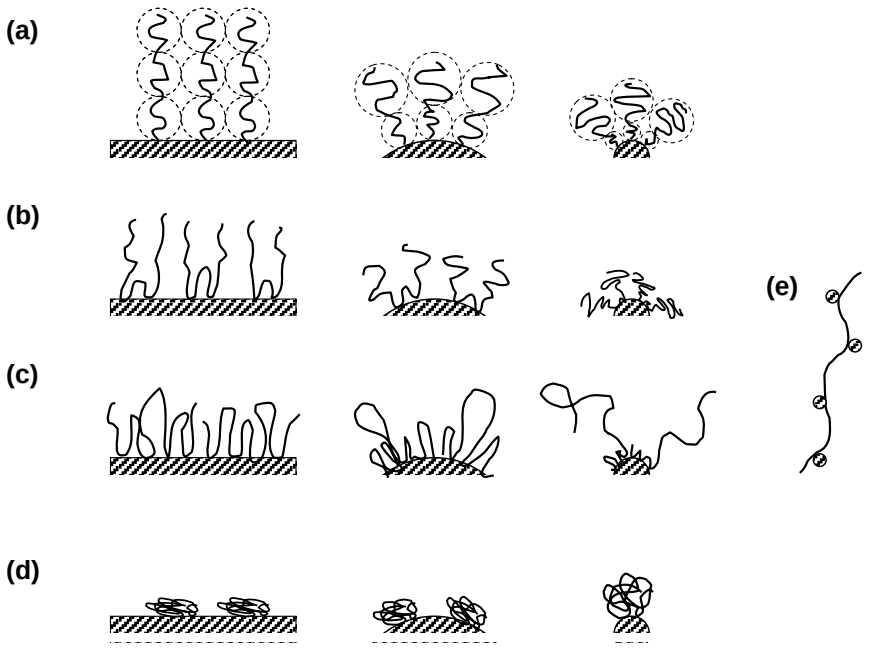

Figure 2.3. Effects of surface curvature (nanoparticle size) on the conformation of the adsorbed layer for end-grafted, neutral polymers (a); physisorbed homopolymers, following geometric considerations (b) or loop density models (c); and globular proteins (d). Nanoparticles can also be bridged by polymer (e). Diagrams are redrawn based on figures presented elsewhere for (a), flat[19] and curved[29] surfaces; (b)[41]; (c)[35]; and (d).[36-38]

Steric interaction models for extended DLVO computations are limited in incorporating these non-uniform segment distributions. For example, Vincent et al. only present analytical expressions for a few non-uniform distributions for the mixing term ($V_{s,mix}$); only the uniform distribution was presented for the elastic contribution ($V_{s,el}$).[27] The use of uniform segment distributions results in an overprediction of the steric interaction for high curvature nanoparticles.[42]

Non-uniform or unsaturated surface coverage (laterally around the particle) should also be considered. Saturation amounts are typically one to a few milligrams per square meter for uncharged homopolymers or a few tenths of a milligram per square meter for polyelectrolytes.[17] Below (and even at) saturation, portions of the particle surface are likely to be exposed. This has important consequences for nanoparticle reactivity, as discussed later in this review. The heterogeneous surface coverage can affect ENM interactions. For example, polyelectrolytes are known to form inhomogeneous, "patchy" coatings on oppositely charged particles – attractive forces then result between oppositely charged patches[43,44] (Figure 2.4). The surface charge distribution (i.e. striped versus random charge patches) has also been shown to affect the attachment behavior of ENMs coated with small, charged or neutral organic molecules.[45]

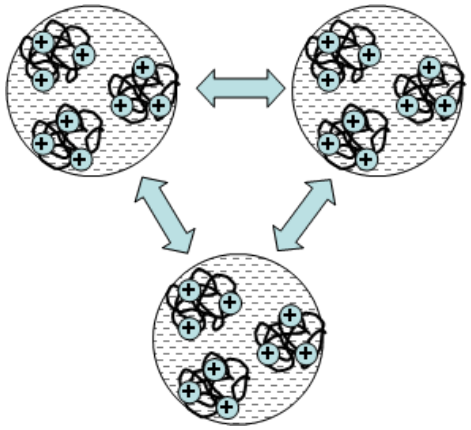

Figure 2.4. Patch-charge attraction for polyelectrolytes on oppositely-charged particles. Other conformations are also possible (e.g., wrapping of the polyelectrolyte around the particle).

Although forces such as patch-charge attraction can be included in an extended DLVO model, application of these models to real systems would require adsorbed layer characterization at a level of detail far beyond that which is currently achievable (e.g. atomic force microcscopy using nanoparticle-amended tips). In general, the constraints (assumptions) of most analytical solutions to the extended DLVO models are not met for most real NP-macromolecule systems, limiting their use to qualitative explanations of behaviors, rather than quantitative or predictive explanations. Therefore, empirical correlations developed using extensive experimental data will likely be needed to predict attachment behavior for coated NPs.

2.2. Macromolecules of interest for environmental nanotechnology

The scope of the environmental nanotechnology discipline is broad, spanning the period of the ENM life cycle from its release into the natural environment during manufacture or application (e.g. in consumer products or biomedical applications) to transport of the nanomaterial in the environment and possible uptake by and toxicity to organisms.

Macromolecules will play an important role in ENM behavior in all of these processes; these include both intentionally applied macromolecules used in nanomaterial production and unintentionally acquired macromolecules from the natural environment. We focus this review primarily on bio- and geo-macromolecules that are likely to be encountered from release of the NP into the environment until uptake by an organism. Other macromolecules, e.g. serum protein mixtures, will be encountered after biouptake and will control the ENM pharmacokinetics and toxicity,[7-10,15] but are outside the scope of this review. However, many of the fundamental behaviors and characterization challenges described here are also apply to the interactions of biological macromolecules with nanoparticles.

2.2.1 Intentionally applied macromolecules

Macromolecular coatings that are commonly used in industry include synthetic polymers (e.g., poly(ethylene glycol) (PEG), poly(vinylpyrrolidone) (PVP), poly(acrylic acid) (PAA)), naturally derived polymers (e.g., dextran, chitosan, carboxymethylcellulose), and biomacromolecules (e.g., proteins, DNA). Although these coatings can be relatively simple with respect to the known chemical structure of the polymer, we emphasize that polymers composed of the same monomers but having different molecular weight (MW) or polydispersity will have different adsorption kinetics and produce adsorbed layers with different properties on the ENM.[17] These variables can significantly affect the coated ENM behavior (e.g. stability against aggregation),[46,47] so reporting MW distributions of the polymers used, in addition to the type of polymer and its average MW, would improve the ability to compare behaviors across studies.

Engineered macromolecular coatings are often used to stabilize ENMs against aggregation[18,48-51] where stable, homogeneous suspensions are required for the product

functionality (e.g., in paints or sunscreens) or for improved delivery of the ENM (e.g., in drug delivery or for subsurface remediation).[52-54] The coating may also provide other functionalities such as biocompatibility or targeting of specific cells or organs for biomedical applications.[50,55-60] Finally, the coating can be used to tune reactivity of the ENM, e.g., for catalysis.[49,61] ENMs may also be embedded into polymeric matrices or thin films to form nanocomposite materials, e.g., for water treatment membranes,[62] food packaging,[63] or medical devices;[64] any ENM released from these materials will likely have polymer adsorbed. ENMs with highly specialized, engineered coatings such as those for drug delivery may be of interest for future studies if they impart unique behavior that results in a greater risk for exposure or toxicity.

2.2.2. Incidentally obtained, environmental macromolecules

Geochemical or biological macromolecules will be encountered by ENMs in the environment or upon uptake by an organism.[4,5,11] Dissolved organic carbon concentrations in natural waters can range from 0.5 to over 30 ppm.[65] Natural organic matter (NOM) in aquatic systems is derived from organisms, either via exudation of biomacromolecules or decay of biomass.

Higher concentrations of biological exudates are likely to be encountered when an ENM comes into close proximity with an organism (e.g., bacteria, algae, and plant roots) or is exposed to an environment with high concentrations of biota (e.g. the secondary treatment process of a wastewater treatment plant[66]). Release of biomacromolecules can also be stimulated upon exposure of organisms to stressors, including ENMs.[67-70] These exudates include extracellular polymeric substances (EPS) and mucilage. EPS and mucilage are comprised primarily of carbohydrates (including high molecular weight polysaccharides) and proteins or amino acids, as

well as lipids, nucleic acids, and organic acids.[71-73] For example, in bacterial EPS, the polysaccharide, protein, and lipid content can range from 40 to 95%, 1 to 60%, and <1 to 40%, respectively.[72] The molecular weights of different components can vary considerably: for example, alginate in the EPS from *Pseudomonas aeruginosa* can have molecular weights of 1 to 2 million Da,[74] whereas protein molecular weights are typically in the range of 10 to 100 kDa. The extreme size difference was illustrated by Flemming and Wingender and is reprinted in Figure 2.5.[72]

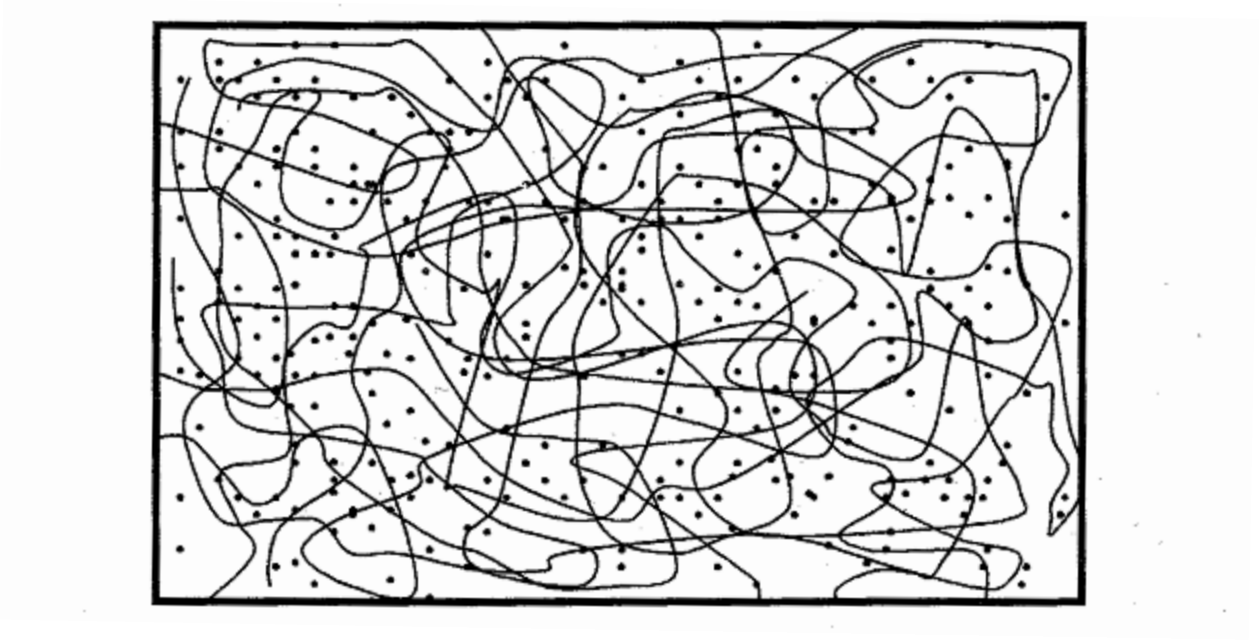

Figure 2.5. Representation of 10 molecules of alginate (2 million Da) and 300 molecules of protein (30 kDa) in an area and thickness of 1 μm^2 and 1 nm, respectively. Reproduced from Flemming, H. C.; Wingender, J. (2001) Relevance of microbial extracellular polymeric substances (EPSs) - Part I: Structural and ecological aspects. *Water Sci. Technol.* **43** (6), 1-8,[72] with permission from the copyright holders, IWA Publishing.

Simple carbohydrates, proteins, and lipids tend to be labile (i.e., rapidly degraded);[65,75,76] hence, in natural waters, refractory (degradation-resistant) humic and fulvic substances will accumulate[77,78] and can account for 60-80% of the total dissolved organic matter.[76] Humic and

fulvic substances (and NOM in general) have been described as “supermixtures” because of their broad heterogeneity with respect to the number and variety of different molecules present, the polydispersity in molecular weight, and the dynamic equilibrium state in which supramolecular assemblies may associate or dissociate depending on the solution conditions.[79] Size ranges of humic and fulvic acids and other organic components of natural organic matter are depicted in Figure 2.6. No truly pure component of “humic substances” can be isolated.[79] Measuring and predicting possible interactions of nanoparticles with NOM will be more difficult than with simpler exudates or synthetic polymers because of the structural complexity of the natural macromolecules (i.e., lack of repeating monomeric units), the heterogeneous mixture of components, and the spatial and temporal variability of the NOM in the environment.

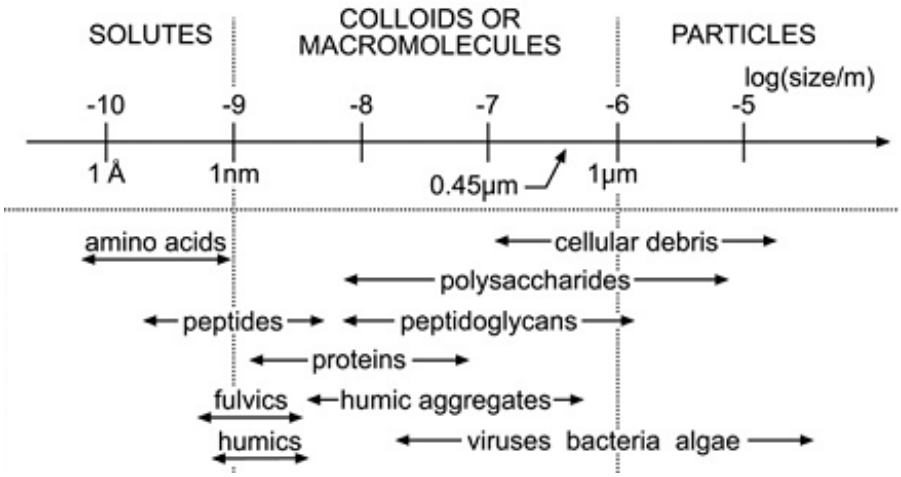

Figure 2.6. Classes of components and size ranges of natural organic matter. Note that each class itself (e.g., “humics”) is heterogeneous. Figure adapted from Wilkinson, K. J. and Lead, J. R. (2007) *Environmental colloids and particles: Behaviour, separation and characterization*, with permission from John Wiley and Sons.

Samples of natural macromolecules can be collected or extracted from a natural water or soil sample or from an organism for use in laboratory studies. Variability among different

sources, and hence different studies, should be acknowledged when comparing or extrapolating findings. Alternatively, purer samples may be purchased or synthetic analogs can be used, e.g., poly(acrylic acid) as an NOM analog,[80] alginate as a representative EPS,[81] or bovine serum albumin or human serum albumin as representative proteins. Effects of heterogeneity and advantages or disadvantages afforded by the use of heterogeneous versus purified substances are discussed later in this review. In any case, the conformation of any particular macromolecule adsorbed to an ENM will also depend on the type of ENM and the solution conditions,[82] emphasizing the need for either thorough characterization of the coated ENM in the medium of interest, or development of a correlation between the macromolecule and solution properties and the adsorbed layer conformation.

2.3 Characterization approaches to enable mechanistic inferences of ENM-macromolecule interactions and effects

Important physicochemical properties of the adsorbed layer include the composition of the layer, the adsorbed mass, the distribution or surface coverage around the ENM surface, and the conformation of the macromolecules on the ENM (i.e., the layer thickness, charge, permeability or segment density profile, moieties that adsorb directly onto the ENM surface, and orientation of the macromolecule extending into the solution). These properties will affect the electrostatic and steric interactions between the nanoparticles and other surfaces. Specific interactions can also be imparted, e.g., binding of the macromolecule coating to biological receptors for cellular recognition and uptake of the coated nanoparticle. Thorough characterization of the coated ENM will be required to identify the mechanisms contributing to the ENM interfacial behavior.

2.3.1. Characterization methods and applications

Characterization methods that can be applied to measure adsorbed layer properties on nanoparticles are summarized in Table 2.1. The use of multiple methods to probe different properties of the coated ENM is ideal. Most of these methods can be categorized under the following:

(1) microscopy techniques to visualize the coated ENM, e.g. transmission electron microscopy (TEM) and scanning electron microscopy (SEM);

(2) light, x-ray, or neutron scattering methods to determine the size or structure of the coated ENMs or ENM aggregates, e.g. dynamic light scattering (DLS), static or multi-angle light scattering (SLS, MALS), small angle x-ray scattering (SAXS), and small angle neutron scattering (SANS);

(3) size separation methods, e.g. asymmetric flow field flow fractionation (FFF or AF4) or disc centrifugal sedimentation (DCS), followed by a concentration detector, to determine ENM size distribution; these methods can also be coupled with further characterization such as MALS;

(4) spectroscopic techniques to assess the layer composition, the moietities that closely bind to the ENM, or the conformation or chemistry of the macromolecule, e.g. fluorescence spectroscopy or excitation-emission matrices (EEM), Fourier transform infrared (FTIR) spectroscopy, x-ray photoelectron spectroscopy (XPS), energy-dispersive x-ray (EDX) spectroscopy, and circular dichroism (CD);

(5) charge characterization and electrokinetic methods to assess the charge or electron transfer behavior of the coated ENM, e.g. titration, electrophoretic mobility, capillary electrophoresis, voltammetry; and

(6) solution-depletion based methods, i.e., deducing the quantity or types of macromolecules adsorbed to ENMs by characterizing the initial macromolecule solution and the free macromolecules in solution after exposure to ENMs using techniques such as total organic carbon (TOC) analysis, UV-vis absorbance, size exclusion chromatography (SEC), or liquid chromatography with mass spectrometry.

Table 2.1. Methods to characterize macromolecular coatings on nanoparticles

Method	Coating properties that can be assessed	Advantages	Technical limitations	Applications in coated ENM studies (environmental studies, where available)
Transmission electron microscopy (TEM)	Morphology	High resolution Cryo-TEM or embedding in hydrophilic resins may preserve structure	Poor sensitivity to thin, low electron density organic coatings without staining[83] Artifacts due to sample preparation (e.g. drying, staining)	Adsorption of NOM and morphology of NOM-coated ENM[83-85]
Scanning electron microscopy (SEM)	Morphology	Possibility to perform under hydrated conditions (ESEM) Possibility to perform EDX spectroscopy for elemental analysis	Lower resolution than TEM	Adsorption of NOM and morphology of coated ENM / ENM aggregates[86]
Atomic force microscopy (AFM)	Morphology Forces of interaction Layer thickness	High sensitivity to the adsorbed layer Ability to measure forces *In situ* measurements on liquid suspensions if liquid cell available	Artifacts due to sample preparation, AFM tip size, disturbance of the layer during measurement[83,87]	Adsorption of NOM and morphology of coated ENM[83] Measurement of (electro)steric forces or attractive patch-charge forces due to polymer layers[42,43,88] Measurement of humic acid layer thickness[89]
Dynamic light scattering (DLS)	Hydrodynamic layer thickness	Ease of operation and availability of equipment *In situ* measurements on liquid suspensions	Polydispersity (bias toward large ENMs or aggregates)[90-93]	Measurement of NOM layer thickness to explain coated ENM deposition[94-96]
Nanoparticle tracking analysis (NTA)	Hydrodynamic layer thickness	*In situ* measurements on liquid suspensions	Polydispersity (small ENMs may not be detected)[92,93]	

Method	Coating properties that can be assessed	Advantages	Technical limitations	Applications in coated ENM studies (environmental studies, where available)
Flow field flow fractionation (FFF)	Hydrodynamic layer thickness	*In situ* measurements on liquid suspensions Fractionation improves size measurements on polydisperse ENMs Ability to add online detectors for further characterization	Possibility for aggregation during measurement[92] Artifacts due to interactions with the membrane and between different ENM components[97] Adsorbed layer thickness may be difficult to resolve for broadly polydisperse samples	Adsorption of NOM onto ENMs[70,98,99]
Disc centrifugal sedimentation (DCS) or analytical ultracentrifugation (AUC)	Layer thickness	*In situ* measurements on liquid suspensions Fractionation improves size measurements on polydisperse ENMs	Assumptions of adsorbed layer density required Adsorbed layer thickness may be difficult to resolve for broadly polydisperse samples	Adsorbed layer thickness of proteins and DNA[100,101]
Small angle neutron scattering (SANS)	Layer thickness Segment density or volume fraction profile[102]	*In situ* measurements on liquid suspensions Contrast matching of ENMs aids analysis of adsorbed coatings	Model required to fit layer parameters	Aggregation behavior and size/structure of natural colloids with NOM[103,104]
Thermogravimetric analysis (TGA)	Adsorbed mass and composition	High sensitivity to coating mass loss Ability to distinguish coating exchange via temperature-resolved profiles	Large quantities of dried ENMs required (mg scale) Selectivity may be poor	Quantification of adsorbed mass of polymer[105] Exchange of small molecule and polymer coatings[106]

Method	Coating properties that can be assessed	Advantages	Technical limitations	Applications in coated ENM studies (environmental studies, where available)
Differential scanning calorimetry (DSC); microcalorimetry	Presence of layer Structural changes of macromolecule upon adsorption	*In situ* measurements on liquid suspensions Can distinguish free vs. adsorbed macromolecules	Will not detect adsorption of macromolecules that do not undergo conformational changes resulting in thermal phase transitions	Adsorption and denaturation of proteins on ENMs[107,108] Structure of polymer-grafted ENMs[109]
UV-vis spectroscopy	Presence of adsorbed layer	*In situ* measurements on liquid suspensions	Interferences due to ENM aggregation	Identification of adsorbed protein on ENMs due to change in localized surface plasmon resonance[110]
Fluorescence spectroscopy	Presence of layer and changes in composition	*In situ* measurements on liquid suspensions Changes in fluorescence spectrum (e.g. quenching) can be selective to distance of fluorescing moiety from ENM surface	Interferences due to ENM aggregation Interpretation of peak shifts and intensity changes may not be straightforward Macromolecule must fluoresce	Estimation of protein binding constants[110,111] Identification of bound proteins on gold ENMs (sensor applications)[112]
Proton neutron magnetic resonance (^{1}H NMR) spectroscopy	Attachment/confinement of molecules on ENM surface Exchange of adsorbates	Can distinguish free vs. adsorbed molecules	Sample preparation may perturb coating, e.g. lyophilization and exchange into D_2O	Adsorption and exchange of humic acid[113] or polymers[114] on ENMs
X-ray photoelectron spectroscopy (XPS)	Attached functional groups Layer thickness	Selective for surface coating	Interferences due to sample drying	Evaluation of changes in polymer adsorption during ENM transformation processes[115] Layer thickness of carbon in adsorbed NOM on ENMs[116]

Method	Coating properties that can be assessed	Advantages	Technical limitations	Applications in coated ENM studies (environmental studies, where available)
Hyperspectral imaging (HSI)	Layer composition	*In situ* measurements in liquid Selective for surface-bound molecules	Interferences due to ENM aggregation Library of known coated particle spectra is required to identify unknown layer composition	Adsorption of macromolecules in wastewater samples[117]
Surface-enhanced Raman spectroscopy (SERS)	Layer composition	*In situ* measurements in liquid Selective for surface-bound molecules	Only relevant for ENMs with strong LSPR (e.g., gold, silver ENMs) Library of known spectra is required to identify unknown layer composition	Binding of proteins to gold ENMs[110] Sensing of biomolecules[118] Analysis of humic acid structure[119]
Circular dichroism (CD)	Adsorbed mass Structural conformation of macromolecule	*In situ* measurements on liquid suspensions Selectivity, e.g. for proteins Can provide quantitative information	Will only detect optically active, chiral molecules	Binding and conformation of bound protein to ENMs[120-122]
Attenuated total reflectance - Fourier transform infrared (ATR-FTIR) spectroscopy	Attached functional groups	*In situ* measurements in liquid Selective for surface-bound molecules	May not be sensitive enough to detect small quantities of bound macromolecules	Adsorption and displacement of ligands, polymers, and NOM on ENMs[123-125]
Isothermal titration calorimetry (ITC)	Energy of adsorption / binding constants	Sensitivity to small changes in energy absorbed or released	Interferences due to interactions that may not be of interest, e.g. entropy change upon dilution of injected sample High ENM concentrations may be required Required pH buffer concentrations may induce ENM aggregation	Adsorbed amount and binding energy of proteins to ENMs[126-128] Assessment of depletion and bridging flocculation by polymers[129]

Method	Coating properties that can be assessed	Advantages	Technical limitations	Applications in coated ENM studies (environmental studies, where available)
Charge titration	Charge	Not sensitive to adsorbed layer hydrodynamics (as opposed to electrokinetic methods)	Charges must be titratable by acid/base (i.e., strong polyelectrolytes will not be titratable) Model fitting required (e.g. assuming two classes of acidic functional groups such as carboxyl and phenolic groups[130])	Charge of bacteria with adsorbed humic acid (and effect on ENM deposition)[131]
Electrophoretic mobility (EPM); electrokinetic modeling	Layer thickness Charge density Permeability Segment density profile	Ease of operation and equipment availability Can be insensitive to particle aggregation and polydispersity	EPM cannot be converted directly to zeta potential or charge due to dependence on hydrodynamic properties of the coating Statistical uncertainty inherent in modeling approaches	Estimation of adsorbed layer charge and thickness for polymers and NOM to assess (electro)steric interactions for coated ENMs[54,88,131,132]
Capillary electrophoresis	Similar information as EPM Interactions of adsorbates with ENMs	Can separate ENMs and excess macromolecules and assess both in the same measurement Variation in experimental setup possible to probe different interactions	ENM aggregation Undesired interactions with the capillary	Interactions of NOM with ENMs[133]
Electrospray Differential Mobility Analysis (ES-DMA)	Particle size (from electrical mobility)	Surface coverage can be deduced by comparison with hydrodynamic diameter (e.g., by DLS)	Artifacts due to required ENM drying Adsorbates must have distinguishable size difference to identify exchange or competitive adsorption	Adsorption and displacement of polymers and ligands on ENMs[124,134]

Method	Coating properties that can be assessed	Advantages	Technical limitations	Applications in coated ENM studies (environmental studies, where available)
Adsorption/binding of small molecules to the adsorbed layer	Hydrophobicity Adsorbed mass	Ease of detection and quantification due to features of molecular probe selected (e.g. fluorescence)	Artifacts due to incomplete reaction with or sorption to coatings Interferences due to the ENM	Hydrophobicity of polymer-coated ENMs[135] Quantification of adsorbed protein on ENMs[136]
Removal of NPs and analysis of supernatant for concentration (solution depletion method) or other characterization (e.g. UV-vis absorbance, SEC, etc.)	Adsorbed mass Composition of adsorbed layer	Ease of operation and equipment availability	May not be sensitive enough to assess removal of macromolecules from solution, particularly if macromolecule to ENM ratio is high	Adsorbed mass of NOM, polymer, and protein coatings to explain ENM aggregation and deposition behavior[47,82]
Protein cleaving and analysis	Adsorbed mass Composition of adsorbed layer	Ability to characterize proteins after removal	Possibility for incomplete removal of adsorbed macromolecules	Identification of proteins adsorbed to ENMs[101]

Advantages and limitations for these methods are listed in Table 2.1. We do not intend to review all of the ENM-macromolecule characterization literature; rather, a few examples demonstrating each method are specified, highlighting published environmental papers where available. It is noted that a larger and more detailed set of characterization studies is generally available for ENMs coated with well-defined synthetic polymer or protein coatings than for natural organic matter coatings, which are more difficult to characterize due to their heterogeneity.

2.3.2. Challenges and limitations for adsorbed layer characterization

Each method has limitations that can preclude its ability to provide accurate or reliable adsorbed layer properties. These limitations may be exacerbated by the nature of the ENM sample. In particular, ENM polydispersity or aggregation will limit the usability of many sizing methods to determine adsorbed layer thicknesses, especially when the method is significantly biased toward larger particles, as in DLS[90] (Figure 2.7). Methods that incorporate size separation methods followed by detection (e.g. FFF, DCS) can provide more accurate size distributions,[91-93] but adsorbed layer thicknesses that are small relative to the width of the size distribution of the uncoated ENM core will still be difficult to distinguish. Spectroscopic measurements can also be affected by ENM aggregation; for example, the surface plasmon resonance peak observed in UV-vis spectroscopy for gold and silver ENMs will decrease as the ENMs aggregate.[137]

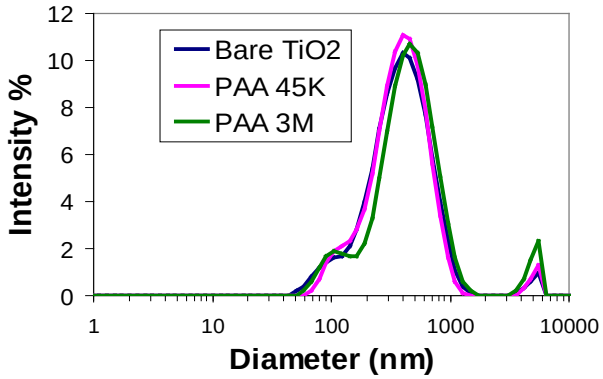

Figure 2.7. Intensity-weighted size distributions by DLS for bare and coated TiO_2 nanoparticles. Coatings are poly(acrylic acid) with molecular weights of 45,000 (45K) and 3,000,000 (3M). Size increases attributable to the adsorbed coatings cannot be determined on these polydisperse nanoparticles.

Another possible issue is the introduction of artifacts due to the sample preparation method required. For example, any method that requires drying (e.g. SEM/TEM) can induce ENM aggregation; furthermore, drying will perturb the physical conformation of the macromolecular layer, precluding the measurement of a layer thickness that is accurate for relevant, hydrated conditions. Therefore, application or development of *in situ* characterization methods will be important.

Other challenges arise due to the complexity of the adsorbed layer and a lack of suitable methods to measure the layer properties of interest on particles in suspension. For example, characterization methods may not have sufficient sensitivity to determine low adsorbed masses, or sufficient selectivity to distinguish different components in an adsorbed layer. Some of the methods listed in Table 2.1 will require further testing to assess their usability for ENMs coated with complex environmental macromolecules such as NOM. For example, fluorescence spectroscopy is expected to be sensitive to molecules bound to or near the ENM surface, but this method has been demonstrated primarily for well-defined systems of one or a few types of

polymers or proteins interacting with ENMs or for specialized applications (e.g. sensing) in which the ENM is designed with a coating that can bind or react with specific compounds or proteins.[118,138]

The conformation of a macromolecule on the ENM surface (e.g., volume fraction profile of macromolecule around the ENM) and the layer homogeneity (i.e., patchiness of the coating) can have important effects on ENM behavior but are difficult to probe at the nanoscale. This information may be obtained by SANS[102,139] or deduced from AFM force measurements on larger particles.[43] Comparison of orthogonal methods may provide more complete characterization of the macromolecular layer: for example, hydrodynamic sizing methods such as DLS will be sensitive to long tails (even at low densities), whereas a mass sensitive method (e.g., SANS) will give smaller sizes representing the more densely packed loop region near the ENM surface rather than the sparser, extended loops and tails.[17,140,141] It has been shown that the aggregation of coated ENMs is sensitive to even a small proportion of extended macromolecule tails,[140] so selection of the most appropriate characterization methods will be important in order to explain the coated ENM behavior.

2.3.3. Improvements in characterization or data reporting

Given the characterization methods currently available and the implementation of these methods in environmental nanotechnology research, some possible improvements are suggested. First, studies seeking to compare ENM behavior with different coatings do not always provide sufficient characterization to describe the coated ENM. Minimal characterization recommendations have been made for uncoated ENMs and include size, shape, core composition, and surface charge;[142] for coated ENMs, additional characteristics specifically describing the

macromolecular coating should be measured but are not always provided. For example, many studies provide only size and EPM data, but these measurements may not be sufficient to determine important adsorbed layer properties such as layer thickness. It is also noted that ionic strength and pH must be reported for EPM measurements or other coating characterization to be meaningful because the value of EPM and coating conformation are highly sensitive to both.

Interpretation of data can also be improved. In particular, electrophoretic mobility (EPM) measurements are often compared for coated and uncoated ENMs and interpreted as differences in zeta potential or surface charge, using Smoluchowski's equation for hard spheres to estimate zeta potential from EPM. However, for particles coated with a "soft" (i.e. hydrodynamically permeable) layer, the shear plane is not well defined and hence a "zeta potential" is not strictly defined. More importantly, the electrophoretic mobility will be affected not only by surface charge or potential but also by hydrodynamic effects due to the drag imparted by the layer (a function of layer thickness and permeability). For example, the magnitude of the EPM for a charged particle coated with a like-charged macromolecule can *decrease* if the layer produces enough drag to overcompensate for the force imparted by the charges on the adsorbed macromolecules. Interpretation of this EPM as a decrease in charge (and, ultimately, electrostatic force between the coated ENM and another surface) would then be inaccurate. A discussion of appropriate interpretation of zeta-potentials for coated nanoparticles has been provided by Doane et al.[143] and is also illustrated and discussed in Chapter 3 of this thesis.

The integrity of the attached macromolecular layer is also rarely reported. The ability of the coating to degrade, desorb, or to be displaced under environmentally relevant conditions is rarely reported, but is necessary to assess long term fate of the ENM in the environment. Finally,

the presence of more than one type of macromolecule on a surface may be important to know, but it is currently difficult to measure.

Here, we focused on characterization methods that provide information on the adsorbed layer on the ENM. It is noted that additional characterization of the free macromolecule would also be useful, because these characteristics will affect the conformation and properties of the adsorbed layer on the ENM and hence may be useful to predict ENM behavior even if complete characterization of the resultant coated ENM is unavailable. Lack of macromolecule characterization (e.g. molecular weight and polydispersity) is also a shortcoming in many published ENM studies; similar issues have been discussed specifically regarding NOM characterization in environmental studies.[76] In practice, better characterization of the free macromolecule, including molecular weight distribution, chemical composition, and charge density, will likely be easier to address than adsorbed layer characterization because methods have been developed in the polymer science and NOM research community to determine these characteristics.[65,144]

2.4 Effects of adsorbed macromolecules on critical physicochemical processes affecting ENM environmental behavior

Adsorbed macromolecules change the surface chemistry of ENMs and hence their behavior in the environment, but these effects are not yet understood to the extent that coated ENM fate and transport can be quantitatively predicted, or in some cases even qualitatively predicted (e.g. when an ENM will flocculate as opposed to being stabilized when encountering natural organic matter in a wastewater treatment plant). As discussed above, the properties of the coated ENMs and their behavior will be difficult to model from fundamental polymer or

colloid theory (e.g. SCF adsorption theories and extended DLVO theories), particularly for natural or incidental coatings that have complex macromolecular structures or comprise heterogeneous supermixtures.

Furthermore, the range of possible ENM-macromolecule interactions is vast, due to the number of different ENM types that might be released (including those manufactured with a macromolecular coating) and the variety of macromolecules and water chemistries that can be encountered. Important variables include the type of macromolecule, concentration of macromolecule, composition or heterogeneity of the macromolecule mixture, solution chemistry (ionic strength, pH, divalent counter-ions), and ENM type. Macromolecule-ENM interactions that can be assessed include the extent of macromolecular adsorption (adsorbed mass), kinetics of adsorption, and interactions or displacement of macromolecular components (either from a mixture or upon sequential exposure) on the ENM surface (Figure 2.8). These interactions will then determine the properties and environmental behavior of the coated ENM. Synthesizing the knowledge from all of these studies into a generalized, quantitative prediction of ENM behavior with various macromolecular coatings remains a major challenge.

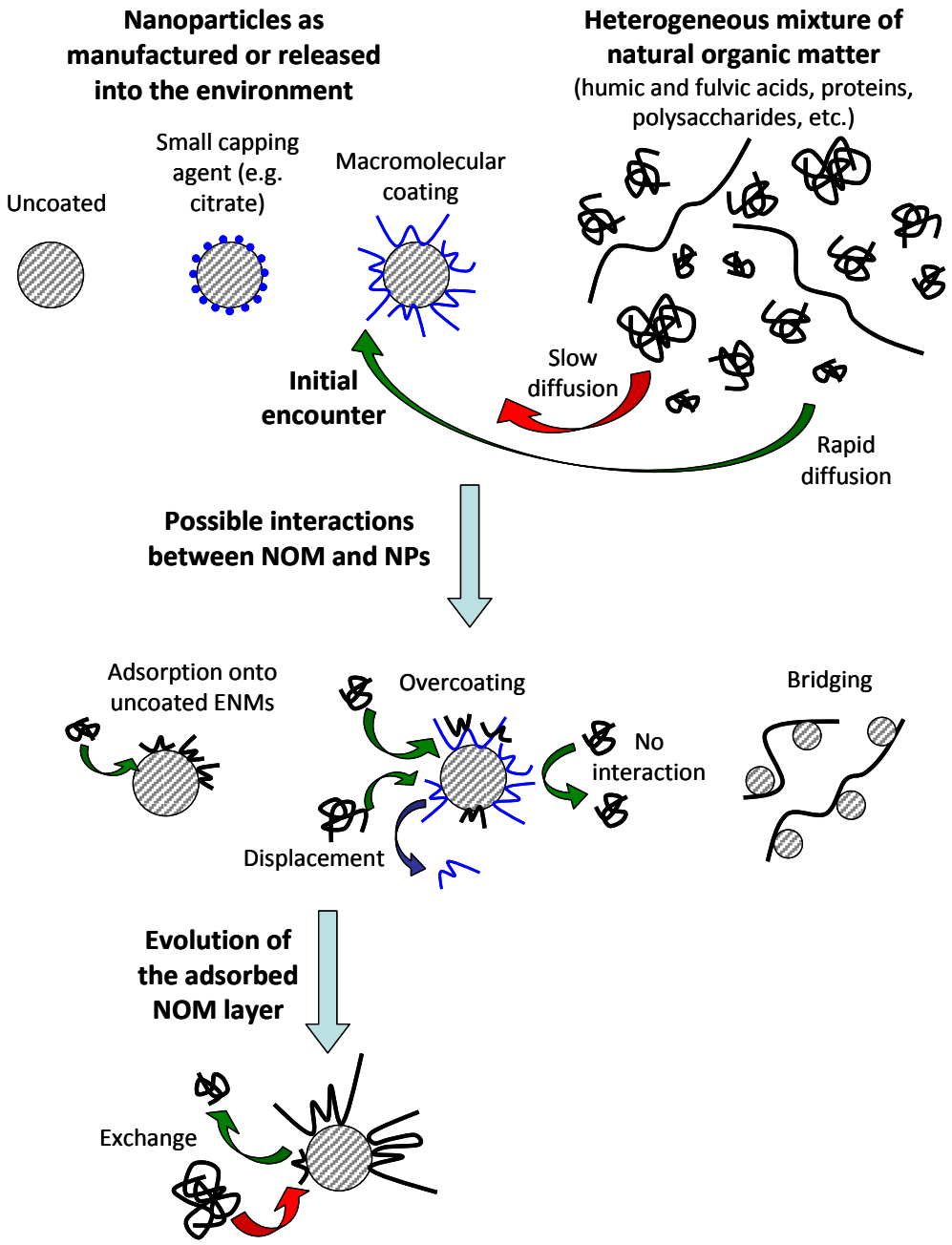

Figure 2.8. Possible interactions of ENMs initially and further exposed to NOM. These interactions are also relevant for other macromolecules. The characteristics of the adsorbed layer, transformations of the adsorbed layer, and the kinetics of these processes will determine ENM fate in the environment. The ability to assess these interactions will rely on the development of sensitive and selective detection or characterization methods for adsorbed coatings.

In this section, we review the current state of knowledge about two categories of processes that are strongly affected by the adsorbed macromolecules: attachment of ENM to surfaces (i.e., aggregation and deposition), and ENM reactivity (including dissolution, photoreactivity, and oxidation-reduction reactivity). These processes will affect the transport behavior and ultimate fate of the ENMs, as well as their toxicity. We aim to identify important mechanisms that dictate the macromolecule-ENM interactions and behavior in the environment, as well as the role of the variables listed above (concentration and composition of macromolecule and system properties) in these processes.

2.4.1. Attachment of ENMs to surfaces (aggregation and deposition)

Macromolecular coatings are well known to modify the attachment behavior of colloids and nanoparticles to surfaces, i.e., their likelihood to homoaggregate, heteroaggregate with other suspended particles, or be removed from suspension due to deposition onto mineral or biological surfaces (Figure 2.9). Many studies have been published regarding nanomaterial aggregation and deposition, as summarized by Petosa *et al.*.[14] These studies include nanoparticles that are engineered specifically with macromolecular coatings to provide function, or exposed to macromolecules during the experiment. The collective body of literature on colloid and NP interactions with macromolecules provides a good qualitative understanding of the effects of these coatings. For example, macromolecular coatings often reduce aggregation or deposition[4,5,11] by imparting electrostatic, steric, or electrosteric repulsion, which are related to adsorbed layer properties such as charge, layer thickness and density, solvency, and adsorbed mass. Alternatively, enhanced attachment may occur due to charge neutralization (if the

macromolecule and ENM are oppositely charged)[98,145,146] or bridging.[40,80,85,147,148] These effects have been demonstrated across a very large number of aggregation and deposition studies.

In general, the fundamentals of colloid science are able to qualitatively explain the observed behaviors, i.e. enhanced dispersion of ENMs due to macromolecule adsorption, or flocculation due to bridging or charge neutralization. However, in real environmental samples, such as sediment porewater or wastewater biosolids, the complexity of those samples and generally poor characterization of the matrix components (e.g. MW distribution of organic matter, or concentration of divalent cations, or the presence of other surfactants) makes it challenging to predict *a priori* the response of a particular ENM in that environment. This is true for coatings specifically engineered as part of the ENM, and for coatings that are acquired incidentally upon release into the environment. Thus, functional assays have recently been proposed to directly measure the behavior of classes of ENMs in complex environmental media.[149] The following sections summarize what is known about the effects of key environmental variables on the attachment behavior of coated ENMs.

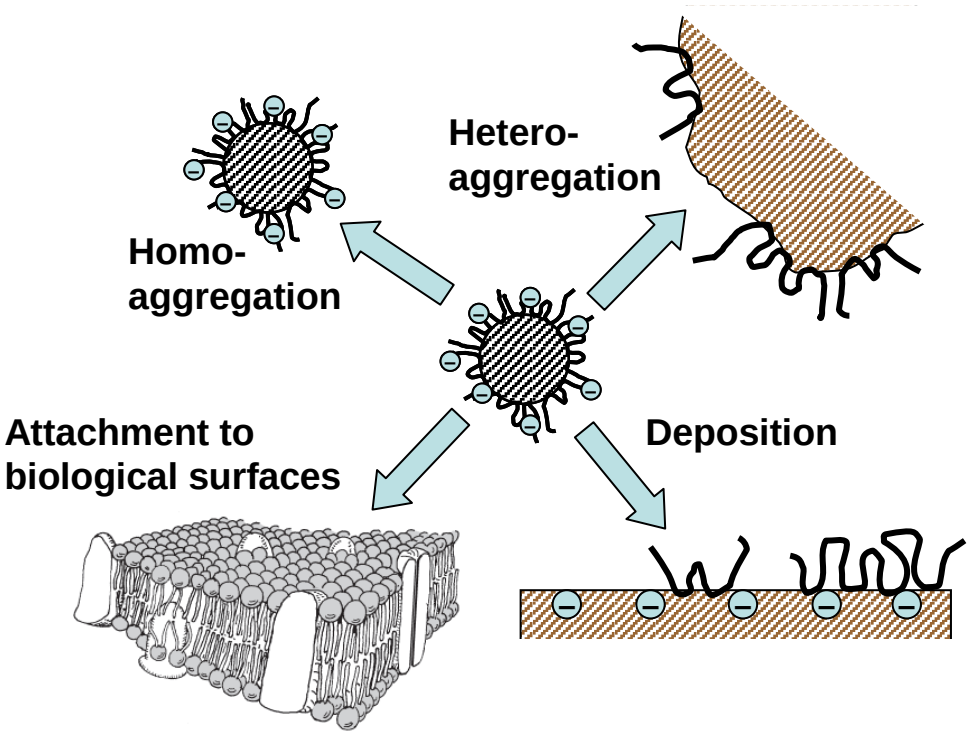

Figure 2.9. Attachment processes for ENMs in natural environments, including homoaggregation, heteroaggregation, deposition to mineral surfaces, and attachment to biological surfaces. Adsorbed macromolecules on the ENM will modify its surface properties and hence its interactions with other surfaces. Other surfaces in the environment can also be coated with macromolecules, e.g. humic substances or polysaccharides. Cell membrane drawing from Massachusetts Department of Elementary and Secondary Education.[150]

2.4.1.1 Effects of macromolecule concentration and solution chemistry

It is well known that the concentration of macromolecule and the solution chemistry (i.e., pH and ionic strength and composition) will be significant factors on aggregation and deposition behavior. These effects have been probed in previous studies.[151,152] Increased macromolecule concentration results in increased adsorbed mass of NOM until surface saturation is achieved. For many macromolecules and nanomaterials, the adsorption isotherm is quite steep, meaning that the macromolecules have a high affinity to the surface, although isotherms for polydisperse macromolecules tend to be rounded (lower affinity at low concentrations).[17] Adsorption data can

be fitted to a model isotherm to quantify the affinity, as demonstrated for the adsorption of various types of NOM to MWCNTs using a Freundlich isotherm.[153] While the adsorption maximum is both macromolecule and nanomaterial specific and difficult to predict, e.g. from N_2-BET surface area and macromolecule composition, most adsorbed macromolecule masses lie in range of 0.1 to 1 or 2 mg/m^2 for many macromolecule-NP combinations regardless of MW.[17]

For macromolecule-coated ENMs, the solution chemistry will affect not only the DLVO forces between a coated ENM and another surface (e.g. due to charge screening by counterions or pH dependence of ionization of acidic/basic functional groups), but also the adsorption and conformation of NOM onto the ENM. For example, increased charge screening of the electrostatic repulsion between charged macromolecules or macromolecule segments can result in increased adsorbed mass, but perhaps more importantly the shrinking of the adsorbed layer thickness, as has been shown for polyelectrolyte brushes.[154,155] The changes in adsorbed mass and layer structure will modify steric forces and hence the aggregation and deposition behavior of the coated ENMs.

The composition of the background electrolyte is also important, particularly for calcium ions, which can induce aggregation at high concentrations by charge neutralization of negatively charged coatings or by specific bridging interactions. Enhanced aggregation by calcium has been demonstrated for NOM in several studies.[147,148,156-158] Calcium bridging is also relevant for polysaccharides. For example, alginate can stabilize hematite ENMs[81] and MWCNTs[159] in monovalent electrolytes due to electrostatic repulsion, but calcium induces alginate gel formation and ENM bridging. Cherchi et al. found that algal exudates may have caused disaggregation of TiO_2 ENMs,[68] whereas Joshi et al. found that bacterial EPS enhanced Ag ENM aggregation in calcium-containing exposure medium.[160] These contrasting results may be due in part to the

presence of calcium. Although calcium typically encourages aggregation, contradictory results have been shown as well: Schwyzer et al. observed *enhanced* stability of carbon nanotubes in the presence of NOM within a certain Ca^{2+} concentration range.[86] This was postulated to be due to either floating of the ENMs aggregated in loose network structures of NOM, or multilayer adsorption of NOM due to Ca^{2+}. These studies highlight the need for improved characterization and reporting of the layer properties as determined in the medium of interest, along with the chemical species present in the medium.

2.4.1.2 Effects of the composition of NOM or macromolecules

Beyond macromolecule adsorbed concentration and solution chemistry, additional characterization of the composition of the free macromolecules or those adsorbed to the ENM may be required to predict ENM attachment with different types of macromolecules. Important properties include the types and of macromolecules present (e.g. polysaccharides or humic and fulvic substances) and their proportions, the presence of specific functional groups (e.g., carboxylic and phenolic acids, organic sulfur groups, aromaticity), hydrophobicity, charge, and molecular weight (discussed in detail in the next sub-section). Some of these properties, such as aromaticity, can covary with other properties such as molecular weight.[161,162]

The effects of the chemical composition of the macromolecule (or mixture of macromolecules) have been discussed in a "three-colloidal component" approach by Buffle et al., which describes NOM interactions with inorganic colloids, in which humic and fulvic substances tend to stabilize colloids, whereas rigid biopolysaccharides can bridge or destabilize them,[40] leading to enhanced aggregation and deposition.[163] Many studies focus on single classes of macromolecules, e.g., EPS (which contains a high proportion of polysaccharides) or humic

substances. Comparison across different macromolecule classes, e.g., comparing the effects of synthetic polymers, EPS, proteins, and humic substances on one type of ENM, will assist in the development of broader correlations. For example, one study by Saleh et al. demonstrated that BSA provided the best stabilization of SWCNTs, followed by humic acid, a cell culture medium, and alginate (which induced aggregation at high Ca^{2+} concentrations); it was suggested that BSA produced the greatest steric repulsion due to its globular structure and hence thicker adsorbed layer. Further work is needed to assess whether the effects of different types of coatings (synthetic polymers, humic substances, EPS, and proteins) are comparable based on fundamental principles, or whether they differ too substantially in structure or chemistry to be incorporated together in correlations of coated ENM behavior.

For NOM, some qualitative trends of ENM attachment with the NOM properties have been established in the literature. Keller et al. and Ottofuelling et al. found that charge (or, electrophoretic mobility of the coated ENM) was a significant factor for ENM stability in various natural or synthetic water samples with NOM,[151,152] suggesting electrostatic stabilization due to adsorption of negatively charged NOM; however, the role of other properties of the NOM were not assessed. Deonarine et al. provided a more comprehensive correlation of various NOM properties with nanoaprticle aggregation: upon short-term exposure to nine different NOM samples, reduction in the growth and aggregation of zinc sulfide nanoparticles correlated primarily with aromaticity and average molecular weight of the bulk NOM sample, as opposed to other properties such as elemental composition (including sulfur content), carboxyl content, and the electrophoretic mobility of the coated particles.[164] Similarly, many studies comparing the effects of humic acids and fulvic acids on ENM aggregation[165,166] or deposition[167] have

shown that humic acids, which typically have higher molecular weight and aromaticity, result in lower ENM attachment efficiency.

The postulated mechanism for these effects is that higher aromaticity or molecular weight NOM can have higher adsorption affinity and adsorbed mass[153] or will produce a thicker adsorbed layer, resulting in stronger (electro)steric repulsion. This steric or electrosteric repulsion explanation is typically used when lesser aggregation or deposition of ENMs coated with humic acids versus fulvic acids cannot be explained solely by electrostatic effects (i.e., electrophoretic mobility).[95,96,165,168] Phenrat et al. developed another correlation of transport behavior with a variety of macromolecular coatings (synthetic polymers and humic substances) and determined that adsorbed layer thickness, adsorbed mass, and molecular weight were important parameters, further emphasizing the role of steric effects.[132] Other phenomena beyond electrosteric repulsion have also been invoked when unexpected behavior of coated ENMs is encountered. For example, hydrophobicity was suggested to contribute to the enhanced aggregation of citrate-stabilized Au ENMs in the presence of Pony Lake fulvic acid at high concentrations.[166]

Overall, colloid science can be used to explain the behaviors of many NOM types once the properties of the NOM are determined.[132,164,169] However, these NOM properties are rarely determined, making comparisons across studies difficult, and some important outliers continue to exist as described next.

2.4.1.3 Effects of polydispersity

Because NOM is a complex "supermixture"[79] and different components in the mixture can have different chemistries, bulk parameters may not be sufficient to fully describe the

interactions of NOM with ENMs. Here, we specifically discuss the effects of polydispersity or molecular weight (MW) distribution, which are relatively easy to assess (compared to multiplicity and molecular diversity) because of the availability of MW characterization methods (e.g., SEC or FFF) and size separation methods (e.g., ultrafiltration).

From fundamental polymer theory, higher MW macromolecules are expected to adsorb preferentially and be able to displace smaller molecules due to their lesser entropic loss upon adsorption and higher number of attachment points.[17] For NOM, preferential adsorption of higher MW components has been observed on MWCNTs,[153] iron oxide colloids or ENMs,[170,171] aluminum oxide colloids.[172] The preferential adsorption of these higher MW components is expected to be important for ENM aggregation and deposition behavior because higher MW NOM can impart strong repulsive steric forces. For example, NOM fractions containing higher MW components produced significantly lower deposition of hematite colloids in column experiments.[173] Ghosh et al. also found that less polar, higher molecular weight fractions of a humic acid sample provided better stability of aluminum oxide ENMs by producing a thick, 10 nm layer (as determined by AFM)[89] (although it could also induce bridging under different solution conditions).[174]

It is noted that preferential adsorption of high MW components should only be assumed if the chemistry of different components are the same (e.g., as in a polydisperse sample of a synthetic homopolymer). For chemically heterogeneous macromolecules, lower molecular weight components can adsorb preferentially if they have higher affinity functional groups, e.g., ones that can chemisorb, ligate, or hydrogen bond to the ENM surface. Some studies of NOM adsorption onto colloids or sands have shown preferential adsorption of lower molecular weight components in NOM, e.g., for purified Aldrich humic acid on hematite,[175] Suwannee River

humic acid onto iron oxide,[176] and peat humic acid on metal (hydr)oxide-coated sands.[177] Furthermore, higher MW components may not always provide better ENM stability against aggregation if the lower MW components have higher affinity (and hence higher adsorbed mass) or higher charge and electrostatic repulsion. For example, no significant difference in ENM stabilization with humic versus fulvic acids was observed in some studies.[178,179] These studies contradict the correlation between NOM MW and ENM stability against aggregation that was observed by Deonarine et al. and Nason et al.,[164,166] suggesting that physicochemical properties in addition to MW can also be important. These findings again emphasize the need for thorough characterization (e.g., of the adsorbed layer composition) to explain the mechanisms by which heterogeneous coatings affect ENM behavior.

2.4.1.4 Kinetic and synergistic considerations for heterogeneous macromolecules

Thermodynamic affinity is not the only parameter that must be considered for macromolecule-ENM interactions. This is primarily because these systems are not typically at equilibrium with their surroundings. As such, rate-limited processes such as kinetic competition and exchange, as well as the order of exposure to macromolecules, will often also be important. That is, macromolecules with lower adsorption affinities may still adsorb to the ENM if they adsorb more quickly. Therefore, ENM behavior in a mixture of macromolecules is not necessarily predictable solely by assessing its interactions with individual components. For example, low molecular weight molecules can diffuse more quickly to the ENM surface and occupy surface sites to prevent bridging by slower-diffusing, high molecular weight components (Figure 2.10).[47]

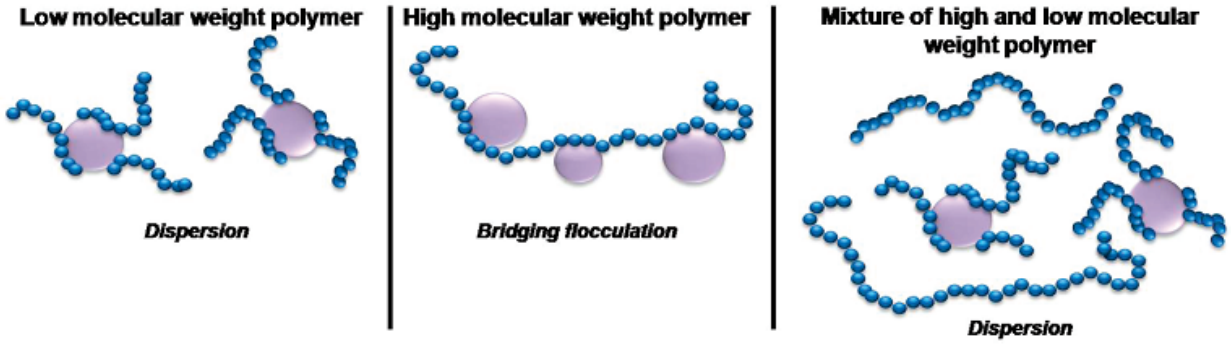

Figure 2.10. Interactions of nanoparticles with polymers of different MW and polydispersity. The presence of low MW polymers can prevent bridging by higher MW polymers by occupying surface sites more quickly. Figure reprinted with permission from Golas, P. L., et al. Comparative study of polymeric stabilizers for magnetite nanoparticles using ATRP. *Langmuir* **2010**, *26* (22), 16890-16900.[47] Copyright 2010 American Chemical Society.

Exchange of lower affinity components for higher affinity components can occur over time and has been demonstrated in NOM adsorption studies on large particles or bulk surfaces. For example, Joo et al. observed an initial phase of rapid adsorption of lower MW fractions onto FeO(OH)-coated or Al_2O_3-coated sand within 15 min by specific interactions (e.g., ligand exchange between carboxylic and phenolic acid groups and metal oxide surfaces), followed by exchange with higher MW fractions over 4 hours due to hydrophobic interactions.[177] Hur and Schlautman observed similar behavior, but exchange continued over 120 hours.[175] Exchange kinetics on ENMs have been well studied for protein mixtures in the context of ENM pharmacokinetics and toxicity, and conceptual models of "hard" (intransient) and "soft" (transient) protein coronas have been developed.[9,101] Further studies are needed to assess NOM exchange on ENMs.

While not necessarily kinetically controlled, interactions between different macromolecules on the ENM surface that can promote co-sorption should also be considered. For protein stabilization of ENMs, two- or three-component mixtures of proteins from fetal

bovine serum (FBS) provided better stability than any single protein alone;[180] in this study, the co-sorption of three components was required in order to obtain similar stability to the complete FBS mixture. It is unknown if this synergistic effect resulted from kinetic effects described above, or from the formation of a mixed-component adsorbed layer that provides better ENM stability, e.g. by overcoating of components (greater adsorbed mass) or by formation of a more uniform (less patchy) mixed coating around the ENM.

Another important kinetic consideration for macromolecule-ENM interactions and their effect on attachment behavior is the sequential exposure that may occur over the lifetime of the ENM. During the various life stages of the ENM in the environment, the ENM will be exposed sequentially to different macromolecules; for example, an ENM may be manufactured with a synthetic polymer coating, then encounter NOM in the environment, followed by EPS when encountering an organism. Prediction of these interactions will require an understanding of macromolecule-macromolecule interactions or exchange on the ENM surface. Sequential coating interactions of stabilizing ligands or polymers with NOM have been probed in a limited number of studies. Stankus et al. compared the effect of humic acid on the aggregation of gold nanoparticles initially coated with four different small molecule capping agents of different charges (neutral, positive, and negative) and found that humic acid generally produced the same response (reduced aggregation in monovalent electrolyte, enhanced aggregation in Ca^{2+} and Mg^{2+}) regardless of the initial coating.[157] On the other hand, Liu et al. found that NOM had opposite effects (i.e. reduced and enhanced aggregation) on citrate- versus mercaptoundecanoic acid-capped gold nanoparticles in the presence of Ca^{2+}.[181] The reason for these differences is unclear; further characterization of the interactions between the NOM and the initial coating (e.g. exchange, overcoating) would be helpful to explain the contrasting results.

Even characterization-focused studies can produce contradictory results. For example, no interaction of humic acid with PVP-coated gold NPs was detectable from measurements of UV-vis absorbance (surface plasmon resonance), size, ENM aggregation behavior, or surface chemistry.[182] However, some interaction of humic acid with PVP-coated silver NPs was observed by Raman spectroscopy.[113] These results highlight the need to provide characterization of the initial coated ENM, and the ENM exposed to different macromolecules, (preferably using multiple techniques) in each individual experiment to enable cross-study comparisons.

2.4.1.5 Additional considerations for heteroaggregation and deposition

Prediction of the heteroaggregation or deposition behavior of coated ENMs will require more information than prediction of homoaggregation behavior because the surface chemistry of a second surface must be considered simultaneously. For example, if the macromolecular coating on an ENM has an affinity to attach to the uncoated substrate, it can enhance attachment due to bridging.[183] However, if the substrate is also coated (or if free macromolecules are included in the background solution and allowed to adsorb before and during the experiment),[94,131,168,173,179,184,185] steric repulsion will be imparted and deposition will be prevented.[183] This phenomenon was also directly demonstrated by Chen and Elimelech[186] and Furman et al.[165] Hydrophobic or hydrophilic effects may also affect deposition: Song et al. demonstrated that the deposition of coated silver ENMs onto hydrophobic or hydrophilic surfaces correlated with the hydrophobicity of the macromolecular coating on the ENMs.[187]

Overall, the observations of macromolecule-coated ENM behaviors in environmental media are consistent with the principles of colloid and polymer science once the system properties and ENM properties are fully characterized. However, for naturally occurring

macromolecular “supermixtures” with a high degree of heterogeneity, characterization is not trivial, and contradictory results can be obtained when comparing systems that appear to be similar but are not (e.g., two humic acid samples that may be prepared differently). There are additional unresolved areas that require additional attention. For example, it is currently unclear how the transformations of environmental coatings (e.g. NOM) over time will affect ENM behavior in the context of their residence time among various environmental compartments. The propensity for various macromolecular components to adsorb to an ENM and the rates of exchange between them is not well documented. Further study is needed to assess the simultaneous effects of chemical heterogeneity, polydispersity, and exchange kinetics in realistic environments containing a broad variety of macromolecules.

2.4.2. Solubility and reactivity

Adsorbed macromolecules can modify the reactions and physicochemical transformations of the underlying inorganic ENM (Figure 2.11). The energy of surface atoms on the ENM may be directly modified via chemical binding (chemisorption) of the macromolecule, thereby changing the solubility and reactivity of the ENM. More generally, adsorbed macromolecules that coat the ENM surface can modify the availability of ENM surface sites for adsorption and reaction, the interactions of the ENM with light (and hence its photoactivity), and the flux of reactants to or from the ENM surface. The current state of knowledge pertaining to the effects of adsorbed macromolecules on the solubility, photoreactivity, and chemical reactivity of ENMs is presented, and remaining questions are discussed.

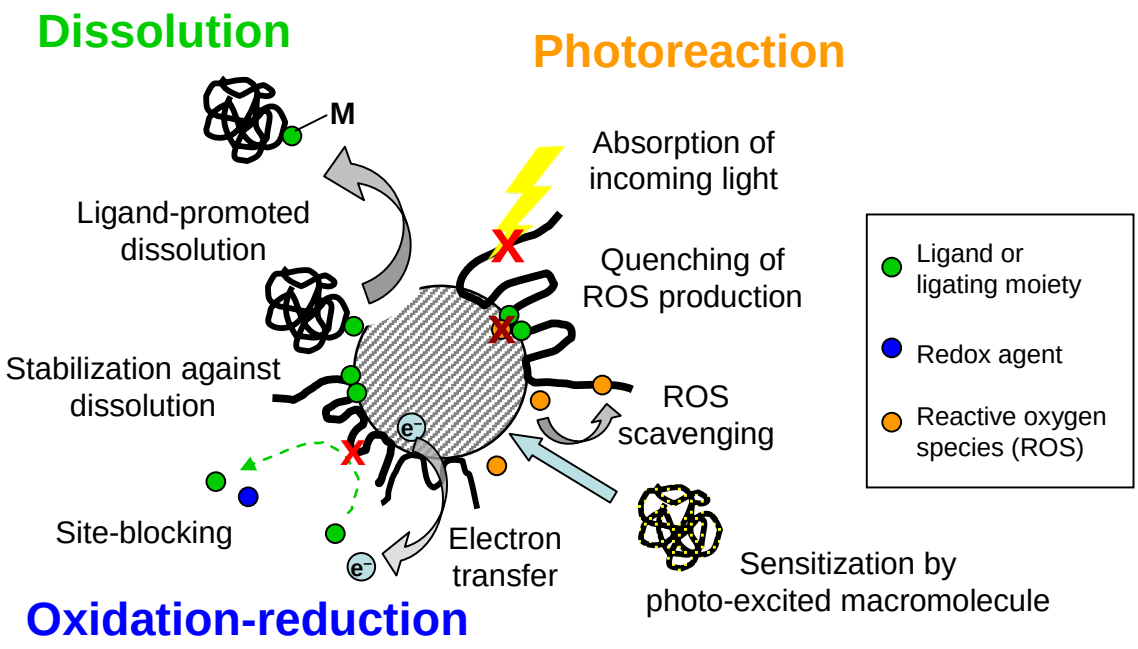

Figure 2.11. Possible effects of adsorbed macromolecules on ENM dissolution, oxidation-reduction reactions, and photoactivity. For strongly binding (e.g., chemisorbing) macromolecules, the inherent chemistry or surface energy of the ENM can be modified; the chemistry of binding will dictate whether reactivity is enhanced or reduced. Weakly binding (physisorbing) macromolecules will not change the inherent solubility or reactivity of the ENM, but can participate in light absorption, electron transfer, and binding or scavenging of chemical species of interest (e.g., redox agents and ROS). A photo-excited macromolecule can also transfer energy to the ENM to sensitize its photoreaction.

2.4.2.1 Solubility

The solubility of many metal and metal oxide ENMs is of interest in environmental contexts because dissolved metal species, such as Ag^{+} or Cd^{2+}, are toxic to a variety of aquatic species and humans. The solubility of the ENMs, as well as the rate of dissolution, will determine the persistence of the ENMs in the environment and the potential for localized delivery of dissolved species from deposited or attached ENMs (e.g. to bacteria).

Adsorbed organic coatings that chemically bind to the ENM surface can in some cases change the equilibrium solubility of the ENMs and/or their rate of dissolution. General mechanisms by which organic molecules can promote the dissolution of some metals and metal oxides have been determined for bulk (larger scale) materials. These same mechanisms will likely also apply to ENMs of the same chemical composition. Dissolution can be enhanced by both protons (i.e. acids) and inorganic or organic ligands in solution; simple rate laws for these two dissolution mechanisms for mineral dissolution were presented by Fürrer and Stumm in 1986.[188] Alternatively, complexation of the dissolved metal ions in solution by some macromolecules can act as a sink for dissolved metal ions to promote ENM dissolution without changing the equilibrium solubility of the ENM itself, i.e. its surface energy. In addition, oxidation or reduction reactions, e.g. oxidation of silver or reduction or photoreduction of iron oxides,[189] can promote dissolution. For macromolecules interacting with ENMs, both the ligation mechanisms and the effects of the adsorbed macromolecule layer on redox reactions will be relevant.

Important strong ligating moieties for metals and metal oxide ENMs include carboxylate and thiol groups. The formation of complexes that are both mononuclear (i.e., ligand binding to only one metal atom rather than multiple surface atoms) and bi- or polydentate (i.e., two or more ligands binding to the same metal atom) can enhance dissolution by weakening the bonds between the surface metal atom and the bulk metal or metal oxide.[188] For example, siderophores and small organic acids excreted by organisms promote the dissolution of iron oxides.[190-192] On the other hand, polynuclear surface complexes can be formed by large macromolecules that bind to multiple metal atoms; these coatings may inhibit dissolution due to the high energy barrier for simultaneous detachment of multiple surface atoms.

Currently available data in environmental nanotechnology generally support these trends. In toxicological studies, small organic acids were shown to enhance CeO_2 ENM dissolution,[193] and humic acid was shown to enhance ZnO ENM dissolution.[194] More rigorous dissolution studies were performed by Mudunkotuwa et al[195]. and Bian et al.,[145] in which pH was controlled (thereby controlling for proton-mediated dissolution) and dissolution over time was measured. These studies demonstrated enhanced ZnO ENM dissolution by citrate (a small molecule with three carboxylate groups per molecule and often used as a surrogate for NOM functional groups),[195] but no significant difference in either the dissolution rate or solubility of ZnO ENMs for humic acid.[145] Organic thiol ligands have a particularly high affinity for ENMs made from soft metals like Ag, Au, and Zn. For organic thiol ligands, cysteine was shown to enhance the dissolution of citrate-stabilized silver ENMs (i.e. higher concentrations of dissolved silver were observed after 50 hours of dissolution than for citrate-stabilized silver in ligand-free water), whereas serine (the OH analog to cysteine) showed no effect. [196] However, cysteine was found to reduce the dissolution of silver ENMs in another study;[197] further study is needed to determine why contrasting results were obtained.

While a fairly extensive literature exists on the effects of small molecule organic acids on mineral dissolution, additional work is needed to determine if the enhanced dissolution observed for small molecules and/or bulk minerals also holds for large macromolecules interacting with small ENMs with high surface curvature, and the dependence of these effects on the system parameters (e.g. ionic strength, pH). Comparing between ENMs and bulk materials, the adsorbed macromolecule can also take a different conformation on the surface, which can affect the nature of the binding (e.g. mononuclear versus polynuclear) and hence the enhancement or reduction of dissolution. This will likely depend on the density and spatial distribution of the

ligating moieties on the macromolecule and the steric effects between macromolecules adsorbing to the ENM surface. Finally, the pH of the system will affect the protonation or deprotonation of functional groups on the macromolecule, changing its binding to the ENM surface, as proposed by Ochs to explain pH-dependent effects of humic substances on mineral dissolution.[198]

In contrast to macromolecules with functional groups that act as strong complexing ligands, physisorbed or weakly adsorbed macromolecules do not appear to change the solubility of the ENMs, as demonstrated by Ma et al. when comparing poly(vinylpyrrolidone) (PVP) and gum arabic coated silver ENMs.[199] Similarly, Gondikas et al. found that PVP coatings on silver ENMs did not significantly change their solubility compared to citrate-stabilized silver ENMs (in the presence of cysteine and serine).[196]

Both chemisorbed and physisorbed coatings can change the kinetics of ENM dissolution, which can greatly affect the outcomes of acute toxicity testing. Mechanisms include blocking access or reducing the flux of oxidants or reactants to the ENM surface, or affecting the aggregation state of the ENMs. For example, PVP coatings on silver ENMs decreased the dissolution rate compared to citrate stabilizers (a small molecule), both in the presence of cysteine[196] or under UV irradiation.[200] The surface coverage or conformation of the macromolecule around the ENM can be very important for site blocking. Schulz et al. compared the stability of gold ENMs against etching by cyanide, a process involving complexation of CN^- with Au and oxidation of Au(0) to Au(I).[201] In this study, thiolated PEG_{2000} coatings were compared, varying only the spacer used between the thiol end group and the PEG tail. PEG conjugated with mercaptoundeanoate (MUA) stabilized the ENMs against chemical etching significantly better than either mercaptoproprionate (MPA) or mercaptophenylethanoate (MPAA). The stability imparted by the MUA coating was attributed to the packing of the MUA

to form a thick and dense (highly ordered) hydrophobic layer around the gold ENM, protecting it against cyanide etching. Differences in aggregation state were proposed to contribute to the faster dissolution of silver ENMs coated in Tween 80 surfactant, compared to citrate-stabilized or bare silver ENMs.[202] The various mechanisms suggested in the cited studies will be difficult to disentangle, although well-designed laboratory experiments can control for some effects (e.g. tethering nanoparticles to a substrate to prevent aggregation).

2.4.2.2 Oxidation-reduction reactions

ENMs can undergo oxidation-reduction (redox) reactions with other species in the environment. These reactions can be utilized beneficially for contaminant remediation, e.g., reduction of trichloroethylene (TCE) by nanoscale zerovalent iron (NZVI) or Fe(II) produced by microbial processes that reduce bulk or nanoscale ferric materials.[203,204] Alternatively, redox active ENMs can impose a toxicity hazard to organisms, either by direct oxidation or reduction of biological components or the formation of hazardous species, such as reactive oxygen speices (ROS), via redox reactions.[10,205]

Adsorbed macromolecules can affect the ENM redox activity by directly participating in electron transfer processes. For example, Kang et al. found that NOM adsorbed to NZVI enhanced electron transfer to dissolved oxygen to form hydrogen peroxide and hydroxyl radical, thereby enhancing the degradation of 4-chlorophenol.[206] Niu et al. also observed that humic acid resulted in faster degradation of sulfathiazole by a Fenton-like reaction with Fe(II) in magnetite and hydrogen peroxide.[207] The enhanced degradation was attributed to reduction of Fe(III) to Fe(II) by humic acid, enhancing the production of hydroxyl radical.

Adsorbed macromolecules can also indirectly affect ENM reactivity by blocking active sites on the ENM or acting as a physical barrier to electron transfer. Niu et al. showed that, in contrast to humic acid, adsorbed PEG, PAA, and CMC coatings reduced the rate of sulfathiazole degradation by magnetite, which was attributed to site blocking effects.[207] Saleh et al.,[208] Phenrat et al.,[209] and Wang et al.[210] also found that adsorbed polymers reduced the rate of reductive TCE dechlorination by NZVI (which is oxidized); the results were consistent with site blocking effects as well as partitioning of TCE to the adsorbed polymer (reducing its flux to the reactive NZVI surface). However, in more complex systems in which the coating and ENM interact with multiple species, the effect of the coating can differ. For example, when studying the competitive reduction of TCE, chromate, and nitrate by CMC-coated versus uncoated NZVI, Kaifas et al. observed higher reduction of TCE with the coated ENMs because the negatively-charged coating repelled the negatively charged chromate and nitrate ions.[211]

The effects of NOM coatings on redox activity will be particularly difficult to predict because of the ability of NOM to participate in redox reactions while also acting as a physical barrier around the ENM. Xie et al. found that humic acid reduced the rate of bromate reduction by NZVI and attributed this behavior to site blocking as well as complexation of reactive $Fe(II)_{(aq)}$ species.[212] However, they also found that these effects were moderated by the reduction of Fe(III) to Fe(II) by humic acid, which could encourage bromate reduction. Many other studies on have observed that NOM decreases the rate of reduction of organic contaminants by NZVI and iron oxides.[213-216]

Most studies on the effects of coatings on ENM redox activity have focused on iron or iron oxide ENMs for environmental remediation. Redox transformations of other ENMs (e.g.,

oxidation of silver NPs) are of interest for environmental implications, but relatively little is known about the effects of adsorbed macromolecular coatings on these processes.[13]

2.4.2.3 Photoreactivity

Under illumination (e.g., sunlight or UV irradiation), photoreactive ENMs can act as photocatalysts to degrade organic compounds via oxidation or reduction reactions, or they can produce reactive oxygen species (ROS) in water which can react with organic compounds or biota. Photoreactive ENMs include e.g. anatase TiO_2, ZnO, and single-walled carbon nanotubes, fullerenes, and fullerols. The development of doped or composite nanomaterials with enhanced photoreactivity is also a large and active field of research. The interactions of adsorbed macromolecules with the ENM itself or with incoming light, produced reactive oxygen species, or the compound or organism of interest will affect the photoreactivity of the ENM and its environmental effects. These interactions can either quench or sensitize the ENM photoreaction. Most environmental studies to date that assess the effects of macromolecules on ENM photoreactivity are focused on NOM, often in the context of ENM toxicity [202,217-223] or the utilization of ENMs for contaminant photodegradation.[224]

Adsorbed macromolecules can directly change the photoreactivity of the underlying ENM by static mechanisms, in which the macromolecule forms a complex with the ENM material, changing its photochemical properties prior to photoexcitation. Kong et al. assessed quenching and sensitization kinetics to explain the observed fullerene photoreaction quenching by NOM and fullerenol sensitization by NOM.[225] The fullerene quenching was attributed to static mechanisms (i.e., formation of an NOM-fullerene complex, reducing the number of photoreactive sites) rather than energy transfer from the excited fullerene to dissolved NOM

molecules, because the colloision rate between fullerene and NOM was estimated to be too slow to explain the observed behavior. On the other hand, fullerenol has lesser association with NOM, and NOM was observed to sensitize its photoreaction, which was attributed to energy transfer from excited NOM molecules that collided with the fullerenol.

More indirectly, macromolecules (either free or adsorbed) can absorb incoming light, reducing the energy reaching the ENM surface and hence reducing the photoreaction.[226] Macromolecules can also scavenge the produced ROS,[217] or they can act as a physical barrier around the ENM surface, hindering interactions of ROS produced at the ENM surface with organisms or species of interest, e.g., contaminants. Alternatively, sorption of small molecules in an adsorbed layer of macromolecules can result in higher concentrations of contaminants near the ENM surface and hence enhanced interaction with the produced ROS.[226] Finally, adsorbed macromolecules can change the ENM aggregation state, which has been shown to affect ROS production and quenching. [227,228]

Currently, few studies are available that compare the effects of different types of adsorbed coatings on ENM photoreactivity. For synthetic polymers with simple and known chemistries, the effect of the coating may ultimately be predictable from the photochemistry of the polymer and the interaction of its functional groups with the ENM surface. For NOM, the heterogeneity of the NOM and its potential to either quench or sensitize photoreaction in different scenarios results in a complex system that may not be predictable. Further study is required to assess the role of various types of NOM across various types of ENM to determine a correlation between material properties and quenching or sensitization behavior.

2.5. Approaches for quantitative prediction of coated ENM behavior

The macromolecular coating on an ENM surface in part defines that surface and therefore its interaction with other surfaces, organisms, and its reactivity and environmental fate. A better understanding of the macromolecule on the ENM surface is needed to assess, mechanistically, ENM behaviors. Considering the large number of contradictory findings in the current body of literature on the effects of macromolecules on ENM behavior, it is clear that better measurements of the macromolecules on the ENM surface are needed, along with a better understanding of what factors affects the phycicochemcial identity of that surface, before we can accurately predict the behavior of coated ENMs.

Quantitative correlations to predict the transport and fate of coated ENMs will be necessary for risk assessments. However, these correlations will be especially difficult to develop because of the high degree of complexity inherent in the system, in which the underlying ENM, macromolecular coating, and dispersion medium are all expected to affect the coated ENM behavior. We discuss experimental design, characterization, and reporting that can help to enable the development of quantitative correlations. We also discuss possible approaches for the development of correlations to predict coated ENM behavior, e.g. its aggregation, deposition, or reactivity. These approaches are followed in the studies comprising this thesis.

2.5.1. Characterization and experimental design to elucidate mechanisms of adsorbed layer effects

A significant obstacle to the development of correlations for coated ENM behavior is the wide disparity of materials and system conditions used across the literature that is currently available. Although much data is available, it is unfeasible to synthesize these into an

overarching model due to the differences among the studies and the lack of detailed characterization of the coating properties. This problem could be ameliorated in two ways. First, provision of more thorough adsorbed layer characterization would better allow different studies to be compared. Second, new studies can be undertaken that systematically vary adsorbed layer properties and correlate these to endpoints of interest (e.g., attachment or toxicity behavior). In most of the current literature, only a few types of coatings are compared, and often no particular hypothesis regarding the coating effect is explicitly tested. Differences between the few macromolecules tested may be too extreme to elucidate more nuanced effects (for example, comparison of the toxicity of ENMs with positively versus negatively charged coatings, without assessment of intermediate charges). The use of model engineered coatings on ENMs would enable hypothesis testing; for example, end-grafted polymer brushes with different molecular weights could be used to test the effect of layer thickness. However, systematic variation of layer properties will be difficult to achieve in practice due to covariance of layer properties and the nature of the adsorption process. For example, adsorbed mass and charge density in a polyelectrolyte coating would be expected to covary. Even for grafted polymers, intentional control of adsorbed layer parameters will be especially difficult to achieve when comparing among different ENM and coating types due to the propensity for different adsorption affinities and layer conformations. Regardless, significant improvements in experimental design and control are still achievable in light of the currently available environmental nanotechnology studies.

Understanding ENM behavior in heterogeneous “supermixtures” of macromolecules, such as natural organic matter, will pose significant challenges. Different approaches to use heterogeneous samples are depicted in Figure 2.12, along with the potential advantages and

disadvantages of the various approaches. To our knowledge, few studies have compared across multiple levels of heterogeneity to assess how and to what extent the heterogeneity will affect ENM behavior.

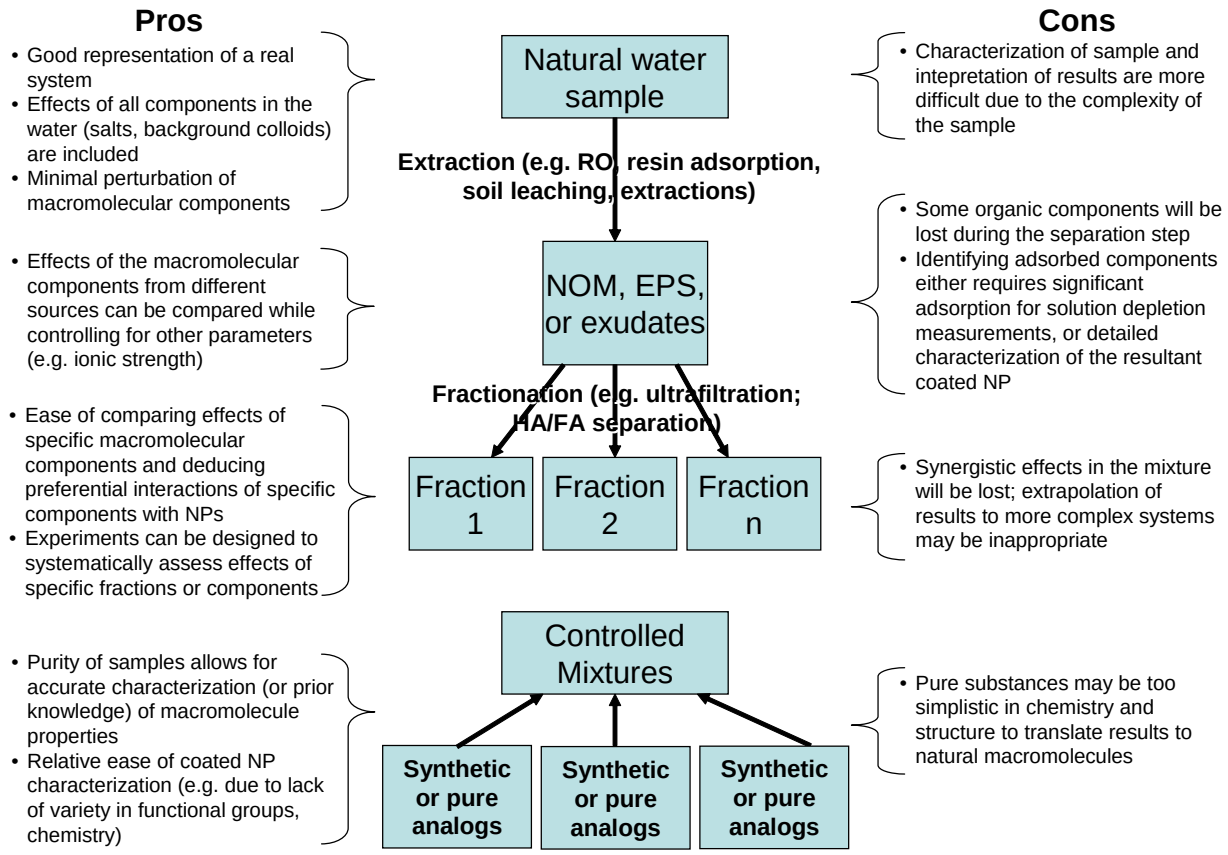

Figure 2.12. Experimental considerations and challenges presented by the heterogeneity of natural macromolecular "supermixtures" such as NOM. Sample heterogeneity decreases from top to bottom. The use of more complex and realistic samples versus fractionated samples or synthetic analogs has both advantages and disadvantages for elucidating the effects of natural macromolecules on ENM behavior. It is currently unknown how well results can be translated between different levels of heterogeneity, e.g., whether ENM behavior with fractionated NOM can quantitatively predict ENM behavior in a more complex, natural water sample.

2.5.2. Approaches to develop correlations for coated ENM behavior

Different approaches may be taken to correlate characterization data to ENM behavior, considering the multi-step nature of the process (i.e. adsorption of macromolecule leading to the formation of an adsorbed layer, resulting in an effect imparted by the coating on ENM behavior), as presented in Figure 2.13.

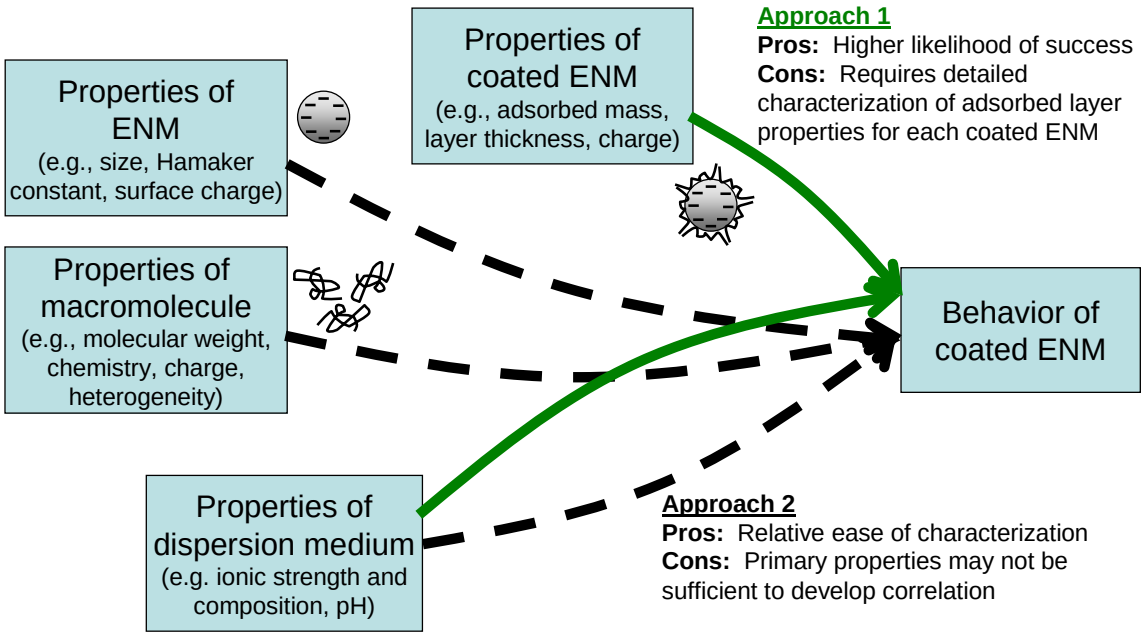

Figure 2.13. Possible approaches to correlate the properties of coated ENMs to their behavior. In Approach 1 (solid green arrows), the properties of the coated ENM are measured and, along with the properties of the dispersion medium, correlated to the coated ENM behavior (e.g., aggregation, deposition). In Approach 2 (dashed black arrows), the properties of the uncoated ENM and free macromolecule are used to develop the correlation.

In one approach (Fig. 2.13, Approach 1), ENM behavior can be correlated to the properties of the coated ENM (e.g., the overall charge or potential at the edge of the adsorbed layer, layer thickness, adsorbed mass) and the dispersion medium (e.g., ionic strength). This approach is likely to produce the most accurate predictions of coated ENM behavior because it includes all aspects of the system (particle, coating, and solution) simultaneously, but

characterization of the adsorbed layer properties will be challenging and will require new measurement techniques or methods of analysis. Additionally, each coated ENM that is likely to be formed must be characterized, resulting in high testing requirements. Not all published studies will provide sufficient characterization information, so a limited data set is available to develop correlations. This approach has been demonstrated by Phenrat et al. for deposition of a variety of ENMs with different macromolecular coatings, including synthetic polymers and NOM.[132] It is currently unknown how detailed the adsorbed layer characterization must be to reasonably estimate the attachment behavior of coated NPs. Phenrat et al. found that layer thickness and adsorbed mass contributed significantly to improve the correlation between coated ENM properties and ENM attachment efficiency when compared to an existing correlation that did not include these adsorbed layer properties.[132] These layer properties are expected to be important based on extended DLVO theories for steric interactions. Additional conformational information, e.g. lateral heterogeneity (patchiness) of the adsorbed layer, or chemical information, e.g. hydrophobicity, may also be required to better predict ENM behavior. However, these properties are not readily measurable, particularly on polydisperse ENM samples, so parameter reduction would be highly desirable. The research presented in Chapters 3 and 4 of this thesis falls under this approach: an electrokinetic method to estimate adsorbed layer properties is assessed, and its application to explain ENM deposition behavior is evaluated.

Alternatively, one may characterize the initially manufactured ENM and the free macromolecule (e.g., NOM), then correlate these properties to the ENM behavior of interest (Figure 2.13, Approach 2). This approach was taken by Deonarine et al. when correlating coated zinc sulfide ENM growth and aggregation behavior to the properties of various NOM samples.[164] The advantage to this approach is that the properties of the free macromolecule (e.g. molecular

weight) are more easily measurable than properties of the adsorbed layer on the ENM. The matrix of required sample characterizations would also be reduced to the initial ENM and macromolecule solution, excluding the need to characterize all relevant combinations of ENM and macromolecule. However, further studies are required to determine whether this approach can accommodate a broad range of ENM types and coatings: this approach implicitly assumes that the properties of the macromolecule and uncoated ENM will correlate predictably to coated ENM properties and hence the coated ENM behavior. However, the adsorption process may be too complex for this simplification to be made. Heterogeneity of the macromolecule will also present several complications in this approach. For example, can the average molecular weight for a bulk NOM sample be a sufficient predictor of adsorbed layer properties and coated ENM attachment behavior, or is a molecular weight distribution required? If so, can that distribution be adequately incorporated into a correlation via only one or a few parameters (e.g. average molecular weight and polydispersity index)? These issues are addressed in the study on the effects of heterogeneous NOM on gold nanoparticle aggregation presented in Chapters 5, 6, and 7.

In either approach, thorough characterization will be essential to the development of correlations to predict ENM behavior. This problem was highlighted in a study by Hotze et al. in which correlations of deposition behavior were attempted for three ENMs (silver, titanium dioxide, and fullerene), either uncoated or coated with one of three macromolecules (poly(acrylic acid), humic acid, and bovine serum albumin)[82]. This study tested the hypothesis that the macromolecular coating would control the deposition of the ENM to silica surfaces, such that the behavior of different ENMs could be predicted solely from the macromolecule's properties (a simplification of Approach 2 in Figure 2.13). However, this hypothesis was definitively

disproven, suggesting that the same macromolecule takes significantly different conformations on different ENMs. Then, correlations for the coated ENM deposition behavior were attempted using the coated ENM properties (size, electrophoretic mobility, adsorbed mass, and layer thickness from electrokinetic modeling), as in Approach 1, but these properties were also insufficient to explain the observed deposition. This problem was attributed to the need for more thorough or more accurate characterization. Although several methods for adsorbed layer characterization are now available or in development (Table 2.1), research that bridges these fundamental characterization studies with ENM behavior studies will be needed to develop a robust correlation to predict coated ENM behavior. Alternatively, the use of model, well-controlled systems would greatly alleviate difficulties in characterization and allow for better control over individual variables (e.g., layer thickness) to simplify the development of a correlation.

References for Chapter 2

(1) Lowry, G. V.; Gregory, K. B.; Apte, S. C.; Lead, J. R. Transformations of nanomaterials in the environment. *Environ. Sci. Technol.* **2012**, *46* (13), 6893-6899.
(2) Klaine, S. J.; Alvarez, P. J. J.; Batley, G. E.; Fernandes, T. F.; Handy, R. D.; Lyon, D. Y.; Mahendra, S.; McLaughlin, M. J.; Lead, J. R. Nanomaterials in the environment: Behavior, fate, bioavailability, and effects. *Environ. Toxicol. Chem.* **2008**, *27* (9), 1825-1851.
(3) Nowack, B.; Ranville, J. F.; Diamond, S.; Gallego-Urrea, J. A.; Metcalfe, C.; Rose, J.; Horne, N.; Koelmans, A. A.; Klaine, S. J. Potential scenarios for nanomaterial release and subsequent alteration in the environment. *Environ. Toxicol. Chem.* **2012**, *31* (1), 50-59.
(4) Christian, P.; Von der Kammer, F.; Baalousha, M.; Hofmann, T. Nanoparticles: Structure, properties, preparation and behaviour in environmental media. *Ecotoxicology* **2008**, *17* (5), 326-343.
(5) Ju-Nam, Y.; Lead, J. R. Manufactured nanoparticles: An overview of their chemistry, interactions and potential environmental implications. *Sci. Total Environ.* **2008**, *400* (1-3), 396-414.
(6) Lin, D. H.; Tian, X. L.; Wu, F. C.; Xing, B. S. Fate and transport of engineered nanomaterials in the environment. *J. Environ. Qual.* **2010**, *39* (6), 1896-1908.

(7) Lynch, I.; Cedervall, T.; Lundqvist, M.; Cabaleiro-Lago, C.; Linse, S.; Dawson, K. A. The nanoparticle - protein complex as a biological entity; a complex fluids and surface science challenge for the 21st century. *Adv. Colloid Interface Sci.* **2007**, *134-35*, 167-174.
(8) Moghimi, S. M.; Hunter, A. C.; Andresen, T. L. Factors controlling nanoparticle pharmacokinetics: An integrated analysis and perspective. *Annu. Rev. Pharmacol. Toxicol.* **2012**, *52*, 481-503.
(9) Monopoli, M. P.; Aberg, C.; Salvati, A.; Dawson, K. A. Biomolecular coronas provide the biological identity of nanosized materials. *Nat. Nanotechnol.* **2012**, *7* (12), 779-786.
(10) Nel, A. E.; Madler, L.; Velegol, D.; Xia, T.; Hoek, E. M. V.; Somasundaran, P.; Klaessig, F.; Castranova, V.; Thompson, M. Understanding biophysicochemical interactions at the nano-bio interface. *Nat. Mater.* **2009**, *8* (7), 543-557.
(11) Aiken, G. R.; Hsu-Kim, H.; Ryan, J. N. Influence of dissolved organic matter on the environmental fate of metals, nanoparticles, and colloids. *Environ. Sci. Technol.* **2011**, *45* (8), 3196-3201.
(12) Hotze, E. M.; Phenrat, T.; Lowry, G. V. Nanoparticle aggregation: Challenges to understanding transport and reactivity in the environment. *J. Environ. Qual.* **2010**, *39* (6), 1909-1924.
(13) Levard, C.; Hotze, E. M.; Lowry, G. V.; Brown, G. E. Environmental transformations of silver nanoparticles: Impact on stability and toxicity. *Environ. Sci. Technol.* **2012**, *46* (13), 6900-6914.
(14) Petosa, A. R.; Jaisi, D. P.; Quevedo, I. R.; Elimelech, M.; Tufenkji, N. Aggregation and deposition of engineered nanomaterials in aquatic environments: Role of physicochemical interactions. *Environ. Sci. Technol.* **2010**, *44* (17), 6532-6549.
(15) Walkey, C. D.; Chan, W. C. W. Understanding and controlling the interaction of nanomaterials with proteins in a physiological environment. *Chem. Soc. Rev.* **2012**, *41* (7), 2780-2799.
(16) Sharma, V. K.; Siskova, K. M.; Zboril, R.; Gardea-Torresdey, J. L. Organic-coated silver nanoparticles in biological and environmental conditions: Fate, stability and toxicity. *Adv. Colloid Interface Sci.* **2014**, *204*, 15-34.
(17) Fleer, G. J.; Cohen Stuart, M. A.; Scheutjens, J. M. H. M.; Cosgrove, T.; Vincent, B. *Polymers at interfaces*; Chapman & Hall: London, **1993**.
(18) Krumpfer, J. W.; Schuster, T.; Klapper, M.; Mullen, K. Make it nano-Keep it nano. *Nano Today* **2013**, *8* (4), 417-438.
(19) de Gennes, P. G. Conformations of polymers attached to an interface. *Macromolecules* **1980**, *13* (5), 1069-1075.
(20) Elimelech, M.; Gregory, J.; Jia, X.; Williams, R. A. *Particle deposition and aggregation: Measurement, modelling and simulation*; Butterworth-Heinemann: Woburn, MA, **1995**.
(21) Ryan, J. N.; Elimelech, M. Colloid mobilization and transport in groundwater. *Colloids Surf., A* **1996**, *107*, 1-56.
(22) Israelachvili, J. N. *Intermolecular and surface forces*; 3rd ed.; Academic Press: Amsterdam, **2011**.
(23) Lin, S. H.; Wiesner, M. R. Exact analytical expressions for the potential of electrical double layer interactions for a sphere-plate system. *Langmuir* **2010**, *26* (22), 16638-16641.
(24) Grasso, D.; Subramaniam, K.; Butkus, M.; Strevett, K.; Bergendahl, J. A review of non-DLVO interactions in environmental colloidal systems. *Rev. Environ. Sci. Biotechnol.* **2002**, *1* (1), 17-38.

(25) Einarson, M. B.; Berg, J. C. Electrosteric stabilization of colloidal latex dispersions. *J. Colloid Interface Sci.* **1993**, *155* (1), 165-172.
(26) Fritz, G.; Schadler, V.; Willenbacher, N.; Wagner, N. J. Electrosteric stabilization of colloidal dispersions. *Langmuir* **2002**, *18* (16), 6381-6390.
(27) Vincent, B.; Edwards, J.; Emmett, S.; Jones, A. Depletion flocculation in dispersions of sterically-stabilized particles (soft spheres). *Colloids and Surfaces* **1986**, *18* (2-4), 261-281.
(28) Hiemenz, P. C.; Rajagopalan, R. *Principles of colloid and surface chemistry*; Marcel Dekker: New York, **1997**.
(29) Daoud, M.; Cotton, J. P. Star shaped polymers - A model for the conformation and its concentration-dependence. *J. Phys.* **1982**, *43* (3), 531-538.
(30) Zhulina, E. B.; Birshtein, T. M.; Borisov, O. V. Curved polymer and polyelectrolyte brushes beyond the Daoud-Cotton model. *Eur. Phys. J. E* **2006**, *20* (3), 243-256.
(31) Garvey, M. J.; Tadros, T. F.; Vincent, B. A comparison of the adsorbed layer thickness obtained by several techniques of various molecular weight fractions of poly(vinyl alcohol) on aqueous polystyrene latex particles. *J. Colloid Interface Sci.* **1976**, *55* (2), 440-453.
(32) Biver, C.; Hariharan, R.; Mays, J.; Russel, W. B. Neutral and charged polymer brushes: A model unifying curvature effects from micelles to flat surfaces. *Macromolecules* **1997**, *30* (6), 1787-1792.
(33) Grainger, D. W.; Castner, D. G. Nanobiomaterials and nanoanalysis: Opportunities for improving the science to benefit biomedical technologies. *Adv. Mater.* **2008**, *20* (5), 867-877.
(34) de Gennes, P. G. Polymer solutions near an interface. 1. Adsorption and depletion layers. *Macromolecules* **1981**, *14* (6), 1637-1644.
(35) Aubouy, M.; Raphael, E. Scaling description of a colloidal particle clothed with polymers. *Macromolecules* **1998**, *31* (13), 4357-4363.
(36) Lundqvist, M.; Sethson, I.; Jonsson, B. H. Protein adsorption onto silica nanoparticles: Conformational changes depend on the particles' curvature and the protein stability. *Langmuir* **2004**, *20* (24), 10639-10647.
(37) Roach, P.; Farrar, D.; Perry, C. C. Surface tailoring for controlled protein adsorption: Effect of topography at the nanometer scale and chemistry. *J. Am. Chem. Soc.* **2006**, *128* (12), 3939-3945.
(38) Vertegel, A. A.; Siegel, R. W.; Dordick, J. S. Silica nanoparticle size influences the structure and enzymatic activity of adsorbed lysozyme. *Langmuir* **2004**, *20* (16), 6800-6807.
(39) Ulrich, S.; Seijo, M.; Laguecir, A.; Stoll, S. Nanoparticle adsorption on a weak polyelectrolyte. Stiffness, pH, charge mobility, and ionic concentration effects investigated by Monte Carlo simulations. *J. Phys. Chem. B* **2006**, *110* (42), 20954-20964.
(40) Buffle, J.; Wilkinson, K. J.; Stoll, S.; Filella, M.; Zhang, J. W. A generalized description of aquatic colloidal interactions: The three-colloidal component approach. *Environ. Sci. Technol.* **1998**, *32* (19), 2887-2899.
(41) Baker, J. A.; Pearson, R. A.; Berg, J. C. Influence of particle curvature on polymer adsorption layer thickness. *Langmuir* **1989**, *5* (2), 339-342.
(42) Lin, S. H.; Wiesner, M. R. Theoretical investigation on the steric interaction in colloidal deposition. *Langmuir* **2012**, *28* (43), 15233-15245.
(43) Borkovec, M.; Szilagyi, I.; Popa, I.; Finessi, M.; Sinha, P.; Maroni, P.; Papastavrou, G. Investigating forces between charged particles in the presence of oppositely charged polyelectrolytes with the multi-particle colloidal probe technique. *Adv. Colloid Interface Sci.* **2012**, *179*, 85-98.

(44) Szilagyi, I.; Trefalt, G.; Tiraferri, A.; Maroni, P.; Borkovec, M. Polyelectrolyte adsorption, interparticle forces, and colloidal aggregation. *Soft Matter* **2014**, *10* (15), 2479-2502.
(45) Huang, R. X.; Carney, R. P.; Stellacci, F.; Lau, B. L. T. Colloidal stability of self-assembled monolayer-coated gold nanoparticles: The effects of surface compositional and structural heterogeneity. *Langmuir* **2013**, *29* (37), 11560-11566.
(46) Ditsch, A.; Laibinis, P. E.; Wang, D. I. C.; Hatton, T. A. Controlled clustering and enhanced stability of polymer-coated magnetic nanoparticles. *Langmuir* **2005**, *21* (13), 6006-6018.
(47) Golas, P. L.; Louie, S.; Lowry, G. V.; Matyjaszewski, K.; Tilton, R. D. Comparative study of polymeric stabilizers for magnetite nanoparticles using ATRP. *Langmuir* **2010**, *26* (22), 16890-16900.
(48) Kamiya, H.; Iijima, M. Surface modification and characterization for dispersion stability of inorganic nanometer-scaled particles in liquid media. *Sci. Technol. Adv. Mater.* **2010**, *11* (4).
(49) Pachon, L. D.; Rothenberg, G. Transition-metal nanoparticles: Synthesis, stability and the leaching issue. *Appl. Organomet. Chem.* **2008**, *22* (6), 288-299.
(50) Wu, W.; He, Q. G.; Jiang, C. Z. Magnetic iron oxide nanoparticles: Synthesis and surface functionalization strategies. *Nanoscale Res. Lett.* **2008**, *3* (11), 397-415.
(51) Tolaymat, T. M.; El Badawy, A. M.; Genaidy, A.; Scheckel, K. G.; Luxton, T. P.; Suidan, M. An evidence-based environmental perspective of manufactured silver nanoparticle in syntheses and applications: A systematic review and critical appraisal of peer-reviewed scientific papers. *Sci. Total Environ.* **2010**, *408* (5), 999-1006.
(52) Zhang, W. X. Nanoscale iron particles for environmental remediation: An overview. *J. Nanopart. Res.* **2003**, *5* (3-4), 323-332.
(53) Phenrat, T.; Cihan, A.; Kim, H. J.; Mital, M.; Illangasekare, T.; Lowry, G. V. Transport and deposition of polymer-modified Fe-0 nanoparticles in 2-D heterogeneous porous media: Effects of particle concentration, Fe-0 content, and coatings. *Environ. Sci. Technol.* **2010**, *44* (23), 9086-9093.
(54) Phenrat, T.; Saleh, N.; Sirk, K.; Kim, H. J.; Tilton, R. D.; Lowry, G. V. Stabilization of aqueous nanoscale zerovalent iron dispersions by anionic polyelectrolytes: adsorbed anionic polyelectrolyte layer properties and their effect on aggregation and sedimentation. *J. Nanopart. Res.* **2008**, *10* (5), 795-814.
(55) Amstad, E.; Textor, M.; Reimhult, E. Stabilization and functionalization of iron oxide nanoparticles for biomedical applications. *Nanoscale* **2011**, *3* (7), 2819-2843.
(56) Galvin, P.; Thompson, D.; Ryan, K. B.; McCarthy, A.; Moore, A. C.; Burke, C. S.; Dyson, M.; MacCraith, B. D.; Gun'ko, Y. K.; Byrne, M. T.; Volkov, Y.; Keely, C.; Keehan, E.; Howe, M.; Duffy, C.; MacLoughlin, R. Nanoparticle-based drug delivery: Case studies for cancer and cardiovascular applications. *Cell. Mol. Life Sci.* **2012**, *69* (3), 389-404.
(57) Gupta, A. K.; Naregalkar, R. R.; Vaidya, V. D.; Gupta, M. Recent advances on surface engineering of magnetic iron oxide nanoparticles and their biomedical applications. *Nanomedicine* **2007**, *2* (1), 23-39.
(58) Otsuka, H.; Nagasaki, Y.; Kataoka, K. PEGylated nanoparticles for biological and pharmaceutical applications. *Adv. Drug Delivery Rev.* **2012**, *64*, 246-255.
(59) Shan, J.; Tenhu, H. Recent advances in polymer protected gold nanoparticles: Synthesis, properties and applications. *Chem. Commun.* **2007**, (44), 4580-4598.

(60) Yoo, J. W.; Chambers, E.; Mitragotri, S. Factors that control the circulation time of nanoparticles in blood: Challenges, solutions and future prospects. *Curr. Pharm. Des.* **2010**, *16* (21), 2298-2307.
(61) Grubbs, R. B. Roles of polymer ligands in nanoparticle stabilization. *Polym. Rev.* **2007**, *47* (2), 197-215.
(62) Diagne, F.; Malaisamy, R.; Boddie, V.; Holbrook, R. D.; Eribo, B.; Jones, K. L. Polyelectrolyte and silver nanoparticle modification of microfiltration membranes to mitigate organic and bacterial fouling. *Environ. Sci. Technol.* **2012**, *46* (7), 4025-4033.
(63) Duncan, T. V. Applications of nanotechnology in food packaging and food safety: Barrier materials, antimicrobials and sensors. *J. Colloid Interface Sci.* **2011**, *363* (1), 1-24.
(64) Taylor, E.; Webster, T. J. Reducing infections through nanotechnology and nanoparticles. *Int. J. Nanomed.* **2011**, *6*, 1463-1473.
(65) Thurman, E. M. *Organic geochemistry of natural waters*; Martinus Nijhoff/Dr W. Junk Publishsers: Dordrecht, **1985**.
(66) Brar, S. K.; Verma, M.; Tyagi, R. D.; Surampalli, R. Y. Engineered nanoparticles in wastewater and wastewater sludge - Evidence and impacts. *Waste Manage.* **2010**, *30* (3), 504-520.
(67) Bone, A. J.; Colman, B. P.; Gondikas, A. P.; Newton, K. M.; Harrold, K. H.; Cory, R. M.; Unrine, J. M.; Klaine, S. J.; Matson, C. W.; Di Giulio, R. T. Biotic and abiotic interactions in aquatic microcosms determine fate and toxicity of Ag nanoparticles: Part 2-Toxicity and Ag speciation. *Environ. Sci. Technol.* **2012**, *46* (13), 6925-6933.
(68) Cherchi, C.; Chernenko, T.; Diem, M.; Gu, A. Z. Impact of nano titanium dioxide exposure on cellular structure of Anabaena variabilis and evidence of internalization. *Environ. Toxicol. Chem.* **2011**, *30* (4), 861-869.
(69) Miao, A. J.; Schwehr, K. A.; Xu, C.; Zhang, S. J.; Luo, Z. P.; Quigg, A.; Santschi, P. H. The algal toxicity of silver engineered nanoparticles and detoxification by exopolymeric substances. *Environ. Pollut.* **2009**, *157* (11), 3034-3041.
(70) Unrine, J. M.; Colman, B. P.; Bone, A. J.; Gondikas, A. P.; Matson, C. W. Biotic and abiotic interactions in aquatic microcosms determine fate and toxicity of Ag nanoparticles: Part 1 - Aggregation and dissolution. *Environ. Sci. Technol.* **2012**, *46* (13), 6915-6924.
(71) Chaboud, A. Isolation, purification and chemical composition of maize root cap slime. *Plant and Soil* **1983**, *73* (3), 395-402.
(72) Flemming, H. C.; Wingender, J. Relevance of microbial extracellular polymeric substances (EPSs) - Part I: Structural and ecological aspects. *Water Sci. Technol.* **2001**, *43* (6), 1-8.
(73) Rovira, A. D. Plant root exudates. *Bot. Rev.* **1969**, *35* (1), 35-&.
(74) Grobe, S.; Wingender, J.; Truper, H. G. Characterization of mucoid *Pseudomonas aeruginosa* strains isolated from technical water systems. *J. Appl. Bacteriol.* **1995**, *79* (1), 94-102.
(75) Bura, R.; Cheung, M.; Liao, B.; Finlayson, J.; Lee, B. C.; Droppo, I. G.; Leppard, G. G.; Liss, S. N. Composition of extracellular polymeric substances in the activated sludge floc matrix. *Water Sci. Technol.* **1998**, *37* (4-5), 325-333.
(76) Filella, M. Freshwaters: Which NOM matters? *Environ. Chem. Lett.* **2009**, *7* (1), 21-35.
(77) Aluwihare, L. I.; Repeta, D. J. A comparison of the chemical characteristics of oceanic DOM and extracellular DOM produced by marine algae. *Mar. Ecol. Prog. Ser.* **1999**, *186*, 105-117.

(78) Frimmel, F. H. Aquatic humic substances. In *Lignin, humic substances and coal*; Hofrichter, M., Steinbüchel, A., Eds.; Wiley-Blackwell: Weinheim, Germany, **2001**; Vol. 1, pp 301-310.
(79) MacCarthy, P.; Ghabbour, E. A.; Davies, G. The principles of humic substances: An introduction to the first principle. In *Humic substances: Structures, models and functions*; The Royal Society of Chemistry, **2001**; pp 19-30.
(80) Tiller, C. L.; Omelia, C. R. Natural organic matter and colloidal stability: Models and measurements. *Colloids Surf., A* **1993**, *73*, 89-102.
(81) Chen, K. L.; Mylon, S. E.; Elimelech, M. Aggregation kinetics of alginate-coated hematite nanoparticles in monovalent and divalent electrolytes. *Environ. Sci. Technol.* **2006**, *40* (5), 1516-1523.
(82) Hotze, E. M.; Louie, S. M.; Lin, S.; Wiesner, M. R.; Lowry, G. V. Nanoparticle core properties affect attachment of macromolecule-coated nanoparticles to silica surfaces. *Environ. Chem.* **2014**, *11* (3), 257-267.
(83) Wilkinson, K. J.; Balnois, E.; Leppard, G. G.; Buffle, J. Characteristic features of the major components of freshwater colloidal organic matter revealed by transmission electron and atomic force microscopy. *Colloids Surf., A* **1999**, *155* (2-3), 287-310.
(84) Filella, M.; Buffle, J.; Leppard, G. G. Characterization of submicrometre colloids in freshwaters: Evidence for their bridging by oganic structures. *Water Sci. Technol.* **1993**, *27* (11), 91-102.
(85) Chen, K. L.; Mylon, S. E.; Elimelech, M. Enhanced aggregation of alginate-coated iron oxide (hematite) nanoparticles in the presence of calcium, strontium, and barium cations. *Langmuir* **2007**, *23* (11), 5920-5928.
(86) Schwyzer, I.; Kaegi, R.; Sigg, L.; Nowack, B. Colloidal stability of suspended and agglomerate structures of settled carbon nanotubes in different aqueous matrices. *Water Res.* **2013**, *47* (12), 3910-3920.
(87) Patra, M.; Linse, P. Reorganization of nanopatterned polymer brushes by the AFM measurement process. *Macromolecules* **2006**, *39* (13), 4540-4546.
(88) Pensini, E.; Sleep, B. E.; Yip, C. M.; O'Carroll, D. Forces of interactions between bare and polymer-coated iron and silica: Effect of pH, ionic strength, and humic acids. *Environ. Sci. Technol.* **2012**, *46* (24), 13401-13408.
(89) Ghosh, S.; Mashayekhi, H.; Bhowmik, P.; Xing, B. S. Colloidal stability of Al_2O_3 nanoparticles as affected by coating of structurally different humic acids. *Langmuir* **2010**, *26* (2), 873-879.
(90) Min, G. K.; Bevan, M. A.; Prieve, D. C.; Patterson, G. D. Light scattering characterization of polystyrene latex with and without adsorbed polymer. *Colloids Surf., A* **2002**, *202* (1), 9-21.
(91) Dieckmann, Y.; Colfen, H.; Hofmann, H.; Petri-Fink, A. Particle size distribution measurements of manganese-doped ZnS nanoparticles. *Anal. Chem.* **2009**, *81* (10), 3889-3895.
(92) Domingos, R. F.; Baalousha, M. A.; Ju-Nam, Y.; Reid, M. M.; Tufenkji, N.; Lead, J. R.; Leppard, G. G.; Wilkinson, K. J. Characterizing manufactured nanoparticles in the environment: Multimethod determination of particle sizes. *Environ. Sci. Technol.* **2009**, *43* (19), 7277-7284.
(93) Mahl, D.; Diendorf, J.; Meyer-Zaika, W.; Epple, M. Possibilities and limitations of different analytical methods for the size determination of a bimodal dispersion of metallic nanoparticles. *Colloids Surf., A* **2011**, *377* (1-3), 386-392.

(94) Franchi, A.; O'Melia, C. R. Effects of natural organic matter and solution chemistry on the deposition and reentrainment of colloids in porous media. *Environ. Sci. Technol.* **2003**, *37* (6), 1122-1129.
(95) Morales, V. L.; Sang, W. J.; Fuka, D. R.; Lion, L. W.; Gao, B.; Steenhuis, T. S. Correlation equation for predicting attachment efficiency (alpha) of organic matter-colloid complexes in unsaturated porous media. *Environ. Sci. Technol.* **2011**, *45* (23), 10096-10101.
(96) Morales, V. L.; Zhang, W.; Gao, B.; Lion, L. W.; Bisogni, J. J.; McDonough, B. A.; Steenhuis, T. S. Impact of dissolved organic matter on colloid transport in the vadose zone: Deterministic approximation of transport deposition coefficients from polymeric coating characteristics. *Water Res.* **2011**, *45* (4), 1691-1701.
(97) Gigault, J.; Hackley, V. A. Observation of size-independent effects in nanoparticle retention behavior during asymmetric-flow field-flow fractionation. *Anal. Bioanal. Chem.* **2013**, *405* (19), 6251-6258.
(98) Baalousha, M.; Manciulea, A.; Cumberland, S.; Kendall, K.; Lead, J. R. Aggregation and surface properties of iron oxide nanoparticles: Influence of pH and natural organic matter. *Environ. Toxicol. Chem.* **2008**, *27* (9), 1875-1882.
(99) Cumberland, S. A.; Lead, J. R. Particle size distributions of silver nanoparticles at environmentally relevant conditions. *J. Chormatogr. A* **2009**, *1216* (52), 9099-9105.
(100) Falabella, J. B.; Cho, T. J.; Ripple, D. C.; Hackley, V. A.; Tarlov, M. J. Characterization of Gold Nanoparticles Modified with Single-Stranded DNA Using Analytical Ultracentrifugation and Dynamic Light Scattering. *Langmuir* **2010**, *26* (15), 12740-12747.
(101) Monopoli, M. P.; Walczyk, D.; Campbell, A.; Elia, G.; Lynch, I.; Bombelli, F. B.; Dawson, K. A. Physical-chemical aspects of protein corona: Relevance to *in vitro* and *in vivo* biological impacts of nanoparticles. *J. Am. Chem. Soc.* **2011**, *133* (8), 2525-2534.
(102) Cosgrove, T.; Heath, T. G.; Ryan, K.; Crowley, T. L. Neutron scattering from adsorbed polymer layers. *Macromolecules* **1987**, *20* (11), 2879-2882.
(103) Jarvie, H. P.; King, S. M. Small-angle neutron scattering study of natural aquatic nanocolloids. *Environ. Sci. Technol.* **2007**, *41* (8), 2868-2873.
(104) King, S. M.; Jarvie, H. P. Exploring how organic matter controls structural transformations in natural aquatic nanocolloidal dispersions. *Environ. Sci. Technol.* **2012**, *46* (13), 6959-6967.
(105) Joo, S. H.; Al-Abed, S. R.; Luxton, T. Influence of carboxymethyl cellulose for the transport of titanium dioxide nanoparticles in clean silica and mineral-coated sands. *Environ. Sci. Technol.* **2009**, *43* (13), 4954-4959.
(106) Xie, J.; Xu, C.; Kohler, N.; Hou, Y.; Sun, S. Controlled PEGylation of monodisperse Fe3O4 nanoparticles for reduced non-specific uptake by macrophage cells. *Adv. Mater.* **2007**, *19* (20), 3163-3166.
(107) Larsericsdotter, H.; Oscarsson, S.; Buijs, J. Thermodynamic analysis of proteins adsorbed on silica particles: Electrostatic effects. *J. Colloid Interface Sci.* **2001**, *237* (1), 98-103.
(108) Welzel, P. B. Investigation of adsorption-induced structural changes of proteins at solid/liquid interfaces by differential scanning calorimetry. *Thermochim. Acta* **2002**, *382* (1-2), 175-188.
(109) Shan, J.; Chen, J.; Nuopponen, M.; Tenhu, H. Two phase transitions of poly(N-isopropylacrylamide) brushes bound to gold nanoparticles. *Langmuir* **2004**, *20* (11), 4671-4676.

(110) Iosin, M.; Toderas, F.; Baldeck, P. L.; Astilean, S. Study of protein-gold nanoparticle conjugates by fluorescence and surface-enhanced Raman scattering. *J. Mol. Struct.* **2009**, *924-26*, 196-200.
(111) Wangoo, N.; Suri, C. R.; Shekhawat, G. Interaction of gold nanoparticles with protein: A spectroscopic study to monitor protein conformational changes. *Appl. Phys. Lett.* **2008**, *92* (13).
(112) You, C. C.; Miranda, O. R.; Gider, B.; Ghosh, P. S.; Kim, I. B.; Erdogan, B.; Krovi, S. A.; Bunz, U. H. F.; Rotello, V. M. Detection and identification of proteins using nanoparticle-fluorescent polymer 'chemical nose' sensors. *Nat. Nanotechnol.* **2007**, *2* (5), 318-323.
(113) Lau, B. L. T.; Hockaday, W. C.; Ikuma, K.; Furman, O.; Decho, A. W. A preliminary assessment of the interactions between the capping agents of silver nanoparticles and environmental organics. *Colloids Surf., A* **2013**, *435*, 22-27.
(114) Cooper, C. L.; Cosgrove, T.; van Duijneveldt, J. S.; Murray, M.; Prescott, S. W. Competition between polymers for adsorption on silica: A solvent relaxation NMR and small-angle neutron scattering study. *Langmuir* **2013**, *29* (41), 12670-12678.
(115) Levard, C.; Reinsch, B. C.; Michel, F. M.; Oumahi, C.; Lowry, G. V.; Brown, G. E. Sulfidation processes of PVP-coated silver nanoparticles in aqueous solution: Impact on dissolution rate. *Environ. Sci. Technol.* **2011**, *45* (12), 5260-5266.
(116) Baer, D. R.; Gaspar, D. J.; Nachimuthu, P.; Techane, S. D.; Castner, D. G. Application of surface chemical analysis tools for characterization of nanoparticles. *Anal. Bioanal. Chem.* **2010**, *396* (3), 983-1002.
(117) Badireddy, A. R.; Wiesner, M. R.; Liu, J. Detection, characterization, and abundance of engineered nanoparticles in complex waters by hyperspectral imagery with enhanced darkfield microscopy. *Environ. Sci. Technol.* **2012**, *46* (18), 10081-10088.
(118) Vikesland, P. J.; Wigginton, K. R. Nanomaterial enabled biosensors for pathogen monitoring - A review. *Environ. Sci. Technol.* **2010**, *44* (10), 3656-3669.
(119) Corrado, G.; Sanchez-Cortes, S.; Francioso, O.; Garcia-Ramos, J. V. Surface-enhanced Raman and fluorescence joint analysis of soil humic acids. *Anal. Chim. Acta* **2008**, *616* (1), 69-77.
(120) Shao, Q.; Wu, P.; Gu, P. A.; Xu, X. Q.; Zhang, H.; Cai, C. X. Electrochemical and spectroscopic studies on the conformational structure of hemoglobin assembled on gold nanoparticles. *J. Phys. Chem. B* **2011**, *115* (26), 8627-8637.
(121) Gebauer, J. S.; Malissek, M.; Simon, S.; Knauer, S. K.; Maskos, M.; Stauber, R. H.; Peukert, W.; Treuel, L. Impact of the nanoparticle-protein corona on colloidal stability and protein structure. *Langmuir* **2012**, *28* (25), 9673-9679.
(122) Treuel, L.; Malissek, M.; Grass, S.; Diendorf, J.; Mahl, D.; Meyer-Zaika, W.; Epple, M. Quantifying the influence of polymer coatings on the serum albumin corona formation around silver and gold nanoparticles. *J. Nanopart. Res.* **2012**, *14* (9).
(123) Navarro, D. A.; Depner, S. W.; Watson, D. F.; Aga, D. S.; Banerjee, S. Partitioning behavior and stabilization of hydrophobically coated HfO2, ZrO2 and HfxZr1-xO2 nanoparticles with natural organic matter reveal differences dependent on crystal structure. *J. Hazard. Mater.* **2011**, *196*, 302-310.
(124) Tsai, D. H.; Shelton, M. P.; DelRio, F. W.; Elzey, S.; Guha, S.; Zachariah, M. R.; Hackley, V. A. Quantifying dithiothreitol displacement of functional ligands from gold nanoparticles. *Anal. Bioanal. Chem.* **2012**, *404* (10), 3015-3023.
(125) Tsai, D. H.; Davila-Morris, M.; DelRio, F. W.; Guha, S.; Zachariah, M. R.; Hackley, V. A. Quantitative determination of competitive molecular adsorption on gold nanoparticles using

attenuated total reflectance-Fourier transform infrared spectroscopy. *Langmuir* **2011**, *27* (15), 9302-9313.
(126) Baier, G.; Costa, C.; Zeller, A.; Baumann, D.; Sayer, C.; Araujo, P. H. H.; Mailander, V.; Musyanovych, A.; Landfester, K. BSA adsorption on differently charged polystyrene nanoparticles using isothermal titration calorimetry and the influence on cellular uptake. *Macromol. Biosci.* **2011**, *11* (5), 628-638.
(127) Cedervall, T.; Lynch, I.; Lindman, S.; Berggard, T.; Thulin, E.; Nilsson, H.; Dawson, K. A.; Linse, S. Understanding the nanoparticle-protein corona using methods to quantify exchange rates and affinities of proteins for nanoparticles. *Proc. Natl. Acad. Sci. U.S.A.* **2007**, *104* (7), 2050-2055.
(128) De, M.; You, C. C.; Srivastava, S.; Rotello, V. M. Biomimetic interactions of proteins with functionalized nanoparticles: A thermodynamic study. *J. Am. Chem. Soc.* **2007**, *129* (35), 10747-10753.
(129) McFarlane, N. L.; Wagner, N. J.; Kaler, E. W.; Lynch, M. L. Calorimetric study of the adsorption of poly(ethylene oxide) and poly(vinyl pyrrolidone) onto cationic nanoparticles. *Langmuir* **2010**, *26* (9), 6262-6267.
(130) Ritchie, J. D.; Perdue, E. M. Proton-binding study of standard and reference fulvic acids, humic acids, and natural organic matter. *Geochim. Cosmochim. Acta* **2003**, *67* (1), 85-96.
(131) Chowdhury, I.; Cwiertny, D. M.; Walker, S. L. Combined factors influencing the aggregation and deposition of nano-TiO_2 in the presence of humic acid and bacteria. *Environ. Sci. Technol.* **2012**, *46* (13), 6968-6976.
(132) Phenrat, T.; Song, J. E.; Cisneros, C. M.; Schoenfelder, D. P.; Tilton, R. D.; Lowry, G. V. Estimating attachment of nano- and submicrometer-particles coated with organic macromolecules in porous media: Development of an empirical model. *Environ. Sci. Technol.* **2010**, *44* (12), 4531-4538.
(133) Celiz, M. D.; Colon, L. A.; Watson, D. F.; Aga, D. S. Study on the effects of humic and fulvic acids on quantum dot nanoparticles using capillary electrophoresis with laser-induced fluorescence detection. *Environ. Sci. Technol.* **2011**, *45* (7), 2917-2924.
(134) Tsai, D. H.; DelRio, F. W.; MacCuspie, R. I.; Cho, T. J.; Zachariah, M. R.; Hackley, V. A. Competitive adsorption of thiolated polyethylene glycol and mercaptopropionic acid on gold nanoparticles measured by physical characterization methods. *Langmuir* **2010**, *26* (12), 10325-10333.
(135) Xiao, Y.; Wiesner, M. R. Characterization of surface hydrophobicity of engineered nanoparticles. *J. Hazard. Mater.* **2012**, *215*, 146-151.
(136) Tsai, D. H.; DelRio, F. W.; Keene, A. M.; Tyner, K. M.; MacCuspie, R. I.; Cho, T. J.; Zachariah, M. R.; Hackley, V. A. Adsorption and conformation of serum albumin protein on gold nanoparticles investigated using dimensional measurements and in situ spectroscopic methods. *Langmuir* **2011**, *27* (6), 2464-2477.
(137) Stebounova, L. V.; Guio, E.; Grassian, V. H. Silver nanoparticles in simulated biological media: A study of aggregation, sedimentation, and dissolution. *J. Nanopart. Res.* **2011**, *13* (1), 233-244.
(138) Kong, H.; Lu, Y. X.; Wang, H.; Wen, F.; Zhang, S. C.; Zhang, X. R. Protein discrimination using fluorescent gold nanoparticles on plasmonic substrates. *Anal. Chem.* **2012**, *84* (10), 4258-4261.

(139) Cosgrove, T.; Finch, N.; Webster, J. Nuclear magnetic resonance, small-angle neutron scattering and Monte Carlo studies of adsorbed random copolymers. *Colloids and Surfaces* **1990**, *45*, 377-389.
(140) Stenkamp, V. S.; Berg, J. C. The role of long tails in steric stabilization and hydrodynamic layer thickness. *Langmuir* **1997**, *13* (14), 3827-3832.
(141) Vaccaro, A.; Hierrezuelo, J.; Skarba, M.; Galletto, P.; Kleimann, J.; Borkovec, M. Structure of an adsorbed polyelectrolyte monolayer on oppositely charged colloidal particles. *Langmuir* **2009**, *25* (9), 4864-4867.
(142) Pettitt, M. E.; Lead, J. R. Minimum physicochemical characterisation requirements for nanomaterial regulation. *Environ. Int.* **2013**, *52*, 41-50.
(143) Doane, T. L.; Chuang, C. H.; Hill, R. J.; Burda, C. Nanoparticle zeta-potentials. *Acc. Chem. Res.* **2012**, *45* (3), 317-326.
(144) Flory, P. J. *Principles of polymer chemistry*; 1st ed.; Cornell University Press: Ithaca, **1953**.
(145) Bian, S. W.; Mudunkotuwa, I. A.; Rupasinghe, T.; Grassian, V. H. Aggregation and dissolution of 4 nm ZnO nanoparticles in aqueous environments: Influence of pH, ionic strength, size, and adsorption of humic acid. *Langmuir* **2011**, *27* (10), 6059-6068.
(146) Illes, E.; Tombacz, E. The effect of humic acid adsorption on pH-dependent surface charging and aggregation of magnetite nanoparticles. *J. Colloid Interface Sci.* **2006**, *295* (1), 115-123.
(147) Abe, T.; Kobayashi, S.; Kobayashi, M. Aggregation of colloidal silica particles in the presence of fulvic acid, humic acid, or alginate: Effects of ionic composition. *Colloids Surf., A* **2011**, *379* (1-3), 21-26.
(148) Liu, X. Y.; Wazne, M.; Chou, T. M.; Xiao, R.; Xu, S. Y. Influence of Ca2+ and Suwannee River Humic Acid on aggregation of silicon nanoparticles in aqueous media. *Water Res.* **2011**, *45* (1), 105-112.
(149) Westerhoff, P.; Nowack, B. Searching for global descriptors of engineered nanomaterial fate and transport in the environment. *Acc. Chem. Res.* **2013**, *46* (3), 844-853.
(150) Massachusetts Department of Elementary and Secondary Education. *2008 MCAS High School Biology*; **2014**; http://www.doe.mass.edu/mcas/student/2008/question.aspx?GradeID=100&SubjectCode=bio_hs&QuestionTypeName=&QuestionID=5944.
(151) Keller, A. A.; Wang, H. T.; Zhou, D. X.; Lenihan, H. S.; Cherr, G.; Cardinale, B. J.; Miller, R.; Ji, Z. X. Stability and aggregation of metal oxide nanoparticles in natural aqueous matrices. *Environ. Sci. Technol.* **2010**, *44* (6), 1962-1967.
(152) Ottofuelling, S.; Von der Kammer, F.; Hofmann, T. Commercial titanium dioxide nanoparticles in both natural and synthetic water: Comprehensive multidimensional testing and prediction of aggregation behavior. *Environ. Sci. Technol.* **2011**, *45* (23), 10045-10052.
(153) Hyung, H.; Kim, J. H. Natural organic matter (NOM) adsorption to multi-walled carbon nanotubes: Effect of NOM characteristics and water quality parameters. *Environ. Sci. Technol.* **2008**, *42* (12), 4416-4421.
(154) Guo, X.; Ballauff, M. Spatial dimensions of colloidal polyelectrolyte brushes as determined by dynamic light scattering. *Langmuir* **2000**, *16* (23), 8719-8726.
(155) Hariharan, R.; Biver, C.; Mays, J.; Russel, W. B. Ionic strength and curvature effects in flat and highly curved polyelectrolyte brushes. *Macromolecules* **1998**, *31* (21), 7506-7513.

(156) Chen, K. L.; Elimelech, M. Influence of humic acid on the aggregation kinetics of fullerene (C-60) nanoparticles in monovalent and divalent electrolyte solutions. *J. Colloid Interface Sci.* **2007**, *309* (1), 126-134.
(157) Stankus, D. P.; Lohse, S. E.; Hutchison, J. E.; Nason, J. A. Interactions between natural organic matter and gold nanoparticles stabilized with different organic capping agents. *Environ. Sci. Technol.* **2011**, *45* (8), 3238-3244.
(158) Zhang, Y.; Chen, Y. S.; Westerhoff, P.; Crittenden, J. Impact of natural organic matter and divalent cations on the stability of aqueous nanoparticles. *Water Res.* **2009**, *43* (17), 4249-4257.
(159) Saleh, N. B.; Pfefferle, L. D.; Elimelech, M. Influence of biomacromolecules and humic acid on the aggregation kinetics of single-walled carbon nanotubes. *Environ. Sci. Technol.* **2010**, *44* (7), 2412-2418.
(160) Joshi, N.; Ngwenya, B. T.; French, C. E. Enhanced resistance to nanoparticle toxicity is conferred by overproduction of extracellular polymeric substances. *J. Hazard. Mater.* **2012**, *241*, 363-370.
(161) Carder, K. L.; Steward, R. G.; Harvey, G. R.; Ortner, P. B. Marine humic and fulvic-acids - Their effects on remote-sensing of ocean chlorophyll. *Limnol. Oceanogr.* **1989**, *34* (1), 68-81.
(162) Chin, Y. P.; Aiken, G.; Oloughlin, E. Molecular-weight, polydispersity, and spectroscopic properties of aquatic humic substances. *Environ. Sci. Technol.* **1994**, *28* (11), 1853-1858.
(163) Espinasse, B.; Hotze, E. M.; Wiesner, M. R. Transport and retention of colloidal aggregates of C-60 in porous media: Effects of organic macromolecules, ionic composition, and preparation method. *Environ. Sci. Technol.* **2007**, *41* (21), 7396-7402.
(164) Deonarine, A.; Lau, B. L. T.; Aiken, G. R.; Ryan, J. N.; Hsu-Kim, H. Effects of humic substances on precipitation and aggregation of zinc sulfide nanoparticles. *Environ. Sci. Technol.* **2011**, *45* (8), 3217-3223.
(165) Furman, O.; Usenko, S.; Lau, B. L. T. Relative importance of the humic and fulvic fractions of natural organic matter in the aggregation and deposition of silver nanoparticles. *Environ. Sci. Technol.* **2013**, *47* (3), 1349-1356.
(166) Nason, J. A.; McDowell, S. A.; Callahan, T. W. Effects of natural organic matter type and concentration on the aggregation of citrate-stabilized gold nanoparticles. *J. Environ. Monit.* **2012**, *14* (7), 1885-1892.
(167) Liu, X. Y.; Chen, G. X.; Su, C. M. Influence of collector surface composition and water chemistry on the deposition of cerium dioxide nanoparticles: QCM-D and column experiment approaches. *Environ. Sci. Technol.* **2012**, *46* (12), 6681-6688.
(168) Pelley, A. J.; Tufenkji, N. Effect of particle size and natural organic matter on the migration of nano- and microscale latex particles in saturated porous media. *J. Colloid Interface Sci.* **2008**, *321* (1), 74-83.
(169) Louie, S. M.; Tilton, R. D.; Lowry, G. V. Effects of molecular weight distribution and chemical properties of natural organic matter on gold nanoparticle aggregation. *Environ. Sci. Technol.* **2013**, *47* (9), 4245-4254.
(170) Gu, B. H.; Schmitt, J.; Chen, Z.; Liang, L. Y.; Mccarthy, J. F. Adsorption and desorption of different organic-matter fractions on iron-oxide. *Geochim. Cosmochim. Acta* **1995**, *59* (2), 219-229.

(171) Vermeer, A. W. P.; Koopal, L. K. Adsorption of humic acids to mineral particles. 2. Polydispersity effects with polyelectrolyte adsorption. *Langmuir* **1998**, *14* (15), 4210-4216.
(172) Davis, J. A.; Gloor, R. Adsorption of dissolved organics in lake water by aluminum-oxide - Effect of molecular-weight. *Environ. Sci. Technol.* **1981**, *15* (10), 1223-1229.
(173) Amirbahman, A.; Olson, T. M. Transport of humic matter-coated hematite in packed-beds. *Environ. Sci. Technol.* **1993**, *27* (13), 2807-2813.
(174) Ghosh, S.; Mashayekhi, H.; Pan, B.; Bhowmik, P.; Xing, B. S. Colloidal behavior of aluminum oxide nanoparticles as affected by pH and natural organic matter. *Langmuir* **2008**, *24* (21), 12385-12391.
(175) Hur, J.; Schlautman, M. A. Molecular weight fractionation of humic substances by adsorption onto minerals. *J. Colloid Interface Sci.* **2003**, *264* (2), 313-321.
(176) Chi, F. H.; Amy, G. L. Kinetic study on the sorption of dissolved natural organic matter onto different aquifer materials: the effects of hydrophobicity and functional groups. *J. Colloid Interface Sci.* **2004**, *274* (2), 380-391.
(177) Joo, J. C.; Shackelford, C. D.; Reardon, K. F. Association of humic acid with metal (hydr)oxide-coated sands at solid-water interfaces. *J. Colloid Interface Sci.* **2008**, *317* (2), 424-433.
(178) Jones, E. H.; Su, C. M. Fate and transport of elemental copper (Cu-0) nanoparticles through saturated porous media in the presence of organic materials. *Water Res.* **2012**, *46* (7), 2445-2456.
(179) Wang, Y. G.; Li, Y. S.; Costanza, J.; Abriola, L. M.; Pennell, K. D. Enhanced mobility of fullerene (C-60) nanoparticles in the presence of stabilizing agents. *Environ. Sci. Technol.* **2012**, *46* (21), 11761-11769.
(180) Ji, Z. X.; Jin, X.; George, S.; Xia, T. A.; Meng, H. A.; Wang, X.; Suarez, E.; Zhang, H. Y.; Hoek, E. M. V.; Godwin, H.; Nel, A. E.; Zink, J. I. Dispersion and stability optimization of TiO_2 nanoparticles in cell culture media. *Environ. Sci. Technol.* **2010**, *44* (19), 7309-7314.
(181) Liu, J. F.; Legros, S.; Von der Kammer, F.; Hofmann, T. Natural organic matter concentration and hydrochemistry influence aggregation kinetics of functionalized engineered nanoparticles. *Environ. Sci. Technol.* **2013**, *47* (9), 4113-4120.
(182) Hitchman, A.; Smith, G. H. S.; Ju-Nam, Y.; Sterling, M.; Lead, J. R. The effect of environmentally relevant conditions on PVP stabilised gold nanoparticles. *Chemosphere* **2013**, *90* (2), 410-416.
(183) Lin, S. H.; Cheng, Y. W.; Liu, J.; Wiesner, M. R. Polymeric coatings on silver nanoparticles hinder autoaggregation but enhance attachment to uncoated surfaces. *Langmuir* **2012**, *28* (9), 4178-4186.
(184) Johnson, R. L.; Johnson, G. O.; Nurmi, J. T.; Tratnyek, P. G. Natural organic matter enhanced mobility of nano zerovalent iron. *Environ. Sci. Technol.* **2009**, *43* (14), 5455-5460.
(185) Khan, I. A.; Berge, N. D.; Sabo-Attwood, T.; Ferguson, P. L.; Saleh, N. B. Single-walled carbon nanotube transport in representative municipal solid waste landfill conditions. *Environ. Sci. Technol.* **2013**, *47* (15), 8425-8433.
(186) Chen, K. L.; Elimelech, M. Interaction of fullerene (C-60) nanoparticles with humic acid and alginate coated silica surfaces: measurements, mechanisms, and environmental implications. *Environ. Sci. Technol.* **2008**, *42* (20), 7607-7614.
(187) Song, J. E.; Phenrat, T.; Marinakos, S.; Xiao, Y.; Liu, J.; Wiesner, M. R.; Tilton, R. D.; Lowry, G. V. Hydrophobic Interactions Increase Attachment of Gum Arabic- and PVP-Coated Ag Nanoparticles to Hydrophobic Surfaces. *Environ. Sci. Technol.* **2011**, *45* (14), 5988-5995.

(188) Fürrer, G.; Stumm, W. The coordination chemistry of weathering: I. Dissolution kinetics of δ-Al_2O_3 and BeO. *Geochim. Cosmochim. Acta* **1986**, *50* (9), 1847-1860.
(189) Panias, D.; Taxiarchou, M.; Paspaliaris, I.; Kontopoulos, A. Mechanisms of dissolution of iron oxides in aqueous oxalic acid solutions. *Hydrometallurgy* **1996**, *42* (2), 257-265.
(190) Hersman, L.; Lloyd, T.; Sposito, G. Siderophore-promoted dissolution of hematite. *Geochim. Cosmochim. Acta* **1995**, *59* (16), 3327-3330.
(191) Holmen, B. A.; Casey, W. H. Hydroxamate ligands, surface chemistry, and the mechanism of ligand-promoted dissolution of goethite [alpha-FeOOH(s)]. *Geochim. Cosmochim. Acta* **1996**, *60* (22), 4403-4416.
(192) Jones, D. L. Organic acids in the rhizosphere - a critical review. *Plant and Soil* **1998**, *205* (1), 25-44.
(193) Zhang, P.; Ma, Y. H.; Zhang, Z. Y.; He, X.; Zhang, J.; Guo, Z.; Tai, R. Z.; Zhao, Y. L.; Chai, Z. F. Biotransformation of ceria nanoparticles in cucumber plants. *ACS Nano* **2012**, *6* (11), 9943-9950.
(194) Li, L. Z.; Zhou, D. M.; Peijnenburg, W. J. G. M.; van Gestel, C. A. M.; Jin, S. Y.; Wang, Y. J.; Wang, P. Toxicity of zinc oxide nanoparticles in the earthworm, Eisenia fetida and subcellular fractionation of Zn. *Environ. Int.* **2011**, *37* (6), 1098-1104.
(195) Mudunkotuwa, I. A.; Rupasinghe, T.; Wu, C. M.; Grassian, V. H. Dissolution of ZnO nanoparticles at circumneutral pH: A study of size effects in the presence and absence of citric acid. *Langmuir* **2012**, *28* (1), 396-403.
(196) Gondikas, A. P.; Morris, A.; Reinsch, B. C.; Marinakos, S. M.; Lowry, G. V.; Hsu-Kim, H. Cysteine-induced modifications of zero-valent silver nanomaterials: Implications for particle surface chemistry, aggregation, dissolution, and silver speciation. *Environ. Sci. Technol.* **2012**, *46* (13), 7037-7045.
(197) Pokhrel, L. R.; Dubey, B.; Scheuerman, P. R. Impacts of select organic ligands on the colloidal stability, dissolution dynamics, and toxicity of silver nanoparticles. *Environ. Sci. Technol.* **2013**, *47* (22), 12877-12885.
(198) Ochs, M. Influence of humified and non-humified natural organic compounds on mineral dissolution. *Chem. Geol.* **1996**, *132* (1-4), 119-124.
(199) Ma, R.; Levard, C.; Marinakos, S. M.; Cheng, Y. W.; Liu, J.; Michel, F. M.; Brown, G. E.; Lowry, G. V. Size-controlled dissolution of organic-coated silver nanoparticles. *Environ. Sci. Technol.* **2012**, *46* (2), 752-759.
(200) Grillet, N.; Manchon, D.; Cottancin, E.; Bertorelle, F.; Bonnet, C.; Broyer, M.; Lerme, J.; Pellarin, M. Photo-oxidation of individual silver nanoparticles: A real-time tracking of optical and morphological changes. *J. Phys. Chem. C* **2013**, *117* (5), 2274-2282.
(201) Schulz, F.; Vossmeyer, T.; Bastus, N. G.; Weller, H. Effect of the spacer structure on the stability of gold nanoparticles functionalized with monodentate thiolated poly(ethylene glycol) ligands. *Langmuir* **2013**, *29* (31), 9897-9908.
(202) Li, X.; Lenhart, J. J. Aggregation and dissolution of silver nanoparticles in natural surface water. *Environ. Sci. Technol.* **2012**, *46* (10), 5378-5386.
(203) Bose, S.; Hochella, M. F.; Gorby, Y. A.; Kennedy, D. W.; McCready, D. E.; Madden, A. S.; Lower, B. H. Bioreduction of hematite nanoparticles by the dissimilatory iron reducing bacterium Shewanella oneidensis MR-1. *Geochim. Cosmochim. Acta* **2009**, *73* (4), 962-976.
(204) Fredrickson, J. K.; Gorby, Y. A. Environmental processes mediated by iron-reducing bacteria. *Curr. Opin. Biotechnol.* **1996**, *7* (3), 287-294.

(205) Auffan, M.; Achouak, W.; Rose, J.; Roncato, M. A.; Chaneac, C.; Waite, D. T.; Masion, A.; Woicik, J. C.; Wiesner, M. R.; Bottero, J. Y. Relation between the redox state of iron-based nanoparticles and their cytotoxicity toward Escherichia coli. *Environ. Sci. Technol.* **2008**, *42* (17), 6730-6735.
(206) Kang, S. H.; Choi, W. Oxidative degradation of organic compounds using zero-valent iron in the presence of natural organic matter serving as an electron shuttle. *Environ. Sci. Technol.* **2009**, *43* (3), 878-883.
(207) Niu, H. Y.; Zhang, D.; Zhang, S. X.; Zhang, X. L.; Meng, Z. F.; Cai, Y. Q. Humic acid coated Fe_3O_4 magnetic nanoparticles as highly efficient Fenton-like catalyst for complete mineralization of sulfathiazole. *J. Hazard. Mater.* **2011**, *190* (1-3), 559-565.
(208) Saleh, N.; Sirk, K.; Liu, Y. Q.; Phenrat, T.; Dufour, B.; Matyjaszewski, K.; Tilton, R. D.; Lowry, G. V. Surface modifications enhance nanoiron transport and NAPL targeting in saturated porous media. *Environ. Eng. Sci.* **2007**, *24* (1), 45-57.
(209) Phenrat, T.; Liu, Y. Q.; Tilton, R. D.; Lowry, G. V. Adsorbed polyelectrolyte coatings decrease Fe-0 nanoparticle reactivity with TCE in water: Conceptual model and mechanisms. *Environ. Sci. Technol.* **2009**, *43* (5), 1507-1514.
(210) Wang, W.; Zhou, M. H.; Jin, Z. H.; Li, T. L. Reactivity characteristics of poly(methyl methacrylate) coated nanoscale iron particles for trichloroethylene remediation. *J. Hazard. Mater.* **2010**, *173* (1-3), 724-730.
(211) Kaifas, D.; Malleret, L.; Kumar, N.; Fetimi, W.; Claeys-Bruno, M.; Sergent, M.; Doumenq, P. Assessment of potential positive effects of nZVI surface modification and concentration levels on TCE dechlorination in the presence of competing strong oxidants, using an experimental design. *Sci. Total Environ.* **2014**, *481*, 335-342.
(212) Xie, L.; Shang, C. Role of humic acid and quinone model compounds in bromate reduction by zerovalent iron. *Environ. Sci. Technol.* **2005**, *39* (4), 1092-1100.
(213) Colon, D.; Weber, E. J.; Anderson, J. L. Effect of natural organic matter on the reduction of nitroaromatics by Fe(II) species. *Environ. Sci. Technol.* **2008**, *42* (17), 6538-6543.
(214) Klausen, J.; Vikesland, P. J.; Kohn, T.; Burris, D. R.; Ball, W. P.; Roberts, A. L. Longevity of granular iron in groundwater treatment processes: Solution composition effects on reduction of organohalides and nitroaromatic compounds. *Environ. Sci. Technol.* **2003**, *37* (6), 1208-1218.
(215) Tratnyek, P. G.; Scherer, M. M.; Deng, B. L.; Hu, S. D. Effects of natural organic matter, anthropogenic surfactants, and model quinones on the reduction of contaminants by zero-valent iron. *Water Res.* **2001**, *35* (18), 4435-4443.
(216) Zhang, M.; He, F.; Zhao, D. Y.; Hao, X. D. Degradation of soil-sorbed trichloroethylene by stabilized zero valent iron nanoparticles: Effects of sorption, surfactants, and natural organic matter. *Water Res.* **2011**, *45* (7), 2401-2414.
(217) Alrousan, D. M. A.; Dunlop, P. S. M.; McMurray, T. A.; Byrne, J. A. Photocatalytic inactivation of E. coli in surface water using immobilised nanoparticle TiO2 films. *Water Res.* **2009**, *43* (1), 47-54.
(218) Brunet, L.; Lyon, D. Y.; Hotze, E. M.; Alvarez, P. J. J.; Wiesner, M. R. Comparative photoactivity and antibacterial properties of C-60 fullerenes and titanium dioxide nanoparticles. *Environ. Sci. Technol.* **2009**, *43* (12), 4355-4360.
(219) Chae, S. R.; Xiao, Y.; Lin, S. H.; Noeiaghaei, T.; Kim, J. O.; Wiesner, M. R. Effects of humic acid and electrolytes on photocatalytic reactivity and transport of carbon nanoparticle aggregates in water. *Water Res.* **2012**, *46* (13), 4053-4062.

(220) Hwang, Y. S.; Li, Q. L. Characterizing photochemical transformation of aqueous nC(60) under environmentally relevant conditions. *Environ. Sci. Technol.* **2010**, *44* (8), 3008-3013.
(221) Jiang, G. X.; Shen, Z. Y.; Niu, J. F.; Bao, Y. P.; Chen, J.; He, T. D. Toxicological assessment of TiO_2 nanoparticles by recombinant *Escherichia coli* bacteria. *J. Environ. Monit.* **2011**, *13* (1), 42-48.
(222) Li, Y.; Niu, J. F.; Zhang, W.; Zhang, L. L.; Shang, E. X. Influence of aqueous media on the ROS-mediated toxicity of ZnO nanoparticles toward green fluorescent protein-expressing *Escherichia coli* under UV-365 irradiation. *Langmuir* **2014**, *30* (10), 2852-2862.
(223) Wang, S. Z.; Gao, R. M.; Zhou, F. M.; Selke, M. Nanomaterials and singlet oxygen photosensitizers: potential applications in photodynamic therapy. *J. Mater. Chem.* **2004**, *14* (4), 487-493.
(224) Lin, C.; Lin, K. S. Photocatalytic oxidation of toxic organohalides with TiO_2/UV: The effects of humic substances and organic mixtures. *Chemosphere* **2007**, *66* (10), 1872-1877.
(225) Kong, L. J.; Mukherjee, B.; Chan, Y. F.; Zepp, R. G. Quenching and sensitizing fullerene photoreactions by natural organic matter. *Environ. Sci. Technol.* **2013**, *47* (12), 6189-6196.
(226) Enriquez, R.; Pichat, P. Interactions of humic acid, quinoline, and TiO2 in water in relation to quinoline photocatalytic removal. *Langmuir* **2001**, *17* (20), 6132-6137.
(227) Hotze, E. M.; Bottero, J. Y.; Wiesner, M. R. Theoretical framework for nanoparticle reactivity as a function of aggregation state. *Langmuir* **2010**, *26* (13), 11170-11175.
(228) Jassby, D.; Budarz, J. F.; Wiesner, M. Impact of aggregate size and structure on the photocatalytic properties of TiO_2 and ZnO nanoparticles. *Environ. Sci. Technol.* **2012**, *46* (13), 6934-6941.

Part I:

Characterization of adsorbed layers on nanoparticles

Chapter 3. Assessment of statistical uncertainty in soft particle electrokinetic modeling approaches

3.1 Introduction

Adsorbed macromolecular layers on nanoparticles can significantly modify the surface properties, and hence the interaction forces, that control nanoparticle transport and fate in the environment. The inclusion of adsorbed macromolecule layer properties has been shown to significantly improve correlations to predict the deposition of coated nanoparticles in porous media.[1] A major challenge to the use and refinement of these correlations is the difficulty in measuring important properties of adsorbed layers on nanoparticles. This problem motivates the pursuit of innovative and reliable methods to characterize adsorbed layers. This chapter assesses a soft particle electrokinetic modeling approach to estimate adsorbed layer properties. Here, this method is primarily assessed for the determination of layer thickness, which is difficult to obtain on realistic, polydisperse nanoparticle samples using common approaches based on nanoparticle sizing methods. The estimation of charge density and permeability of the adsorbed layer using electrokinetic modeling is briefly discussed as well.

Soft particle electrokinetic models are founded on theory describing the electrophoresis (i.e., movement in an applied electric field) of "soft" particles, where "soft" denotes an adsorbed layer that is partially permeable to fluid and electrolytes. The formalism for this theory was first established by Ohshima,[2] with various analytical and numerical solutions to the model provided by Ohshima,[2,3] Hill et al.,[4] Duval and Ohshima,[5] Lopez-García et al.,[6,7] and Ahualli et al.[8] In application, the model can be used to fit electrophoretic mobility data to estimate one or more adsorbed layer properties that contribute to electrophoretic mobility: layer thickness (d); charge

density (N); permeability or the Brinkman screening length (λ^{-1}); and homogeneity (α) (i.e., the radial segment distribution).[9] This method has previously been used to investigate a wide range of systems, including bacterial cells coated with fibrils or extracellular polymeric substances (EPS),[10-16] red blood cells,[17,18] and nanoparticles or colloids coated with polymers or polyelectrolytes.[1,17,19-24] Free macromolecules (i.e., those not adsorbed onto a hard particle core) can also be assessed with these models, as shown for humic substances.[25] A compilation of the method of model fitting (i.e., the parameters that were fitted or measured externally) and range of layer properties obtained in these studies is presented in Appendix A. Fitted parameters for d, N, and λ^{-1} range from < 1 to 200 nm, 0 to 180 mol m^{-3}, and < 1 to 55 nm.

Statistical uncertainty in the fitted parameter values is often neglected, although parameter identifiability problems are not uncommon in nonlinear, multi-parameter models.[26,27] Previously, Phenrat et al. accounted for uncertainty in the electrophoretic mobility data by repeating data regressions using measured electrophoretic mobility values +/- one standard deviation.[19] In addition, nanoparticle size polydispersity was shown to have an insignificant effect on the modeled electrophoretic mobilities given a simulated particle set containing a distribution of particle sizes. [19] Hence, application of the model may be advantageous in contrast to other methods that are hampered by particle polydispersity issues. The effect of particle polydispersity on the dynamic mobility (in an AC electric field) has also been investigated by Ahualli et al.[28] Sensitivity to fitted parameters for experimental cases has been briefly discussed by analyzing changes in electrophoretic mobility upon adjusting fitted parameters, either holding measured parameters constant[25] or allowing them to vary.[18] A qualitative discussion of the sensitivity to segment distribution for a multilayer soft particle is provided by Langlet et al.[14] Hill et al. acknowledge that the multi-parameter model can be poorly identifiable and assesses

dielectric spectroscopy as a complementary technique to provide independent measures or verification of layer parameters[29,30] (however, this approach has yet to be widely applied in practice[31]). Duval and Gaboriaud also suggest coupling electrokinetic measurements and atomic force microscopy (AFM).[32]

Currently, little guidance is available regarding the types of coated particles for which model fitting is a viable approach, the maximum number of parameters that can be fitted together without overfitting the model, and the scenarios in which parameter reduction or orthogonal measurements are necessary or sufficient to improve confidence in the fitted parameters. Another problem is that, upon application of the model, the uncertainty in the fitted parameters cannot be readily assessed due to the complexity of the model. Identification of simple measures to estimate uncertainty would be beneficial. These issues are addressed in this study. This chapter also demonstrates and discusses applications of the model to estimate layer properties in environmental deposition studies for coated nanoparticles.

3.2 Objectives

The primary objective of this research is to assess the confidence in adsorbed layer parameters obtained by fitting analytical and numerical solutions of the soft particle electrokinetic model. This study includes a rigorous statistical analysis using likelihood plots as well as an assessment of the feasibility of using simplified sensitivity and collinearity indices. Based on these results, recommendations are made regarding the types of coated particles that are amenable to characterization by this modeling method and feasible approaches for uncertainty analysis in future studies. This research was published by Louie et al. in *Langmuir*.[33]

The second objective of this research is to apply soft particle electrokinetic modeling to experimental systems and to assess the utility of these characterization data to predict nanoparticle deposition in porous media. The first application assesses a set of three coated nanoparticles having selected properties with the specific aim of confirming the theoretical uncertainty analysis performed here; this research accompanied the *Langmuir* publication.[33] The second project was performed in support of the publication by Hotze et al.[34] to obtain adsorbed layer thicknesses on nanoparticles and to qualitatively determine whether thick adsorbed layers could control the deposition behavior of different types of nanoparticles by masking the interaction of the hard nanoparticle surface with a silica substrate. In addition, the layer thickness estimates were used in attempted correlations between the properties of the coated nanoparticles and their deposition behavior. Overall, these application studies confirm limitations in application of the electrokinetic modeling method and systematic biases in model fitting estimates identified in the uncertainty analysis. Implications for the development of correlations for predicting the attachment efficiency of nanoparticles from measured layer properties are discussed.

3.3 Background

3.3.1 Soft particle electrokinetic theory

Soft particle electrokinetic theory and analytical and numerical solutions to the electrokinetic model are presented here. Soft particle electrokinetic theory describes the electrophoresis of hard particles coated with a soft layer, uniting previous theories for hard particles and fully permeable soft particles such as microgels.[2] The adsorbed layer can include

natural or synthetic macromolecules that are either charged or uncharged. The adsorbed layer changes the electrophoretic mobility of a particle by (1) the presence of any charges on the macromolecules, which contribute to the electrophoretic force on the particle, and (2) increased friction imparted by the adsorbed layer, which contributes to the drag force or resistance to particle motion. The resultant electrophoretic mobility is therefore determined by the balance between the electrophoretic and drag forces (Figure 3.1). It is noted that no rigorous slipping or shear plane exists when a soft layer is present; hence, the "zeta-potential" (potential at the shear plane) loses meaning and the application of hard particle theories (e.g., models by Smoluchowski, Debye, and Henry, or O'Brien and White)[35] to estimate zeta-potential from electrophoretic mobility is inappropriate for soft particles. However, the layer thickness and permeability can be loosely representative of the "effective" layer thickness, or the hydrodynamic thickness for uncharged layers.[17]

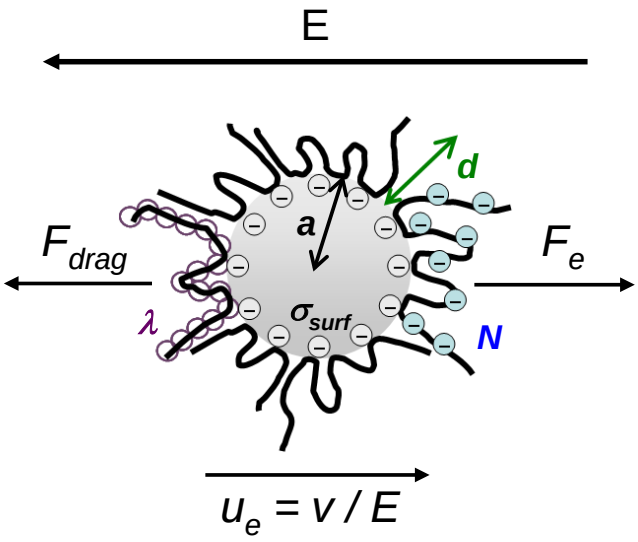

Figure 3.1. Illustration of electrophoretic mobility and the particle and adsorbed layer parameters in soft particle electrokinetic theory. The electrophoretic mobility of the particle, u_e, is the ratio of the particle velocity, v, to the applied electric field, E, and is determined by the electrophoretic force (F_e) and drag force (F_{drag}) acting on the coated particle. Important properties that affect these forces include the particle radius, a; particle surface charge, σ_{surf}; charge density in the polyelectrolyte layer, N; and polyelectrolyte layer thickness, d. The parameter λ is representative of hydrodynamic drag in the layer or permeability to flow, where λ^{-1} is the Brinkman screening length.

In the formalism presented by Ohshima,[2] the hard particle core is modeled as a sphere of radius a with uncoated zeta-potential ζ or surface charge σ_{surf}. The adsorbed layer is modeled as a homogeneous layer of thickness d with unit charges Z_p (which can be zero or non-zero) and homogeneous charge density N (Figure 3.1). In numerical models, inhomogeneous segment and charge distributions may be modeled using an additional homogeneity parameter, α. The Brinkman screening length, λ^{-1}, relates to the drag of the polymer segments and is representative of the permeability or "softness" of the coating; the relationship between λ^{-1} and the density and properties of the polymer segments is described in detail elsewhere.[4,5] The bulk fluid is

described by the relative permittivity ε_r and viscosity η, and contains $i = 1,\ldots,N_{el}$ species of mobile electrolytes (e.g. N_{el}=2 for Na^+ and Cl^-), molar concentration c_i or number concentration n_i, and ionic strength I (or Debye parameter κ).

The governing equations for the electrokinetic model are the Navier-Stokes equation for incompressible fluid flow around the particle (Equation 3.1), where the third and fourth terms represent the electrostatic and frictional forces, respectively, on the particle. Equation 3.2 is obtained by combining the flow and continuity equations for the mobile electrolyte ions.[2,4,5]

$$\eta\nabla\times\nabla\times\vec{u}(\vec{r})+\nabla p(\vec{r})+\rho_{el}(\vec{r})\nabla\psi(\vec{r})+k(\vec{r})\vec{u}(\vec{r})=\vec{0} \tag{3.1}$$

$$\nabla\cdot\left\{c_i(\vec{r})\vec{u}(\vec{r})-\frac{1}{\bar{\lambda}_i}c_i(\vec{r})\nabla\mu_i(\vec{r})\right\}=0\ ; \qquad i=1,\ldots,N_{el} \tag{3.2}$$

where $\vec{u}(\vec{r})$ is the liquid velocity, $p(\vec{r})$ is the pressure, $\psi(\vec{r})$ is the electric potential around the particle, and $k(\vec{r})$ is the friction coefficient at radial position $\vec{r}$. For the mobile electrolyte (i.e., dissolved ions in the dispersion medium), ρ_{el} is the electrolyte charge density (units of charge, e.g. Coulomb, per volume), c_i is the molar concentration of electrolyte, μ_i is the electrochemical potential, and $\bar{\lambda}_i$ is the drag coefficient of the mobile ion i, defined as $\bar{\lambda}_i=|z_i|eF/\lambda_i^0$, where z_i is the charge of the ion, e is the elementary charge, F is Faraday's constant, and λ_i^0 is the limiting conductivity (5.01 and 7.63 $mS{\cdot}m^2/mol$ for Na^+ and Cl^-, respectively).

After writing the ion concentration, electric potential, and chemical potential as a sum of their equilibrium values and the perturbation due to the applied electric field, the following

equations are obtained by Ohshima[2] and are also presented in the solution by Duval and Ohshima[5] (note, Equations 3.1 and 3.2 are also the basis of other solutions[4]).

$$\eta\nabla\times\nabla\times\vec{u}(\vec{r})+\nabla p(\vec{r})-\sum_{i=1}^{N_{el}}\delta\mu_i(\vec{r})\nabla c_i^{(0)}(\vec{r})+\rho_{el}^{(0)}(\vec{r})\nabla\psi^{(0)}(\vec{r})+\nabla(\rho_{el}^{(0)}(\vec{r})\delta\psi(\vec{r}))+k(\vec{r})\vec{u}(\vec{r})=\vec{0} \tag{3.3}$$

$$\nabla\cdot\left\{c_i^{(0)}(\vec{r})\vec{u}(\vec{r})-\frac{1}{\bar{\bar{\lambda}}_i}c_i^{(0)}(\vec{r})\nabla\delta\mu_i(\vec{r})\right\}=0\ ;\ i=1,\ldots,N_{el} \tag{3.4}$$

The superscript (0) denotes equilibrium conditions, and δ denotes perturbations from equilibrium due to the application of the electric field (polarization and relaxation effects). The equilibrium potential profile $\psi^{(0)}(\vec{r})$ is given by the Poisson-Boltzmann equation:

$$\nabla^2\psi^{(0)}(r)=-\frac{1}{\varepsilon_0\varepsilon_r}\left\{\rho_{el}^{(0)}(r)+\rho_0 f(r)g(\mathrm{pH},\psi^{(0)}(r))\right\} \tag{3.5}$$

where $f(r)$ is a function of the heterogeneity parameter, α, defining the radial segment distribution, and g(pH, $\psi^{(0)}$(r)) is an isotherm defining the protonation or deprotonation of functional groups (here, $f \sim 1$ at all r for a nearly homogeneous layer and no effects of the pH or local potential on the charge in the coating). $\rho_{el}^{(0)}(r)$ is related to the electrolyte concentration and the potential by the following equation:

$$\rho_{el}^{(0)}(r) = F\sum_{i=1}^{N_{el}} z_i c_{,}^{(0)}(r) = F\sum_{i=1}^{N_{el}} z_i c_i^{\infty} \exp\left\{\frac{-z_i e\psi^{(0)}(r)}{k_B T}\right\} \tag{3.6}$$

For the equilibrium potential problem, the boundary condition is that the potential is zero far from the particle surface; at the particle surface, either (1) constant potential or (2) constant charge (establishing the slope of the potential profile at the surface) is provided. For the flow problem, the boundary conditions are set such that fluid velocity relative to the particle is zero at the hard particle surface and is expressed in terms of the electrophoretic mobility far from the particle surface. Given all other parameters describing the system (including d, N, and λ^{-1}), the electrophoretic mobility that satisfies the boundary value problem is determined.

Ohshima's analytical approximations[2] are derived upon neglecting polarization and relaxation (non-equilibrium perturbations); that is, $\delta\rho_{el}(\vec{r}) = 0$, and hence $\delta\psi(\vec{r}) = 0$ and $\delta\mu_i(\vec{r}) = 0$. Expressions are available for all combinations of uncharged and charged hard particles and soft layers. For a charged hard particle with a charged coating in a symmetric (z_{el}:z_{el}) electrolyte, after taking the assumptions that $\kappa a >> 1$, $\kappa d >> 1$, and $\lambda d >> 1$, the electrophoretic mobility u_e is:[2]

$$\begin{aligned} u_e = {} & \frac{\varepsilon_r \varepsilon_0}{\eta}\left(\frac{\psi_0/\kappa_m + \psi_{DON}/\lambda}{1/\kappa_m + 1/\lambda}\right) f(d/a) + \frac{Z_p eN}{\eta\lambda^2} \\ & + \frac{8\varepsilon_r \varepsilon_0 k_B T}{\eta\lambda z_{el} e}\tanh\left(\frac{z_{el} e\zeta}{4k_B T}\right)\left[\frac{\exp(-\lambda d)/\lambda - \exp(-\kappa_m d)/\kappa_m}{1/\lambda^2 - 1/\kappa_m^2}\right] \end{aligned} \tag{3.7}$$

where ε_0 is the permittivity of vacuum, k_B is Boltzmann's constant and T is the temperature. ψ_0, the potential at the interface between the polyelectrolyte layer and the solvent, is given by:

$$\psi_0 = \psi_{DON} - \frac{k_B T}{z_{el} e}\left(\tanh\frac{z_{el} e \psi_{DON}}{2k_B T}\right) + \frac{4k_B T}{z_e e}\exp(-\kappa_m d)\tanh\left(\frac{z_{el} e \zeta}{4k_B T}\right) \quad (3.8)$$

The Donnan potential, ψ_{DON}, is given by Equation 3.9:

$$\psi_{DON} = \frac{k_B T}{z_{el} e}\sinh^{-1}\left(\frac{Z_p N}{2 z_{el} n^{\infty}}\right) \quad (3.9)$$

where n is the bulk electrolyte concentration.

κ_m is a modified Debye parameter accounting for the effect of charges in the polyelectrolyte layer, and $f(d/a)$ is a function of d/a which ranges from 2/3 for $d/a \rightarrow 0$ to 1 for $d/a \rightarrow \infty$:

$$\kappa_m = \kappa\left(\cosh(z_{el} e \psi_{DON} / k_B T)\right)^{1/2} \quad (3.10)$$

$$f(d/a) = 2/3\left(1 + \frac{1}{2(1 + d/a)^3}\right) \quad (3.11)$$

Numerical solutions relax the assumptions on particle size and layer thickness and allow for the specification of α to represent an inhomogeneous segment and fixed charge distribution, where $\alpha = 0$ represents a completely homogeneous layer (with a discontinuous polymer/solvent boundary). These numerical models also account for polarization and relaxation effects by

inclusion of the perturbation terms. Various approaches have been presented to solve the boundary value flow and electrostatic problems; for a detailed treatment of the problem, the reader is referred to the references.[4-8] In this study, both the analytical and numerical solutions will be assessed and compared.

3.3.2 Application of soft particle electrokinetic models to estimate layer properties

The experimental approach for application of electrokinetic modeling is depicted in Figure 3.2. First, the electrophoretic mobilities of the bare and coated particles are measured at several ionic strengths. Layer parameters (N, d, λ^{-1}, and/or α) that are not known or measured by orthogonal methods are obtained by weighted least-squares fitting to minimize the weighted residual sum of squared errors between the experimental data and modeled electrophoretic mobilities. Here, the squared error for each datum is weighted (divided) by the variance in the measured datum.

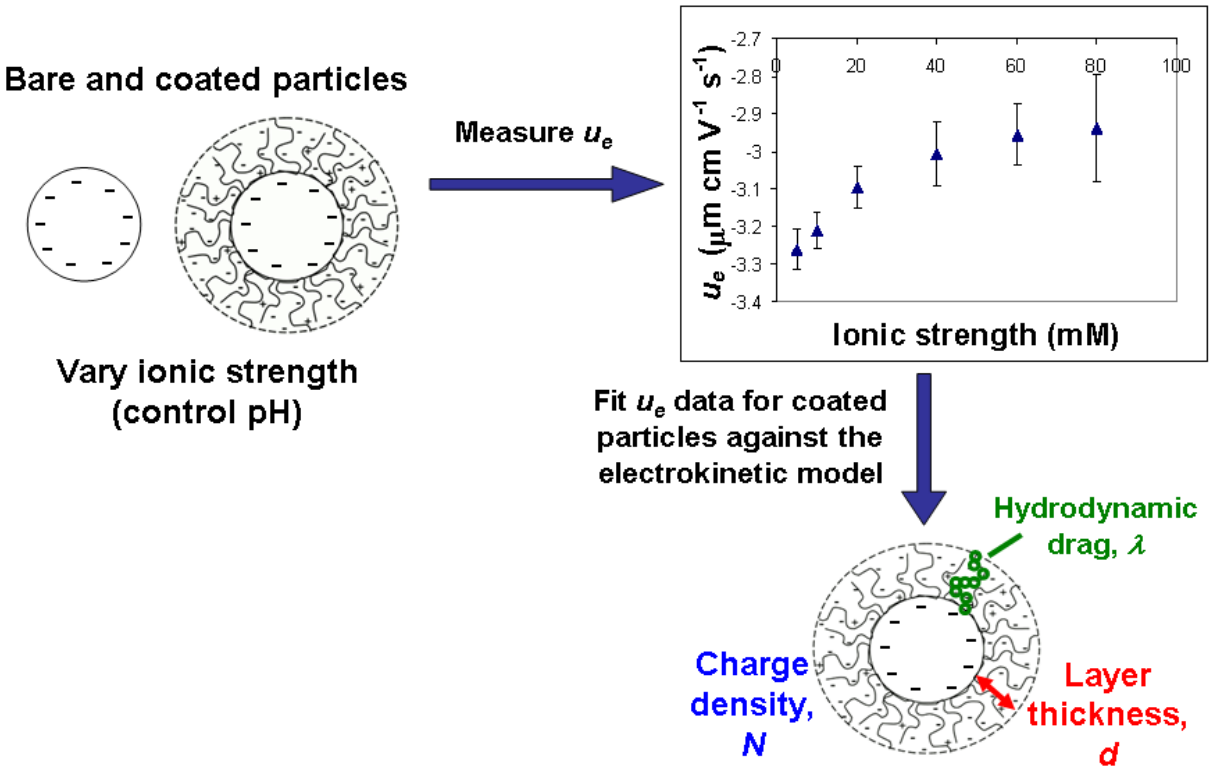

Figure 3.2. Method for estimation of adsorbed layer properties by application of soft particle electrokinetic modeling. Bare and coated nanoparticle suspensions are prepared at several ionic strengths, and their electrophoretic mobilities are measured. The bare particle electrophoretic mobilities and ionic strengths are used as inputs for the electrokinetic model, and the coated particle electrophoretic mobilities are fitted to obtain the weighted least squares estimate of three layer properties: layer thickness, charge density, and permeability or hydrodynamic drag.

It is emphasized that this study focuses on statistical uncertainty in fitted parameters. Discussion of model accuracy and the applicability of the Brinkman equation for λ^{-1} in representing physical details of experimental systems is provided elsewhere[5,32,36] but is outside the scope of this study. Shrinking or swelling of the layer with ionic strength has also been disregarded, although this behavior may be included by representing d as a function of ionic strength. Alternatively, swelling can be estimated by fitting N and λ^{-1} at high ionic strength where α is insignificant, then determining the α values that best represent each low ionic

strength datum.[12,18] Although the most accurate model representation is desired, identifiability problems inherent in the model itself can limit the utility of even the most physically accurate model. In addition, uncertainty in fitted parameters due to model inaccuracy may be small compared to the uncertainty due to poor identifiability. In application, the model should both be accurate and allow for good identifiability of layer properties. The latter topic is addressed in this research.

3.3.3 Likelihood plots for rigorous uncertainty analysis

Parameter identifiability analysis is used to determine confidence intervals on fitted parameters; that is, the range of each parameter for which statistically similar (e.g. within experimental uncertainty) model outputs are obtained. Confidence intervals are easily determined for simple models, such as linear fits, but become complicated for multi-parameter, nonlinear models such as the soft particle electrokinetic model. Rigorous analyses become more difficult to interpret as the number of fitted parameters increases; furthermore, they may be infeasible to perform on a regular basis for computationally intensive models.

In this study, parameter identifiability analysis is performed following standard methods to identify "likelihood" or confidence regions for the fitted parameters, as presented by Bates and Watts.[26] In addition, "practical" methods to represent identifiability through simple sensitivity and collinearity indices are applied and assessed, following the methods by Brun et al. for large environmental models.[27] These analyses are typically applied to experimental data. Here, both experimental and simulated data (i.e., theoretical electrophoretic mobilities obtained from the soft particle electrokinetic model) are assessed. Modifications to the procedure when using simulated data are noted.

In general, any model can be written $\boldsymbol{Y} = \boldsymbol{\eta}(\boldsymbol{\theta}) + \boldsymbol{Z}$, where $\boldsymbol{Y}$ is the observation vector (here, the *measured* u_e at 10 ionic strengths), $\boldsymbol{\theta}$ contains the set of fitted parameters (e.g., N, d, and λ^{-1}), $\boldsymbol{\eta}(\boldsymbol{\theta})$ represents the model outputs (the *modeled* u_e curve for given parameter values over 10 ionic strengths), and $\boldsymbol{Z}$ is the error between the observed and fitted u_e data. Bolded variables represent vectors. For simulated cases, $\boldsymbol{Y}$ is modeled for the parameter set of interest or the "true" parameters, and $\boldsymbol{Z}$ is then zero for the true parameters and non-zero for other parameter sets (assuming a unique solution). Generally, the weighted residual sum of squared errors (WRSS), $S(\boldsymbol{\theta})$, is assessed. The weighting is performed by dividing the squared errors by the variance of the experimental data to increase the relative importance of data points with lower uncertainty. The parameters are fitted to determine the least squares estimate (i.e., the parameter set that produces the minimum WRSS) is denoted $\hat{\boldsymbol{\theta}}$.

Identifiability analysis considers the range of parameter sets that produce similar WRSS to the minimum WRSS, $S(\hat{\boldsymbol{\theta}})$, at a confidence level of 1-β (e.g., 95% confidence). Note that β is used here instead of the typical symbol, α, to distinguish from the radial segment distribution function defined previously. A parameter can be poorly identifiable if the model is not sensitive to it or if it is collinear with other parameters (i.e., its effects on the model output can be offset by adjusting the other fitted parameters). Graphical representations of exact parameter identifiability include conditional and profile likelihood contour plots, in which the likelihood or confidence region is drawn on a plot. The likelihood region contains all parameter sets, $\boldsymbol{\theta}$, whose WRSS is low enough to satisfy the follow condition:[26]

$$S(\boldsymbol{\theta}) \le S(\hat{\boldsymbol{\theta}})\left[1 + \frac{m}{n-m} F(m, n-m; \beta)\right] \tag{3.12}$$

where m is the number of parameters that are fitted, n is the number of observations (ionic strengths), and $F(m,n\text{-}m;\beta)$ is the upper β quantile (β = 0.05 and 0.20 for 95% and 80% likelihood, respectively) for the F distribution with m parameters and $n–m$ degrees of freedom.

Likelihood regions can be determined using Equation 3.12 for experimental data with a non-zero $S(\hat{\theta})$. For simulated data, $S(\hat{\theta})$ = 0 at the true parameter set, and the likelihood region would be a single point. Given that error will exist in the measurement of electrophoretic mobility, we instead determine a region where the error is within 4% relative to the true u_e curve, based on typical experimental errors achieved in this lab for measurements of metal oxide nanoparticles, ~2-7%, at 30 ppm concentration on a Zetasizer 3000 instrument (Malvern Instruments, Westborough, MA). The limit of 4% error is defined as follows:

$$S(\theta) \le S(\hat{\theta}) + \sum_{i=1}^{n} \left(0.04\eta_i(\hat{\theta})\right)^2, \qquad i = 1, 2, \ldots, n \tag{3.13}$$

where $\hat{\theta}$ is the simulated case used and $S(\hat{\theta})$=0. Here, the term “likelihood region” will be used loosely to represent this region. For experimental data with higher than 4% error, rigorous likelihood regions defined by Equation 3.12 will be larger than the region defined by Equation 3.13.

To produce a likelihood plot, parameters can be systematically varied, and those satisfying Equation 3.12 or 3.13 are plotted. For ease of visualization, pairwise likelihood plots are typically generated showing only two parameters at a time, e.g. N and d instead of N, d, and λ^{-1}. “Conditional” and “profile” likelihood plots are distinguished by whether the additional

parameters not shown are held constant or allowed to vary. In conditional likelihood plots, the parameters not shown on the axes are held constant at their least squares estimate. Conditional plots show effects of pairs of parameters and can be used to gauge sensitivity to individual parameters, but collinearity of the entire set of parameters is neglected since some are held constant. In profile likelihood plots, parameters not shown on the axes are fitted to achieve the lowest $S(\theta)$, which is assessed per Equation 3.12 or 3.13. Profile plots account for collinearity of all parameters, so the profile likelihood region is larger than the conditional region. Hypothetical plots are shown in Figure 3.3.

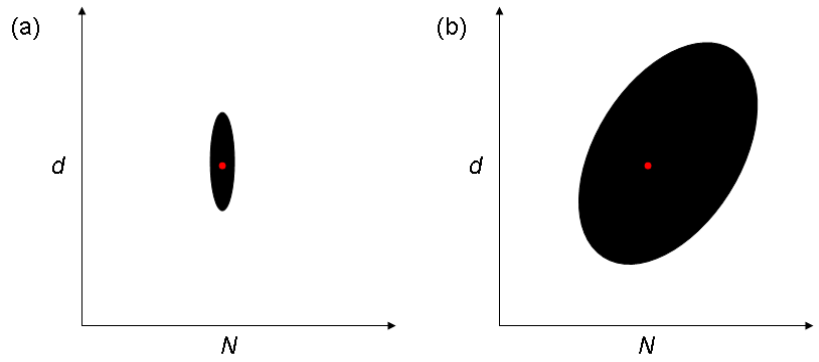

Figure 3.3. Hypothetical plots of (a) conditional and (b) profile likelihood regions. The red point represents the best fit, and the black region represents the likelihood region accounting for uncertainty in measurements (all points where Equation 3.12 is satisfied). Plots for λ^{-1} vs. N and d vs. λ^{-1} (not shown here) are also created. In the conditional plot (a), λ^{-1} is held constant at its least squares estimate. Sensitivity can be deduced from the extent of the likelihood region. In the profile plot (b), λ^{-1} is fitted to produce the lowest RSS at each point (N, d), so the region expands. Collinearity of d and N can be deduced from the shape of the plot.

3.3.4 Sensitivity and collinearity indices for large models

Likelihood contour plots can be computationally intensive to produce and difficult to interpret for large models with multiple fitted parameters. To alleviate these problems, Brun et

al. recommend computing sensitivity and collinearity indices as surrogate measures of identifiability.[27] These indices are less rigorous than the likelihood plots because they assume a linear model and are based on extrapolation of an analysis of only the local parameter space around $\hat{\boldsymbol{\theta}}$. Therefore, an assessment is made in this study to determine the appropriateness of these indices to represent the likelihood plot before they are recommended for use with the soft particle electrokinetic model.

Sensitivity expresses how much the model output $\eta(\boldsymbol{\theta})$ (electrophoretic mobility) is expected to change due to a change of $\Delta\theta_j$ in each of the fitted parameters (N, d, and λ^{-1}), and is calculated using Equation 3.14.

$$s_{ij} = \upsilon_{ij} \frac{\Delta\theta_j}{SC_i} \qquad i = 1, 2, \ldots, n \qquad j = 1, 2, \ldots, m \tag{3.14}$$

where $\Delta\theta_j$ is a reasonable range of θ_j that can be expected based on expert knowledge, SC_i is a scaling factor on the electrophoretic mobility, and υ_{ij} is the derivative of $u_{e,i} = \eta_i(\boldsymbol{\theta})$ with respect to parameter θ_j, taken at $\boldsymbol{\theta} = \boldsymbol{\theta_0}$, shown in Equation 3.15:

$$\upsilon_{ij} = \left.\frac{\partial \eta_i(\theta_j)}{\partial \theta_j}\right|_{\boldsymbol{\theta}=\boldsymbol{\theta_0}} \tag{3.15}$$

Here, $\boldsymbol{\theta_0}$ is taken to be the least squares estimate, $\hat{\boldsymbol{\theta}}$, and the slope υ_{ij} is computed for each parameter using a linear approximation between the points $\eta_i(\theta_{j0})$ and $\eta_i(1.1\theta_{j0})$, holding the other two parameters at their values in $\boldsymbol{\theta_0}$. Guidelines for choosing $\Delta\theta_j$ and SC_i are presented

in detail by Brun et al.[27] Briefly, $\Delta\theta_j$ scales and accounts for expected ranges in the parameters (N, d, and λ^{-1}), whereas SC_i scales the output by measurement uncertainty. Here, $\Delta\theta_j$ is taken as 1 mol/m^3 for N and 1 nm for d and λ^{-1}. SC_i is chosen as $\left|\eta_i\left(\hat{\Theta}\right)\right|$ for theoretical cases since the measurement standard deviation is taken to be approximately proportional to $u_{e,i}$; therefore, the sensitivity index describes the effect of parameters on u_e relative to the true u_e curve.

Sensitivity of the model output to each of the j parameters (e..g, N, d, and λ^{-1}) is summarized over all n data points as the root mean square average δ_j^{msqr}: [27]

$$\delta_j^{msqr} = \sqrt{\frac{1}{n}\sum_{i=1}^{n} s_{ij}^2} \tag{3.16}$$

Lower δ_j^{msqr} indicates poorer model sensitivity, which implies that parameter j may not be identifiable even if the other parameters are accurately known or measured. It is noted that the exact values of δ_j^{msqr} will depend on the values of $\Delta\theta_j$, SC_i, and the points used to compute υ_{ij}; therefore, these details must be kept consistent in future application for comparison against the values in this study. A sample calculation is provided in Appendix A.

Collinearity indices are used to determine joint influence of parameters. Collinearity can be calculated for the model for subsets K of parameters, e.g. fitting all parameters together so K =(N, d, λ^{-1}), or two parameters while holding one at a known/estimated value, so K = (N, d), K = (N, λ^{-1}), or K = (d, λ^{-1}). First, the sensitivity vectors $\boldsymbol{s_j}$ (each containing n values) for each j are divided by their norms to obtain normalized sensitivities $\tilde{s}_j$.[27]

$$\tilde{s}_j = \frac{s_j}{\|s_j\|} \tag{3.17}$$

The collinearity index γ_K is calculated for each subset K as follows:[27]

$$\gamma_K = \frac{1}{\sqrt{\lambda_K}} \tag{3.18}$$

where λ_K is the smallest eigenvalue of $\tilde{S}_K^T \tilde{S}_K$ and $\tilde{S}_K$ is the matrix with columns $\tilde{s}_j$ for only the parameters j in the subset K of interest. A higher collinearity index indicates that parameters can more effectively offset each other's effect on $\eta(\theta)$, resulting in poor parameter identifiability.

Sensitivity and collinearity indices are computed for all cases for analytical and "exact" numerical models. A full set of likelihood plots for the numerical model was not produced due to the computational requirements. Instead, Ohshima's analytical approximations are analyzed in full, using conditional and profile likelihood plots to determine rigorous confidence intervals, which are then correlated with sensitivity and collinearity measures. Conditional likelihood plots for the numerical model are demonstrated for select theoretical cases and for the experimental sets to confirm the correlations with sensitivity and collinearity measures.

3.4 Materials and methods

3.4.1 Confidence in parameter estimates from soft particle electrokinetic models

In the first part of this study, theoretically generated electrophoretic mobilities are assessed to provide a fundamental uncertainty analysis and to determine cases where parameters

are identifiable under ideal circumstances. Both Ohshima's analytical expressions[2] and the exact numerical model are used and compared. The MPEK-0.02 software for the numerical model was provided by Dr. Reghan Hill and implements the numerical model as presented by Hill and Saville.[4] Other approaches to the numerical solution such as those by Duval and Ohshima[5] and Lopez-García et al.[7] are equivalent. It is emphasized that the numerical model is necessary for the cases explored here where polarization effects are significant (e.g., ψ > 25 mV) and for systems that do not fit the constraints of $\kappa a >> 1$, $\kappa d >> 1$, and $\lambda d >> 1$. Because these cases are of interest for nanoparticle systems or thin coatings, we include these cases but emphasize that the analytical model is not appropriate in practice for these scenarios. However, analysis of the analytical model for these cases is necessary as a starting point for the identifiability analysis, because complete analysis of the numerical model for every simulated case would be computationally prohibitive. The comparison of the two models will also show how identifiability can differ when using the more accurate numerical model.

The theoretical coated particle electrophoretic mobility data $u_{e,true}$ are computed at each of ten ionic strengths (5, 10, 15, 20, 30, 40, 50, 60, 70, and 80 mM NaCl) using either Equations 3.7 to 3.11 (analytical model) or the MPEK-0.02 numerical model for chosen values of N, d, λ^{-1}, and the bare particle surface charge density, σ_{surf}. The heterogeneity parameter α is set to $10^{-5}d$ (nearly homogeneous) in the numerical model. Here, one of the segment distributions $f(r)$ defined in prior studies is used:[4,5]

$$f(r) = n_s/n_0 \, (1/2)\mathrm{erfc}[(r-a-d)/\alpha] \tag{3.19}$$

where r is the distance from the particle surface, n_s is the segment density, and n_0 is the nominal segment density for a homogeneous layer with equivalent number of segments and layer thickness d. The limit $\alpha = 0$ specifies a completely homogeneous layer; as α increases to 1 and higher, the distribution broadens. Although heterogeneity (non-zero α) can have significant effects on electrophoretic mobility,[5] we consider only the homogeneous case here and acknowledge that inclusion of α as another fitted parameter, while a more accurate physical representation of the system, can result in poorer identifiability from a statistical viewpoint.

The fluid is taken to be water at 298 K with 1:1 electrolyte (z_{el} = 1), and the polyelectrolyte unit charge Z_p is -1. The polyelectrolyte parameters are assumed to remain constant in the range of ionic strengths used. The bare particle radius a is chosen to be 20 nm.

180 cases are analyzed for all combinations of the following parameters:

- Hard particle surface charge density, σ_{surf} (C/m^2): -3×10^{-4}, -3×10^{-3}, -9×10^{-3}
- Layer thickness, d (nm): 5, 10, 20, 40
- Ratio of the Brinkman screening length to layer thickness, λ^{-1}/d: 0.2, 0.5, 0.8
- Layer charge density (number density), N (m^{-3}): 10^{20}, 10^{22}, 10^{24}, $5\text{x}10^{24}$, and 10^{25} m^{-3}

The range of σ_{surf} is equivalent to uncoated particle zeta-potentials of 2 to 48 mV at 5 mM ionic strength (calculated from the Gouy-Chapman equation). The range of N is equivalent to 1.7×10^{-4} to 16.6 mol m^{-3}. These values are chosen to encompass a broad range of systems of a nanoparticle or colloid coated with synthetic or natural polyelectrolytes (Table A.1).

Conditional and profile likelihood plots are produced for all cases defined above, showing the confidence regions for parameters when the electrokinetic model is applied to fit

either two or three adsorbed layer parameters. Sensitivity and collinearity indices are computed, as described in Section 3.3.4, and correlated to the identifiability of layer thickness determined in the likelihood plots.

3.4.2 Experimental validation of theoretical uncertainty analysis

Three experimental samples of macromolecule-coated nanoparticles are assessed using the analytical and numerical soft particle electrokinetic models to estimate the adsorbed layer properties. The uncertainty analyses described above are applied to these systems and compared against the findings from the simulations. The nanoparticles and macromolecules assessed include (1) citrate-reduced gold (Au) nanoparticles (13 ± 1.3 nm primary particle diameter by TEM (unpublished data from Stella Marinakos); 28 nm intensity-weighted diameter, polydispersity index (PdI) 0.17, by dynamic light scattering (Malvern Instruments, Westborough, MA)) with adsorbed poly(ethylene glycol) (PEG) methoxy thiol, molecular weight 1000; (2) magnetite (Fe_3O_4) nanoparticles (20-30 nm primary particle diameter, PdI 0.26) with adsorbed polyacrylic acid (PAA), degree of polymerization 157 or molecular weight ~14,400; and (3) reactive nano-iron particles (RNIP) (40 nm primary particle diameter) with adsorbed polystyrene sulfonate (PSS), molecular weight ~70,000. RNIP has a zerovalent iron (Fe^0) core and an iron oxide shell that is comparable to Fe_3O_4. For each sample, the polymer was adsorbed to the particles, and excess polymer was removed by centrifuging the particles and resuspending them in polymer-free medium. The PEG-coated Au nanoparticles were prepared and measured for this study. The PAA-coated Fe_3O_4 nanoparticles were prepared previously,[37] and their electrophoretic mobility was measured in this study. Electrophoretic mobility data for PSS-coated RNIP was used as published elsewhere.[19] Electrophoretic mobility was measured at

several ionic strengths for the bare and coated particles, at pH 8.3 for Au and pH 8.5 for Fe_3O_4 and RNIP. Materials and methods are fully described in Appendix A.

Layer parameters were estimated by weighted least-squares fitting of the numerical model as described in Section 3.3.2. It is noted that we assume the citrate coating on Au nanoparticles (obtained upon synthesis by citrate reduction) establishes surface charge immediately at the hard particle surface and is neither part of, nor perturbed by, the soft PEG layer, although other studies have treated similar systems as an uncharged Au core with citrate contributing to the soft layer.[22] Neither representation is perfectly accurate, but this detail is outside the scope of this paper and can be addressed in further studies.

3.4.3 Application of the electrokinetic modeling method to estimate adsorbed layer properties for nanoparticle transport experiments

Electrokinetic modeling was applied in a study by Hotze et al.[34] to estimate adsorbed layer properties on nanoparticles and correlate these properties to their deposition. In this study, nanoparticle deposition was measured in packed column experiments, as described in the associated publication.[34] The deposition of silver, titanium dioxide, and fullerene nanoparticles, each coated with a synthetic polyelectrolyte (poly(acrylic acid) (PAA)), a protein (bovine serum albumin (BSA)), or a natural organic matter sample (Aldrich humic acid (HA)) were measured. The substrate used was silica beads, and the suspension medium was 20 mM NaCl in water at pH 7.6. Briefly, the nanoparticles were pumped through a water-saturated packed column (pre-equilibrated in the dispersion medium used for the nanoparticle suspensions), and their attachment efficiency to the substrate was calculated from the measured effluent concentration

using Equation A.1 (described in Section A.6 in Appendix A) and the Tufenkji-Elemelech correlation[38] to obtain the single-collector contact efficiency (Equation A.2 in Section A.6).

Adsorbed layer thicknesses were estimated by least squares fitting of electrophoretic mobility data collected over an ionic strength range of 1 to 61 mM (as NaCl) at pH 7.6, using Hill's numerical solution to the electrokinetic model.[4] The layer thicknesses were used to assess whether deposition behavior correlated to the adsorbed layer properties, and the statistical analyses presented in this study were applied to assess confidence in the fitted parameters.

Another study re-assesses data used by Phenrat et al.[1]to develop a semi-empirical correlation between the properties of coated nanoparticles (including the adsorbed layer thickness) and their attachment efficiency. The materials used in this study include polystyrene latex (PSL), hematite (Fe_2O_3), and titanium dioxide (TiO_2) nanoparticles coated with humic and fulvic acids (HA and FA), poly(styrene sulfonate) (PSS), polyaspartate (PAP), and carboxymethylcellulose (CMC). The electrophoretic mobility data and nanoparticle deposition data were collected by Phenrat et al.,[1] Amirbahman and Olson,[39,40] and Franchi and O'Melia.[41] For the original correlation, Ohshima's analytical solution to the electrokinetic model[2] was used to estimate layer thicknesses. Here, layer thickness estimates are revised using Hill's numerical solution.[4] The attachment efficiency correlation was then revised by Tanapon Phenrat using the Buckingham-Π approach, as described previously.[1] The ability of the modified correlation to capture the observed deposition data was compared to the original model.

3.5. Results

Results of the uncertainty analysis are presented, first assessing Ohshima's analytical solution of the electrokinetic model for which ease of computation allows for a rigorous

assessment using likelihood plots as well as an assessment of the validity of sensitivity and collinearity indices for the model. Then, the uncertainty analysis is applied to a numerical solution of the electrokinetic model, and results are compared to those for the analytical model. We focus on the confidence in the layer thickness parameter; identifiability of charge density and permeability are briefly presented as well. Finally, results for experimental systems and environmental applications are presented.

3.5.1 Identifiability of layer thickness in the analytical model

Parameter identifiability analysis was performed for the synthetic parameter sets described in Methods. Conditional and profile likelihood plots for the analytical model[2] are shown in Figure 3.4. These plots show the exact confidence intervals in parameters, where a narrow likelihood region is desirable; furthermore, analysis of the bounds on the likelihood regions on the conditional and profile likelihood plots indicates whether parameters are identifiable when one, two, or three parameters are fitted together. Based on the extent of the likelihood regions, cases were split into four groups by the identifiability of layer thickness d. Only the pairwise plots for d vs. N and d vs. λ^{-1} are shown here; plots of λ^{-1} vs. N are provided in Appendix A (Figure A.1). Plots are cut off at d = 100 nm, an arbitrary but very large value for layer thickness.

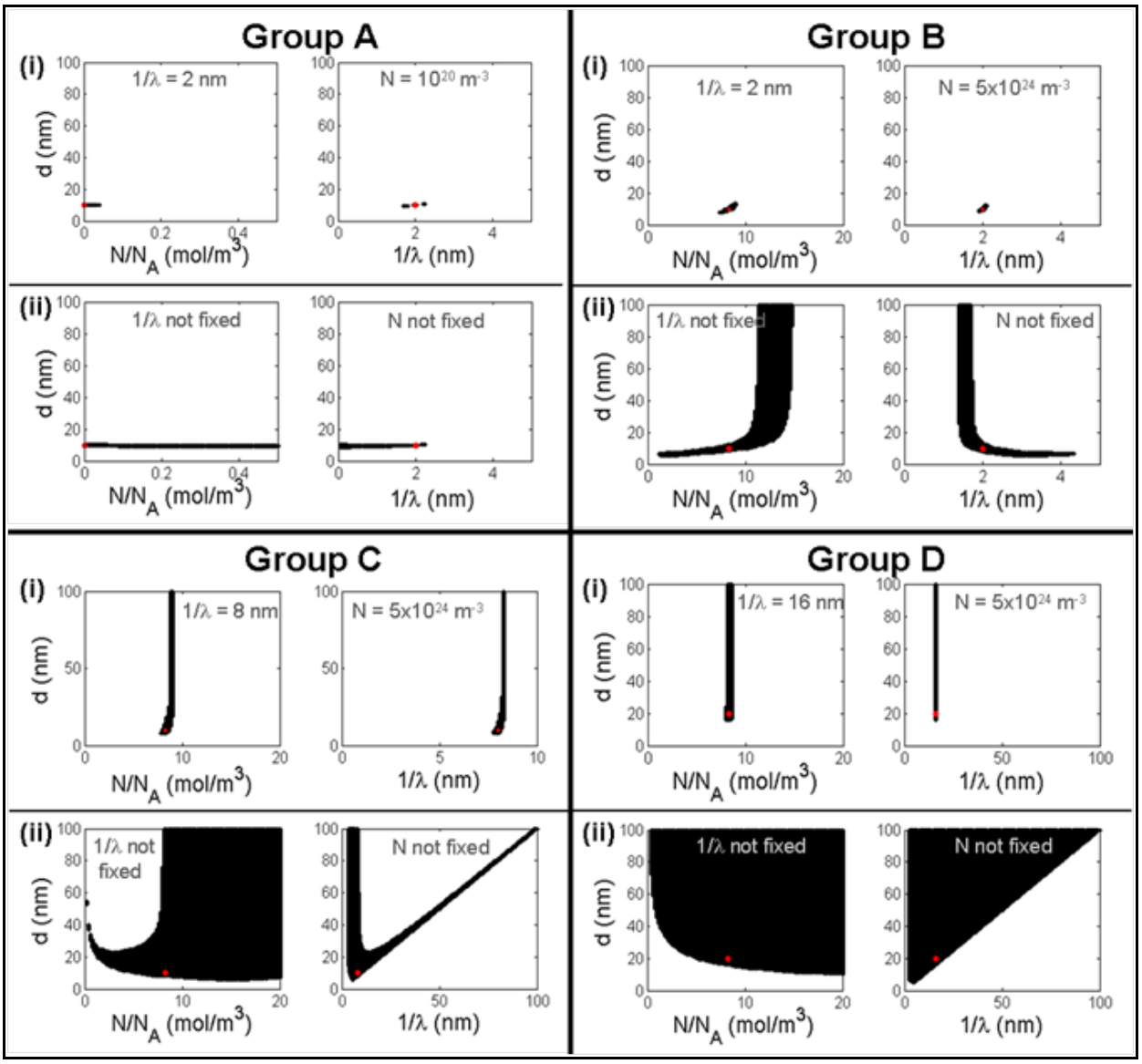

Figure 3.4. (i) Conditional and (ii) profile likelihood plots for representative cases in Groups A, B, C, and D for the analytical model[2]. Cases (Table A.2) shown are (A) Case 66 (σ_{surf}=3x10^{-3} C/m^2, N=10^{20} m^{-3}, d=10 nm, $(\lambda d)^{-1}$=0.2), (B) Case 69 (σ_{surf}=3x10^{-3} C/m^2, N=5x10^{24} m^{-3}, d=10 nm, $(\lambda d)^{-1}$=0.2), (C) Case 109 (σ_{surf}=3x10^{-3} C/m^2, N=5x10^{24} m^{-3}, d=10 nm, $(\lambda d)^{-1}$=0.8), and (D) Case 114 (σ_{surf}=3x10^{-3} C/m^2, N=5x10^{24} m^{-3}, d=20 nm, $(\lambda d)^{-1}$=0.8). Red dots indicate $\boldsymbol{\theta}_{true}$(=$\hat{\boldsymbol{\Phi}}$); black regions indicate parameter sets with low RSS satisfying Equation 3.13. Discontinuities in regions are artifacts of the grid plotting resolution. Diagonal cutoffs in C(ii) and D(ii) are a result of the constraint $d \geq \lambda^{-1}$. In the conditional plots, the parameter not shown on the axes is fixed at its true value; in the profile plots, it is allowed to vary. Group A, B, and C systems are defined such that the likelihood region is bounded in d within 100 nm upon fixing 0, 1, or 2 of the other parameters (N and λ^{-1}), respectively. Layer thickness is never identifiable for Group D systems.

Based on the likelihood plots alone, four groups can be defined as follows. These groups will later be correlated to physical properties of the coated particles.

• Group A: Layer thickness is identifiable (within 100 nm with 95% confidence) when all three parameters are fitted (i.e., no prior knowledge or orthogonal measurement is provided for either N, d, or λ^{-1}). That is, profile likelihood regions, where all parameters can vary, are bounded along d at all N and λ^{-1} (Figure 3.4, group A(ii)).

• Group B: Layer thickness is identifiable when two, but not three, parameters are fitted. Profile likelihood regions (Figure 3.4, group B(ii)) are only bounded along d if either N or λ^{-1} (or both) is fixed at its true value, which can be observed by following the extent of the likelihood region along a vertical line drawn at N_{true} or $\lambda_{b,true}^{-1}$. Equivalently, one or both conditional likelihood regions (Figure 3.4, group B(i)), where one parameter is already fixed at its true value, are bounded along d. This analysis assumes no error on N or λ^{-1}; if an erroneous value of N or λ^{-1} is provided, then d is not necessarily identifiable.

• Group C: Layer thickness is identifiable only if both N and λ^{-1} are fixed at their true values. Profile likelihood regions are unbounded in d even when fixing N or λ^{-1} (Figure 3.4, group C(ii)). Conditional likelihood regions are unbounded in d unless both are fixed (Figure 3.4, group C(i)).

• Group D: Layer thickness is never identifiable, even if both N and λ^{-1} are known. That is, neither profile nor conditional likelihood regions are bounded for d, regardless of whether N and λ^{-1} are fixed (Figure 3.4, group D).

The profile likelihood regions (Figure 3.4(ii)) represent confidence regions where a higher number of parameters are fitted (rather than fixed) and are thus larger than the conditional

likelihood regions (Figure 3.4(i)). The shapes of the plots show a nonlinear correlation among the parameters N, d, and λ^{-1}. Because the likelihood plots extend toward large d values, they also suggest that layer thicknesses are likely to be overestimated when identifiability problems are encountered (independent of physical accuracy) when using the analytical model.

δ^{msqr} (sensitivity) and γ_K (collinearity) indices are faster to compute and simpler to analyze than likelihood plots. Because likelihood plots are computationally expensive to produce for the numerical model, the sensitivity and collinearity indices are first correlated to the parameter identifiability from the likelihood plots for the analytical model. We focus on the sensitivity to d (δ_d^{msqr}) and the collinearity among all three parameters ($\gamma_{N,d,1/\lambda}$). These indices are plotted in Figure 3.5 with Groups A, B, C, and D indicated. Computation of δ_d^{msqr} and $\gamma_{N,d,1/\lambda}$ relies on linear approximations, so these indices do not perfectly describe the model, which is highly nonlinear, as can be discerned from the non-ellipsoidal confidence regions. However, these measures tend to correlate well with the groups defined above from the likelihood plots. Group A and B cases have the highest δ_d^{msqr} values, indicating highest sensitivity to the layer thickness, d. Group D cases have the lowest δ_d^{msqr} values, indicating that d will not be identifiable for these cases regardless of whether N and λ^{-1} are known because the model has very low sensitivity to d. For these simulated cases, Group D cases all have $\delta_d^{msqr} \leq 0.005$, and Group C cases have $\delta_d^{msqr} \leq 0.009$. For experimental cases, the cutoffs for δ_d^{msqr} may differ when the goodness of fit of the least squares estimate is considered (Equation 3.12). Groups are less clearly distinguished by collinearity, but collinearity tends to increase as δ_d^{msqr} decreases and identifiability of d worsens.

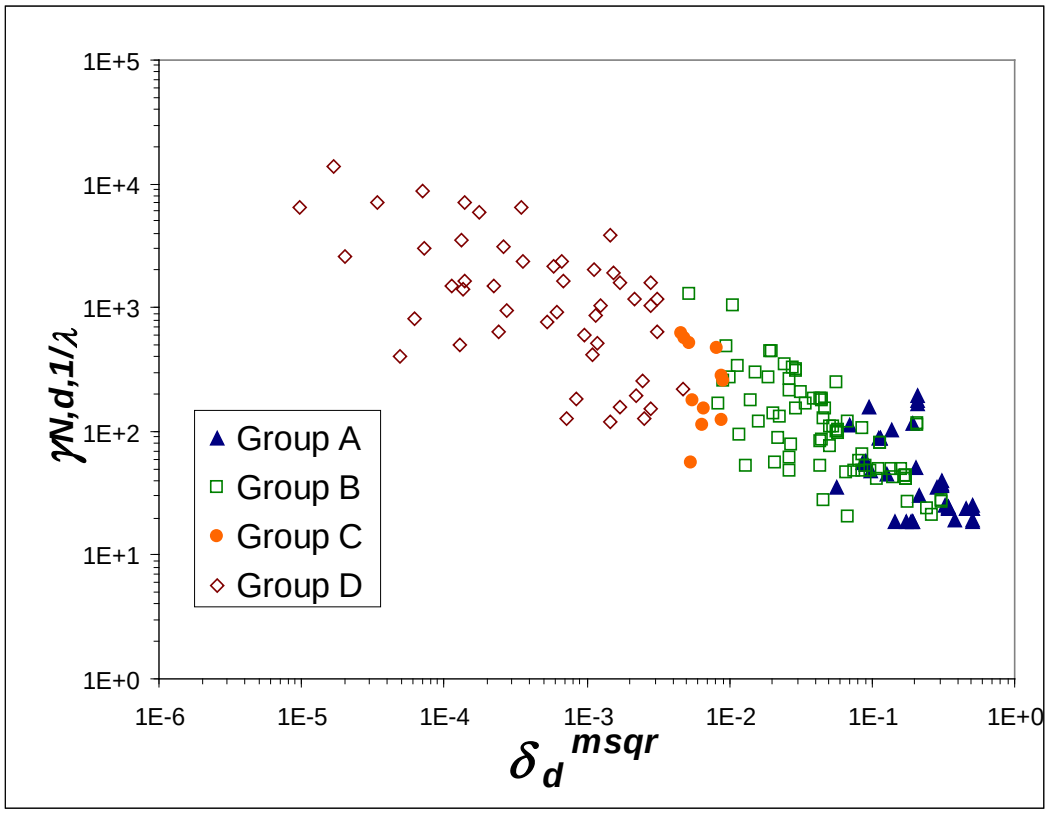

Figure 3.5. Correlation of likelihood plot groupings to sensitivity and collinearity indices for the analytical model.[2] Sensitivity cutoffs distinguishing B/C and C/D groups are estimated at δ_d^{msqr} = 0.009 and 0.005, respectively. Collinearity generally correlates inversely with sensitivity, but distinct collinearity cutoffs distinguishing Groups A/B/C/D are not apparent for layer thickness.

The sensitivity to d is plotted against N, d, and λ^{-1} to show trends in identifiability with particle and coating properties for σ_{surf} = 3×10^{-4} (Figure 3.6). As N, d, and λ^{-1} increase, identifiability in d becomes poorer. Higher magnitudes of σ_{surf} result in slightly higher sensitivity (Figure A.2 and A.3 in Appendix A). Limiting cases described by Ohshima[2] are approached in the range of cases explored here and interpreted in the context of model sensitivity to layer thickness.

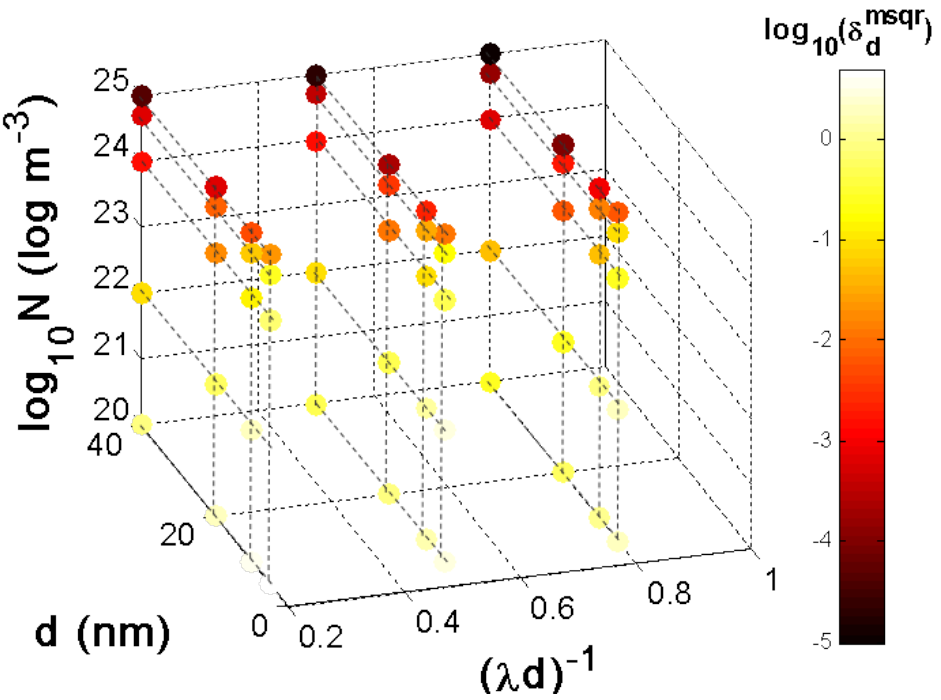

Figure 3.6. Correlation of δ_d^{msqr} to polyelectrolyte parameters N, d, and λ^{-1} for the analytical model[2], at σ_{surf} = 3x10^{-4} C/m^2. Darker colors indicate poorer sensitivity. Model sensitivity to d decreases as N, d, and λ^{-1}/d increase. Trends are similar at higher surface charges, with slightly higher sensitivity overall.

First, a mathematical interpretation of the trend in layer thickness identifiability is given. It is noted that, for the analytical model, electrophoretic mobility depends only on N and λ^{-1} at high ionic strength.[2,30,42] Therefore, in understanding identifiability of d, the low ionic strength data (where the Debye length is large) are most important. Here, 5 mM was the lowest ionic strength used (κ^{-1} = 4.3 nm at 298 K). The trends in sensitivity to d observed here are consistent with Equations 3.7 to 3.11. In all terms except $f(d/a)$, d appears as exp(-d). For thicker layers, d becomes less significant (e.g., changing d by 1 nm has a greater impact on exp(-d) at d_{true} = 5 nm than at d_{true} = 40 nm), and the electrophoretic mobility thus becomes less sensitive to d. As N and λ^{-1} increase, relative contributions of terms without d increase (u_e becomes increasingly

dominated by the second term in Equation 3.7), so the impact of d on u_e becomes less.

The trends can also be interpreted from basic physicochemical principles, considering that for a limiting case of a spherical polyelectrolyte (without a hard particle core), the electrophoretic mobility is independent of the size ("thickness") of the polyelectrolyte in the analytical electrokinetic model; i.e., the model is completely insensitive to layer thickness. This case is approached as the layer thickness becomes large ($\kappa d >> 1$) or as the charge density in the adsorbed layer becomes large, obscuring the electrostatic effect of the surface charge on the hard particle. On the other hand, for a nearly-uncharged coating (e.g. $N = 10^{-20}$ m^{-3}), the surface charge on the hard particle core sets the potential profile around the particle, and the magnitude of the potential decays toward zero within a few Debye lengths. Within this region (e.g. for a thin layer, κd not >> 1), the electrophoretic mobility is sensitive to a shift in the "slipping plane" due to drag imparted by the layer, so layer thickness can be identifiable. The electrical potential profiles for these two cases (thick, highly-charged layer versus thin, low-charge layer) are illustrated in Figure 3.7.

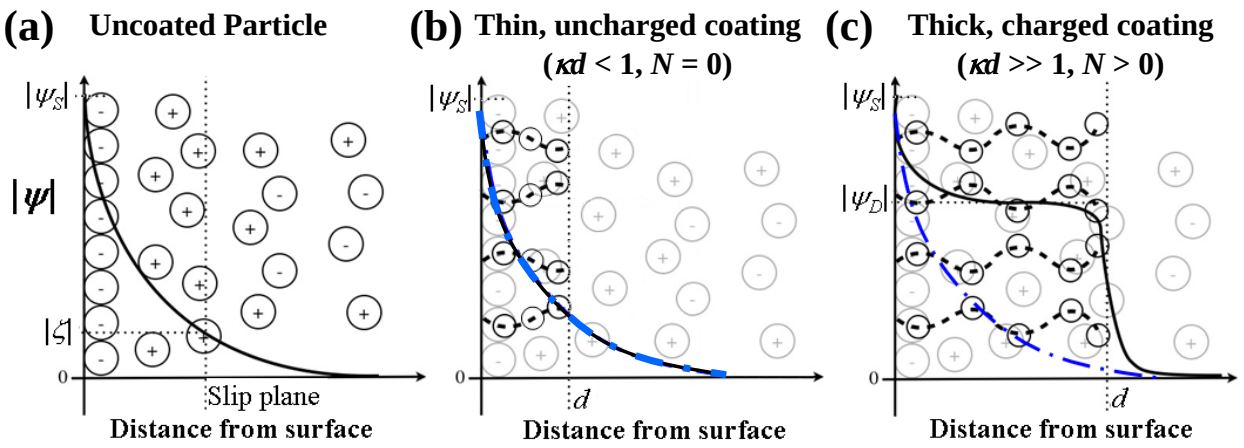

Figure 3.7. Illustration of the magnitude of the electrical potential profile, $|\psi|$, for a charged particle with surface potential ψ_S that is uncoated (a) or coated with a thin, uncharged coating (b) or thick, highly charged coating (c). In (b) and (c), the blue dash-dotted line indicates the potential attributable to the particle core, and the black solid line indicates the total potential. The uncharged coating (b) will impart drag without changing the potential profile, resulting in a significant change in the net force (electrophoretic vs. drag forces) on the particle. On the other hand, for a thick and highly charged layer (c), the Donnan potential associated with the layer charge, ψ_D, is attained and establishes the overall potential such that the net force on the particle is relatively insensitive to the layer extent or thickness.

Collinearity indices indicate how much the three parameters can offset each other's effects on u_e. No single critical value of the collinearity index determines identifiability, but critical values often lie between 5 and 20, and severe problems occur above 100.[27] For the analytical model, collinearity indices $\gamma_{N,d,1/\lambda}$ are often > 20, and all Group C and D cases have $\gamma_{N,d,1/\lambda}$ > 100 (Figure 3.5). Collinearity tends to be higher when sensitivity to d is low, such that small changes in N or λ^{-1} can easily offset the effect of d on u_e. However, $\gamma_{N,d}$ and $\gamma_{d,1/\lambda}$.(not shown here) are typically < 10 with some exceptions. Therefore, reducing the number of fitted model parameters by fixing N and/or λ^{-1} improves identifiability of d in Groups B and C (Figure

3.4(groups B, C)) because collinearity effects are lessened. Fixing both N and λ^{-1} removes collinearity effects altogether, leaving only sensitivity effects.

3.5.2 Identifiability of layer thickness in the numerical model

To compare the behavior of the numerical model with the analytical model, sensitivity and collinearity indices were computed using the exact, numerical electrokinetic model[4] and are plotted in Figure 3.8. The full set of indices for all cases is provided in Table A.2 in Appendix A. Comparison to the analytical model is shown in Figure 3.9. Sensitivity indices were used for the analysis since they were shown to correlate well with likelihood plots for the analytical model. δ_d^{msqr} is similar between the analytical and numerical models at low to moderate σ_{surf}, N, and λ^{-1} as expected, since polarization and relaxation effects are less significant in this regime. At high σ_{surf}, N, and λ^{-1}, sensitivity to d is improved compared to the analytical model, although some cases are still poorly identifiable. In this regime and at low ionic strength (where d is most important), polarization and relaxation effects – which are sensitive to d – significantly distort the double layer from its equilibrium state, and the force on the particle due to the charges becomes less dominant relative to the drag imparted by the layer. In extreme cases, the magnitude of u_e can become larger at high ionic strength than at low ionic strength as layer thickness is increased while holding N and λ^{-1} constant. Therefore, the electrophoretic mobility is more sensitive to the coating thickness when polarization and relaxation are accounted for in the numerical model.

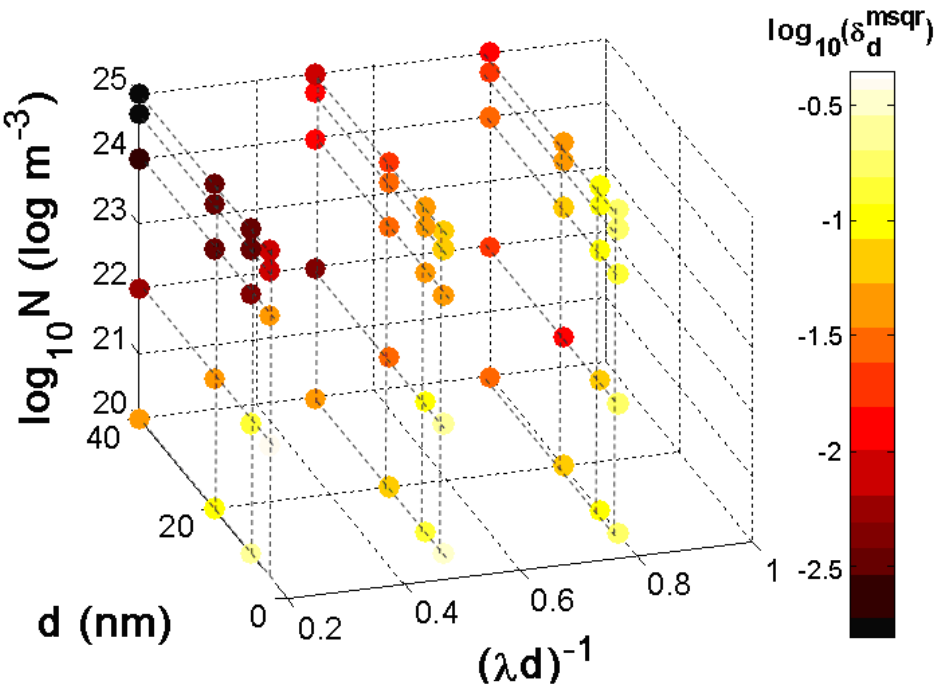

Figure 3.8. Correlation of δ_d^{msqr} to N, d, and λ^{-1} for the numerical model[4], at $\sigma_{surf} = 3\text{x}10^{-4}$ C/m^2. Trends are similar to those for the analytical model, except sensitivity is improved at high N and λ^{-1} where polarization and relaxation are more significant.

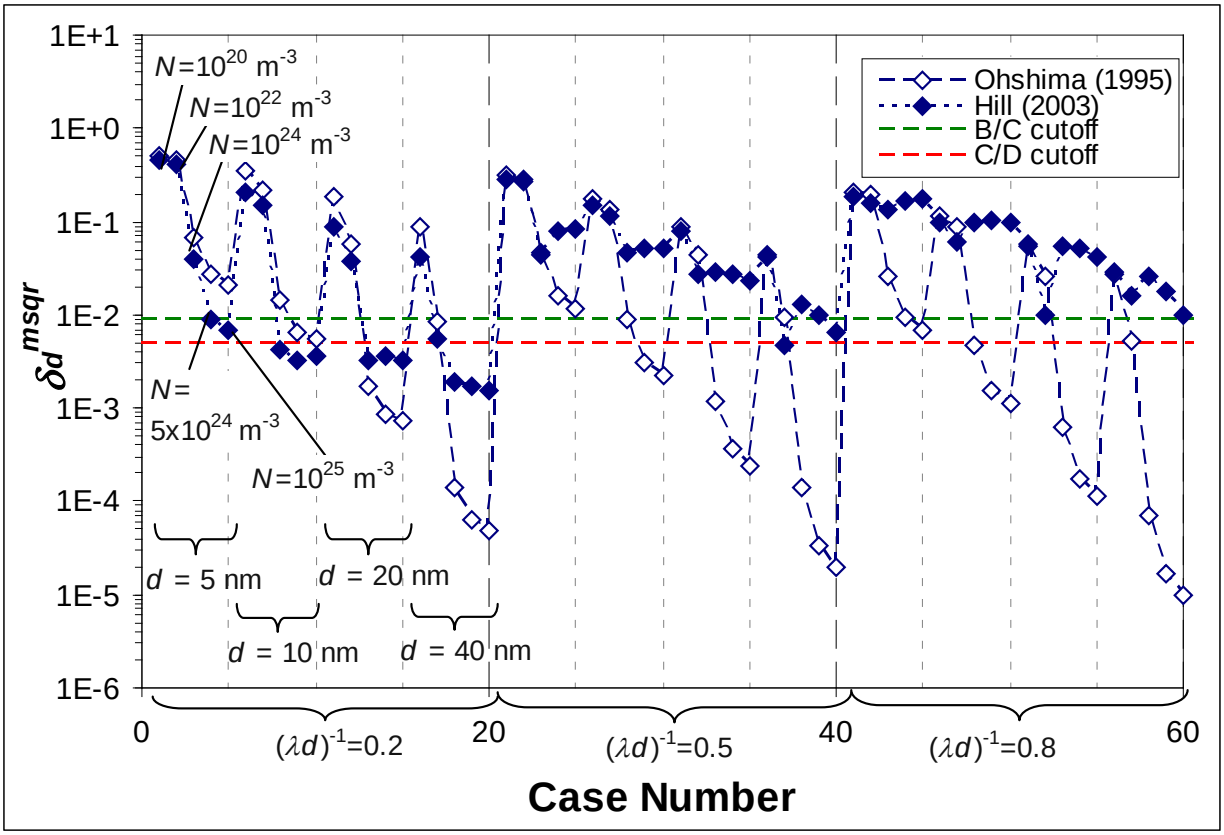

Figure 3.9. Comparison of δ_d^{msqr} for the analytical[2] and numerical[4] models at σ_{surf} = 3x10^{-4} C/m^2. N is systematically increased from 10^{20} m^{-3} (Cases 1, 6, 11, etc.) to 10^{25} m^{-3} (Cases 5, 10, 15, etc.) for each layer thickness. Layer thickness is systematically varied from 5 nm (Cases 1 to 5) to 40 nm (Cases 16 to 20). Systematic variation of N and d in the first third of the plot (Cases 0 to 20) is repeated in the following sections, where (λd) is varied (Cases 0 to 60). Green and red dashed lines show approximate sensitivity cutoffs distinguishing Groups B/C and C/D, respectively. Results for higher surface charges are shown in Figures A.2 and A.3 in Appendix A. Sensitivity for the numerical model[4] is improved compared to the analytical model[2] when polarization and relaxation effects are significant (high N and λ^{-1}).

Collinearity of the full set of parameters, $\gamma_{N,d,1/\lambda}$, is typically lower for the numerical model than the analytical model, although the majority of the cases analyzed here still have $\gamma_{N,d,1/\lambda} > 20$. Again, $\gamma_{N,d}$, $\gamma_{N,1/\lambda}$ and $\gamma_{d,1/\lambda}$ are significantly lower. $\gamma_{N,d}$ is often lower than $\gamma_{d,1/\lambda}$ in

the numerical model, suggesting that λ^{-1} can be more important to identify in order to determine *d*. Although layer permeability is not easily measured on a particle, the permeability can be written in terms of *d* and adsorbed mass, or it can,be correlated to the charged density in the adsorbed layer.[17] In this manner, parameter reduction can be applied to improve estimates of *d*.

Conditional likelihood plots for the subset of *d* and *N* were produced for select cases in Figure 3.10 to confirm that assessment of identifiability is valid using the sensitivity indices, which make linear approximations and were only fully compared to likelihood plots for the analytical model. Groups A and B are not distinguishable in these plots since one parameter is held at its least squares estimate. Despite using a linear approximation, the likelihood plots tend to agree with predictions of identifiability from the sensitivity indices. A notable exception is that layers with very high charge density (10^{25} m^{-3} or 16.6 mol/m^3) can have better identifiability of layer thickness than suggested by δ_d^{msqr}, where polarization effects become significant and linear assumptions made when deducing identifiability from δ_d^{msqr} break down further.

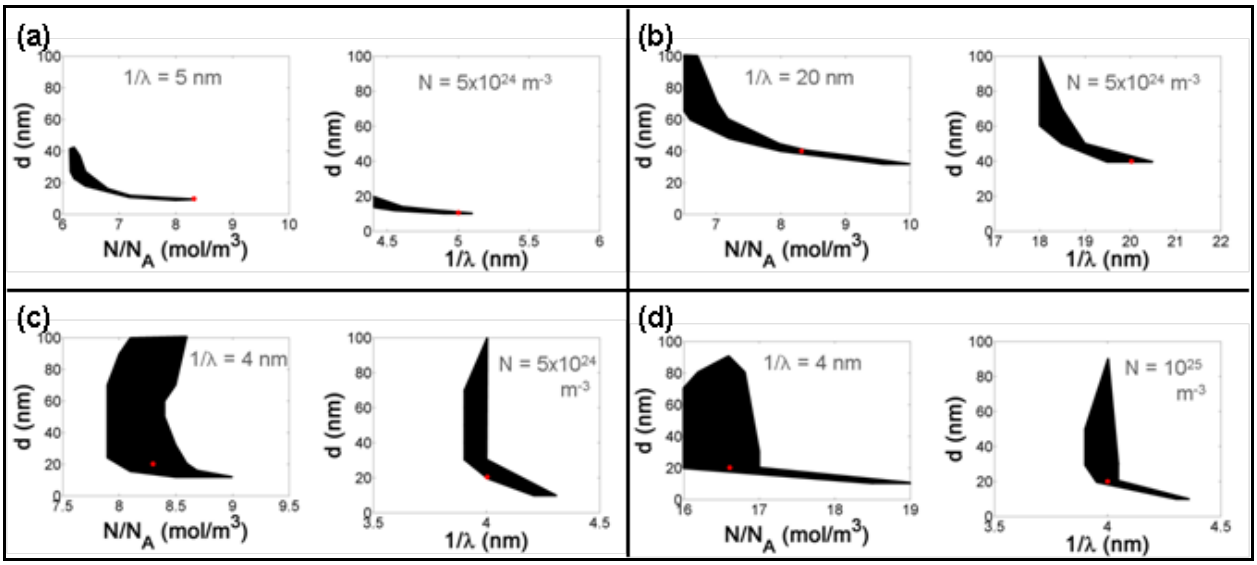

Figure 3.10. Conditional likelihood plots using the numerical model for (a) Case 24 (σ_{surf}=3x10^{-4} C/m^2, N=5x10^{24} m^{-3}, d=10 nm, $(\lambda d)^{-1}$=0.5); (b) Case 99 (σ_{surf}=3x10^{-3} C/m^2, N=5x10^{24} m^{-3}, d=40 nm, $(\lambda d)^{-1}$=0.5); (c) Case 74 (σ_{surf}=3x10^{-3} C/m^2, N=5x10^{24} m^{-3}, d=20 nm, $(\lambda d)^{-1}$=0.2); and (d) Case 75 (σ_{surf}=3x10^{-3} C/m^2, N=10^{25} m^{-3}, d=20 nm, $(\lambda d)^{-1}$=0.2), which are expected to fall in Groups A/B, C, D, and D, respectively, based on sensitivity indices. The plots confirm that the sensitivity indices (correlated to grouping using the analytical model) are adequate to assess identifiability of d for the numerical model, except at the highest charge density (N=10^{25} m^{-3}). Sharp edges on regions are artifacts of drawing regions on lower resolution plots.

3.5.3 Identifiability of charge density and permeability

For many studies, d is measured on flat surfaces or relatively monodisperse particles, and (N, λ^{-1}) is the parameter subset of interest (Table A.1). Parameter identifiability for N and λ^{-1} is briefly discussed here. These parameters typically have better identifiability than d, but can be poorly identifiable when two or three parameters are fitted together in the electrokinetic models. In contrast to identifiability of d (which was primarily determined by sensitivity), collinearity effects are also of importance for identifiability of N and λ^{-1}. The correlation between N and λ^{-1} is apparent in the conditional likelihood plots (Figure A.1 in Appendix A), and agrees with

physical expectations that increased drag in the layer would compensate for higher charge. Plots analogous to Figure 3.5 are provided for N and λ^{-1} in Appendix A (Figures A.4 and A.5, respectively). No distinct cut-offs are apparent to determine identifiability as were observed for layer thickness; however, identifiability problems occur primarily where $\gamma_{N,1/\lambda}$ is high and δ_N^{msqr} or $\delta_{1/\lambda}^{msqr}$ are low, as expected. In the analytical model, identifiability worsens as N, d, and $(\lambda d)^{-1}$ increase. Identifiability of N and λ^{-1} should be significantly better in the numerical model because collinearity indices are lower. However, a plot of collinearity and sensitivity indices suggests that λ^{-1} will still be poorly identifiable for some systems (Figure A.5); these points can be identified in Table A.2 and generally correspond to moderate to highly charged layers (e.g. N=10^{24} to $5x10^{24}$ m^{-3}).

3.5.4 Recommendations for application of the soft particle electrokinetic model

Based on the statistical analyses presented above, recommendations are made for the assessment of confidence in fitted parameters obtained from soft particle electrokinetic modeling methods. In addition, implications are discussed regarding systematic errors that can be expected in fitted layer thicknesses and the effectiveness of parameter reduction to improve confidence.

1. Trends in identifiability for different types of particles and adsorbed layers can be considered *a priori* to guide appropriate application of electrokinetic modeling methods.

The results of this study can inform decisions on whether to pursue electrokinetic modeling methods to attempt to estimate adsorbed layer properties. Given *a priori* knowledge about the layer thickness and charge, or upon obtaining the least squares estimate from a set of

electrophoretic mobility data, rough interpolation on Table A.2 in Appendix A can suggest whether a parameter is expected to be identifiable. General trends for identifiability of coating types are also summarized in Table 3.1. In the experimental section (Section 3.5.5), three types of coated nanoparticles that are expected to have distinctive adsorbed layer properties (based on their chemistries, i.e. functional groups, and molecular weights) are assessed, and the identifiability of layer thickness is compared to expectations from the theoretical cases assessed above.

Table 3.1. General trends between layer thickness identifiability and coating types for the numerical model[4]

Identifiability of layer thickness	**Physical properties of layer**	**Coating examples**
Good to moderate (Group A or B)	Low charge density	Neutral polymers
	Most thin layers (d on the order of κ^{-1} at low-ionic-strength experimental data)	Fulvic acid; some small humic acid fractions; low molar mass polymers
	High charge density, moderate to large layer thickness, and high permeability	Synthetic polyelectrolytes
Poor (Group C or D)	High charge density, moderate to large layer thickness, and low permeability	Synthetic polyelectrolytes

2. Uncertainty analysis should be provided when applying the electrokinetic modeling method; simplified approaches (sensitivity and collinearity indices) can be utilized.

The existence of a wide range of cases for which parameter identifiability problems are non-trivial indicates that uncertainty analysis should be undertaken when fitting layer parameters using the electrokinetic model, even when only one or two parameters are being fitted.

Sensitivity and collinearity indices can be calculated after the fitted parameters are obtained to roughly assess identifiability (these indices should be computed following the exact method presented here and demonstrated in Appendix A for direct comparison against the values obtained in this study). These indices also suggest whether parameter reduction by orthogonal measurements can improve identifiability. Likelihood plots are required for a rigorous analysis. Although producing profile likelihood plots will be computationally prohibitive when using the numerical electrokinetic model, conditional likelihood plots require fewer computations and will demonstrate the identifiability of any system of two fitted parameters.

3. Layer thicknesses are likely to be overestimated, especially when using the analytical model.

From the plots of the confidence regions, it is apparent that layer thickness is likely to be overestimated because "thick" and "very thick" layers (where $\kappa d >> 1$) will have similar electrophoretic mobilities, and the electrokinetic model thus has poor sensitivity to layer thickness in this regime. This problem is expected to be more significant for the analytical model for moderately- to highly-charged layers, both because of the poorer identifiability of layer thickness in the analytical model as well as its poorer accuracy (neglect of polarization effects).

4. Parameter reduction will be effective in some, but not all, scenarios.

The profile and conditional likelihood plots demonstrate that parameter reduction can improve confidence in the estimated layer parameters for coated particles in Groups B and C. Potential approaches for parameter reduction are described in Chapter 4. However, parameter reduction will not improve confidence in the layer thickness estimates for coated particles in

Group D. Therefore, confidence in layer thickness estimates should always be assessed, even when only one parameter is fitted.

3.5.5 Parameter identifiability for select experimental systems

Parameter identifiability analysis was demonstrated using experimental electrophoretic mobility data for PEG-coated citrate-reduced Au NPs (13 nm primary particle diameter), PAA-coated Fe_3O_4 NPs (20-30 nm), and PSS-coated RNIP (40 nm). This assessment accompanies the statistical analysis published by Louie et al.[33] The electrophoretic mobilities of the "bare" (including citrate-stabilized) and polymer-coated particles were measured over a range of ionic strengths. The zeta-potentials of the bare particles (inputs for the electrokinetic model) were calculated from their electrophoretic mobilities using Smoluchowski's theory. All bare particles in this study had a moderate to high negative charge at the pH used for the measurement (electrophoretic mobilities of -4.73, -3.67, and -3.29 μm-cm/V-s for citrate-reduced Au, Fe_3O_4, and RNIP, respectively, in 4 to 6 mM NaCl). The electrophoretic mobility data for the coated particles were fitted to obtain layer parameters using the MPEK numerical model.[4]

Based on the types of polymers used in this study, qualitative expectations of layer properties can be made. The PEG is uncharged and has a relatively small molecular weight (1,000 g/mol) with a short contour length (< 10 nm), which will result in a thin, uncharged adsorbed layer. The PEG used was thiol-terminated, and it is expected that the PEG attaches (chemisorbs) to the Au NP surface only at the thiol end group to produce a dense, end-grafted layer (small λ^{-1}). The PAA (MW ~11,000 g/mol) and PSS (MW ~70,000 g/mol) are longer polyelectrolytes and are expected to form thicker layers consisting of loops, trains and tails. These layers will likely have higher permeability due to electrostatic repulsion between charged

segments. At the pH used, 8.5, the carboxylate and sulfonate groups on PAA and PSS should be deprotonated, resulting in a relatively high charge density in the adsorbed layer.

The least-squares estimates for the layer parameters obtained by model fitting for the three data sets are provided in Table 3.2. The trend in these estimates is in agreement with expectations. Electrophoretic mobility data and fits are shown in Appendix A. For PEG, the parameter fitting was performed holding N at 0, although the effect of varying N can still be probed in the likelihood plots. It is also possible to fit the data without specifying N, and similar results are obtained for d and λ^{-1}. Considering the theoretical analyses presented earlier and the properties described above, the PEG-coated Au particles are expected to have good (Group A or B) identifiability, and PAA-coated Fe_3O_4 and PSS-coated RNIP are expected to have poor (Group C or D) identifiability, respectively.

Table 3.2. Least squares estimates for experimental cases

System	N/N_A **(mol/m^{-3})**	d **(nm)**	λ^{-1} **(nm)**
PEG-coated Au	0 (known)	2.1	0.2
PAA-coated Fe_3O_4	11	15	5.3
PSS-coated RNIP[19]	19	14	4.2

Statistical analysis of identifiability was then performed. Sensitivity indices (δ^{msqr}) and collinearity indices are provided in Table 3.3. Sensitivity to d is highest for the PEG-coated Au (δ_d^{msqr} = 0.24), near the Group B/C cutoff for PAA-coated Fe_3O_4 (δ_d^{msqr} = 0.011), and in the Group D range for PSS-coated RNIP (δ_d^{msqr}=0.0045). These indices suggest that the model is identifiable in d for PEG-coated Au but not for PAA-coated Fe_3O_4 or PSS-coated RNIP. The

collinearity indices suggest that collinearity between d and λ^{-1} can be problematic for PEG-coated Au, whereas identifiability may be poor whether either N or λ^{-1} are fixed (measured) for PAA-coated Fe_3O_4 and PSS-coated RNIP.

Table 3.3. Sensitivity and collinearity indices for experimental cases

System	δ^{msqr} **summaries**			γ_K **collinearity indices**			
	δ_N^{msqr}	δ_d^{msqr}	$\delta_{1/\lambda}^{msqr}$	$\gamma_{N,d,1/\lambda}$	$\gamma_{N,d}$	$\gamma_{N,1/\lambda}$	$\gamma_{d,1/\lambda}$
PEG-coated Au	0.12	0.24	0.10	40	1.3	1.3	39
PAA-coated Fe_3O_4	0.076	0.011	0.27	127	9.5	124	9.3
PSS-coated RNIP	0.036	0.0045	0.31	73	2.1	63	2.1

Conditional 95% and 80% likelihood plots are shown in Figures 3.11, 3.12, and 3.13 for PEG-coated Au, PAA-coated Fe_3O_4, and PSS-coated RNIP, respectively. For these experimental cases, these plots do not assume a fixed (e.g. 4%) relative error on u_e as in the simulated cases (Equation 3.13); rather, the likelihood region is defined using the goodness of fit and the number of data, as specified in Equation 3.12.

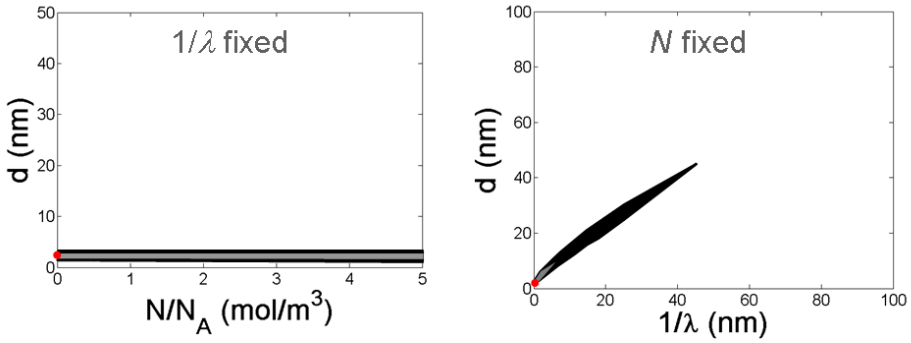

Figure 3.11. 95% and 80% conditional likelihood regions for PEG-coated Au, a Group A or B system. 95% regions are shown in black; 80% in grey. Sharp edges on regions are artifacts due to drawing regions on lower resolution plots.

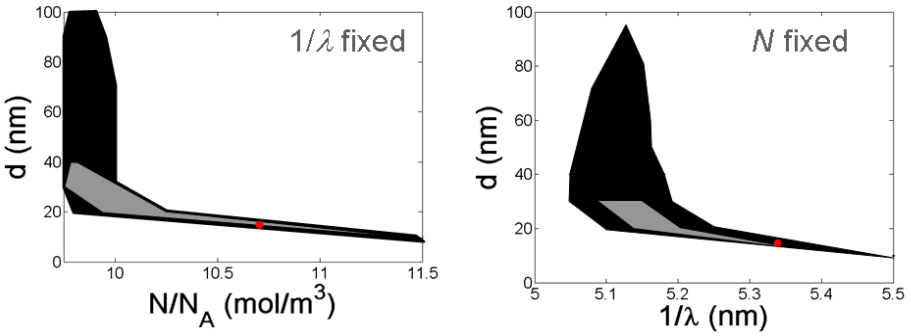

Figure 3.12. 95% and 80% conditional likelihood regions for PAA-coated Fe_3O_4, a Group C system.

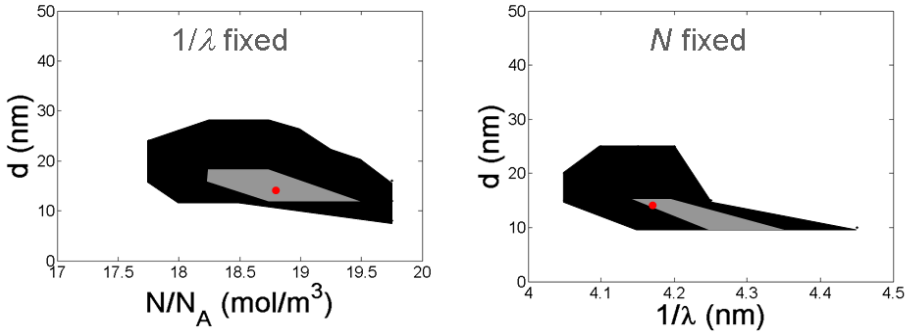

Figure 3.13. 95% and 80% conditional likelihood regions for PSS-coated RNIP, a Group A/B system. Sensitivity indices predicted a Group D system, but the likelihood region is bounded due to nonlinear polarization effects not captured in the sensitivity index.

The likelihood plots for PEG-coated Au and PAA-coated Fe_3O_4 agree with expectations from their sensitivity indices. For PEG-coated Au (Figure 3.11), the 95% likelihood region is bounded in *d* (within 100 nm) as for Group A or B cases, although the range extends to ~40 nm in *d* when accounting for error of the best fit and the number of ionic strengths used (six). Here, the criteria are more stringent (that is, the right-hand side of Equation 3.12 has a higher magnitude) than for the theoretical analysis (Section 3.5.2) using Equation 3.13. However, the 80% likelihood region is bounded within a small region (to 8 nm in *d*). Importantly, including data at additional ionic strengths would further improve confidence. Collinearity between *d* and λ^{-1} is shown to be important as expected, whereas possible variations in *N* are unimportant within the range shown.

Conditional likelihood regions are plotted in Figure 3.12 for PAA-coated magnetite. The 95% likelihood region for *d* vs. *N* is not bounded in *d* within 100 nm unless *N* is fixed. The 80% region is smaller but still extensive (to ~30-40 nm in *d*). Therefore, PAA-coated magnetite is a Group C case, as predicted.

PSS-coated RNIP is predicted to be a Group C or D case based on the sensitivity index alone. However, because of the high layer charge density (18.8 mol/m^3), polarizability becomes significant and the 95% and 80% conditional likelihood regions are bounded to ~30 nm in *d* (Figure 3.13). This result is similar to that observed for theoretical cases with $N = 10^{25}$ m^{-3} (16.6 mol/m^3). However, fixing both *N* and λ^{-1} would not be as helpful for PSS-coated RNIP as for the other two cases due to the poor sensitivity to *d*; that is, the potential for parameter reduction to improve the confidence in the layer thickness estimate is lesser. In summary, identifiability of the experimental cases shown here agrees with expectations from the theoretical analysis.

3.5.6 Application of electrokinetic modeling for nanoparticle deposition studies

Soft particle electrokinetic modeling was employed in support of a study by Hotze et al.[34] to assess the adsorbed layer properties for three sets of nanoparticles (Ag, TiO_2, and C_{60}), each coated with either poly(acrylic acid) (PAA), a coal-derived humic acid (HA), or bovine serum albumin (BSA). The overall objective of the study was to determine whether knowledge of the coating type alone could be used to predict the deposition of coated nanoparticles to silica surfaces, or whether different nanoparticles coated with the same macromolecule must be assessed individually to predict their transport behavior. In addition, the study aimed to identify important properties of the adsorbed layer that correlate to the nanoparticle deposition behavior. Soft particle electrokinetic modeling was applied to estimate the adsorbed layer thickness for these correlations.

The adsorbed coating was hypothesized to mask interaction of the nanoparticle core (i.e. its surface and charge) with the silica substrate if a thick (i.e., $\kappa d >> 1$) and coherent coating of macromolecule was established on each nanoparticle (Figure 3.14). The thick coating would be expected to prevent approach of the nanoparticle core and silica substrate within separation distances much less than the layer thickness due to steric effects (osmotic and elastic forces). Furthermore, at this separation distance, forces attributable to the nanoparticle core (e.g., van der Waals interaction forces or electrostatic forces) would be insignificant; instead, the adsorbed macromolecule would control these interactions. The attachment efficiency would then depend solely on the type of macromolecule and be independent of the type of nanoparticle. If this behavior is shown to occur, the data requirements and experimental testing needed to parameterize transport models could be greatly reduced to disregard the specific properties of the nanoparticle core for macromolecule-coated nanoparticles.

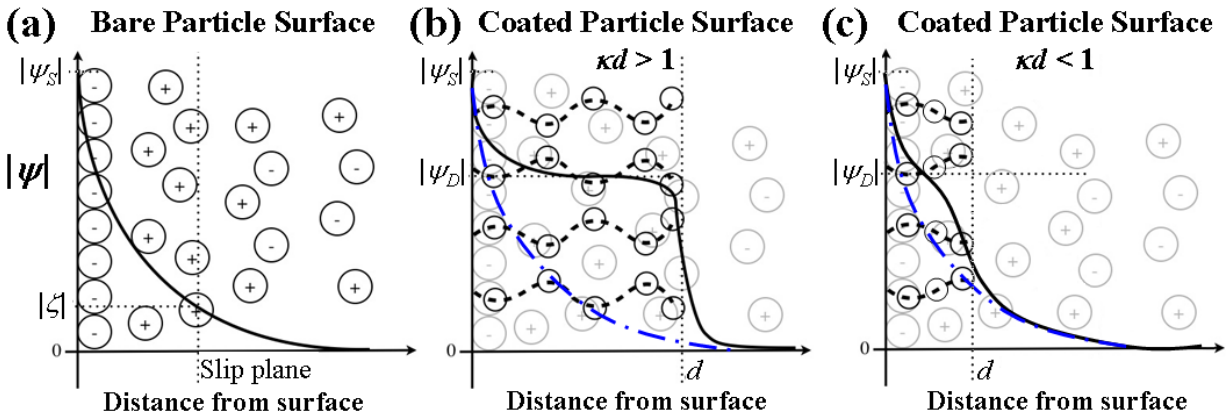

Figure 3.14. Illustration of the electrical potential profile, ψ, around a bare particle (a), and a coated particle with either a thick, charged coating (b) or a thin, charged coating (c). For the bare particle, the electrophoretic mobility is proportional to the zeta-potential, following Smoluchowski's equation (or, more generally, Henry's equation). For a particle coated with a thick, highly charged layer, the Donnan potential (ψ_D) is attained within the layer, and particle surface has little influence on the energy at the edge of the adsorbed layer. For a particle coated with a thin layer, the Donnan potential is not achieved and the underlying particle surface will influence interactions beyond the edge of the adsorbed layer.

The overall results of the study are summarized here. First, the hypothesis that the coating alone would control the coated nanoparticle deposition behavior was disproven: the attachment efficiency of the coated nanoparticles could not be predicted solely from the type of adsorbed macromolecule (i.e., different nanoparticles coated with the same macromolecule showed different attachment efficiencies) (Figure 3.15). Furthermore, the trend in attachment for each macromolecule differed across the nanoparticles (e.g., adsorption of PAA and HA resulted in lower attachment efficiencies for Ag and TiO_2 compared to the uncoated nanoparticles, but higher attachment efficiencies for C_{60}). The following mechanisms were suggested to explain this result: on some or all of the nanoparticles, (1) the adsorbed layer was thin (as illustrated in

Figure 3.14) or incomplete surface coverage was attained, such that the underlying nanoparticle influenced the surface interaction forces; or (2) the adsorbed mass or conformation of the adsorbed macromolecule varied among different nanoparticles, such that the electrostatic or steric forces imparted by the layer were different.

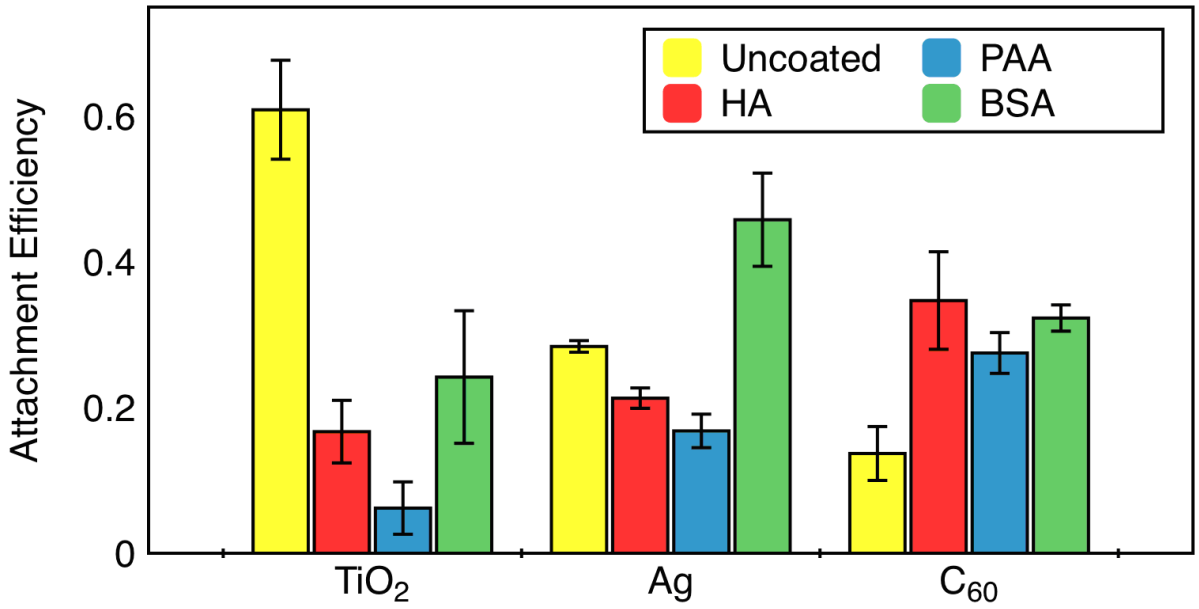

Figure 3.15. Attachment efficiencies for TiO_2, Ag, and C_{60}, either uncoated (or citrate-stabilized, in the case of Ag) or coated with HA, PAA, or BSA. The coatings did not produce consistent attachment efficiencies of the nanoparticles; furthermore, the trend in their effect differed among the nanoparticles. Deposition experiments and attachment efficiency calculations were performed by Ernest Hotze and Shihong Lin.

Because the adsorbed layer composition alone was insufficient to explain the measured nanoparticle attachment efficiencies, correlations of attachment efficiency with more specific properties of the coated nanoparticle and the adsorbed layer were explored. In particular, the effects of electrophoretic mobility, adsorbed mass, and adsorbed layer thickness (estimated by fitting electrophoretic mobility data to Hill's numerical electrokinetic model) were assessed.

These properties are reported in Table 3.4: the estimated adsorbed layer thickness and weight-average molecular weight of humic acid (determined by size exclusion chromatography with multi-angle light scattering) were provided by S. Louie; measurements of hydrodynamic diameter, adsorbed mass, and electrophoretic mobility were taken by Ernest Hotze.

Table 3.4. Properties of the nanoparticles and adsorbed layers

Particle Type	**Coating molecular weight*** **(kg/mol)**	**Particle hydrodynamic diameter, number / intensity average★ (nm)**	**Adsorbed mass of coating❖ (mg/m^2)**	**Estimated adsorbed layer thickness✚ (nm)**	**Particle electrophoretic mobility◆ (μm•cm/V•s)**
TiO_2	_	132 / 511	_	_	-1.94
Ag-Citrate	0.294	99 / 101	_	_	-3.74
C_{60}	_	204 / 205	_	_	-0.83
TiO_2 + HA	60	103 / 481	0.18	5	-2.84
Ag + HA	60	165 / 168	1.97	31	-2.17
C_{60} + HA	60	50 / 414	5.38	14	-2.01
TiO_2 + PAA	44	183 / 662	0.04	10	-2.70
Ag + PAA	44	228 / 232	below detection	31	-1.37
C_{60} + PAA	44	87 / 89	below detection	10	-1.75
TiO_2 + BSA	67	439 / 498	0.27	5	-2.17
Ag + BSA	67	58 / 190	2.90	20	-1.82
C_{60} + BSA	67	108 / 109	below detection	7	-1.41

*Coating molecular weight was measured by multi-angle light scattering. For HA, the weight-average molecular weight is reported, but the sample has high polydispersity. For BSA, the monomer molecular weight is reported. ★Particle hydrodynamic diameter was measured by dynamic light scattering by fitting multiple exponentials to the correlation function to obtain the distribution of particle sizes using a non-negative least squares algorithm. ❖Coating surface concentration was estimated by solution depletion following adsorption. ✚Least squares estimates of coating layer thickness were obtained by fitting electrophoretic mobility data with a numerical soft particle electrokinetic model.[4] ◆Electrophoretic mobility measurements were measured in 1 mM $NaHCO_3$ at pH 7.6.

Poor correlation ($R^2 \leq 0.33$) was observed between the attachment efficiency and any of the individual properties (electrophoretic mobility, adsorbed mass, and adsorbed layer thickness). In addition, attachment efficiencies predicted from a multi-parameter correlation for coated nanoparticle deposition[1] showed poor agreement with the measured attachment efficiencies, where attachment efficiencies were underestimated by approximately an order of magnitude for all cases (Figure A.6). The poor correlations may be attributable to the need to include additional properties of the coated nanoparticles (e.g., hydrophobicity to estimate Lewis acid-base interactions), inaccuracies in the characterization provided, or error in the multi-parameter correlation used.

Here, we focus on the uncertainty in the layer thickness estimates from the numerical soft particle electrokinetic model. Following the methods presented in this chapter, the sensitivity indices for layer thickness were computed (Table 3.5).

Table 3.5. Sensitivity indices for fitted layer thickness of coated NP systems

Particle Type	δ_d^{msqr}
TiO_2 + HA	0.02
Ag + HA	0.004
C_{60} + HA	0.02
TiO_2 + PAA	0.03
Ag + PAA	0.04
C_{60} + PAA	0.03
TiO_2 + BSA	0.03
Ag + BSA	0.005
C_{60} + BSA	0.03

As determined in Section 3.5.1, δ_d^{msqr} values lower than 0.009 typically correspond to cases for which layer thickness is not identifiable, whereas cases with identifiable layer thicknesses generally have δ_d^{msqr} values higher than ~0.06.[33] Therefore, confidence in the estimates for Ag coated with HA and BSA is poor, and these layer thicknesses are likely overestimated. Conditional likelihood regions were also plotted (not shown) to more rigorously assess the extent of the uncertainty in layer thickness at 80% and 95% confidence intervals (based on the standard deviation in the experimental electrophoretic mobility data). These plots indicate that the layer thickness estimates using this method are unreliable for the coated Ag and C_{60} nanoparticles (one Group C and five Group D cases as defined in Section 3.5.1), with uncertainty in layer thickness only bounded for the TiO_2 nanoparticles coated with BSA and PAA (Group A or B cases). Additional uncertainty is introduced for the Ag NPs because displacement of the initial stabilizer (negatively-charged citrate) by the macromolecules is possible, which would affect the measured electrophoretic mobility but is not accounted for in the modeling. Overestimation of layer thickness would be consistent with an under-prediction of attachment efficiency by the multi-parameter correlation by Phenrat et al.[1]

The possibilities for additional errors beyond that in the estimated layer thickness should also be considered. Even for particles where the estimated layer thickness was relatively thin (e.g., 5 to 7 nm for HA-coated TiO_2, BSA-coated TiO_2, and BSA-coated C_{60}), an order of magnitude under-prediction of attachment efficiency was observed. This discrepancy suggests that other factors beyond overestimation of the estimated adsorbed layer thickness are likely to be important for at least some of the coated nanoparticles assessed here. Other measured properties, such as adsorbed mass, also have uncertainty. Alternatively, properties that were not measured, such as the uniformity of adsorbed macromolecule around the nanoparticles, the

hydrophobicity of the macromolecules or nanoparticles, or the structure (e.g. fractal dimension) of the nanoparticle aggregates, could be important. Finally, the mechanism of particle removal in the column may differ across the types of nanoparticles used: straining or ripening mechanisms can enhance nanoparticle deposition but are not represented in the models used here.

Finally, the multi-parameter correlation[1] may be inaccurate for these particular systems or may have inherent error. In particular, this correlation utilized layer thicknesses estimated using Ohshima's analytical solution to the electrokinetic model, which is less accurate and less sensitive to layer thickness than the numerical solutions. The possibility to revise the correlation using layer thicknesses estimated from the numerical electrokinetic models is demonstrated in Appendix A (Section A.8). A minor improvement is observed for some of the nanoparticles coated with high molecular weight macromolecules; however, the results suggest that further improvements beyond layer thickness characterization will be needed to predict nanoparticle transport with better accuracy.

References for this chapter are listed at the end of Chapter 4.

Chapter 4. Summary of results, significance, and future needs for application of soft particle electrokinetic models

4.1 New knowledge produced and significance

The parameter identifiability study provided the first rigorous and systematic assessment of confidence in layer parameters estimated from soft particle electrokinetic modeling. Specifically, parameter identifiability analysis was performed for theoretical varied cases of coated particle systems, and coating properties were correlated to identifiability of the layer thickness. Identifiability in the analytical model correlated well to sensitivity indices, suggesting that a sensitivity calculation can be a good surrogate for full likelihood plots for this model. In general, identifiability of the layer thickness is poorest for thick, highly charged layers with high permeability. Layer thickness can be severely overestimated for these cases. For the exact numerical electrokinetic model[4], identifiability of layer thickness was similar except at high charges and permeability, where polarization and relaxation effects yield improved identifiability compared to the analytical model.

The results of this study will have a significant impact on the community of researchers that utilize electrokinetic modeling approaches by demonstrating the limitations of the method and the need for more prudent application of the method in future studies. Furthermore, the analysis presented here can be used to identify systems for which external measurements, such as dielectric spectroscopy suggested by Hill et al.[29,30] or AFM measurements suggested by Duval and Gaboriaud[32], are necessary. A recent demonstration of the use of AFM and electrokinetic modeling methods as orthogonal methods, along with a sensitivity analysis on the fitted

parameters, was provided by Pensini et al. in an assessment of the forces produced by carboxymethylcellulose adsorbed to iron particles.[43]

More broadly, the statistical analysis of the electrokinetic method provided here should be considered in the context of uncertainty in alternative measurements to inform decisions on the best methods to use for adsorbed layer characterization. Studies comparing sizing methods for uncoated nanoparticles have already been performed.[44-46] Analogous studies for adsorbed layer characterization methods would be useful for the colloid and nanoparticle research community. One notable result from this study is that the electrokinetic approach may be most suitable to determine the layer thickness of thin layers because typical sizing methods (e.g., taking the difference in hydrodynamic diameter measured by dynamic light scattering on bare and coated particles) can be inadequate to assess thin layers on polydisperse particles.[47]

The experimental studies confirmed the results of the statistical analysis. First, for three coated nanoparticles that were expected to have distinct adsorbed layer properties (i.e., a thin, uncharged layer versus thicker, charged layers), the identifiability of layer thickness agreed with expectations of the uncertainty analysis. Application of the electrokinetic modeling method to estimate layer thicknesses in studies of nanoparticle deposition further demonstrated the implications of the statistical study. In particular, limitations in the characterization methods were explicitly considered when interpreting the poor predictability of the attachment efficiencies of coated nanoparticles. These limitations are often overlooked in studies of the environmental behavior and effects of nanoparticles. Here, we focused on improvements in the layer thickness estimation. However, the results of the analyses here indicate that other improvements (e.g., measuring and incorporating other parameters) will also be necessary to improve predictions of nanoparticle transport in the environment.

4.2 Future work

Based on the results of this study, research needs or future approaches are identified that would greatly reinforce decision-making and validation regarding the application of soft particle electrokinetic modeling to estimate the properties of adsorbed layers on particles. Considering the problems with parameter identifiability that were determined in this research, one of the main conclusions is that the electrokinetic modeling approach should not be used to fit multiple parameters unless an uncertainty analysis is also provided to demonstrate that good confidence is achieved. However, fitting single parameters can be feasible; approaches for parameter reduction are therefore proposed in Section 4.2.1. Further model validation is also suggested in Section 4.2.2.

Broader needs for characterization were identified upon application of electrokinetic modeling to support nanoparticle deposition studies. These research needs are discussed in the broader conclusions in Chapter 8, in the context of the development of correlations for nanoparticle fate and transport in the environment.

4.2.1 Parameter reduction to expand the applicability of electrokinetic modeling methods

First, routes for parameter reduction or orthogonal characterization should be explored and utilized to improve the identifiability of parameters in the electrokinetic modeling method, and hence expand its applicability. The likelihood plots produced in this study indicate that charge density and permeability should be identifiable if only one parameter is fitted. Layer thickness will still be non-identifiable for some types of coated nanoparticles (i.e., the Group D cases identified in this study), even if it is the sole fitted parameter; however, the range of systems that are identifiable will be expanded.

A simple approach to obtain a single-parameter model uses an external measurement of the adsorbed mass (e.g., by solution depletion methods), an estimate of the charge per mass of the adsorbed macromolecule (e.g., from titration or an acid-base equilibrium model for the macromolecule of interest), and expression of the permeability in terms of the segment density in the layer. The required equations are presented in Appendix A. Other approaches are to couple electrokinetic modeling with other models for dielectric spectroscopy and atomic force microscopy measurements, as suggested or demonstrated by others.[32,43,48,49]

4.2.2 Experimental validation of adsorbed layer properties from electrokinetic modeling

Additional experimental studies are needed to validate that the electrokinetic modeling method can produce accurate parameter estimates (as well as parameter fits with good statistical confidence, as assessed here). Although model fitting results have been compared against theoretical or measured layer properties for a few particle sets,[17] to our knowledge, no study has been undertaken to explicitly validate this approach for coated particles across a wide range of properties. Nevertheless, the electrokinetic modeling approach has already been applied to estimate one or more layer properties for many systems, including inorganic colloids and biological and environmental samples. One approach for model validation would be to assess monodisperse nanoparticles (for which dynamic light scattering can be use to obtain layer thickness). If the layer properties are well-controlled, they can be systematically varied to obtain a range of properties to assess (e.g., by grafting brushes of different molecular weight to vary layer thickness). Additional validation experiments are required to assess polydisperse nanoparticles, for which the electrokinetic modeling approach is expected to be advantageous to dynamic light scattering measurements (which are strongly affected by the aggregation state of

the nanoparticles). Here, bimodal or multimodal mixtures of monodisperse nanoparticles can be assessed to determine if accurate layer thicknesses can be obtained. These validation experiments would provide a more definitive assessment of the applicability of soft particle electrokinetic modeling to estimate layer properties.

References for Part I (Chapters 3 and 4)

(1) Phenrat, T.; Song, J. E.; Cisneros, C. M.; Schoenfelder, D. P.; Tilton, R. D.; Lowry, G. V. Estimating attachment of nano- and submicrometer-particles coated with organic macromolecules in porous media: Development of an empirical model. *Environ. Sci. Technol.* **2010**, *44* (12), 4531-4538.
(2) Ohshima, H. Electrophoresis of soft particles. *Adv. Colloid Interface Sci.* **1995**, *62* (2-3), 189-235.
(3) Ohshima, H. Electrophoretic mobility of a highly charged soft particle: Relaxation effect. *Colloids Surfaces A* **2011**, *376* (1-3), 72-75.
(4) Hill, R. J.; Saville, D. A.; Russel, W. B. Electrophoresis of spherical polymer-coated colloidal particles. *J. Colloid Interface Sci.* **2003**, *258* (1), 56-74.
(5) Duval, J. F. L.; Ohshima, H. Electrophoresis of diffuse soft particles. *Langmuir* **2006**, *22* (8), 3533-3546.
(6) Lopez-Garcia, J. J.; Grosse, C.; Horno, J. Numerical study of colloidal suspensions of soft spherical particles using the network method - 2. AC electrokinetic and dielectric properties. *J. Colloid Interface Sci.* **2003**, *265* (2), 341-350.
(7) Lopez-Garcia, J. J.; Grosse, C.; Horno, J. Numerical study of colloidal suspensions of soft spherical particles using the network method - 1. DC electrophoretic mobility. *J. Colloid Interf. Sci.* **2003**, *265* (2), 327-340.
(8) Ahualli, S.; Jimenez, M. L.; Carrique, F.; Delgado, A. V. AC electrokinetics of concentrated suspensions of soft particles. *Langmuir* **2009**, *25* (4), 1986-1997.
(9) Duval, J. F. L. Electrophoresis of soft colloids: Basic principles and applications. In *Environmental colloids and particles: Behaviour, separation and characterisation*; Wilkinson, K. J., Lead, J. R., Eds.; John Wiley & Sons, Ltd: West Sussex, England, **2007**; pp 315-344.
(10) Kiers, P. J. M.; Bos, R.; van der Mei, H. C.; Busscher, H. J. The electrophoretic softness of the surface of Staphylococcus epidermidis cells grown in a liquid medium and on a solid agar. *Microbiol.-UK* **2001**, *147*, 757-762.
(11) Tsuneda, S.; Aikawa, H.; Hayashi, H.; Hirata, A. Significance of cell electrokinetic properties determined by soft-particle analysis in bacterial adhesion onto a solid surface. *J. Colloid Interface Sci.* **2004**, *279* (2), 410-417.
(12) Clements, A.; Gaboriaud, F.; Duval, J. F. L.; Farn, J. L.; Jenney, A. W.; Lithgow, T.; Wijburg, O. L. C.; Hartland, E. L.; Strugnell, R. A. The Major Surface-Associated Saccharides of Klebsiella pneumoniae Contribute to Host Cell Association. *PLoS One* **2008**, *3* (11).

(13) Duval, J. F. L.; Busscher, H. J.; van de Belt-Gritter, B.; van der Mei, H. C.; Norde, W. Analysis of the interfacial properties of fibrillated and nonfibrillated oral streptococcal strains from electrophoretic mobility and titration measurements: Evidence for the shortcomings of the 'classical soft-particle approach'. *Langmuir* **2005**, *21* (24), 11268-11282.
(14) Langlet, J.; Gaboriaud, F.; Gantzer, C.; Duval, J. F. L. Impact of chemical and structural anisotropy on the electrophoretic mobility of spherical soft multilayer particles: The case of bacteriophage MS2. *Biophys. J.* **2008**, *94* (8), 3293-3312.
(15) Rodriguez, V. V.; Busscher, H. J.; Norde, W.; van der Mei, H. C. Softness of the bacterial cell wall of *Streptococcus mitis* as probed by microelectrophoresis. *Electrophoresis* **2002**, *23* (13), 2007-2011.
(16) Tsuneda, S.; Jung, J.; Hayashi, H.; Aikawa, H.; Hirata, A.; Sasaki, H. Influence of extracellular polymers on electrokinetic properties of heterotrophic bacterial cells examined by soft particle electrophoresis theory. *Colloids Surfaces B* **2003**, *29* (2-3), 181-188.
(17) Hill, R. J.; Saville, D. A. 'Exact' solutions of the full electrokinetic model for soft spherical colloids: Electrophoretic mobility. *Colloids Surfaces A* **2005**, *267* (1-3), 31-49.
(18) Hyono, A.; Gaboriaud, F.; Mazda, T.; Takata, Y.; Ohshima, H.; Duval, J. F. L. Impacts of Papain and Neuraminidase Enzyme Treatment on Electrohydrodynamics and IgG-Mediated Agglutination of Type A Red Blood Cells. *Langmuir* **2009**, *25* (18), 10873-10885.
(19) Phenrat, T.; Saleh, N.; Sirk, K.; Kim, H. J.; Tilton, R. D.; Lowry, G. V. Stabilization of aqueous nanoscale zerovalent iron dispersions by anionic polyelectrolytes: adsorbed anionic polyelectrolyte layer properties and their effect on aggregation and sedimentation. *J. Nanopart. Res.* **2008**, *10* (5), 795-814.
(20) Viota, J. L.; de Vicente, J.; Duran, J. D. G.; Delgado, A. Stabilization of magnetorheological suspensions by polyacrylic acid polymers. *J. Colloid Interface Sci.* **2005**, *284* (2), 527-541.
(21) Viota, J. L.; de Vicente, J.; Ramos-Tejada, M. M.; Duran, J. D. G. Electrical double layer and rheological properties of yttria-stabilized zirconia suspensions in solutions of high molecular weight polyacrylic acid polymers. *Rheol. Acta* **2004**, *43* (6), 645-656.
(22) Lopez-Viota, J.; Mandal, S.; Delgado, A. V.; Toca-Herrera, J. L.; Moller, M.; Zanuttin, F.; Balestrino, M.; Krol, S. Electrophoretic characterization of gold nanoparticles functionalized with human serum albumin (HSA) and creatine. *J. Colloid Interface Sci.* **2009**, *332* (1), 215-223.
(23) Lopez-Leon, T.; Ortega-Vinuesa, J. L.; Bastos-Gonzalez, D.; Elaissari, A. Cationic and anionic poly(N-isopropylacrylamide) based submicron gel particles: Electrokinetic properties and colloidal stability. *J. Phys. Chem. B* **2006**, *110* (10), 4629-4636.
(24) Viota, J. L.; Rudzka, K.; Trueba, A.; Torres-Aleman, I.; Delgado, A. V. Electrophoretic characterization of insulin growth factor (IGF-1) functionalized magnetic nanoparticles. *Langmuir* **2011**, *27* (10), 6426-6432.
(25) Duval, J. F. L.; Wilkinson, K. J.; Van Leeuwen, H. P.; Buffle, J. Humic substances are soft and permeable: Evidence from their electrophoretic mobilities. *Environ. Sci. Technol.* **2005**, *39* (17), 6435-6445.
(26) Bates, D.; Watts, D. *Nonlinear regression analysis and its applications*; John Wiley & Sons: New York, **1988**.
(27) Brun, R.; Reichert, P.; Kunsch, H. R. Practical identifiability analysis of large environmental simulation models. *Water Resour. Res.* **2001**, *37* (4), 1015-1030.

(28) Ahualli, S.; Arroyo, F. J.; Delgado, A. V. Consideration of polydispersity in the evaluation of the dynamic mobility of concentrated suspensions. *J. Colloid Interface Sci.* **2010**, *343* (1), 350-358.
(29) Hill, R. J.; Saville, D. A.; Russel, W. B. Polarizaability and complex conductivity of dilute suspensions of spherical colloidal particles with uncharged (neutral) polymer coatings. *J. Colloid Interface Sci.* **2003**, *268* (1), 230-245.
(30) Hill, R. J.; Saville, D. A.; Russel, W. B. Polarizaability and complex conductivity of dilute suspensions of spherical colloidal particles with charged (polyelectrolyte) coatings. *J. Colloid Interface Sci.* **2003**, *263* (2), 478-497.
(31) Cametti, C.; Fratoddi, I.; Venditti, I.; Russo, M. V. Dielectric Relaxations of Ionic Thiol-Coated Noble Metal Nanoparticles in Aqueous Solutions: Electrical Characterization of the Interface. *Langmuir* **2011**, *27* (11), 7084-7090.
(32) Duval, J. F. L.; Gaboriaud, F. Progress in electrohydrodynamics of soft microbial particle interphases. *Curr. Opin. Colloid Interface Sci.* **2010**, *15* (3), 184-195.
(33) Louie, S. M.; Phenrat, T.; Small, M. J.; Tilton, R. D.; Lowry, G. V. Parameter identifiability in application of soft particle electrokinetic theory to determine polymer and polyelectrolyte coating thicknesses on colloids. *Langmuir* **2012**, *28* (28), 10334-10347.
(34) Hotze, E. M.; Louie, S. M.; Lin, S.; Wiesner, M. R.; Lowry, G. V. Nanoparticle core properties affect attachment of macromolecule-coated nanoparticles to silica surfaces. *Environ. Chem.* **2014**, *11* (3), 257-267.
(35) Hiemenz, P. C.; Rajagopalan, R. *Principles of colloid and surface chemistry*; Marcel Dekker: New York, **1997**.
(36) Dukhin, S. S.; Zimmermann, R.; Duval, J. F. L.; Werner, C. On the applicability of the Brinkman equation in soft surface electrokinetics. *J. Colloid Interface Sci.* **2010**, *350* (1), 1-4.
(37) Golas, P. L.; Louie, S.; Lowry, G. V.; Matyjaszewski, K.; Tilton, R. D. Comparative Study of Polymeric Stabilizers for Magnetite Nanoparticles Using ATRP. *Langmuir* **2010**, *26* (22), 16890-16900.
(38) Tufenkji, N.; Elimelech, M. Correlation equation for predicting single-collector efficiency in physicochemical filtration in saturated porous media. *Environ. Sci. Technol.* **2004**, *38* (2), 529-536.
(39) Amirbahman, A.; Olson, T. M. Transport of humic matter-coated hematite in packed-beds. *Environ. Sci. Technol.* **1993**, *27* (13), 2807-2813.
(40) Amirbahman, A.; Olson, T. M. The role of surface conformations in the deposition kinetics of humic matter-coated colloids in porous-media. *Colloids Surfaces A* **1995**, *95* (2-3), 249-259.
(41) Franchi, A.; O'Melia, C. R. Effects of natural organic matter and solution chemistry on the deposition and reentrainment of colloids in porous media. *Environ. Sci. Technol.* **2003**, *37* (6), 1122-1129.
(42) Ho, C. C.; Kondo, T.; Muramatsu, N.; Ohshima, H. Surface structure of natural rubber latex particles from electrophoretic mobility data. *J. Colloid Interface Sci.* **1996**, *178* (2), 442-445.
(43) Pensini, E.; Sleep, B. E.; Yip, C. M.; O'Carroll, D. Forces of interactions between bare and polymer-coated iron and silica: Effect of pH, ionic strength, and humic acids. *Environ. Sci. Technol.* **2012**, *46* (24), 13401-13408.
(44) Dieckmann, Y.; Colfen, H.; Hofmann, H.; Petri-Fink, A. Particle size distribution measurements of manganese-doped ZnS nanoparticles. *Anal. Chem.* **2009**, *81* (10), 3889-3895.

(45) Domingos, R. F.; Baalousha, M. A.; Ju-Nam, Y.; Reid, M. M.; Tufenkji, N.; Lead, J. R.; Leppard, G. G.; Wilkinson, K. J. Characterizing manufactured nanoparticles in the environment: Multimethod determination of particle sizes. *Environ. Sci. Technol.* **2009**, *43* (19), 7277-7284.
(46) Mahl, D.; Diendorf, J.; Meyer-Zaika, W.; Epple, M. Possibilities and limitations of different analytical methods for the size determination of a bimodal dispersion of metallic nanoparticles. *Colloids Surfaces A* **2011**, *377* (1-3), 386-392.
(47) Min, G. K.; Bevan, M. A.; Prieve, D. C.; Patterson, G. D. Light scattering characterization of polystyrene latex with and without adsorbed polymer. *Colloids Surfaces A* **2002**, *202* (1), 9-21.
(48) Hill, R. J.; Saville, D. A.; Russel, W. B. Polarizability and complex conductivity of dilute suspensions of spherical colloidal particles with charged (polyelectrolyte) coatings. *J. Colloid Interf. Sci.* **2003**, *263* (2), 478-497.
(49) Hill, R. J.; Saville, D. A.; Russel, W. B. Polarizability and complex conductivity of dilute suspensions of spherical colloidal particles with uncharged (neutral) polymer coatings. *J. Colloid Interf. Sci.* **2003**, *268* (1), 230-245.

Part II:

Effects of heterogeneous natural organic matter on nanoparticle aggregation

Chapter 5. Effects of size-fractionated components from polydisperse natural organic matter on gold nanoparticle aggregation

5.1 Introduction

Engineered nanoparticles released into soils and surface waters will encounter natural organic matter (NOM). NOM comprises a highly heterogeneous mixture of components with various molecular weights and chemical properties.[1-3] The origin of the NOM sample and the methods used to collect or fractionate the sample will determine its composition and hence its effects on colloid or NP behavior. Types of NOM are typically defined operationally – for example, the International Humic Substances Society (IHSS) collects "NOM" by reverse osmosis, whereas "humic acid" (HA) and "fulvic acid" (FA) are extracted on an XAD resin and distinguished by solubility at acidic pH. Other descriptors (e.g., based on the origin of the NOM, lability, chemistry, and other properties) and a critical review of variability in collection and preparation methods have been published.[1] The physical structure of NOM is also complex. A supramolecular model has been proposed, in which smaller components form impermanent aggregates held together by hydrogen bonding, cation bridging, dipole-dipole, and hydrophobic interactions.[4] This theory has been supported by the results of neutron magnetic resonance (NMR), which suggest that all components of NOM can be attributed to low molecular weight molecules that can associate (e.g., polysaccharides, polypeptides, aliphatic chains, and aromatic lignin fragments), rather than true macromolecules.[5,6] NOM structure (e.g. aggregation state[4,7-9] and fractal dimension[10,11]), and hence apparent size or molecular weight, can change with concentration, solution chemistry (pH, ionic strength, divalent cations), and removal or addition of metal ions that induce NOM aggregation.

Given the complexity inherent in NOM samples and variability among experimental protocols, it is desirable to understand how specific components in a NOM mixture interact with NPs. It is expected that different components will have different affinities to the NP surface and different effects on NP behavior. Therefore, NP interactions with a heterogeneous NOM sample may differ from those of a relatively homogeneous sample with similar bulk characteristics. The roles of specific chemical moieties or size fractions of NOM have been investigated in soil science (adsorption onto soil or mineral surfaces[12-14]) and other environmental and engineered processes, including colloid or NOM-mediated pollutant transport (binding of dissolved metals or organic pollutants[15,16]), drinking water treatment (e.g. disinfection by-product formation[17]), and membrane fouling.[18]

For NP fate and transport, the properties of adsorbed layer and the macromolecules comprising it (layer thickness and density, charge, solvency, molecular weight) will affect the interaction energy that determines aggregation and deposition, as described in extended DLVO theory.[19-21] However, environmental nanotechnology studies often avoid explicit consideration of the heterogeneity of the NOM used. Bulk NOM typically reduces NP aggregation or deposition onto mineral surfaces.[2,22,23] Using various types of NOM, the stability of ZnS NPs was shown to correlate with aromatic content and *average* molecular weight.[24] Enhanced NP aggregation by NOM is also possible via charge neutralization,[23,25,26] bridging (especially in the presence of divalent cations),[27-29] or hydrophobic interactions.[30] Changes in the aggregation state and fractal characteristics of NOM-NP aggregates upon removal/re-addition of NOM have also been shown.[31,32] However, quantitative inter-study comparison is confounded by the variability across NOM samples and lack of detailed characterization of the heterogeneous NOM,[1] for

which average or bulk characteristics may be inadequate representations of the specific components adsorbing to NPs and controlling their behavior.

Various approaches have been taken to investigate particle interactions with specific NOM components. Distinguishing broad classes of NOM, Buffle *et al*. proposed a "three-colloidal component approach" in which inorganic colloids are stabilized by small fulvic material but bridged by fibrillar polysaccharide material,[33] as observed in aggregation and imaging studies.[34-37] Many NP studies compare effects of large HA and small FA on NP aggregation or deposition, but without considering the heterogeneity of the HA or FA samples themselves.[30,38,39] More detailed characterization of molecular weight distributions has been provided in studies of NOM adsorption onto particles: larger NOM often adsorbs preferentially,[40-43] with some exceptions.[44,45] Few studies take the approach of preparative NOM fractionation followed by comparison of the effects of those fractions on colloidal behavior. In one study of note, Amirbahman and Olson showed that HA filtered through increasingly larger molecular weight cutoff (MWCO) membranes afforded better stability of hematite NPs against deposition.[46]

This study will add to the knowledge obtained in previous studies through the assessment of the effects of very high molecular weight NOM components (> 100 kg/mol) on the aggregation behavior of citrate-reduced gold NPs. The 100 kg/mol cut-off used here is higher than that chosen in other studies; furthermore, the high molecular weight fraction is collected and assessed separately from the lower molecular fraction, allowing for more thorough characterization of these components and their effects on NP aggregation (as opposed to the study by Amirbahman and Olson, where only fitrate portions of the NOM were collected).

5.2 Objectives

The objective of this study is to assess the importance of the heterogeneity of NOM on NP aggregation behavior. We begin with a detailed assessment of one NOM sample, Suwannee River NOM (SRNOM). Aggregation of citrate-reduced gold NPs is compared in the presence of distinct molecular weight fractions of SRNOM, either separately or in combination. Preparative fractionation of the NOM into two fractions (> 100 kg/mol, ~2 wt % of the unfractionated sample; and < 100 kg/mol, 98 wt %) was achieved. Molecular weight distributions were characterized by size exclusion chromatography with multi-angle light scattering (SEC-MALS), and chemical differences between the NOM fractions were assessed by UV-Vis absorbance and fluorescence excitation-emission matrices (EEMs). Time-resolved dynamic light scattering (DLS) was used to observe effects of different concentrations of the individual and combined fractions on NP aggregation. The results of this study help to provide a mechanistic understanding of the effects of heterogeneous NOM samples in NP studies. Five additional NOM samples are assessed and compared in Chapter 6.

5.3 Materials and methods

5.3.1 Citrate-stabilized gold nanoparticles

Citrate-stabilized gold NPs were synthesized by sodium citrate reduction of hydrogen tetrachloroaurate in water at reflux, with starting concentrations of 1 mM $HAuCl_4 \cdot 3H_2O$ and 4 mM sodium citrate dihydrate.[47,48] The NPs were provided in suspension and used as is, without removing excess citrate or unreacted starting material. The remaining free (i.e. non-adsorbed) citrate concentration was determined to be 2.8 mM by centrifuging the stock gold NP suspension at 16,100*g* at room temperature for 60 minutes (Eppendorf Centrifuge 5415D, Hauppauge, NY)

and analyzing the supernatant by total organic carbon analysis (OI Analytical, College Station, TX) against KHP calibration standards. The particle diameter determined by transmission electron microscopy (TEM) was 13 ± 1.3 nm (Appendix A.5). Citrate-stabilized gold was chosen as a model NP to probe NOM effects due to its narrow size distribution.

5.3.2 Natural organic matter isolates

Suwannee River Natural Organic Matter (1R101N) was obtained from the International Humic Substances Society (IHSS, St. Paul, MN). Stock solutions were prepared at 2 g/L in DI water and dissolved overnight on an end-over-end rotator at room temperature, then filtered by syringe through a Durapore 0.22 μm hydrophilic polyvinylidene fluoride (PVDF) membrane (EMD Millipore, Billerica, MA) to prevent clogging of the SEC column. The unmodified stock NOM and the 0.22 μm filtrate are referred to as NOM_0 and NOM_1, respectively. All NP and NOM solutions were stored in a refrigerator at ~4 °C.

5.3.3 Characterization and fractionation of NOM

5.3.3.1 NOM fractionation

A 100 kg/mol nominal molecular weight cutoff (MWCO) Amicon Ultra-15 centrifugal filter (EMD Millipore) was used for preparative fractionation. All filters were rinsed with deionized (DI) water to remove residual glycerol. NOM_1 was loaded into the filter and centrifuged at 6,000 rpm (~3,900 g) at room temperature for 40-50 minutes. The filtrate was collected with no further modifications. The retentate was washed six times by adding DI water to the filter and centrifuging again. To further remove low molecular weight material, the retentate was transferred to a fresh filter and washed an additional six times (until yellow color

was absent in the filtrate). Rinsing of filter foulants or partial disaggregation of NOM may have contributed to the high number of rinses required to obtain a clear filtrate. The highly concentrated retentate was collected and diluted in DI water, yielding a final concentration factor of 6.9 times the original unfiltered material. The 100 kg/mol filtrate and retentate are referred to as NOM_f and NOM_r, respectively.

5.3.3.2 Concentration determination

Concentrations of NOM_0, NOM_1, NOM_f, and NOM_r were measured on an OI Analytical 1010 Total Organic Carbon (TOC) Analyzer (OI Analytical, College Station, TX). 1 mL of sample was reacted with 200 μL of 100 g/L phosphoric acid for 2 minutes to remove inorganic carbon, then with 1.0 mL of 100 g/L sodium persulfate for 2.5 minutes to oxidize organic carbon. The NOM_0 was 35 wt% carbon, as determined against potassium hydrogen phthalate standards. This is lower than the ~45% carbon calculated from reported IHSS data for this material, which could be explained by incomplete oxidation of the NOM during the TOC analysis here. However, increasing the sodium persulfate volume and reaction time to 2.4 mL and 11 minutes, respectively, did not significantly affect the results. The same carbon content was assumed for NOM_1, NOM_f, and NOM_r to determine total concentrations from TOC measurements (here, NOM_r may be distinct, although carbon content is typically similar across unfractionated NOM samples[3]). All concentrations are reported as total NOM concentration, not carbon concentration, except where specified otherwise.

5.3.3.3 Molecular weight determination

Molecular weight distributions for NOM_1, NOM_f, and NOM_r were determined by SEC-MALS. A Superdex 75 10/300 GL analytical SEC column (GE Healthcare, Piscataway, NJ) was connected to an Agilent 1100 series system (binary pump, degasser, and autosampler) (Agilent Inc., Santa Clara, CA). 75 μL of sample (in DI water) was injected into the SEC column. The eluent flowrate was 0.7 mL/min, and the eluent used was 4 mM phosphate buffer with 25 mM NaCl (pH 7). Samples were also analyzed in 2 mM phosphate buffer (pH 7) to reduce adsorptive interactions with the column packing medium and allow a more complete portion of NOM to elute prior to the sample solvent for analysis, as well as in 100 mM NaCl with 1 mM $NaHCO_3$ to represent the conditions used in the aggregation experiments. These data are provided in Appendix B.2.1 and B.2.2.

UV (Agilent Inc.), MALS (Wyatt Technology, Santa Barbara, CA), and RI (Wyatt Technology) detectors are situated in-line after the SEC column. The RI detector measures differential RI (dRI), or the difference between the RI of the sample and a reference cell filled with DI water. The molecular weight of eluting components was determined by MALS. The full procedure and calculation of weight-averaged molecular weights are described in Appendix B.1.3. MALS does not require molecular weight calibration against polymer standards, so molecular weights are determined independently of elution time and will not be affected by the conformation of the molecule and any enthalpic interactions with the column packing medium. It is noted that molecular weights determined by MALS tend to be higher than those determined by other methods or against poly(styrene sulfonate) standards.[49] The difference can be attributed in part to the fact that MALS provides weight-averaged molecular weights, in contrast to number- or viscosity-averaged molecular weights reported elsewhere; furthermore, other studies

using SEC typically calibrate against polyelectrolyte standards,[50] which may result in inaccuracies.

Concentrations required for MALS calculations were calculated from the RI measurement because it provides more universal detection than UV absorption, which is selective for components that absorb (at 280 nm here).[51] The RI increment, dn/dc, was determined to be 0.15 mL/mg by calibration with NOM_0 solutions of known concentrations (0.1 to 1.0 g/L) into the RI detector. The same dn/dc was assumed for NOM_1, NOM_f, and NOM_r.

SEC-MALS data were further analyzed to account for the portion of NOM that could not be analyzed directly by MALS, either due to the low signal to noise ratio for the lowest molecular weight components (on the order of 1 kg/mol or smaller), or elution during and after the negative RI peak for the solvent injected with the NOM. This analysis is fully presented in Appendix B.1.4. Briefly, the late-eluting components are assumed to have lower molecular weights than those that could be analyzed by MALS. The cumulative weight fractions were then adjusted by the percent of mass that was measured by MALS (by dividing the integrated mass from the RI peak by the known mass injected). Then, a lognormal distribution was fitted to the adjusted cumulative weight distribution. The fitted parameters were the mean, μ, and standard deviation, σ, of the lognormal distribution (using base 10). The geometric mean of the weight-averaged molecular weight distribution, M_g, was then computed as the exponential (base 10) of μ.

5.3.3.4 Spectroscopic analyses

NOM_1, NOM_f, and NOM_r were analyzed by fluorescence EEM, and UV absorbance spectroscopy to assess major differences in chemical content. ^1H nuclear magnetic resonance (NMR) spectra were also taken for NOM_1 and NOM_f (Appendix B.2.3).

Fluorescence EEMs were collected on a FluoroMax 4 spectrophotometer (Horiba, Edison, NJ), following the procedure by Westerhoff *et al.*[52] NOM concentrations were 1 ppm as C, prepared in 10 mM KCl and adjusted to pH 3 with HCl. Excitation and emission slit widths were 10 nm. Emission was measured from 290 to 600 nm in 1 nm increments, at excitation wavelengths of 200 to 400 nm in 5 nm increments. A 1 cm pathlength quartz cuvette was used. Correction for the inner filter effect was applied (Appendix B.1.1).

UV absorbance spectra were collected using a Cary 300 Bio UV-Vis spectrophotometer (Agilent Inc.) and a 1 cm quartz cuvette. Samples were prepared at 5 ppm in DI water. The measured pH was ~8.0 for NOM_1 and NOM_f and 7.7 for NOM_r. Specific UV absorbance at low wavelengths, e.g. 254,[53] 272,[54] or 280 nm,[50] is often correlated to aromaticity. Chemical differences can be assessed by calculating ratios of absorbances at different wavelengths[55,56] or modeling the shape of the curve. The latter approach was taken, using the model by Bricaud *et al.*, with the shape of the absorbance curve approximated as a single exponential function:[57]

$$A_\lambda = A_{\lambda_0} \exp\left[-S(\lambda - \lambda_0)\right] \tag{5.1}$$

where A_λ is the absorbance at wavelength λ, λ_0 is an arbitrary reference wavelength (here, 450 nm),[58] and S is the slope coefficient (a fitted parameter used for qualitative comparison).

5.3.4 Nanoparticle aggregation

Aggregation of the citrate-stabilized Au NPs was measured at NaCl concentrations ranging from 0 to 100 mM without NOM, and at 100 mM NaCl in the presence of various concentrations of NOM_1, NOM_f, and NOM_r. DLS measurements were collected on an ALV

CGS-3 goniometer with ALV/LSE-5004 Light Scattering Electronics and ALV-7004 multiple tau digital correlator (ALV-GmbH, Langen, Germany). All samples were prepared in 1 mM $NaHCO_3$, adjusted to pH 8.3 with NaOH/HCl. Following a method similar to that by Nason *et al.*,[30] triplicate DLS measurements of the initial particle size were taken on 1 mL of 40 ppm Au NP. Then, NOM was added and triplicate measurements were taken again. Finally, NaCl solution was added. The final volume and Au NP concentration were 2 mL and 20 ppm, respectively. The order of addition (i.e., adding NOM prior to NaCl solution) was chosen to prevent rapid initial aggregation of uncoated NPs at high ionic strength and to allow observation of any size changes due to NOM adsorption prior to NaCl addition. Analysis of the DLS autocorrelation function was performed with a constrained regularization algorithm (ALV-7004 Edition Correlator Software). Distributions of diffusion coefficients were converted to hydrodynamic radius distributions via the Stokes-Einstein equation. Aggregation was monitored over 20 minutes. A two-minute measurement duration was used for non-aggregating samples to improve data quality for low-scattering, small Au NPs. For rapidly aggregating samples (where scattering count rates are higher for large aggregates), measurements were taken every 15 seconds for the first four minutes, and every two minutes for the next 16 minutes. An approximate 15- to 20-second delay between the addition of NaCl solution and the start of the light scattering measurement was also taken into account. Additional DLS and SEC-MALS measurements made on NOM (without Au NPs) in the solution conditions used for the aggregation experiments (100 mM NaCl with 1 mM $NaHCO_3$, pH 8.3, Appendix B.2.2) showed no aggregation of NOM (DLS), and SEC-MALS showed only minor differences in molecular weight compared to the phosphate/NaCl SEC eluent.

5.3.5 Characterization of nanoparticle-NOM interaction

5.3.5.1 TEM characterization of NOM-coated NPs

Transmission electron microscope (TEM) images of the Au NPs in the presence of NOM were taken using a JEOL 2000-EX TEM. Samples were prepared using 20 ppm Au NP with 10 ppm NOM_f or NOM_r, adjusted to pH 8.3 with NaOH. 5 μL drops were pipetted onto a 300-mesh Cu grid with carbon support film (Electron Microscopy Services, Hatfield, PA).

5.3.5.2 Electrophoretic mobility of NOM-coated NPs

The electrophoretic mobility (EPM) of the NOM-coated NPs was measured using a Malvern Zetasizer Nano ZSP instrument (Malvern Instruments, Westborough, MA) at a setting of 40 V and 15 sub-runs; the mean electrophoretic mobility was calculated over five repeat measurements. The concentrations used were 20 ppm Au NPs and 10 ppm NOM, as in the aggregation experiments. The dispersion medium was 20 mM NaCl with 1 mM $NaHCO_3$ (pH 8.3). Two suspension treatments were tested: either no further treatment (i.e., with excess NOM present; results shown in Appendix B.3.3), or washed three times by centrifuging for 30 minutes at 16,100 *g* (13,172 rpm) at room temperature (Eppendorf Centrifuge 5415D, Hauppauge, NY) and resuspending into NOM-free dispersion medium. The 20 mM concentration of NaCl was chosen (in contrast to 100 mM NaCl in the aggregation experiments) to reduce NP aggregation and corrosion of the electrodes in the disposable capillary cells used for measurement (DTS1070, Malvern Instruments). Although all EPMs in 100 mM NaCl are expected to be lower in magnitude due to charge screening, the trends (or lack of trends) among samples are assumed to be similar to those in 20 mM NaCl.

For Au NPs coated in NOM_1, suspensions were also prepared in 100 mM NaCl, 1 mM $NaHCO_3$ (pH 8.3) and washed three times with resuspension into 20 mM NaCl medium after each centrifugation step. Although a higher adsorbed mass is expected at higher ionic strength (due to screening of electrostatic repulsions between NOM and citrate or other NOM adsorbed onto the Au NP surface), measured electrophoretic mobilities were similar to those for the Au NPs prepared in 20 mM NaCl (Section 6.3.5).

5.4. Results

5.4.1 Molecular weight determination of the whole NOM

Suwannee River NOM was characterized by SEC-MALS, then separated to obtain the fractions used to test the effect of NOM molecular weight distribution on NP stability against aggregation. First, the NOM_1 sample was obtained by filtering the original NOM solutions through a 0.22 μm syringe filter. Mass recovery of NOM in the filtrate was 94-96% by TOC or 93% by batch RI measurements. SEC-MALS analysis for NOM_1 is shown in Figure 5.1, using an eluent of 4 mM phosphate buffer with 25 mM NaCl (pH 7). The UV and dRI signals indicate the concentration of eluting NOM; molecular weights are simultaneously determined by MALS. As expected, molecular weight decreases with elution time as smaller NOM components access more of the pore space in the SEC medium (taking a longer travel distance through the column). The shape of the SEC-MALS chromatogram is similar to those previously published for Suwannee River NOM.[42,50,59] and other humic substances.[60]

For the NOM_1 sample, the weight-average molecular weight, M_w, was 23.3 kg/mol for the MALS measurements from elution time of 10.6 to 21.5 minutes. 1.4 wt% of NOM_1 eluted in a small void peak (10.6 to 13 minutes), comprising a mixture of all NOM larger than the SEC

exclusion size. The molecular weight of NOM in this void fraction was > 100 kg/mol; this NOM is presumably comprised of large humic aggregates. Evidence for aggregation of humic substances has been observed previously.[4,7-9] The majority of NOM_1 (98.6 wt-%) elutes after 13 minutes and has molecular weight ranging from approximately 5 to 100 kg/mol. The lognormal fitting method gives a geometric mean, M_g, of the weight-average molecular weight distribution of 7.9 kg/mol for NOM_1, accounting for the mass that elutes after 21.5 minutes and assuming that molecular weight decreases after 21.5 minutes (as expected from SEC theory).

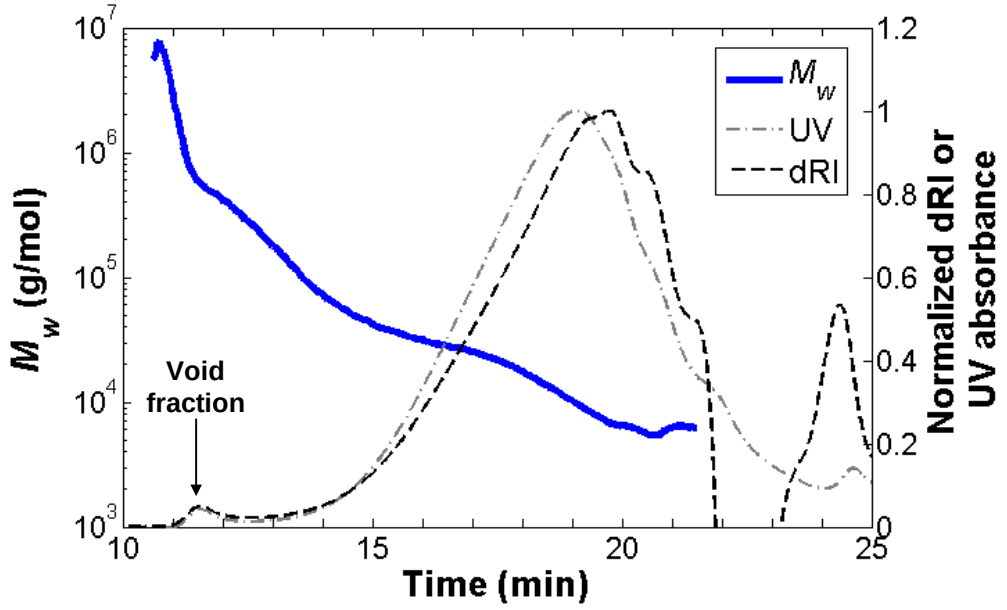

Figure 5.1. Molecular weight and UV and RI chromatograms for NOM_1 using 4 mM phosphate buffer with 25 mM NaCl (pH 7) as the SEC eluent. UV and RI signals are normalized against the peak signal intensity. A void peak is observed (elution time of 10.6 to 13 minutes), consisting of very large NOM aggregates. Most of the sample elutes after 13 minutes and has molecular weight lower than 100 kg/mol. The negative RI peak at t = 22 min is a result of the lower RI signal of eluting DI water (injected as the NOM solvent) compared to the phosphate buffer + NaCl. The UV tail during and after the negative solvent peak indicates some adsorption of NOM to the SEC column media; however, the molecular weight determined from MALS is independent of the elution time. A second analysis using 2 mM phosphate buffer to eliminate adsorption gave similar weight-averaged molecular weights, within 10% (Appendix B.2.1).

Radius of gyration (R_g) was determined using MALS (Zimm model). R_g of NOM in the void fraction and main peak was 17–60 nm and 14–17 nm, respectively. The large sizes obtained have been shown in some studies[61] but not others,[62] depending on the sample and sizing method. It is noted that data quality for the main peak was poorer due to lower scattering counts; in addition, the radius determination by MALS has a lower limit of 10 nm because small molecules scatter 660 nm light approximately isotropically. The expected R_g for individual fulvic and humic molecules (or their constituent components[5,6]) is < 10 nm.[2]

5.4.2 Preparative fractionation of the NOM samples

Preparative fractionation of NOM_1 was performed using a 100 kg/mol MWCO centrifugal ultrafiltration device to separate the main peak and void peak components in Figure 5.1. The filtrate concentration was 1.7 g/L, yielding 91% recovery from the NOM_1 input (~1.9 g/L). The final concentration of the retentate was 150 mg/L (1.1% recovery, adjusting for the concentration factor of 6.9 described in Methods). Therefore, ~8% of NOM_1 is estimated to be lost onto the membrane or during the washing process. Membrane fouling is affected by many factors (e.g. size, hydrophobicity, charge);[63] the specific components lost were not determined but may include hydrophobic NOM that adsorbs or NOM near the MWCO that are entrapped in the membrane.

SEC chromatograms for the retentate (NOM_r) and filtrate (NOM_f) are shown in Figure 5.2. Results using 4 mM phosphate/25 mM NaCl eluent are provided here; results for 2 mM phosphate are provided in Appendix B.2.1. No void peak (t = 10.6 to 13 min) is observed in NOM_f (Figure 5.2a), indicating removal of the larger material. The elution profile appears similar to that of the main peak in NOM_1 (Figure 5.1), suggesting no significant perturbation of

filtrate components during the separation process. The filtrate M_w was 12.8 kg/mol for the portion analyzed by MALS (blue line in Figure 5.2(a)), or M_g = 5.8 kg/mol from the lognormal fitting method.

The SEC chromatogram for NOM_r (Figure 5.2(b)) shows that the void peak is recovered, along with other > 100 kg/mol material eluting after 13 minutes (which may be adsorbing to the SEC column, resulting in peak tailing). The retentate M_w was 691 kg/mol for the portion analyzed by MALS (blue line in Figure 5.2(b)), or M_g = 151 kg/mol from the lognormal fitting method. The recovery of this material in the filter after washing with DI water suggests that the collected components were stable against disaggregation in the conditions used for SEC-MALS (however, possible disaggregation in the presence of the citrate-stabilized gold nanoparticles was not assessed). All samples were also re-analyzed by SEC-MALS over time (after further use); no significant changes in the molecular weight distributions were observed.

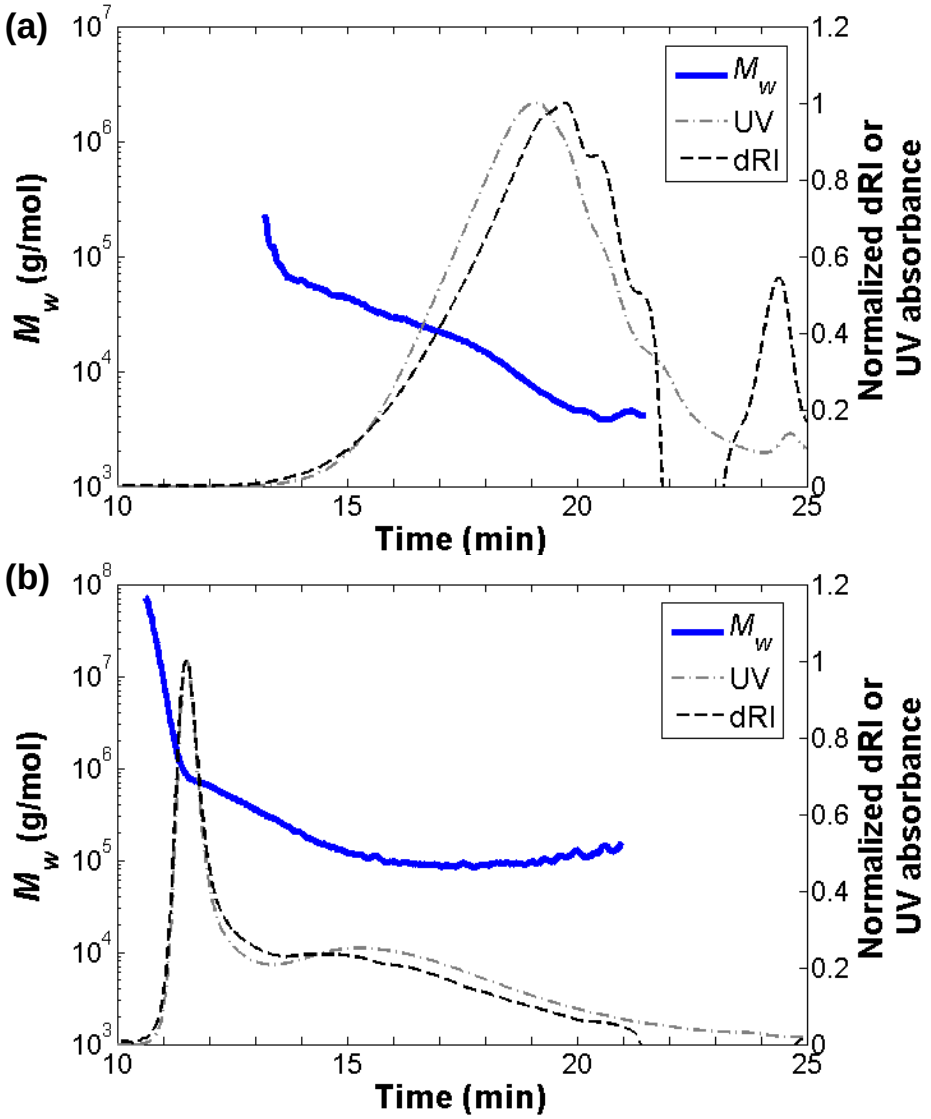

Figure 5.2. Molecular weights and UV and RI chromatograms for NOM_f (a) and NOM_r (b), in 4 mM phosphate buffer with 25 mM NaCl at pH 7. NOM with molecular weight < 100 kg/mol was removed from the retentate, and negligible concentrations of NOM in the void fraction were observed in the filtrate.

5.4.3 Chemical characterization of the NOM fractions

Spectroscopic methods were used to compare chemical characteristics of the NOM samples. ^{1}H NMR spectra for NOM_1 and NOM_f are provided in Appendix B.2.3; insufficient quantities of NOM_r were obtained for this analysis. The NOM_1 and NOM_f spectra had similar

qualitative appearances and peak areas relative to the total integrated area, indicating no significant difference.

Fluorescence EEMs (Figure 5.3) are also similar for NOM_1 and NOM_f. Both spectra show a peak near excitation/emission wavelengths of 335/446 nm, representative of aquatic humic substances (e.g. lignin degradation products).[64] A similar peak (near 340/448 nm) is also observed for NOM_r; however, a secondary peak at 275/322 nm appears, which is representative of protein-like components (e.g., amino acids with aromatic functional groups, such as tryptophan, phenyl alanine, or tyrosine).[64] These results are similar to those reported by Baker *et al.*, in which a protein-like peak was observed for large (>0.2 μm) material and removed in smaller fractions.[65] These components may be of algal or bacterial origin and attributable to free amino acids or those in proteins or cell membranes;[64] biomolecular fragments can also bind strongly to humic compounds and be protected from degradation.[66] Amino acids fluoresce more strongly by weight than humic acids,[67] so the peak observed represents only a low concentration.

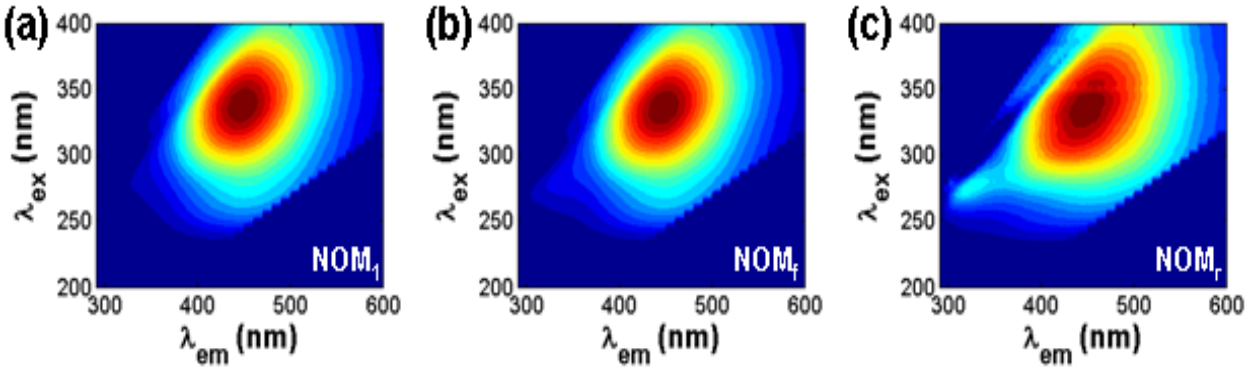

Figure 5.3. Fluorescence EEMs for NOM_1 (a), NOM_f (b), and NOM_r (c), corrected for the inner filter effect. Data in areas in top left and bottom right corners where Rayleigh scattering occurs were set to zeros.[68] All intensities are normalized to the peak intensity, with dark red representing a value of one, dark blue representing zero, and each contour plotted at an increment of 0.05. Peak intensities in counts per second are reported in Figure 6.3.

The UV-Vis absorbance spectra and linearized data fit to Equation 5.1 are shown in Figures 5.4(a) and 5.4(b), respectively. Wavelengths higher than 650 nm were not included for fitting because of the low absorbance. Again, the NOM_1 and NOM_f spectra are similar, whereas the NOM_r spectrum differs. Specific UV absorbance (normalized by concentration) at 280 nm, $SUVA_{280}$, is higher for NOM_r (Figure 5.4(a)). Based on correlations between aromaticity and absorptivity determined for various NOM samples,[50,53,54] the NOM_r is expected to have percent aromaticity only 2 to 5% higher than NOM_f. The slope coefficients for NOM_1 and NOM_f from the exponential model are similar (0.014 and 0.015 nm^{-1}, respectively), whereas NOM_r has a shallower slope (0.011 nm^{-1}), suggesting a different composition (ratio of components that absorb UV versus visible light). For example, Korshin et al.[56] proposed that the UV spectrum could be modeled as a superposition of three absorption bands representing the excitation of benzene groups to three different excited states: the local-excitation band centered at 180 nm, the benzenoid band centered at 203 nm, and the electron-transfer band centered at 253 nm. The intensity of the electron-transfer band is sensitive to the functionalization of the benzene ring by polar groups such as hydroxyl, carbonyl, carboxyl, and ester groups. Thus, a ratio of absorbances or the slope coefficient may be representative of the substitutions on the aromatic groups.

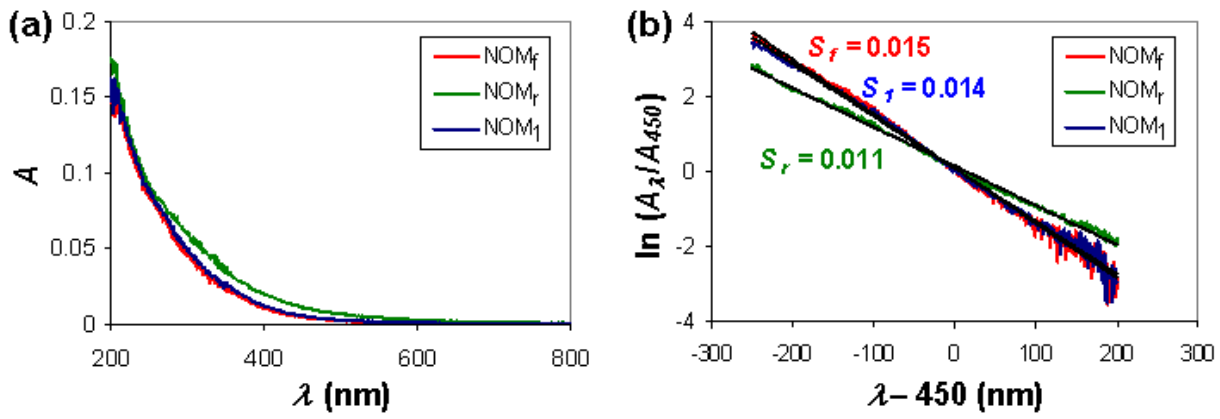

Figure 5.4. UV absorbance spectra (a) and exponential fits (b) for NOM_f, NOM_r, and NOM_1 at 5 ppm in DI water, pH 7.7 to 8.0. NOM_r has a higher $SUVA_{280}$ and lower slope coefficient *S*, suggesting broad differences in composition.

Both the higher SUVA and lower *S* for the retentate fraction of this particular NOM sample are consistent with trends between the properties of the UV-vis absorbance spectrum and molecular weight for other NOM types.[50,58,69,70] The relationship between *S* and molecular weight has been proposed to result from either the presence of a more extended aromatic system that can absorb light of longer wavelengths, or intramolecular charge transfer between chromophores.[69]

5.4.4 Nanoparticle aggregation

Results for time-resolved DLS measurements of Au NP aggregation are presented, followed by a proposed mechanism. Initial aggregation rates are provided in Appendix B.3.7; trends in these rates are consistent with qualitative analysis of the aggregation curves. Aggregation of citrate-stabilized Au NPs without NOM in 0 to 100 mM NaCl (with 1 mM $NaHCO_3$, pH 8.3) is shown in Appendix B.2.4. The NPs were stable against aggregation in ionic

strengths up to 20 mM NaCl, whereas aggregation occurred in 50 and 100 mM NaCl due to charge screening.

The effects of NOM on NP aggregation were tested in 100 mM NaCl to best demonstrate differences in aggregation behavior (similar stabilization against aggregation was achieved using 10 ppm of NOM_f and NOM_r in 50 mM NaCl, shown in Appendix B.2.5). At higher ionic strength, electrostatic stabilization is reduced due to charge screening, and steric or other effects become relatively more important. First, NOM_1, NOM_f, and NOM_r were compared on the same mass basis, 10 ppm of each NOM fraction (Figure 5.5). Results for citrate-stabilized Au without NOM in 0 and 100 mM NaCl are included for comparison against the non- and rapidly-aggregating particles, respectively.

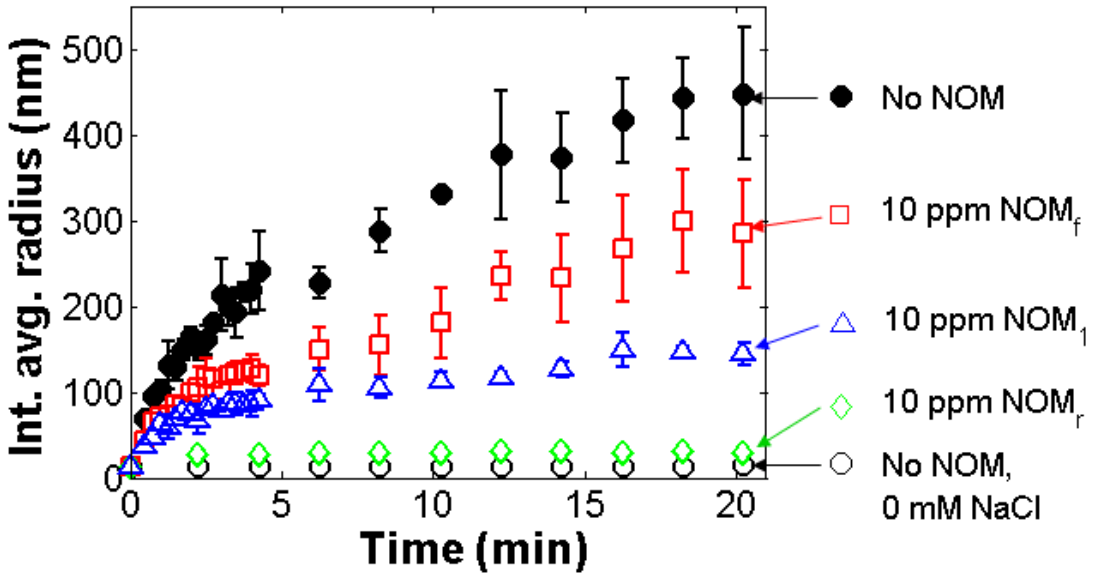

Figure 5.5. Time-resolved intensity averaged radii for citrate-stabilized Au NPs in 100 mM NaCl, 1 mM $NaHCO_3$, pH 8.3, in the presence of 10 ppm of NOM_1, NOM_f, or NOM_r. Rapid aggregation is observed for NOM_f, whereas NOM_r stabilizes the NPs. The NOM_1, which has a constitution of ~98 wt% of < 100 kg/mol NOM and ~2 wt% of > 100 kg/mol NOM by SEC-MALS, behaves intermediately between the two separated fractions. Error bars are standard deviations computed for intensity average diameters from duplicate or triplicate runs.

10 ppm of NOM_f decreases the aggregation rate compared to that without NOM, but aggregation is still rapid and continues throughout the 20-minute measurement duration to reach hydrodynamic radius of over 250 nm. In contrast, 10 ppm of NOM_r provides significant NP stabilization. An initial increase in hydrodynamic radius from 13 nm to 30 nm is observed, but further aggregation is not observed after the first measurement point. This initial size increase did not occur after the addition of NOM_r (prior to NaCl addition), but only after addition of NaCl. Similar results were obtained by Nason *et al.* for citrate-stabilized Au NPs in the presence of unfractionated Suwannee River Humic Acid.[30] This behavior was explained by screening of intramolecular electrostatic repulsion, allowing more NOM to pack onto the particle surface (initially increasing the hydrodynamic size due to the adsorbed layer, then imparting steric stabilization). Brief NP-NP aggregation may also occur between addition of the NaCl and the establishment of the surface layer of NOM. Alternatively, it is noted that NOM_r (R_g > 20 nm by MALS) is of comparable or larger size than the Au NPs (R_h ~13 nm); therefore, a physical model of NPs attaching onto large NOM_r aggregates, rather than NOM_r "coating" individual NPs, may be possible. TEM images for mixtures of 20 ppm Au NPs with 10 ppm NOM_r in DI water show some large globules of low electron density material (presumably NOM) in association with several NPs (Figure 5.6(a)), although this morphology is not consistent across all regions of the grid (Figure 5.6(b)). These images suggest that for small Au NPs and high molecular weight NOM_r, a nanoparticle-decorated NOM morphology may exist, but do not confirm that this morphology is dominant. Bridging of hematite NPs by Suwannee River NOM was also shown by Wilkinson *et al.*,[71] although the bridging component was fibrillar, not globular. No coating was visible by TEM for NOM_f (Appendix B.2.7). NaCl was not added to prevent deposition of salt crystals; at higher ionic strength, greater association of NOM with the Au NPs may occur.

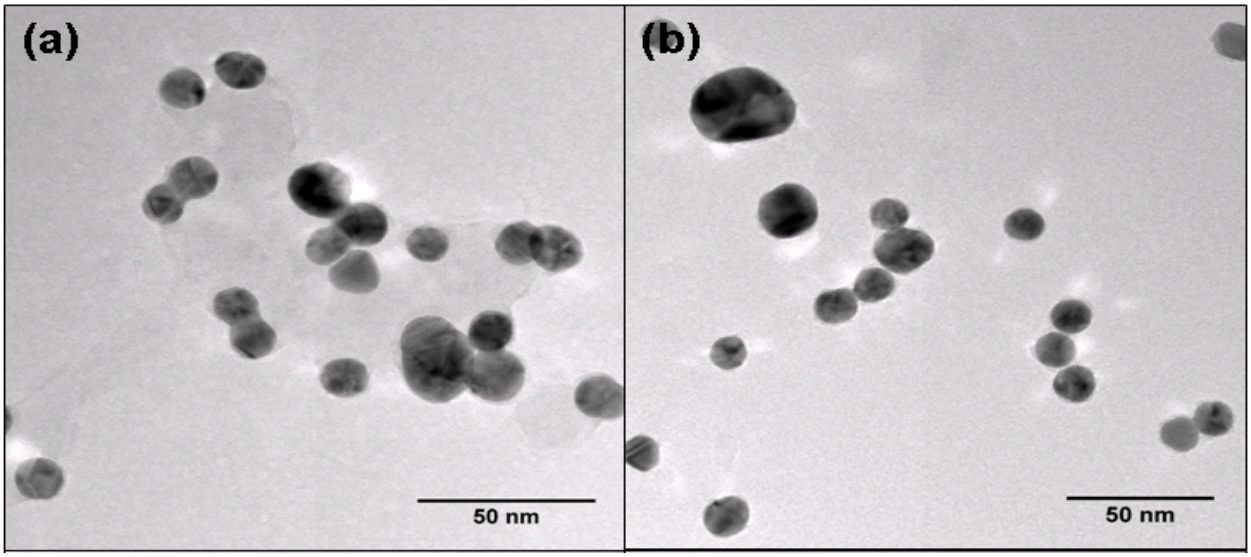

Figure 5.6. TEM images of citrate-stabilized Au NPs in the presence of NOM_r. Samples were prepared with 20 ppm Au NPs and 10 ppm NOM in DI water and drop deposited onto carbon coated copper grids. For NOM_r, particles were well-dispersed, and some particles associated with low electron density material (presumably large NOM aggregates) were observed (a); however, visible coatings were not observed on many other NPs (b).

10 ppm of NOM_1, which contains both NOM_f and NOM_r components, produces behavior intermediate between that of 10 ppm of either fraction alone. Notably, NOM_1 yields better stability against aggregation than the NOM_f fraction alone, even though it is primarily composed of NOM_f and contains only a small amount of NOM_r (< 2 wt%).

The NOM fractions were also compared on a basis of their relative masses in the original NOM_1 sample (1.8 wt% NOM_r and 98 wt% NOM_f), which is relevant for understanding studies using unfractionated NOM samples. Additional aggregation experiments were performed with reduced NOM_r concentrations (Figure 5.7(a)) or increased NOM_f and NOM_1 concentrations (Figure 5.7(b)). Some data from Figure 5.5 are re-plotted where relevant for comparison.

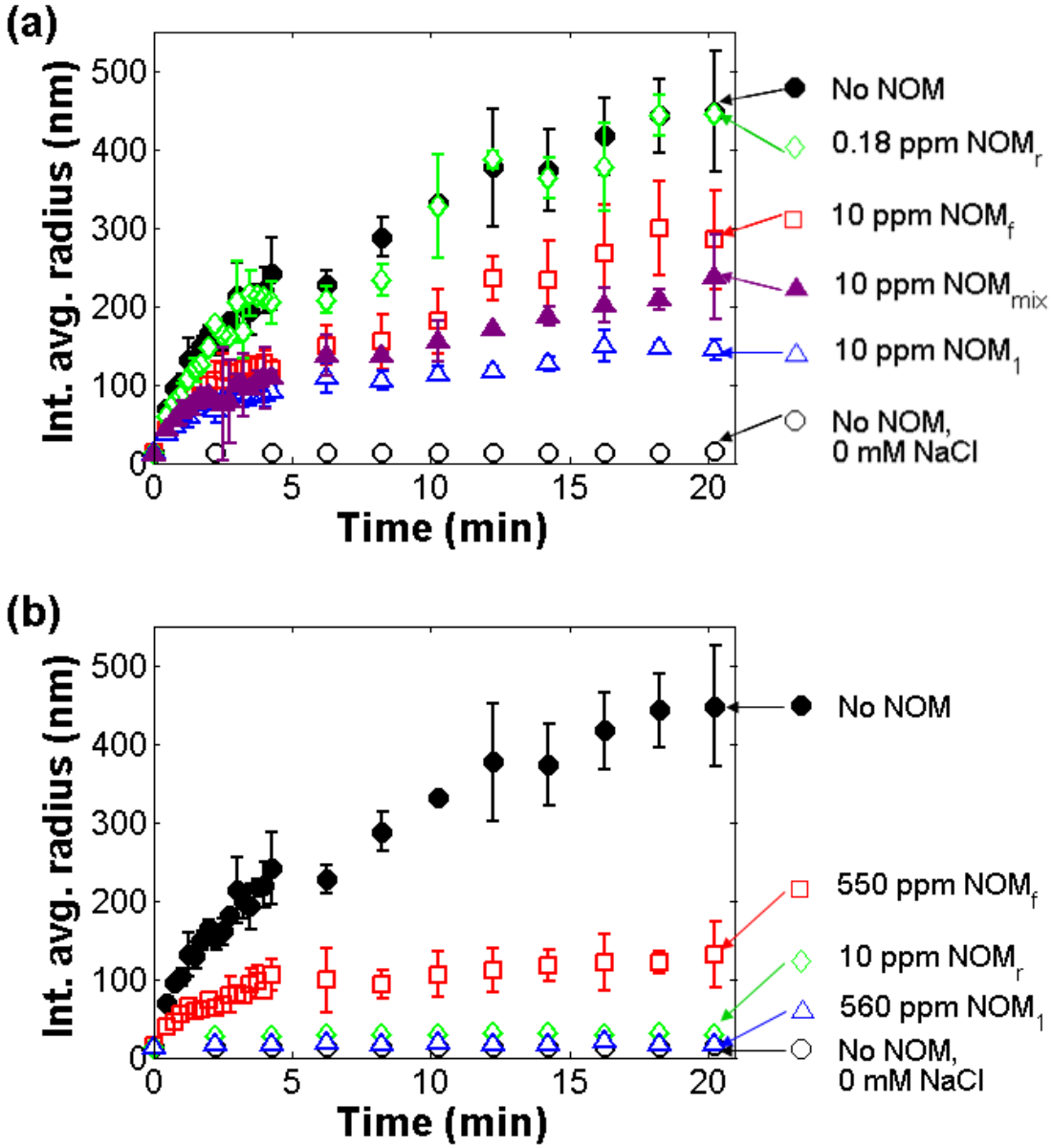

Figure 5.7. Time-resolved DLS for citrate-stabilized Au NPs in 100 mM NaCl, 1 mM $NaHCO_3$, pH 8.3, for a basis of comparison of 10 ppm NOM[1] (~0.18 ppm NOM_r, 9.8 ppm NOM_f by SEC-MALS) (a), or 560 ppm NOM_1 (~10 ppm NOM_r, 550 ppm NOM_f) (b). On a 10 ppm NOM_1 basis, separated NOM_r and NOM_f fractions do not prevent rapid aggregation, although the original or reconstituted mixture provides somewhat improved stability. Mixtures of the components (NOM_1 and NOM_{mix}) impart better stability than either component alone. On a 560 ppm NOM_1 basis, stability is improved for all NOM fractions; however, significant aggregation is still observed for NOM_f whereas NOM_r and NOM_1 provide good stability.

In Figure 5.7(a), the concentrations of NOM_r and NOM_f are chosen to be those present in ~10 ppm NOM_1. A 0.18 ppm concentration of NOM_r fails to enhance stability; aggregation is similar to that in the absence of NOM. Therefore, the improved stability of 10 ppm NOM_1 compared to either 10 ppm NOM_f or 0.18 ppm NOM_r cannot be explained by the presence of either component acting individually. To further investigate this behavior, 9.8 ppm of NOM_f and 0.18 ppm of NOM_r were recombined to form a mixture, NOM_{mix}, similar to NOM_1. Improved stability achieved with this mixture suggests that some interaction between the two components occurs to enhance NP stability, although the stability in 10 ppm NOM_1 is not fully recovered.

The effects of increasing the NOM_r concentration are shown in Appendix B.2.6. In 1.0 ppm of NOM_r, aggregation was reduced. In 1.8 ppm of NOM_r, NP stability significantly improved: as observed with 10 ppm NOM_r, the hydrodynamic radius rapidly increased within the first 15 to 30 seconds, then stabilized (at 60 to 70 nm for this concentration). The rapid size increase followed by stabilization (at decreasing size with increasing NOM_r concentration) may be attributable to formation of NP-NOM heteroaggregates (although large aggregates shown in Figure 5.6(a) were not observed by DLS), or to aggregation of NPs upon salt addition prior to equilibration of the adsorbed NOM layer.

In Figure 5.7(b), concentrations of NOM_f and NOM_1 are increased to 550 and 560 ppm, respectively, for comparison against 10 ppm of NOM_r (1.8% of 560 ppm). In 560 ppm of NOM_1, no significant change in DLS radius is observed over 20 minutes. Stability of the Au NPs improved in 550 ppm NOM_f compared to 10 ppm NOM_f, but rapid aggregation still occurs during the first several minutes. Of particular note, NP stability is much more sensitive to the NOM_r concentration than NOM_f concentration: significant aggregation is observed even with

550 ppm of NOM_f, whereas NP behavior varies from no stability to excellent stability against aggregation within the range of 0.18 to 1.8 ppm of NOM_r (Appendix B.2.6).

A possible mechanism is suggested to explain the behavior across all the aggregation experiments. First, 10 ppm NOM_f or NOM_r provide similar NP stability in 50 mM NaCl (Appendix B.2.5). On the other hand, for 10 ppm of either fraction in 100 mM NaCl (Figure 5.5), where charge is further screened, the higher molecular weight NOM_r enhances stability compared to the lower molecular weight NOM_f. These results may indicate a difference in electrostatic versus steric stabilization mechanisms for the two fractions, with NOM_r presumably imparting greater steric repulsion due to its higher molecular weight and larger radius of gyration.

Comparison of electrophoretic mobilities for the NOM-coated NPs (measured in 20 mM NaCl, 1 mM $NaHCO_3$, at pH 8.3) further suggests the importance of a steric effect rather than an electrostatic effect. Electrophoretic mobilities are compared in Figure 5.8. First, it is noted that the electrophoretic mobilities for all coated nanoparticles are less negative than for the uncoated nanoparticles (similar results have been observed for bovine serum albumin coatings on citrate-stabilized gold NPs[72]). These results suggest that negatively-charged citrate may have been displaced by NOM; alternatively, the increased drag produced by the adsorbed NOM can result in a lower magnitude of electrophoretic mobility, or positively-charged groups on NOM may have bound and neutralized the citrate charge. NPs coated in the filtrate and unfractionated NOM have similar electrophoretic mobilities, whereas NPs coated in the retentate fraction tend to have lower electrophoretic mobility. The lower electrophoretic mobility for the adsorbed layer of retentate NOM may be attributable to greater citrate displacement or binding of positively-charged NOM moieties, a lower charge density in the adsorbed layer, or a thicker or

less permeable adsorbed layer. These scenarios would be consistent with a stronger steric repulsion (rather than electrostatic repulsion) imparted by the retentate NOM.

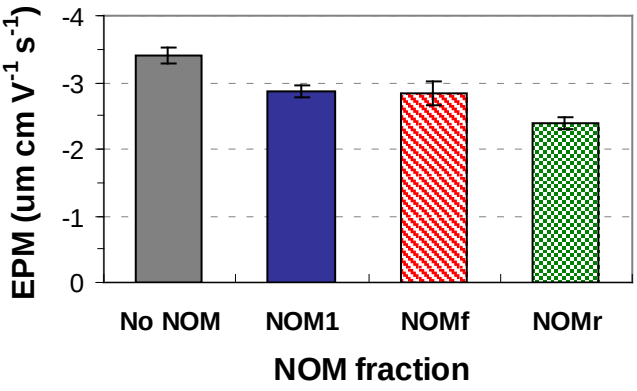

Figure 5.8. Electrophoretic mobilities for citrate-stabilized gold NPs coated with each fraction of SRNOM. NOM-coated NPs were prepared, washed, and measured in 20 mM NaCl, 1 mM $NaHCO_3$, at pH 8.3.

When considering the role of the two fractions in NOM_1 (1.8 wt % NOM_r and 98 wt % NOM_f), concentration-dependent behavior is observed. For 10 ppm NOM_1 (containing 0.18 ppm NOM_r and 9.8 ppm NOM_f), incomplete saturation of the NP surfaces was likely achieved, as supported by the observation that higher concentrations of NOM_f and NOM_r improve stability (compare Figures 5.7(a) and 5.7(b). For the NOM_r component specifically, estimation of the number ratio of NOM_r "molecules" or aggregates to Au NPs suggests that a concentration between 0.1 to 0.7 ppm is required to achieve a NOM_r/NP number ratio of ~1 (based on the lower MWCO of 100 kg/mol, or M_w of 691 kg/mol, respectively). Therefore, no or minimal attachment of NOM_r may occur at 0.18 ppm. When insufficient concentrations of either NOM_r or NOM_f are present to stabilize the NPs on their own, the combination of the two fractions (NOM_1 or NOM_{mix}) affords somewhat better stability. The loss of some unknown NOM

components due to fouling of the 100 kg/mol ultrafiltration membrane as described in Methods may partially explain this behavior (NOM_1 versus NOM_{mix}). Improved stability by recombining the fractions without the fouling components (NOM_{mix}) may be due to NOM_r overcoating adsorbed NOM_f or enhancing further adsorption (e.g. by modifying the NP surface hydrophobicity), or the formation of a more coherent (less patchy) layer of NOM_f and NOM_r. Small NOM_f components are kinetically favored to adsorb first due to faster diffusion, but can be replaced by larger NOM_r components whose adsorption is thermodynamically favored.[43] The adsorbed NOM_f may reduce bridging of NPs by slower-adsorbing NOM_r, as suggested by experiments comparing aggregation of magnetite NPs coated with poly(acrylic acid) of varying polydispersity.[73] The aggregation experiments here do not indicate significant bridging (enhanced aggregation) by 0.18 ppm NOM_r, although bridging may contribute to initial size increases observed for higher concentrations of NOM_r. At the highest NOM concentration assessed (560 ppm NOM_1), where sufficient NOM_r is present to stabilize the NPs, NOM_r effects become dominant: removal of the higher molecular weight material significantly impairs the NOM's stabilizing ability (compare NOM_1 and NOM_f in Figure 5.7(b)).

Differences in other physicochemical characteristics are also considered: the NOM_r sample has higher aromatic and protein-like content than NOM_f. Higher aromaticity of NOM_r may result in higher affinity than NOM_f for the particle surface. The significantly higher molecular weight of NOM_r compared to NOM_f is also expected to increase its strength of adsorption to the Au NPs, as shown for polydisperse NOM or polymers.[43,74] The higher adsorbed mass of NOM_r may result in the formation of a thicker adsorbed layer and stronger steric stabilization. Other studies have shown that aromaticity and molecular weight co-vary, and both correlate to NP aggregation behavior.[24] The influence of these co-varying factors

cannot be separated in this study, so differences in chemical composition (e.g. aromaticity or charge) may play a significant role in NOM adsorption and NP aggregation. However, the chemical differences measured here for the NOM fractions were much less apparent than the molecular weight differences. Assessment of additional samples in Chapter 6 allows for better distinction of the influence of molecular weight as opposed to the chemistry of the NOM. Finally, properties such as hydrophobicity, polysaccharide content, charge, elemental composition, or acid/base functional groups may be important but were not measured here.

Implications of these results are discussed in Chapter 7. Briefly, small amounts of > 100 kg/mol NOM were found to enhance NP stability, even at low concentrations (< 2 wt %) in the unfractionated NOM mixture. Therefore, correlations for NP aggregation may need to account for the polydispersity of the NOM, particularly at the high molecular weight tail of the distribution. Limitations in extrapolating these results to other systems and future work are also discussed in Chapter 7.

References for this chapter are listed at the end of Chapter 7.

Chapter 6. Correlation of the physicochemical properties of natural organic matter samples from different sources to their effects on gold nanoparticle aggregation

6.1 Introduction

Chapter 5 presented a detailed investigation of the effects of heterogeneity (specifically, the role of the NOM components with very high molecular weight, > 100 kg/mol determined from MALS). In this chapter, we extend this analysis to five additional NOM samples from different origins. Furthermore, we assess general correlations of nanoparticle (NP) aggregation behavior to NOM properties across all six samples and the two molecular weight fractions obtained from each sample.

The differences in NP aggregation behavior for the unfractionated SRNOM and the 100 kg/mol filtrate and retentate fractions (Chapter 5) was attributed primarily to the molecular weight distribution: the fractions differed relatively little in aromaticity (although other, unmeasured chemical properties were not assessed). Other NOM sources will have different chemical compositions and may exhibit different behavior, depending on the origin of the NOM (i.e., the type of biomass from which it is derived), the source where it is collected (e.g., soil, freshwater lakes or rivers, or seawater), and the processing or fractionation applied (e.g., separation of humic and fulvic acids). The origin of NOM can be classified as follows: pedogenic NOM derived from terrestrial decomposition of plants and microorganisms, which contains primarily charged, refractory material (e.g., fulvic and humic acids); and aquagenic NOM derived from aquatic organisms such as plankton, which contain more polysaccharides and

proteins.[75] As described in Chapter 2, these types of components can have different effects on colloidal stability. Comparing across sources, NOM extracted from solid samples (peat or soil) is likely to contain more hydrophobic, higher molecular weight components of pedogenic NOM with a higher solid-water partitioning coefficient. Rivers or lakes receiving leached pedogenic NOM will then contain a higher percentage of the more hydrophilic components; aquagenic material will also be present. Seawater will contain primarily aquagenic material. Typically, the user or collector will extract a portion of the NOM from the source (e.g. onto an XAD resin) and then fractionate it further by solubility at pH 1.0 (fulvic vs. humic acids).[76]

This study includes assessment of gold NP aggregation in the presence of Pahokee peat humic acid (PPHA), Suwannee River humic acid (SRHA), Elliott Soil fulvic acid (ESFA), Pony Lake fulvic acid (PLFA), and Pacific Ocean fulvic acid (POFA). These samples cover a range of source types (peat or soil, freshwater river, a saline lake, and seawater) as well as collection or preparation types (i.e., fulvic and humic acids). This study improves upon other studies comparing the effects of various NOM sources on aggregation and dissolution (e.g., the study by Deonarine et al.)[24] by providing more thorough characterization of the NOM (e.g., molecular weight distribution and fluorescence EEMs). In addition, the preparation of ultrafiltration fractions of each NOM source expands the sample size and allows for control of molecular weight, enabling better insight into the role of molecular weight versus other chemical properties of the NOM.

6.2 Objectives

The first objective of this research is to extend the study presented in Chapter 5 to several NOM samples. The effects of the molecular weight and polydispersity of NOM on the

aggregation of gold NPs are assessed. We determine whether observations from Chapter 5 (i.e. high molecular weight fractions providing better NP stability against aggregation, and mixtures of molecular weight fractions providing better stability than the fractions comprising it) are consistent across several NOM types. The second objective is to correlate aggregation rates with the properties of the NOM fractions to assess whether molecular weight distribution is the primary determinant of NP behavior or whether other properties (i.e. NOM chemistry) must be taken into account. Several possible quantitative correlations are assessed. This study will contribute to an improved understanding of the effects of NOM on NP aggregation behavior, at both a detailed level (considering the composition and heterogeneity of the NOM) and a holistic and practical level (across a broad set of NOM types from different water bodies and soils).

6.3 Materials and methods

6.3.1 Citrate-stabilized gold nanoparticles

The same batch of citrate-stabilized gold NPs described in Chapter 5 was used for this study. The size and aggregation rate of the NPs was re-measured several times over the course of the experiments; no significant change was observed over time.

6.3.2 Natural organic matter isolates

Five additional NOM isolates were assessed: Pahokee Peat humic acid (PPHA), Suwannee River humic acid (SRHA), Elliott Soil fulvic acid (ESFA), Pony Lake fulvic acid (PLFA), and Pacific Ocean fulvic acid (POFA). The data for Suwannee River natural organic matter (SRNOM) presented in Chapter 5 are also assessed here in context of the entire set of NOM isolates. All samples except POFA were obtained from the International Humic

Substances Society (IHSS, St. Paul, MN) (catalog numbers listed in Table 6.1). POFA was provided by Dr. George Aiken (U.S. Geological Survey, Boulder, CO) via Dr. Heileen Hsu-Kim (Duke University, Durham, NC). Descriptions of the NOM collection sites are compiled in Table 6.1.

Table 6.1. Descriptions of NOM collection sites

NOM sample	Collection site
PPHA (1R103H-2)	Florida Everglades; agricultural peat soil[77]
SRHA (2S101H); SRNOM (1R101N)	South Georgia, draining the Okefenokee Swamp; blackwater river[77]
ESFA (4S102F)	Indiana; prairie soil[77]
PLFA (1R109F)	Antarctica; eutrophic, saline coastal pond[77]
POFA	170 km southwest of Honolulu, Hawaii; seawater collected at 100 m depth[78]

Elemental composition and functional group distributions were not measured in this study. However, these have been reported in the literature and are provided by the IHSS.[77] Reported values for the bulk, untreated samples are presented in Table 6.2 and 6.3.

Table 6.2. Elemental composition and reduced S content of NOM samples

NOM	Elemental composition (wt %)[77]					Reduced S content	
	C	H	O (wt%)	N (wt%)	S (wt%)	(% of total S)	(% of total mass)
PPHA	56.8	3.6	36.6	3.7	0.7	50% [79]	0.35
SRHA	52.6	4.3	42.0	1.2	0.5	46% [80]	0.25
SRNOM	52.5	4.2	42.7	1.1	0.7	28% [81]	0.18
ESFA	51.0	4.3	44.0	2.7	1.2	34.8% [82]	0.41
PLFA	52.5	5.4	31.4	6.5	3.0	59% [83]	1.8
POFA	56.2	6	36.3	1.1	0.4	12.5% [78]	0.05

Table 6.3. Functional group distributions for NOM samples

NOM	Functional group distributions (^{13}C NMR) and chemical shifts (ppm)					
	Aliphatic I (0–62)	**Aliphatic II (62–90)**	**Acetal (90–110)**	**Aromatic (110–160)**	**Carboxyl (160–190)**	**Ketone (190–230)**
PPHA[77]	19	5	4	47	20	5
SRHA[77]	29	13	7	31	15	6
SRNOM[77]	27	15	7	23	20	8
ESFA[77]	22	9	1	30	25	12
PLFA[77]	61	8.4	0.2	12	17	1.2
POFA[78]	56.9	13.4	1.2	7.3	19.5	1.6

All data from IHSS[77] except for POFA.[78] Data for older stocks of PPHA (1S103H) and ESFA (1S102F) used where data for the stocks used here were unavailable.

Stock solutions of NOM for the IHSS samples were prepared by dissolving the solid material at 2 g/L in water and rotating overnight, similarly to the method described in Chapter 5 except the initial stock was prepared in 1 mM $NaHCO_3$ and adjusted to pH 8.3 with 1 N NaOH to improve solubility of the humic acid samples. Samples were then filtered using a 0.22 μm PVDF syringe filter, with a portion of the unfiltered 2 g/L stock reserved for determination of the carbon content by total organic carbon (TOC) analysis. The POFA sample was provided in aqueous solution, pre-filtered using a 0.22 μm nylon syringe filter (VWR), at a concentration of 283 mg C/L, or 504 mg/L total mass. In this chapter, the 0.22 μm filtered stock solutions are referred to as the "whole" NOM.

6.3.3 Characterization and fractionation of NOM

Fractionation of the NOM was performed using a 15-mL centrifugal ultrafiltration unit (Amicon) with a 100 kg/mol molecular weight cutoff. As described in Chapter 5, centrifugation was performed at 6,000 rpm (3,864*g*) at room temperature on a Marathon 26KM centrifuge

(Hermle Labortechnik). The ultrafiltration membrane was first rinsed by centrifuging 15 mL of DI water; then a 15 mL aliquot of the stock NOM (0.22 μm filtrate) was centrifuged, and a second 10 to 15 mL aliquot of stock NOM was added to the same tube (to collect a greater quantity of retentate) and centrifuged. The filtrate was collected without further modification. The retentate was rinsed by repeated additions of 15 mL of 1 mM $NaHCO_3$ (pH 8.3) and centrifugation until the filtrate appeared clear (except for PPHA, for which light brown color was still observed after ten rinses).

The same NOM characterization methods described in Chapter 5 were applied here. Concentrations were measured on a TOC analyzer against KHP calibration standards (method described in Chapter 5), with the weight percent of carbon determined on the 2 g/L unfiltered stocks. Molecular weight distributions were determined by size exclusion chromatography with multi-angle light scattering (SEC-MALS), using a Superdex 75/300 SEC column (GE Life Sciences) and HELEOS II light scattering detector (Wyatt Technology) connected to a high performance liquid chromatography system with a binary pump, degasser, and autosampler. An ultraviolet (UV) absorbance detector (Agilent) and differential refractometer (t-REX, Wyatt) provided in-line concentration measurements. The eluent used was 4 mM phosphate buffer at pH 7 with 25 mM NaCl, and the sample injection volumes ranged from 50 to 100 μL. The IHSS samples were injected at their stock concentrations (1.1 to 1.9 g/L for all whole and filtrate fractions and the PPHA retentate fraction; ~0.1 to 0.6 g/L for all other retentate fractions). The POFA sample had the lower molecular weight; to obtain a higher light scattering signal, portions of the whole and filtrate fractions for POFA were concentrated to 4.1 to 4.3 g/L by rotary evaporation at 25 mbar and 25 to 35 °C for the SEC-MALS analysis. The refractive index increments (dn/dc) needed to obtain concentration from the differential refractive index (dRI)

measurements were determined by batch dRI measurements on the unfiltered stock NOM samples. Molecular weight distributions were then fitted to a lognormal distribution in order to account for the portion of the SEC chromatogram that could not be analyzed by MALS, as described in Chapter 5 and Appendix B.1.4. When compared, the weight-averaged molecular weights obtained directly from MALS (M_w) are referred to as the "unadjusted" molecular weight, whereas the geometric mean of the fitted lognormal distribution of weight-averaged molecular weights (M_g) are referred to as the "fitted" or "modeled" molecular weights.

UV-vis absorbance spectra and fluorescence excitation emission matrices (EEMs) were collected for the whole, filtrate, and retentate fractions for each NOM sample. Samples for UV-vis absorbance were prepared at 5 ppm in DI water without pH adjustment to prevent KCl contamination from the pH probe. Specific UV absorbance at 254 or 280 nm was used to estimate aromaticity using previously determined correlations.[50,53,54] The UV-vis absorbance spectrum was fitted to an exponential curve to determine exponential slopes.[57] Samples for fluorescence EEMs were prepared at 1 ppm C in 10 mM KCl as recommended by Westerhoff et al.; however, the pH was adjusted to 8.3 instead of 3 to prevent possible precipitation of the less soluble humic acid samples. Fluorescence EEMs were measured on a Fluoromax 4 instrument (Horiba, Edison, NJ). Excitation and emission slit widths were 10 nm. Emission was measured from 290 to 600 nm in 1 nm increments, at excitation wavelengths of 200 to 400 nm in 5 nm increments. Blank subtraction was performed using 10 mM KCl (pH 8.3), and inner filter correction was applied using UV-vis absorbance spectra collected on the same samples used for the fluorescence EEMs.

6.3.4 Nanoparticle aggregation

Aggregation experiments for the citrate-stabilized gold NPs in the presence of NOM were performed using the same methods and instrumentation (ALV) for time-resolved dynamic light scattering (DLS) as presented in Chapter 5. Briefly, the size of the citrate-stabilized gold NPs was measured prior to and after NOM addition. Then, NaCl solution was added and aggregation was monitored over 20 minutes. The final concentrations after NaCl addition were 20 ppm NPs and 100 mM NaCl. All NOM fractions were tested at a concentration of 10 ppm (as in Chapter 5); this concentration is typical of river waters (~5 ppm dissolved organic carbon,[75] or ~10 ppm total NOM assuming 50 wt % carbon). For some NOM samples, no significant NP aggregation was observed with 10 ppm of any fraction, so fractions were also compared at a lower concentration of 1 ppm; this concentration is typical of sea water (~0.5 ppm dissolved organic carbon[75]).

Furthermore, the concentration of retentate present in 10 ppm of the whole NOM sample (determined by SEC-MALS) and recombined fractions of the retentate and filtrate fractions were tested. The recombined fractions are used to confirm whether the effects imparted by the unfractionated NOM are attributable to mixing of the fractions, rather than any components lost during the ultrafiltration process (Table B.4).

Initial aggregation rates (k_{agg}) were estimated and used for quantitative correlations of NP aggregation behavior to NOM properties. Ideally, k_{agg} should be taken as the linear slope (over several data points) of size versus time during the period of doublet formation (between the first measurement and that where the hydrodynamic radius, R_h, reaches 1.3 times the initial R_h).[84] However, particle aggregation was often too rapid in the experiments here to capture this period (i.e., the first measurement after addition of NaCl solution was > 1.3 times the initial size).

Therefore, k_{agg} was computed between the initial size ($R_{h,0}$) and the first measurement after NaCl addition. Despite this issue and other uncertainties in the delay time until the first measurement (Appendix B.3.7), the computed k_{agg} generally captured the overall aggregation behavior over time (Appendix B.3.7). The uncertainty in delay time and standard deviation in R_h over replicate measurements were propagated to estimate uncertainty in k_{agg}.

6.3.5 Characterization of nanoparticle-NOM interaction

Electrophoretic mobility of the citrate-stabilized gold NPs coated with each type and molecular weight fraction of NOM was measured as described in Chapter 5. The preparation and measurement method was the same for all types of NOM.

6.4 Results

6.4.1 Molecular weight determination of the whole NOM samples

SEC-MALS chromatograms are shown in Figure 6.1. As expected, the humic acids (operationally defined as the insoluble portion of the NOM at pH 1.0)[77], PPHA and SRHA, have a higher molecular weight overall (and show earlier elution of the main peak), and components with apparent weight-averaged molecular weights (M_w) > 100 kg/mol comprise a higher percentage of the NOM. The marine fulvic acids (PLFA and POFA) have the lower molecular weights overall, but a small amount of > 100 kg/mol material is also observed in these samples. ESFA and SRNOM have intermediate molecular weights between the humic acids and the marine fulvic acids.

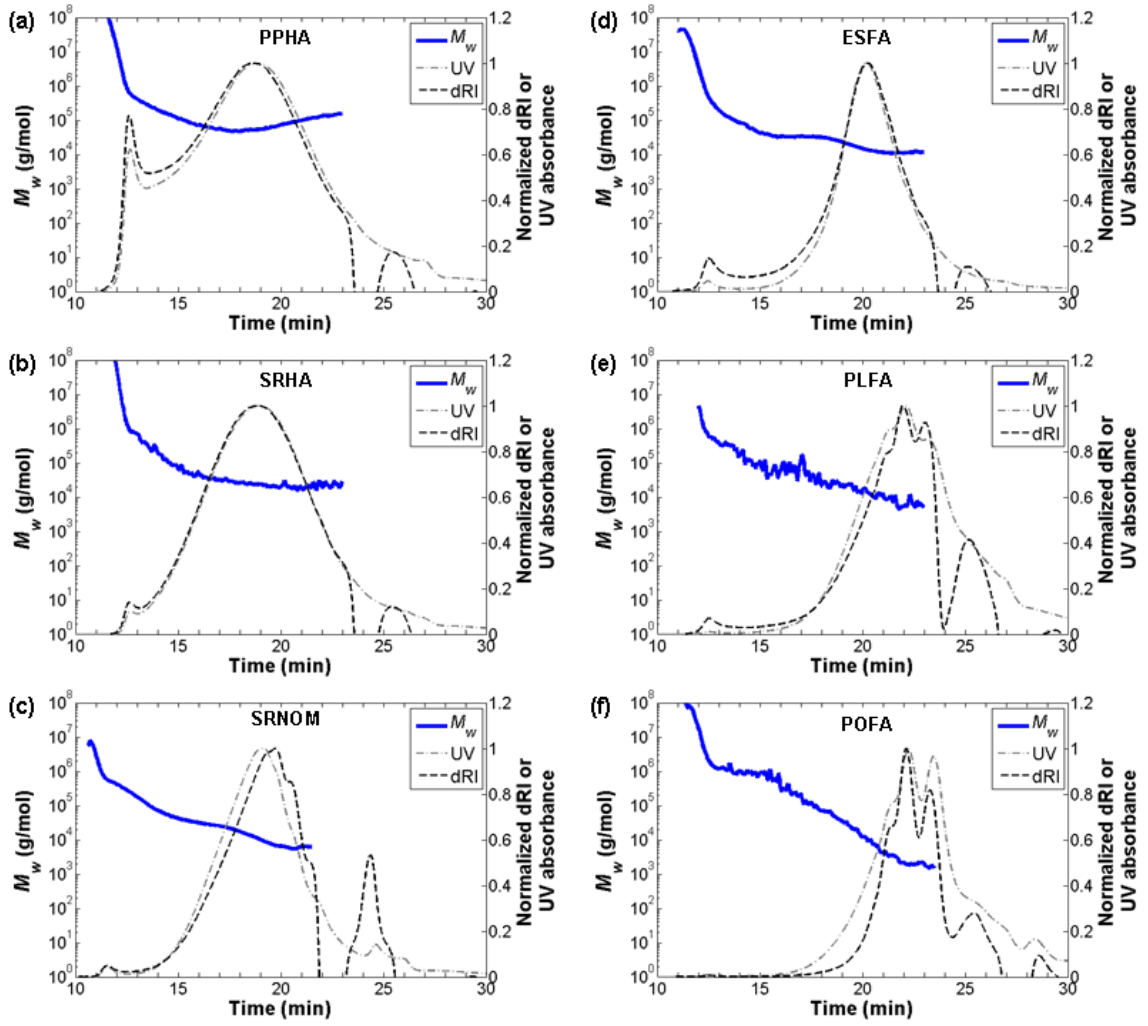

Figure 6.1. SEC-MALS chromatograms for PPHA (a), SRHA (b), SRNOM (c), ESFA (d), PLFA (e), and POFA (f), using eluent of 4 mM phosphate (pH 7) with 25 mM NaCl in water. The solid blue line represents the M_w determined by MALS, and the dash-dotted grey line and dashed black line represent the UV absorbance and dRI, respectively (normalized to the highest measured value). Sharp decreases in the dRI signal after 23 minutes are attributed to eluting solvent injected with the NOM, which has a lower ionic strength (and refractive index) than the eluent.

6.4.2 Preparative fractionation of the NOM samples

SEC-MALS chromatograms for the filtrate and retentate fractions obtained after centrifugal ultrafiltration at a 100 kg/mol molecular weight cutoff are provided in Appendix

B.1.2. Insufficient quantities of retentate were recovered for PLFA or POFA for SEC-MALS analysis (however, sufficient PLFA retentate was recovered for other analyses and aggregation experiments). For all samples, good separation was achieved, i.e. the filtrate and retentate fractions were comprised primarily of < 100 and > 100 kg/mol components, respectively. Recoveries of material from the fractionation process, calculated by a mass balance using the measured concentrations and volumes of filtrate and retentate, are reported in Appendix B.3.1, and range from 86% to 97%.

The fitted lognormal distributions that account for the non-analyzed portion of the NOM are shown in Appendix B.1.4. As stated in the methods, the non-analyzed (later-eluting) portion is assumed to have a lower molecular weight than the analyzed portion; this assumption may not be accurate for PPHA, where adsorption of high molecular weight components was observed (i.e., an increase in molecular weight with elution time). Therefore, molecular weights for PPHA may be underestimated by this method. The geometric mean of the fitted lognormal distribution of weight-averaged molecular weights, M_g, mean of the lognormal distribution, μ, and standard deviation of the lognormal distribution, σ, obtained from least squares fitting of the cumulative distribution function are reported in Table 6.4. In general, similar or lower M_g values are observed for the filtrate compared to the whole NOM. The fitted standard deviation (representative of polydispersity) is expected to be lower for the filtrate than the whole NOM, but this behavior is only observed for half of the samples. The unexpected results are likely attributable to error in the fitted lognormal distribution, which tends not to capture the highest molecular weight portion of the measured distribution (details in Appendix B.1.4). The unadjusted M_w obtained directly from MALS are also presented in Table 6.4. As discussed in

Section 5.3.3.3, the molecular weights obtained from MALS tend to be higher than those obtained by SEC calibration against polymer standards or other (non-SEC) methods.[49]

Table 6.4. Unadjusted M_w, and fitted parameters and M_g of the lognormal distributions for the NOM samples

NOM type	NOM fraction	Unadjusted	Fitted (Equations B.5 and B.6)		
		M_w (kg/mol)	M_g (kg/mol)	μ (log g/mol)	σ (log g/mol)
PPHA	Whole	307	61	4.79	0.34
	Filtrate	67	36	4.56	0.24
	Retentate	857	185	5.27	0.23
SRHA	Whole	114	24	4.38	0.17
	Filtrate	27	27	4.44	0.21
	Retentate	980	372	5.57	0.24
SRNOM	Whole	23	7.9	3.90	0.43
	Filtrate	13	5.8	3.76	0.45
	Retentate	691	151	5.18	0.68
ESFA	Whole	85	12.3	4.09	0.3
	Filtrate	17	12.0	4.06	0.26
	Retentate	1030	231	5.37	0.34
PLFA	Whole	38	4.0	3.61	0.53
	Filtrate	16	4.4	3.64	0.49
	Retentate	n.d.	n.d.	n.d.	n.d.
POFA	Whole	4.2	1.6	3.21	0.35
	Filtrate	2.9	1.3	3.10	0.24

The experimentally-determined distributions of M_w are also plotted in pie charts in Figure 6.2 to visualize the distributions. The non-analyzed portion of the sample was attributed to the < 10 kg/mol portion for SRNOM, ESFA, PLFA, and POFA, and to the 10 to 50 kg/mol portion for PPHA and SRHA (where no < 10 kg/mol material was identified by MALS). A plot comparing the cumulative distribution functions across the six unfractionated NOM samples is also presented in Appendix B.1.4 (Figure B.3).

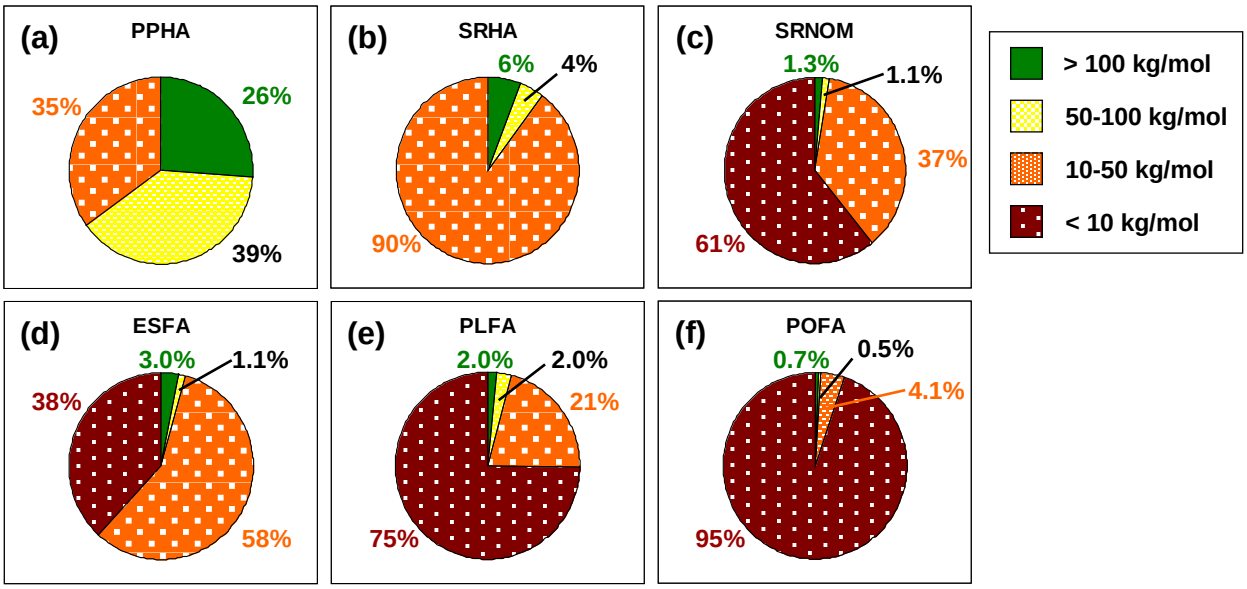

Figure 6.2. Molecular weight distributions for unfractionated PPHA (a), SRHA (b), SRNOM (c), ESFA (d), PLFA (e), and POFA (f). The reported percentages are based on experimental molecular weights obtained directly by MALS, with the non-analyzed portion of the mass attributed to the 10-50 kg/mol fraction for PPHA and SRHA and the < 10 kg/mol fraction for all other NOM samples.

6.4.3 Chemical characterization of the NOM fractions

Fluorescence EEMs for all NOM types and fractions, and the peak locations and intensities, are shown in Figure 6.3 (note that SRNOM was measured at pH 3 following the procedure of Westerhoff et al., whereas other NOM samples were measured at pH 8.3 to ensure solubility; peak intensities at different pH may not be comparable). No trend of peak intensities with molecular weight is apparent when comparing among the six different types of NOM (where M_w or M_g decreases from PPHA > SRHA > ESFA > SRNOM > PLFA > POFA). However, within each sample, the fluorescence intensity for the retentate fraction is consistently lower than that of the filtrate or whole NOM (at the same concentration as C). In addition, a

secondary peak in the protein-like region is observed for the retentate fractions of the SRNOM, ESFA, and PLFA (insufficient retentate was collected for POFA).

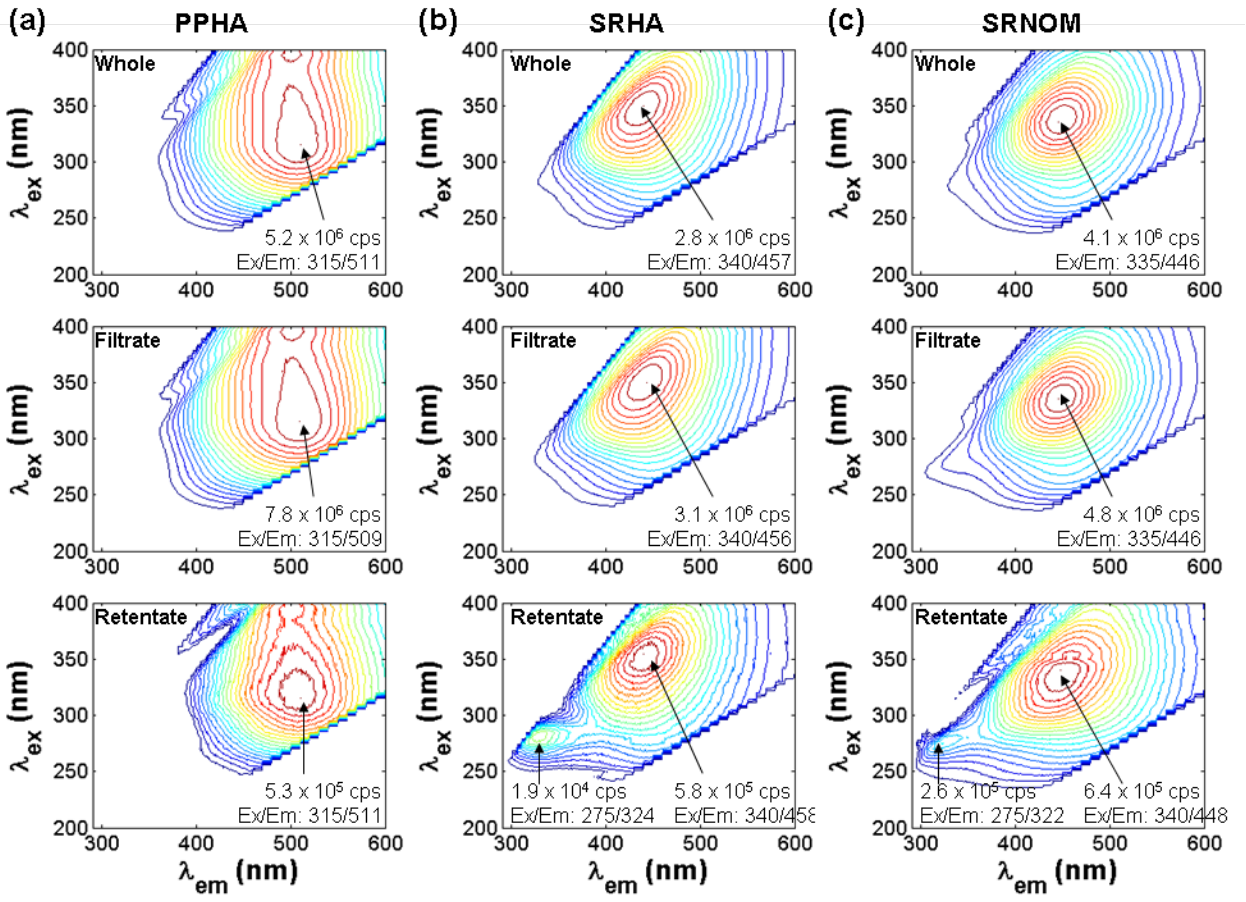

Figure 6.3. *(continued on next page)*

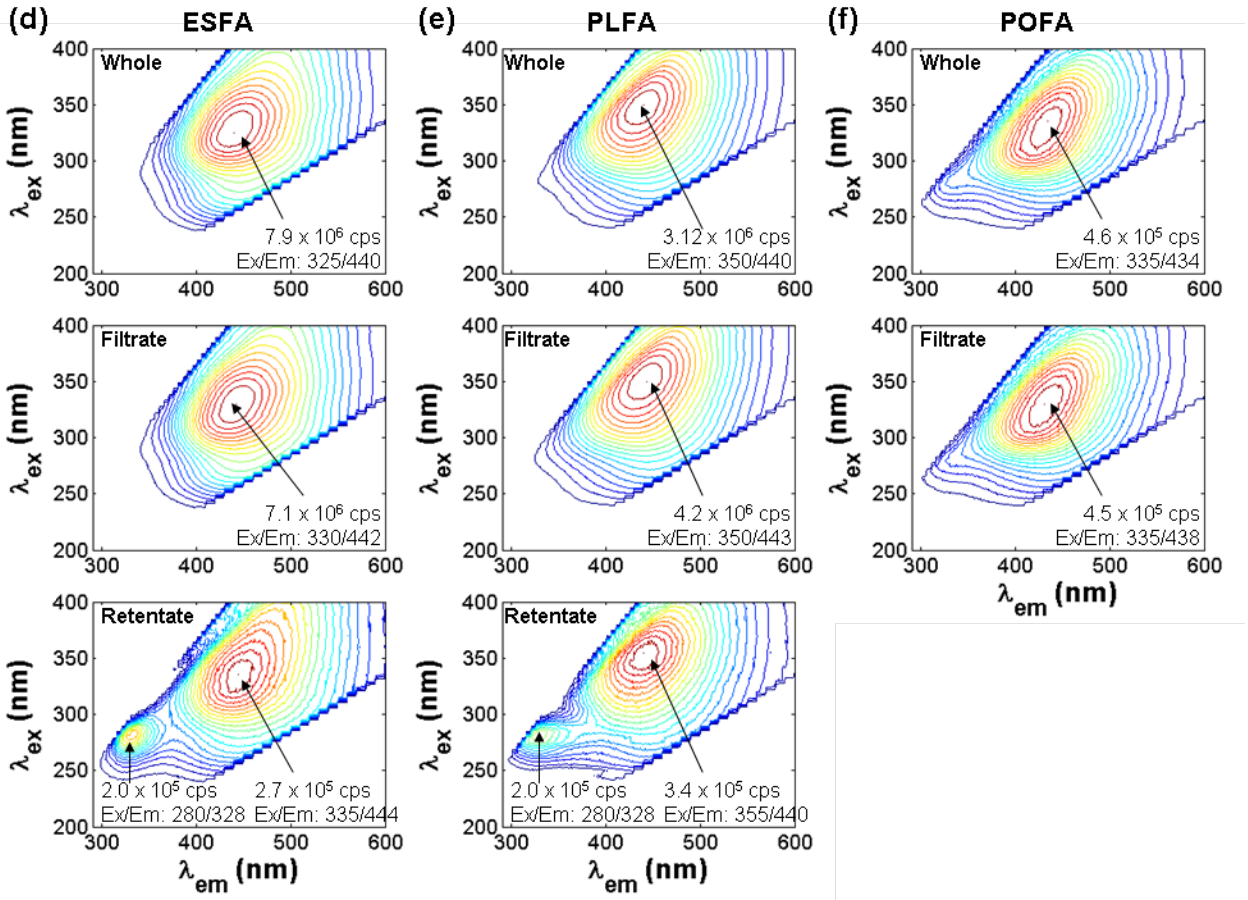

Figure 6.3. Fluorescence EEMs for the whole, filtrate, and retentate fractions of PPHA (a), SRHA (b), SRNOM (c), ESFA (d), PLFA (e), and POFA (f). All samples were prepared at 1 ppm C in 10 mM KCl at pH 8.3 (except SRNOM, at pH 3). Blank subtraction and inner filter correction were applied, and fluorescence intensitye at and outside the 1st and 2nd order Rayleigh scattering regions were set to zero. The retentate fraction generally has lower peak fluorescence intensity and, for all samples except PPHA, shows a secondary peak in the "protein-like" region. Insufficient quantities of POFA were available to collect a retentate fraction.

The UV absorbance spectra and the exponential fits are provided in Figure 6.4. Comparisons across NOM types for each fraction are shown in Appendix B.3.2. Specific UV absorbance at 254 nm ($SUVA_{254}$) and 280 nm ($SUVA_{280}$) and the estimated aromaticity computed from correlations from previous studies[50,53,54] are also reported in Appendix B.3.2. When comparing the unfractionated (whole) samples across the six types of NOM (Figure B.13

in Appendix B), SUVA generally shows a positive correlation with M_w or M_g, and the exponential slope coefficient shows an inverse correlation with M_w or M_g.

However, when comparing fractions within each NOM type, SUVA for the retentate fractions are generally similar (or significantly *lower* in ESFA and PLFA) than the SUVA of the whole or filtrate fractions, despite their higher molecular weights. Therefore, SUVA should not be assumed to always correlate to molecular weight: these two properties are not intrinsically related, and the data obtained here reinforce this fact. The lower SUVA of the retentate material in ESFA and PLFA may suggest that this material contains a higher proportion of polysaccharides (that do not strongly absorb UV light) rather than aromatic "humic" or "fulvic" substances.

On the other hand, the slope coefficient, *S*, better reflects the molecular weight difference between fractions, with the retentate fraction consistently exhibiting a lower *S* than the filtrate and whole NOM, even for ESFA and PLFA. The implications for distinguishing the correlation of NP aggregation with SUVA, *S*, and molecular weight of the NOM (all of which are typically assumed to co-vary) are discussed further in the results (Section 6.4.6). As discussed in Section 5.4.3, *S* may be representative of the composition of the NOM (e.g., the ratio of unsubstituted aromatic groups and those with polar substitutions),[56] or it may reflect extended aromatic structures or intramolecular charge transfer between these structures in higher molecular weight NOM.[69]

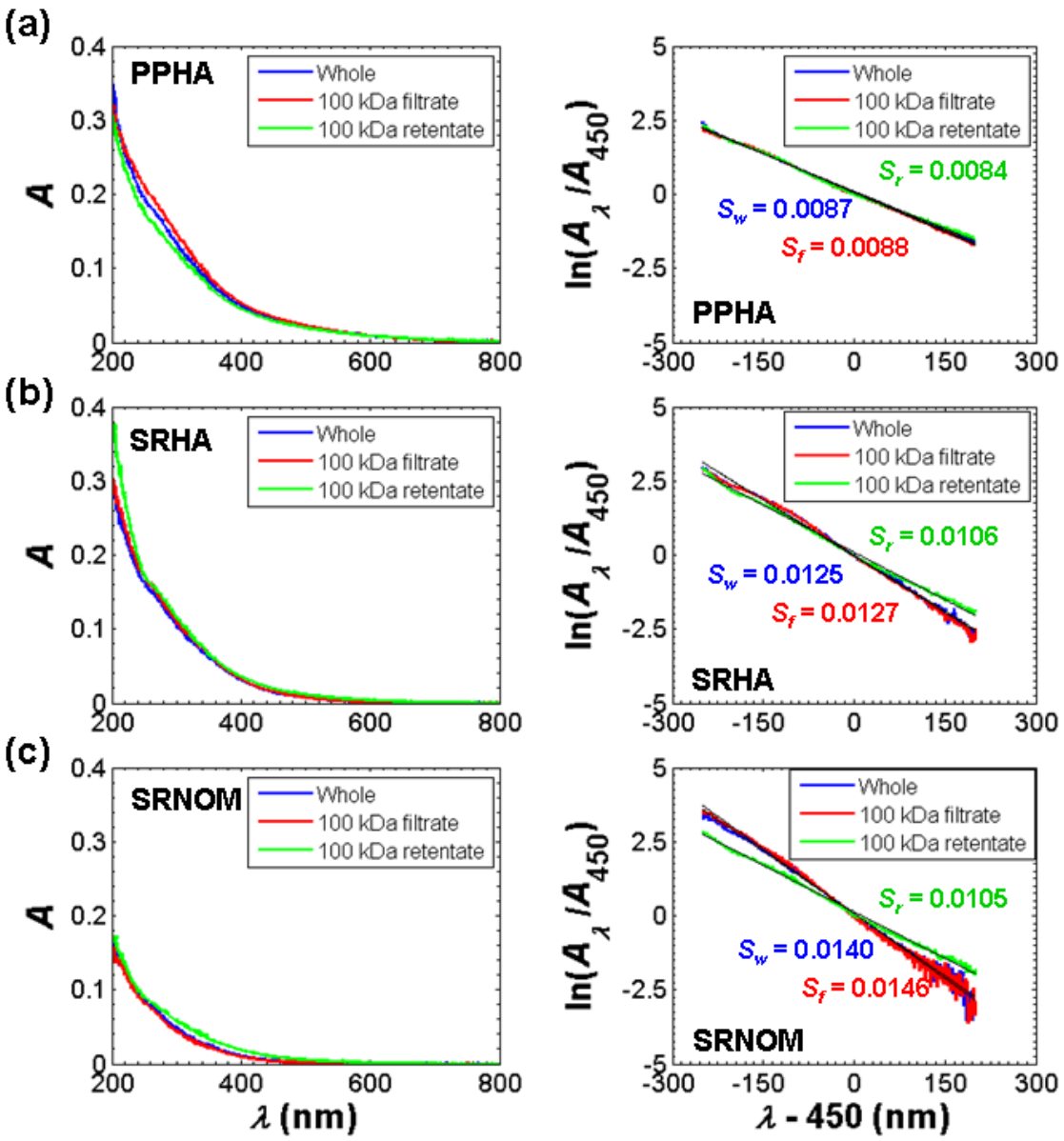

Figure 6.4 *(continued on next page)*

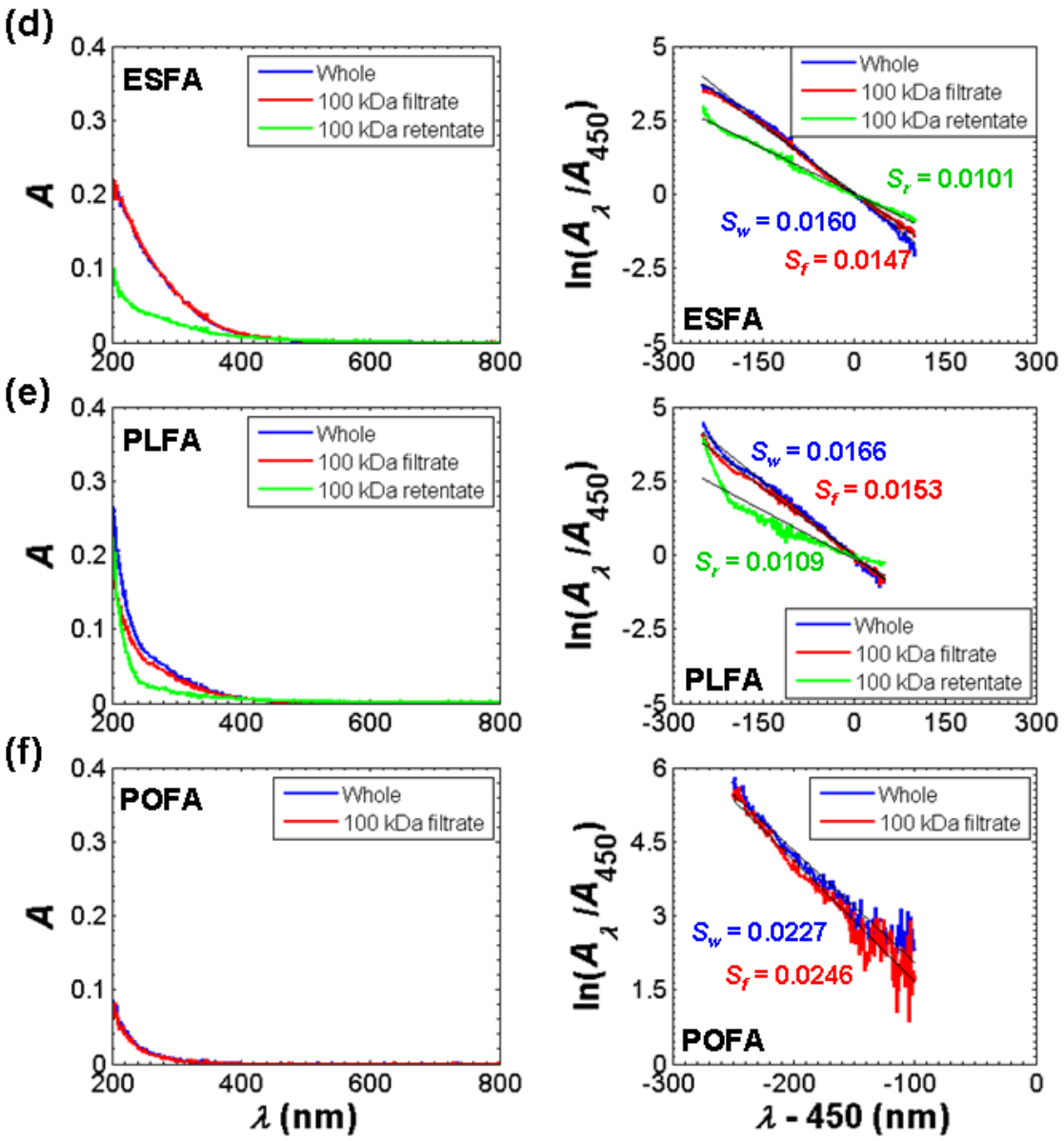

Figure 6.4. UV absorbance spectra (left) and exponential fits (right) for PPHA (a), SRHA (b), SRNOM (c), ESFA (d), PLFA (e), and POFA (f). All samples prepared at 5 ppm in DI water. Comparisons of all six NOM types on the same plot are provided in Appendix B.3.2. Absorbance spectra are similar across the fractions within each NOM type, except for ESFA and PLFA. On the other hand, the slope coefficient for the retentate fraction is consistently smaller for the retentate fraction in each NOM type.

6.4.4 Effect of molecular weight fractions on nanoparticle aggregation

In this section, we focus on the effects of the molecular weight fractions within each NOM sample. Thorough discussion of these effects was provided in Chapter 5 for SRNOM, so an abbreviated discussion is provided here. Comparison across all six samples is discussed in Section 6.4.5.

Aggregation of the citrate-stabilized gold NPs in the presence of 10 ppm NOM and 100 mM NaCl is shown in Figure 6.5. The same trends identified for SRNOM in Chapter 5 are observed for SRHA, ESFA, PLFA, and POFA, i.e., the retentate fraction provides better NP stability against aggregation than the filtrate fraction at the same mass concentration, and the whole NOM provides intermediate stability between the two fractions. An exception is observed for PPHA, for which all fractions stabilize the NPs against aggregation. Additional aggregation experiments were performed using an NOM concentration of 1 ppm (Appendix B.3.4). As for SRNOM (Chapter 5), 1 ppm of retentate NOM provides significantly better NP stability than 1 ppm of filtrate or whole NOM, except for PPHA. No enhancement of aggregation in the presence of NOM (e.g. bridging of NPs) was observed; however, bridging may be induced by the presence of divalent or multivalent cations such as Ca^{2+}, which were not included here.

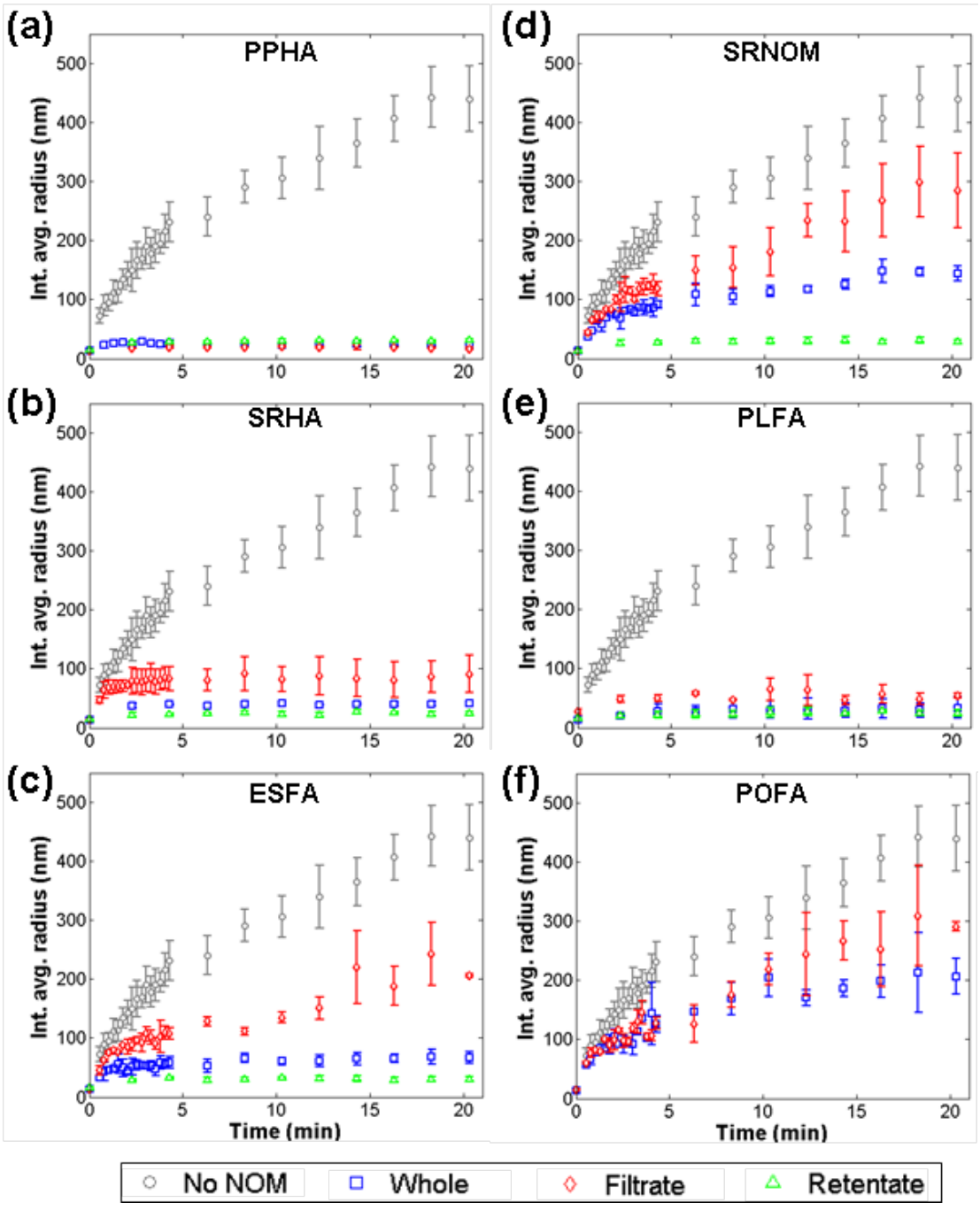

Figure 6.5. Hydrodynamic radius measured by time-resolved DLS for 20 ppm citrate-stabilized gold NPs in the presence of 10 ppm NOM and 100 mM NaCl, in 1 mM $NaHCO_3$ at pH 8.3. All samples were measured in duplicate or more runs; error bars represent the standard deviation in the radius measured at each time point. At the same (10 ppm) NOM concentration, the retentate consistently produces the best NP stability against aggregation, whereas the filtrate produces the poorest NP stability. An exception is observed for PPHA, where all fractions provide similarly good NP stability. The same trends and exception for PPHA are observed in the presence of 1 ppm NOM (Appendix B.3.4). Insufficient retentate was collected for POFA to conduct an aggregation experiment, so it is not included.

The observed behavior is likely attributable to the greater steric repulsion imparted by the larger retentate components, as discussed in Chapter 5. For PPHA, the lack of difference between the fractions may be attributable in part to the fact that all fractions were comprised of relatively high molecular weight components, whereas the filtrate and retentate fractions of the other five samples showed more extreme differences in molecular weight (Table 6.4; Figure 6.2). Another factor that may play a role is the faster diffusion and adsorption of smaller filtrate molecules to the NP surface. Also, at the same mass concentration (10 ppm), the filtrate (M_g = 36 kg/mol) contains a greater number of "molecules" than the retentate (M_g = 185 kg/mol). A low number ratio of NOM to NPs may encourage bridging.

The same trends in electrophoretic mobility identified for SRNOM in Chapter 5 are observed within each of the additional NOM samples. Namely, NPs coated in the filtrate and whole NOM have similar electrophoretic mobilities, whereas NPs coated in the retentate fraction tend to have a less negative electrophoretic mobility. No trend is observed across NOM samples; i.e., the electrophoretic mobility of NPs coated with the whole NOM (dark blue bars) does not correlate with M_w or M_g (decreasing from left (PPHA) to right (POFA) across Figure 6.6). As discussed in Chapter 5, these results support that a steric repulsion effect, rather than an electrostatic effect, is likely responsible for the significantly improved NP stability in the presence of retentate NOM.

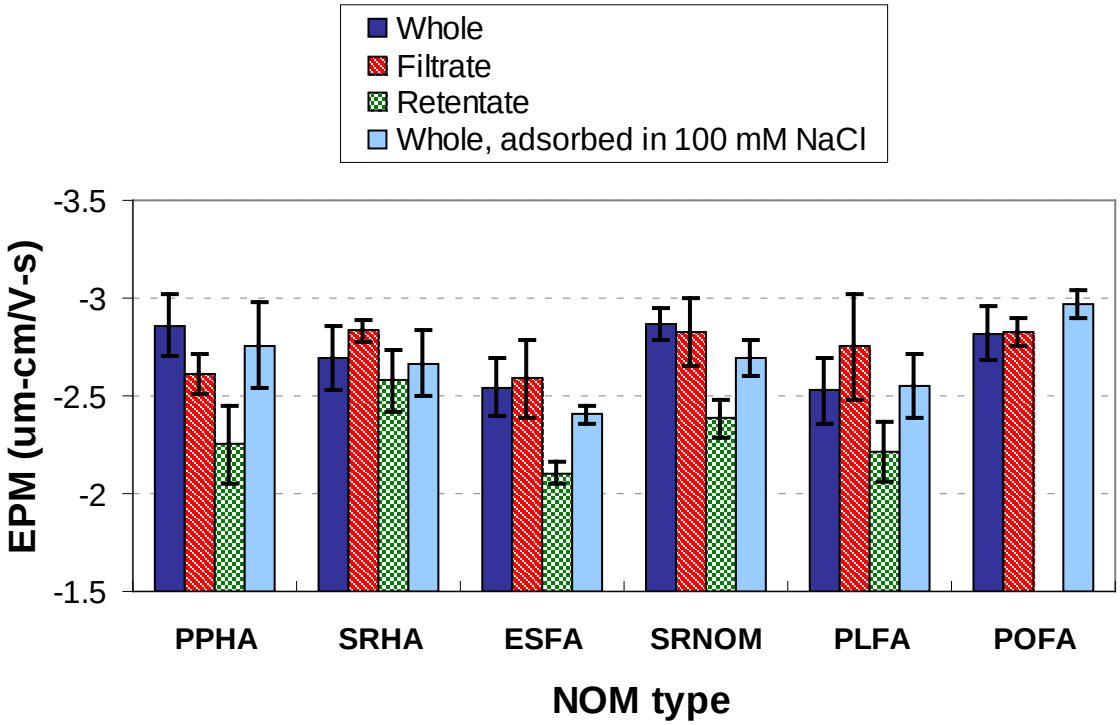

Figure 6.6. Electrophoretic mobilities of NOM-coated NPs, measured in 20 mM NaCl, 1 mM $NaHCO_3$, pH 8.3. Error bars represent the standard deviation across five repeat measurements. Samples were prepared in 20 mM NaCl, 1 mM $NaHCO_3$, pH 8.3 and washed three times by centrifuging and resuspending in NOM-free medium. For whole NOM, initial preparation in 100 mM NaCl (matching the aggregation experiments) followed by washing and resuspension into 20 mM NaCl was tested; results did not differ significantly from the 20 mM NaCl preparation. Data for unwashed samples in 20 mM NaCl are provided in Appendix B (Figure B.14); the same trend (or lack of trend) is observed.

The synergistic effect of the mixture of filtrate and retentate fractions (i.e., the "whole" NOM) is again observed for all samples here except PPHA (where all fractions provided similar NP stability). Figures comparing NP aggregation in the presence of 10 ppm of whole NOM and the relevant concentrations of the constituent molecular weight fractions are shown in Appendix B.3.5. Neither the filtrate or retentate fractions alone provide the full NP stabilization observed for the whole NOM. Re-mixing the separated fractions produces a similar effect to the

unfractionated NOM (indicating that enhanced stabilization by the whole NOM cannot be explained solely by components lost during the fractionation procedure, and that effects due to the retentate are likely not an artifact due to possible modifications during the separation procedure). The broader implications of this result are discussed in Section 6.4.6.

6.4.5 Comparison of nanoparticle aggregation across NOM types

In this section, aggregation results are compared across all six NOM samples (and the molecular weight fractions obtained) and assessed in the context of the molecular weights and chemistries of the different NOM types. Aggregation plots from Section 6.4.4 are re-organized to demonstrate trends with NOM type in the presence of 10 and 1 ppm of the whole, filtrate, and retentate fractions. These plots are presented in Appendix B.3.6. The NP stability against aggregation generally improves as the molecular weight of the NOM increases. However, PLFA does not follow this trend: it provides significantly better NP stability than would be expected from its low molecular weight, similar to or better than the stability provided by the high molecular weight humic acid samples. It is noted that unexpected effects on NP behavior produced by PLFA have also been shown in other recent studies. Nason et al.[30] found that, at low concentrations (< 2 mg C/L) PLFA provided better stability of citrate-stabilized gold NPs than SRNOM (but not SRHA) and postulated that this behavior could result from a higher packing density of the small PLFA molecules on the NP or its high aliphatic content (Table 6.3). These possible mechanisms are explored further in this study. (It is noted that Nason et al. also observed *destabilization* of the NPs at PLFA concentrations higher than 2 mg C/L, but that behavior was not observed in this study).

Possible mechanisms or properties resulting in the good NP stability provided by PLFA are explored. First, we identify physicochemical characteristics that can be dismissed:

- Electrostatic repulsion: It is unlikely that adsorbed PLFA provides higher electrostatic repulsion: the EPMs are not significantly different from those measured for the other types of NOM (Figure 6.6). Furthermore, the carboxyl content (which is expected to correlate to charge due to deprotonation of carboxylate groups) is similar across all NOM samples (Table 6.3).
- SUVA or aromaticity: The better stability also does not correspond to the SUVA (Table B.5 in Appendix B) or aromaticity (Table 6.3; Table B.5), which a previous study identified as significant parameters correlating with ZnS NP growth and aggregation rates.[24] Here, PLFA has a lower SUVA and aromaticity than all other samples except POFA.
- Fluroescence EEM: The fluorescence EEMs do not show any apparent distinction in either the fluorescence peak locations or intensities for PLFA in comparison to the other NOM samples. So overall, there are no distinctive chemical functional groups of the PLFA that could explain the high stability against aggregation that was observed.
- Aliphatic content: PLFA has a significantly higher aliphatic content than the soil and Suwannee River sources (Table 6.2), consistent with its microbial origins; however, POFA has similarly high aliphatic content but does not provide unexpectedly high NP stability.

The only (known) properties that distinguish PLFA from the other NOM sources used here are the high nitrogen and reduced sulfur content of PLFA (Table 6.2). (These characteristics are consistent with its origins from microbial or animal waste.) Amine groups can

form weak covalent bonds with gold, and reduced sulfur will from strong covalent bonds. Therefore, enrichment in these functional groups may result in a higher affinity (and adsorbed mass) of PLFA compared to the other NOM samples. Higher adsorbed mass would contribute to a stronger steric repulsion effect. Although reduced sulfur was not found to correlate to NOM stabilization of precipitating ZnS NPs,[24] the ZnS system contained excess inorganic sulfide that would compete with NOM, whereas the system here contains no competing sources of reduced sulfur. Solution depletion methods were attempted with PLFA and SRHA at the conditions used in the aggregation experiments (20 ppm NPs, 10 ppm PLFA or SRHA, and 100 mM NaCl in 1 mM $NaHCO_3$ at pH 8.3). However, the adsorbed mass was too low to be consistently determined across repeat measurements using this method (using UV-vis absorbance for concentration detection).

Finally, the possible influence of unmeasured properties must also be considered. Differences in layer conformation (e.g. segment density distribution) and homogeneity in surface coverage (e.g. patchiness of the adsorbed NOM) can affect the NP aggregation behavior. The adsorbed components from different sources of NOM may also differ in hydrophobicity or hydrophilicity. However, these properties will be difficult to measure on the coated NPs.

6.4.6 Quantitative correlation of aggregation rates with NOM properties

Quantitative overall correlations of NP aggregation behavior to various NOM properties are assessed here. The qualitative observations from previous sections in this chapter, as well as the correlations observed by others for bulk NOM samples,[24,30] informed the selection of parameters (NOM properties) for attempted correlations. These correlations were performed using aggregation data for 10 ppm of the various NOM types and fractions. Although data were

also collected for 1 ppm of NOM, most aggregation rates measured were near that of the uncoated NPs (likely under diffusion-limited aggregation conditions), so no correlation could be made at this concentration (Appendix B.3.8).

First, the correlation of NP aggregation rate to M_w or M_g of the NOM fractions is assessed (Figure 6.7). The M_g estimated from fitting the adjusted distribution (accounting for the portion of the sample too small to analyze by MALS) and that obtained directly from MALS, $M_{w,unadjusted}$ are compared (full discussion of these methods is provided in Appendix B.1.4). Deonarine et al.[24] and Nason[30] et al. previously found that the growth or aggregation of ZnS and citrate-stabilized gold NPs, respectively, generally correlated with the molecular weight for unfractionated NOM. As discussed previously, molecular weight can be expected to correlate with adsorbed mass and layer thickness, thereby imparting steric repulsion. Here, average molecular weights are plotted on a logarithmic scale (whereas Deonarine et al. used a linear scale in the number-average molecular weight, M_n[24]). No physicochemical mechanism supports either scaling; here, the logarithmic scale was found to better incorporate the high molecular weights (> 100 kg/mol) of the retentate fractions. A log-log model was also assessed (for which negative aggregation rates are precluded); however, lower coefficients of determination, R^2, were obtained (Appendix B.3.9). As expected from the qualitative analyses in Section 6.4.5, the aggregation rates tend to correlate well with either M_w or M_g for all samples except PLFA, which is a noticeable outlier (exclusion of PLFA results in a higher R^2).

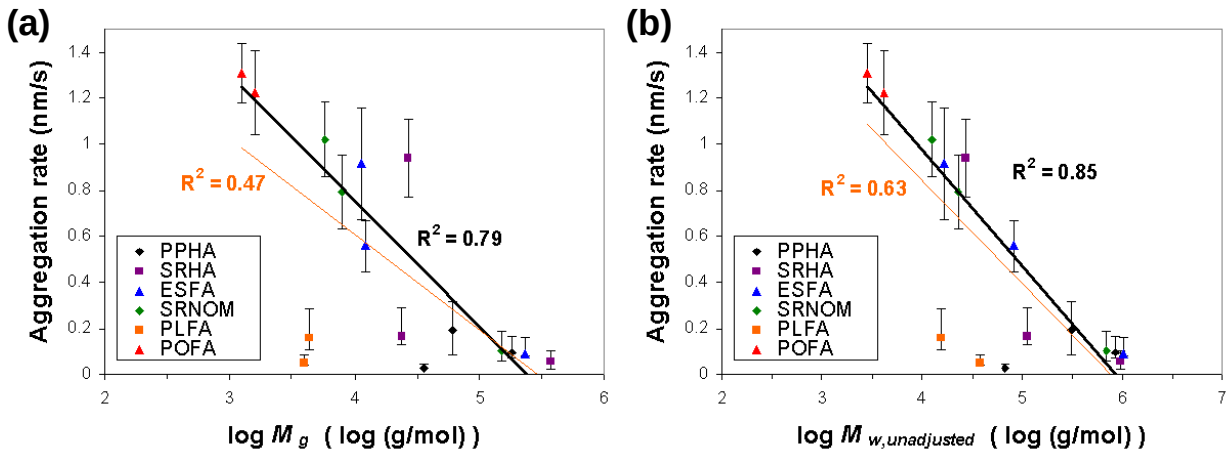

Figure 6.7. Correlation of aggregation rate with log molecular weight, determined from two methods: the geometric mean, M_g, for a fitted lognormal distribution of weight-averaged molecular weights (a), or $M_{w,unadjusted}$ directly measured by MALS (b). The differences between these methods are discussed in Appendix B.1.4 in detail; briefly, $M_{w,unadjusted}$ more strongly weights the high molecular weight tail of the size distribution. $M_{w,unadjusted}$ provides a better correlation, particularly in distinguishing the effects of whole and filtrate NOM on the aggregation rate. In either case, PLFA is an outlier: good correlation is observed when PLFA data are excluded (black line), where little NP aggregation was observed although the molecular weight of PLFA is low; poorer correlation is observed when PLFA data are included (orange line).

The comparison of correlations using the two molecular weight estimates (Figure 6.7(a) and (b)) demonstrates that the method of determining molecular weight can be important. Briefly, the fitted M_g accounts for the smallest 20 to 55 wt% of the NOM, but tends not to capture the high molecular weight tail of the distribution (i.e., > 100 kg/mol components); whereas $M_{w,unadjusted}$ does not include the low molecular weight components but weights more heavily toward the > 100 kg/mol NOM. $M_{w,unadjusted}$ provides better correlation with the aggregation rates measured here; particularly, it better captures differences in filtrate and whole fractions, e.g. in ESFA (blue triangles) and SRHA (purple squares). This result follows from the

qualitative conclusions from Sections 5.4.4 and 6.4.4, where the retentate fraction was shown to contribute significantly to the ability of the heterogeneous NOM to stabilize NPs against aggregation. It is noted that number-average molecular weights are typically reported elsewhere and tend to be more similar to M_g determined here; furthermore, the high molecular weight void peak can not be analyzed in other studies applying SEC when calibration standards are used[50] instead of MALS. Implications for the interpretation of experimental results and correlation across different studies are discussed in Chapter 7.

Next, the correlations between aggregation rates and properties of the UV-vis absorbance spectra of the NOM ($SUVA_{280}$ and the exponential slope coefficient) were assessed (Figure 6.8). ZnS NP stability in the presence of different types of NOM was previously shown to correlate well with both $SUVA_{280}$ and the mean molecular weight;[24] these properties typically co-vary. SUVA is easier to measure than molecular weight and would therefore be the more desirable parameter from a practical standpoint, if the two parameters predicted NP aggregation behavior equally well. In this study, $SUVA_{280}$ and M_w or M_g were correlated for the unfractionated NOM, but not necessarily among the fractions: the retentate for ESFA and PLFA had lower $SUVA_{280}$ than the corresponding filtrate or unfractionated NOM, but significantly higher molecular weight (Figure 6.4). The R^2 coefficient was poorer for the correlation with $SUVA_{280}$ ($R^2 = 0.39$, Figure 6.8(a)) than with M_w or M_g, indicating that molecular weight was a better explanatory variable than $SUVA_{280}$ for the samples assessed here. This result suggests that the mechanism for NP stabilization was driven more by molecular weight effects rather than chemical or hydrophobic interactions with aromatic groups on NOM (which correlates to SUVA).

Although $SUVA_{280}$ produced poorer correlation than M_w or M_f, the slope coefficient representing the shape of the UV-vis absorbance spectrum correlated significantly better with

molecular weight, and thus yielded a better correlation with aggregation rate than $SUVA_{280}$, with R^2 = 0.74 (Figure 6.8(b)). The slope coefficient requires no additional experimental effort to acquire compared to SUVA, and therefore would be feasible to include in future studies to parameterize correlations of NOM properties with NP aggregation or transport behavior. Another option is to use a ratio of two absorbances. Two ratios (A_{254}/A_{436} and A_{250}/A_{365}) were explored (Appendix B.3.10); the former gives similar goodness of fit as the slope coefficient, whereas the latter gives poorer goodness of fit. The use of the slope coefficient is recommended because it incorporates more data.

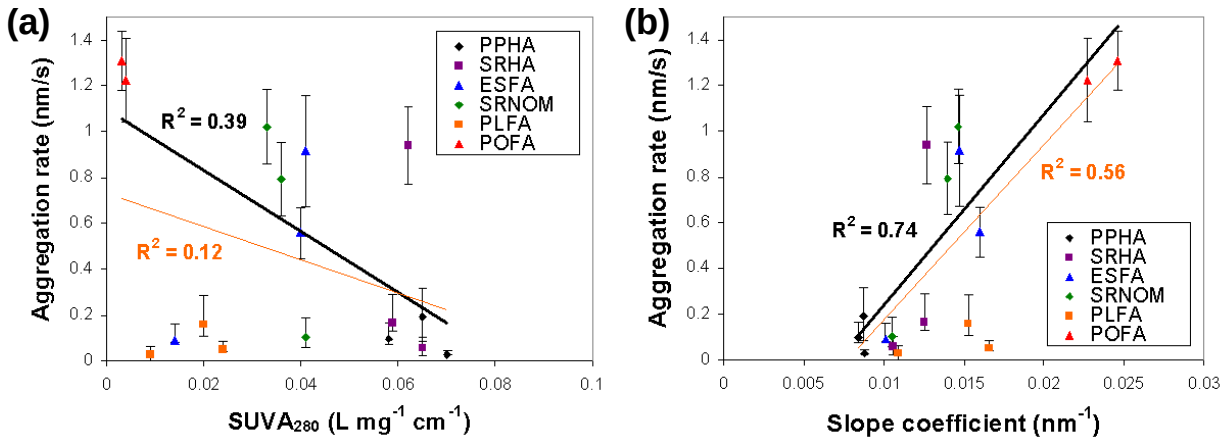

Figure 6.8. Correlation of aggregation rate with $SUVA_{280}$ (a) and the exponential slope coefficient (b) from UV-vis absorbance measurements on NOM. Correlations are shown either excluding or including the PLFA results (black or orange lines, respectively).

Correlations that include *reduced* sulfur (not total S) content in the NOM as an explanatory variable were assessed. Reduced sulfur content of the NOM was qualitatively identified as a possible factor contributing to the behavior of PLFA-coated gold NPs (Section 6.4.5). Figure 6.9(a) shows the correlation of aggregation rate with reduced sulfur content for the six unfractionated NOM samples (elemental compositions were not measured on the filtrate

or retentate fractions). Poor correlation (R^2 = 0.38) was observed, although the stabilizing effect of PLFA appears to be better represented. This relatively poor correlation is likely due to the lack of variance in S content between most of the NOM samples evaluated. Only PLFA contained a reduced sulfur content that was distinct from the other samples (Table 6.2).

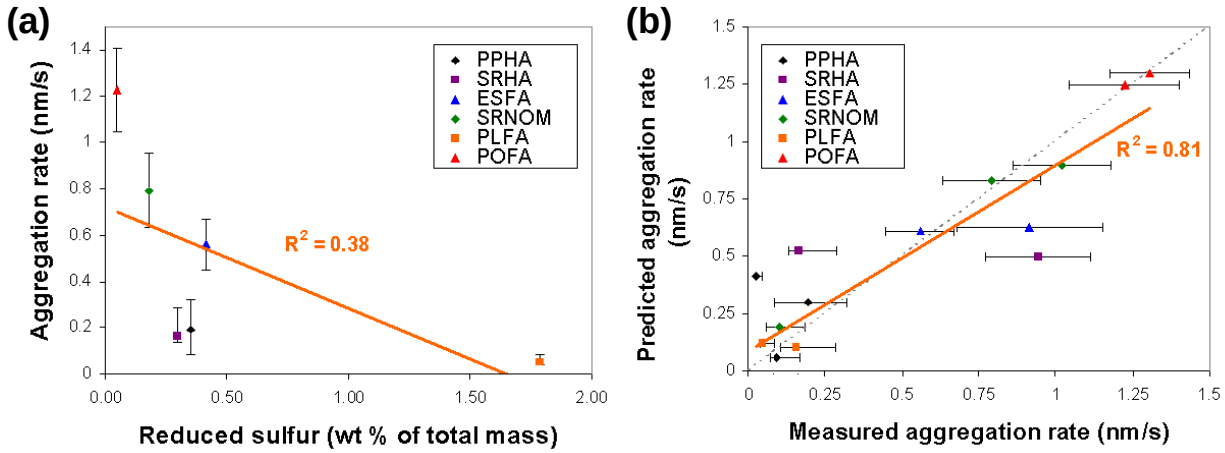

Figure 6.9. Correlation of aggregation rate with reduced sulfur content for the unfractionated NOM samples (a), and predicted versus measured aggregation rates for a two-parameter correlation including log(M_g) and the reduced sulfur content (b). The dotted line in (b) represents a perfect 1:1 correlation.

Finally, the suitability of a linear three-parameter model (Equation 6.1) to predict the initial aggregation rate, k_{agg}, from log(M_g) and the reduced sulfur content, x_S, was determined (where the three parameters are the coefficients, a and b, for log(M_g) and x_S, and the constant, c). The parameters were fitted to minimize the sum of squared errors between the predicted and measured aggregation rates, where ε is the error.

$$k_{agg,predicted} = a\log(M_g) + b(x_S) + c + \varepsilon \qquad (6.1)$$

The correlation for the fitted three-parameter model is shown in Figure 6.9(b) (with a = –0.50, b = –0.53, and c = 2.87; sum of squared errors = 0.64 $(nm/s)^2$). Filtrate and retentate fractions are included by assuming the same reduced sulfur content as reported for the unfractionated NOM (a reasonable assumption for the filtrate, but possibly erroneous for the retentate). It is emphasized that, as for the other correlations assessed, the form of the correlation has no mechanistic basis. Rather, it is used as a rough assessment of whether inclusion of sulfur content (in an arbitrary form) can improve the correlation. Improvement is indeed observed (R^2 = 0.81) compared to the single-parameter correlations with M_g and reduced sulfur content. Notably, the PLFA data no longer appear as outliers.

The two-parameter linear model with $\log(M_g)$ (fitting a slope and intercept, Figure 6.7) and the three-parameter model (Equation 6.1) were compared using Akaike Information Criteria (AIC) to assess the trade-off between the increased model complexity (i.e., number of parameters) and the improved goodness of fit. That is, the possibility for overfitting the model was assessed. The equation for AIC is provided in Appendix B.3.11. When the PLFA data are included, AIC is 14.3 and -0.1 for the two- and three-parameter models respectively, where the lower value indicates a better model. This result suggests that the improvement in the fit (including PLFA data) more than offsets the addition of a parameter. However, if the PLFA data are excluded, AIC is 0.6 and 2.3 for the two- and three-parameter models: inclusion of reduced sulfur content does not provide significant value for the other NOM samples.

We conclude that additional data on other NOM isolates is needed to support or refute the importance of reduced sulfur for gold NP aggregation. Furthermore, it is expected that reduced sulfur will only be relevant for metal NPs where strong binding to sulfur occurs (e.g., gold and

silver NPs), so this property may have limited importance for other NPs. Overall implications of these correlations are discussed in Chapter 7.

References for this chapter are listed at the end of Chapter 7.

Chapter 7. Summary of results, significance, and future needs for Chapters 5 and 6

7.1. New knowledge produced and significance

To our knowledge, this study provides the most detailed assessment of the effects of NOM on nanoparticle (NP) aggregation to date by combining three factors: the use of multiple sources of NOM, the systematic variation of molecular weight (by fractionation) within each NOM source, and the accompaniment of the effects study with extensive characterization of each NOM fraction and the NOM-coated NPs. By performing this assessment on a single controlled system (gold NPs consistently assessed in the same dispersion medium), the effect of the NOM properties could be probed more definitively and mechanistically than would be possible through a meta-analysis of data across different studies with widely varying NP and system properties.

New knowledge produced includes the observation that NP aggregation behavior is sensitive to the molecular weight distribution of NOM, particularly with respect to the presence of small amounts (e.g., < 6 wt%) of very high molecular weight (> 100 kg/mol) components. Furthermore, different molecular weight fractions were observed to interact in a polydisperse mixture; i.e., the unfractionated NOM provided better NP stability than its component fractions. Higher-level correlations identified molecular weight and the slope coefficient of the UV-vis absorbance spectrum as better predictors of aggregation rate than specific UV absorbance (or aromaticity). This distinction was not possible in a previous study[24] because these properties co-varied for bulk samples. The use of fractionated materials here allowed for the roles of molecular weight and specific UV absorbance to be better distinguished. We also suggest that the slope coefficient describing the shape of the UV-vis spectrum be reported and considered for

correlations, in addition to the absorbance at a single wavelength or absorbance ratios. This analysis requires no additional effort compared to measurement of absorbance and incorporates data from the entire UV-vis spectrum. The importance of measuring (and weighting toward) the highest molecular weight components was emphasized in both the qualitative analysis and the correlations. Implications are that weight-averaged (rather than number-averaged) molecular weights may better predict coated NP aggregation. Finally, the ability for other chemical factors (possibly reduced sulfur content) to affect NP stability was observed for PLFA, although the mechanism involved (e.g., higher adsorbed mass resulting in enhanced steric effects) could not be identified through the suite of characterization methods applied here.

The importance of the highest molecular weight components and the observation of synergistic effects in combined fractions of the NOM have several significant implications. These results suggest that NOM sample preparation processes that may be assumed to be trivial (e.g., filtration of an NOM sample, and the selection of a filtration size) can have significant effects on NP behavior. In the environmental nanotechnology research community, the importance of characterization and reporting of sample preparation for the NPs has often been discussed; here, we suggest that better characterization and reporting of NOM is also needed. More broadly, the results imply that the ability to quantitatively extrapolate the results of laboratory studies to real systems should not be assumed. Studies often begin with NOM samples that are already fractionated (e.g., via selective extraction of some NOM components onto an XAD resin, followed by further fractionation into a humic or fulvic acid sample). However, real systems will contain a mixture of humic and fulvic acids, as well as other components. The interactions of all of the components in this “supermixture” may not be adequately captured by experiments using pre-fractionated NOM. This point was strongly

emphasized by Filella in a review of general (i.e., not nanoparticle-specific) environmental studies using NOM[1] and is supported by the results of this study.

7.2 Future work

Future work is proposed that follows from the research presented in Chapters 7 and 8. First, limitations in the ability to generalize this work across a wider range of NPs and environmental systems can be addressed by varying the type of NP, pH, ionic strength, and presence of divalent cations. This research would build upon the results obtained for one specific system here (gold NPs in 100 mM NaCl at pH 8.3). The trend of enhanced stability against aggregation imparted by higher molecular weight NOM (compared to low molecular weight NOM) is expected to be consistent across different types of NPs because the higher affinity of high molecular weight macromolecules to adsorb to surfaces and the steric effect due to a thicker adsorbed layer are independent of the properties of the surface. However, different conformations of NOM adsorbed to different types (or sizes) of NPs may affect the magnitude of the steric effect.

For the dispersion medium, a lower pH and ionic strength (e.g., relevant to typical surface waters) can be investigated than the conditions used here. The effects of divalent cations can also be investigated. The pH will determine the extent of deprotonation of carboxylic acid and phenolic groups on the NOM, which will affect the electrostatic interaction forces between NPs. The ionic strength will control charge screening, which will also change the electrostatic interaction force. At lower ionic strengths, different molecular weight fractions of NOM may produce similar effects on NP aggregation if electrostatic effects become more important than steric effects. Charge screening can also affect the adsorbed mass, composition, and

conformation of the adsorbed layer, changing the steric (or electrosteric) forces. For negatively-charged NPs, lesser adsorption of negatively-charged NOM can be expected at lower ionic strength. However, the adsorbed NOM layer may swell at lower ionic strength due to increased electrostatic repulsion between charges within the NOM. Therefore, different behavior may be observed at lower ionic strength. Other, similar studies have used lower, but still high, ionic strengths (e.g., 50 mM $NaNO_3$ with 4 mM HEPES buffer at pH 7,[24] or 80 mM KCl at pH 5 to 6.[30] It is possible that similarly good NP stability will be observed with any NOM type at lower ionic strength conditions. This result would be useful to simplify data requirements for environmental transport models if electrophoretic mobility of the coated NPs (rather than molecular weight or adsorbed layer conformation) is a sufficient measurement. Finally, divalent cations can significantly change aggregation behavior. Aside from the electrostatic effect (i.e., charge screening following the Schulze-Hardy rule), some divalent cations, particularly Ca^{2+}, can cause bridging between carboxylate groups on NOM or biomacromolecules such as alginate. Enhanced aggregation of NOM-coated NPs due to this effect has been reported previously.[84,85] The chemistry of the NOM (and hence type of NOM) can be expected to affect the extent of the calcium bridging effect.

Additional work is proposed to extend the results of this study. In particular, the concept of heterogeneous mixtures producing better stability than their component fractions will be useful to investigate, particularly in consideration of the heterogeneity present in realistic natural systems. Increased polydispersity of synthetic polymers has been shown to improve NP stability.[73] For protein stabilization of ENMs, two- or three-component mixtures of proteins from fetal bovine serum (FBS) provided better stability than any single protein alone.[86] The co-sorption of three components was required in order to obtain similar stability to the complete

FBS mixture. It is currently unknown (and rarely considered) how many and what types of components of NOM will be needed to adequately represent the effects of the complete "supermixture" of NOM. This knowledge would be useful to inform the design of future studies investigating NOM interactions with NPs or colloids.

Finally, the existence (or lack thereof) of a "nano"-specific effect can be explored. As discussed in Chapter 2, the adsorption of macromolecules and the conformation of the adsorbed layer is expected to differ for large colloids or flat surfaces compared to particles with high surface curvature (i.e. with nanometer-scale radius, comparable or smaller than that of the adsorbing macromolecule). Theories and experimental data have been demonstrated that surface curvature affects the adsorption and conformation of linear homopolymers and brushes.[87-91] The effect of NP size on the unfolding of adsorbing proteins of different shapes (e.g. globular and fibrillar) has also been shown.[92-94] Similar experiments can be performed comparing the adsorption and conformation of NOM on different sizes of NPs, but these experiments will be more difficult than for synthetic polymers (with well-controlled structure and chemistry) or proteins (where techniques sensitive to conformation, such as circular dichroism, are available). Advanced methods such as NMR and Raman spectroscopy may be useful for NOM.[95,96] However, the results of this study generally agree with expectations from basic colloid and macromolecule theories (i.e. preferential adsorption of high molecular weight components, and better NP stability imparted by high molecular weight NOM, consistent with steric mechanisms). It is unknown whether knowledge of possible changes in NOM adsorption or conformation with particle size will be necessary to significantly improve our ability to explain NP behavior (e.g. attachment efficiency) in the environment.

References for Part II (Chapters 5, 6, and 7)

(1) Filella, M. Freshwaters: which NOM matters? *Environ. Chem. Lett.* **2009**, *7* (1), 21-35.
(2) Ju-Nam, Y.; Lead, J. R. Manufactured nanoparticles: An overview of their chemistry, interactions and potential environmental implications. *Sci. Total Environ.* **2008**, *400* (1-3), 396-414.
(3) MacCarthy, P.; Ghabbour, E. A.; Davies, G. The principles of humic substances: An introduction to the first principle. In *Humic substances: Structures, models and functions*; The Royal Society of Chemistry, **2001**; pp 19-30.
(4) Piccolo, A. The supramolecular structure of humic substances. *Soil Sci.* **2001**, *166* (11), 810-832.
(5) Kelleher, B. P.; Simpson, A. J. Humic substances in soils: Are they really chemically distinct? *Environ. Sci. Technol.* **2006**, *40* (15), 4605-4611.
(6) Simpson, A. J.; Kingery, W. L.; Hayes, M. H. B.; Spraul, M.; Humpfer, E.; Dvortsak, P.; Kerssebaum, R.; Godejohann, M.; Hofmann, M. Molecular structures and associations of humic substances in the terrestrial environment. *Naturwissenschaften* **2002**, *89* (2), 84-88.
(7) Avena, M. J.; Wilkinson, K. J. Disaggregation kinetics of a peat humic acid: Mechanism and pH effects. *Environ. Sci. Technol.* **2002**, *36* (23), 5100-5105.
(8) Jones, M. N.; Bryan, N. D. Colloidal properties of humic substances. *Adv. Colloid Interface Sci.* **1998**, *78* (1), 1-48.
(9) Baalousha, M.; Motelica-Heino, M.; Le Coustumer, P. Conformation and size of humic substances: Effects of major cation concentration and type, pH, salinity, and residence time. *Colloids Surf., A* **2006**, *272* (1-2), 48-55.
(10) Senesi, N.; Rizzi, F. R.; Dellino, P.; Acquafredda, P. Fractal dimension of humic acids in aqueous suspension as a function of pH and time. *Soil Sci. Soc. Am. J.* **1996**, *60* (6), 1773-1780.
(11) Diallo, M. S.; Glinka, C. J.; Goddard, W. A.; Johnson, J. H. Characterization of nanoparticles and colloids in aquatic systems 1. Small angle neutron scattering investigations of Suwannee River fulvic acid aggregates in aqueous solutions. *J. Nanopart. Res.* **2005**, *7* (4-5), 435-448.
(12) Oren, A.; Chefetz, B. Sorptive and desorptive fractionation of dissolved organic matter by mineral soil matrices. *J. Environ. Qual.* **2012**, *41* (2), 526-533.
(13) Hur, J.; Schlautman, M. A. Molecular weight fractionation of humic substances by adsorption onto minerals. *J. Colloid Interface Sci.* **2003**, *264* (2), 313-321.
(14) Zhou, Q. H.; Maurice, P. A.; Cabaniss, S. E. Size fractionation upon adsorption of fulvic acid on goethite: Equilibrium and kinetic studies. *Geochim. Cosmochim. Acta* **2001**, *65* (5), 803-812.
(15) Schmitt, D.; Muller, M. B.; Frimmel, F. H. Metal distribution in different size fractions of natural organic matter. *Acta Hydroch. Hydrob.* **2001**, *28* (7), 400-410.
(16) Chefetz, B.; Xing, B. S. Relative role of aliphatic and aromatic moieties as sorption domains for organic compounds: A review. *Environ. Sci. Technol.* **2009**, *43* (6), 1680-1688.
(17) Zhang, H. F.; Zhang, Y. H.; Shi, Q.; Hu, J. Y.; Chu, M. Q.; Yu, J. W.; Yang, M. Study on transformation of natural organic matter in source water during chlorination and its chlorinated products using ultrahigh resolution mass spectrometry. *Environ. Sci. Technol.* **2012**, *46* (8), 4396-4402.

(18) Cai, Z. X.; Benjamin, M. M. NOM fractionation and fouling of low-pressure membranes in microgranular adsorptive filtration. *Environ. Sci. Technol.* **2011**, *45* (20), 8935-8940.
(19) Fritz, G.; Schadler, V.; Willenbacher, N.; Wagner, N. J. Electrosteric stabilization of colloidal dispersions. *Langmuir* **2002**, *18* (16), 6381-6390.
(20) Einarson, M. B.; Berg, J. C. Electrosteric stabilization of colloidal latex dispersions. *J. Colloid Interface Sci.* **1993**, *155* (1), 165-172.
(21) Phenrat, T.; Song, J. E.; Cisneros, C. M.; Schoenfelder, D. P.; Tilton, R. D.; Lowry, G. V. Estimating Attachment of Nano- and Submicrometer-particles Coated with Organic Macromolecules in Porous Media: Development of an Empirical Model. *Environ. Sci. Technol.* **2010**, *44* (12), 4531-4538.
(22) Aiken, G. R.; Hsu-Kim, H.; Ryan, J. N. Influence of Dissolved Organic Matter on the Environmental Fate of Metals, Nanoparticles, and Colloids. *Environ. Sci. Technol.* **2011**, *45* (8), 3196-3201.
(23) Christian, P.; Von der Kammer, F.; Baalousha, M.; Hofmann, T. Nanoparticles: structure, properties, preparation and behaviour in environmental media. *Ecotoxicology* **2008**, *17* (5), 326-343.
(24) Deonarine, A.; Lau, B. L. T.; Aiken, G. R.; Ryan, J. N.; Hsu-Kim, H. Effects of humic substances on precipitation and aggregation of zinc sulfide nanoparticles. *Environ. Sci. Technol.* **2011**, *45* (8), 3217-3223.
(25) Illes, E.; Tombacz, E. The effect of humic acid adsorption on pH-dependent surface charging and aggregation of magnetite nanoparticles. *J. Colloid Interface Sci.* **2006**, *295* (1), 115-123.
(26) Bian, S. W.; Mudunkotuwa, I. A.; Rupasinghe, T.; Grassian, V. H. Aggregation and Dissolution of 4 nm ZnO Nanoparticles in Aqueous Environments: Influence of pH, Ionic Strength, Size, and Adsorption of Humic Acid. *Langmuir* **2011**, *27* (10), 6059-6068.
(27) Liu, X. Y.; Wazne, M.; Chou, T. M.; Xiao, R.; Xu, S. Y. Influence of Ca2+ and Suwannee River Humic Acid on aggregation of silicon nanoparticles in aqueous media. *Water Res.* **2011**, *45* (1), 105-112.
(28) Chen, K. L.; Elimelech, M. Influence of humic acid on the aggregation kinetics of fullerene (C-60) nanoparticles in monovalent and divalent electrolyte solutions. *J. Colloid Interface Sci.* **2007**, *309* (1), 126-134.
(29) Tiller, C. L.; Omelia, C. R. Natural Organic-Matter and Colloidal Stability - Models and Measurements. *Colloids Surf., A* **1993**, *73*, 89-102.
(30) Nason, J. A.; McDowell, S. A.; Callahan, T. W. Effects of natural organic matter type and concentration on the aggregation of citrate-stabilized gold nanoparticles. *J. Environ. Monit.* **2012**, *14* (7), 1885-1892.
(31) King, S. M.; Jarvie, H. P. Exploring How Organic Matter Controls Structural Transformations in Natural Aquatic Nanocolloidal Dispersions. *Environ. Sci. Technol.* **2012**, *46* (13), 6959-6967.
(32) Jarvie, H. P.; King, S. M. Small-angle neutron scattering study of natural aquatic nanocolloids. *Environ. Sci. Technol.* **2007**, *41* (8), 2868-2873.
(33) Buffle, J.; Wilkinson, K. J.; Stoll, S.; Filella, M.; Zhang, J. W. A generalized description of aquatic colloidal interactions: The three-colloidal component approach. *Environ. Sci. Technol.* **1998**, *32* (19), 2887-2899.
(34) Wilkinson, K. J.; Negre, J. C.; Buffle, J. Coagulation of colloidal material in surface waters: The role of natural organic matter. *J. Contam. Hydrol.* **1997**, *26* (1-4), 229-243.

(35) Wilkinson, K. J.; Joz-Roland, A.; Buffle, J. Different roles of pedogenic fulvic acids and aquagenic biopolymers on colloid aggregation and stability in freshwaters. *Limnol. Oceanogr.* **1997**, *42* (8), 1714-1724.
(36) Lead, J. R.; Wilkinson, K. J. Aquatic colloids and nanoparticles: Current knowledge and future trends. *Environ. Chem.* **2006**, *3* (3), 159-171.
(37) Ghosh, S.; Mashayekhi, H.; Pan, B.; Bhowmik, P.; Xing, B. S. Colloidal Behavior of Aluminum Oxide Nanoparticles As Affected by pH and Natural Organic Matter. *Langmuir* **2008**, *24* (21), 12385-12391.
(38) Liu, X. Y.; Chen, G. X.; Su, C. M. Influence of Collector Surface Composition and Water Chemistry on the Deposition of Cerium Dioxide Nanoparticles: QCM-D and Column Experiment Approaches. *Environ. Sci. Technol.* **2012**, *46* (12), 6681-6688.
(39) Jones, E. H.; Su, C. M. Fate and transport of elemental copper (Cu-0) nanoparticles through saturated porous media in the presence of organic materials. *Water Res.* **2012**, *46* (7), 2445-2456.
(40) Davis, J. A.; Gloor, R. Adsorption of Dissolved Organics in Lake Water by Aluminum-Oxide - Effect of Molecular-Weight. *Environ. Sci. Technol.* **1981**, *15* (10), 1223-1229.
(41) Gu, B. H.; Schmitt, J.; Chen, Z.; Liang, L. Y.; Mccarthy, J. F. Adsorption and Desorption of Different Organic-Matter Fractions on Iron-Oxide. *Geochim. Cosmochim. Acta* **1995**, *59* (2), 219-229.
(42) Hyung, H.; Kim, J. H. Natural organic matter (NOM) adsorption to multi-walled carbon nanotubes: Effect of NOM characteristics and water quality parameters. *Environ. Sci. Technol.* **2008**, *42* (12), 4416-4421.
(43) Vermeer, A. W. P.; Koopal, L. K. Adsorption of humic acids to mineral particles. 2. Polydispersity effects with polyelectrolyte adsorption. *Langmuir* **1998**, *14* (15), 4210-4216.
(44) Wang, X. L.; Shu, L.; Wang, Y. Q.; Xu, B. B.; Bai, Y. C.; Tao, S.; Xing, B. S. Sorption of Peat Humic Acids to Multi-Walled Carbon Nanotubes. *Environ. Sci. Technol.* **2011**, *45* (21), 9276-9283.
(45) Illes, E.; Tombacz, E. The role of variable surface charge and surface complexation in the adsorption of humic acid on magnetite. *Colloids Surf., A* **2003**, *230* (1-3), 99-109.
(46) Amirbahman, A.; Olson, T. M. Transport of Humic Matter-Coated Hematite in Packed-Beds. *Environ. Sci. Technol.* **1993**, *27* (13), 2807-2813.
(47) Turkevich, J.; Stevenson, P. C.; Hillier, J. A Study of the Nucleation and Growth Processes in the Synthesis of Colloidal Gold. *Discuss. Faraday Soc.* **1951**, (11), 55-&.
(48) Frens, G. Particle-Size and Sol Stability in Metal Colloids. *Kolloid Z. Z. Polym.* **1972**, *250* (7), 736-&.
(49) Egeberg, P. K.; Christy, A. A.; Eikenes, M. The molecular size of natural organic matter (NOM) determined by diffusivimetry and seven other methods. *Water Res.* **2002**, *36* (4), 925-932.
(50) Chin, Y. P.; Aiken, G.; Oloughlin, E. Molecular-weight, polydispersity, and spectroscopic properties of aquatic humic substances. *Environ. Sci. Technol.* **1994**, *28* (11), 1853-1858.
(51) Song, J. Z.; Huang, W. L.; Peng, P. A.; Xiao, B. H.; Ma, Y. J. Humic Acid Molecular Weight Estimation by High-Performance Size-Exclusion Chromatography with Ultraviolet Absorbance Detection and Refractive Index Detection. *Soil Sci. Soc. Am. J.* **2010**, *74* (6), 2013-2020.

(52) Westerhoff, P.; Chen, W.; Esparza, M. Fluorescence analysis of a standard fulvic acid and tertiary treated wastewater. *J. Environ. Qual.* **2001**, *30* (6), 2037-2046.
(53) Abbt-Braun, G.; Lankes, U.; Frimmel, F. H. Structural characterization of aquatic humic substances - The need for a multiple method approach. *Aquat. Sci.* **2004**, *66* (2), 151-170.
(54) Traina, S. J.; Novak, J.; Smeck, N. E. An ultraviolet absorbance method of estimating the percent aromatic carbon content of humic acids. *J. Environ. Qual.* **1990**, *19* (1), 151-153.
(55) Matilainen, A.; Gjessing, E. T.; Lahtinen, T.; Hed, L.; Bhatnagar, A.; Sillanpaa, M. An overview of the methods used in the characterisation of natural organic matter (NOM) in relation to drinking water treatment. *Chemosphere* **2011**, *83* (11), 1431-1442.
(56) Korshin, G. V.; Li, C. W.; Benjamin, M. M. Monitoring the properties of natural organic matter through UV spectroscopy: A consistent theory. *Water Res.* **1997**, *31* (7), 1787-1795.
(57) Bricaud, A.; Morel, A.; Prieur, L. Absorption by dissolved organic-matter of the sea (yellow substance) in the UV and visible domains. *Limnol. Oceanogr.* **1981**, *26* (1), 43-53.
(58) Carder, K. L.; Steward, R. G.; Harvey, G. R.; Ortner, P. B. Marine Humic and Fulvic-Acids - Their Effects on Remote-Sensing of Ocean Chlorophyll. *Limnol. Oceanogr.* **1989**, *34* (1), 68-81.
(59) Wagoner, D. B.; Christman, R. F.; Cauchon, G.; Paulson, R. Molar mass and size of Suwannee River natural organic matter using multi-angle laser light scattering. *Environ. Sci. Technol.* **1997**, *31* (3), 937-941.
(60) Montoneri, E.; Boffa, V.; Quagliotto, P.; Mendichi, R.; Chierotti, M. R.; Gobetto, R.; Medana, C. Humic Acid-Like Matter Isolated from Green Urban Wastes. Part I: Structure and Surfactant Properties. *Bioresources* **2008**, *3* (1), 123-141.
(61) Baalousha, M.; Motelica-Heino, M.; Galaup, S.; Le Coustumer, P. Supramolecular structure of humic acids by TEM with improved sample preparation and staining. *Microsc. Res. Tech.* **2005**, *66* (6), 299-306.
(62) Balnois, E.; Wilkinson, K. J. Sample preparation techniques for the observation of environmental biopolymers by atomic force microscopy. *Colloids Surf., A* **2002**, *207* (1-3), 229-242.
(63) Sutzkover-Gutman, I.; Hasson, D.; Semiat, R. Humic substances fouling in ultrafiltration processes. *Desalination* **2010**, *261* (3), 218-231.
(64) Hudson, N.; Baker, A.; Reynolds, D. Fluorescence analysis of dissolved organic matter in natural, waste and polluted waters - A review. *River Res. Appl.* **2007**, *23* (6), 631-649.
(65) Baker, A.; Elliott, S.; Lead, J. R. Effects of filtration and pH perturbation on freshwater organic matter fluorescence. *Chemosphere* **2007**, *67* (10), 2035-2043.
(66) Sutton, R.; Sposito, G. Molecular structure in soil humic substances: The new view. *Environ. Sci. Technol.* **2005**, *39* (23), 9009-9015.
(67) Matthews, B. J. H.; Jones, A. C.; Theodorou, N. K.; Tudhope, A. W. Excitation-emission-matrix fluorescence spectroscopy applied to humic acid bands in coral reefs. *Mar. Chem.* **1996**, *55* (3-4), 317-332.
(68) Johnstone, D. W.; Miller, C. M. Fluorescence Excitation-Emission Matrix Regional Transformation and Chlorine Consumption to Predict Trihalomethane and Haloacetic Acid Formation. *Environ. Eng. Sci.* **2009**, *26* (7), 1163-1170.
(69) Blough, N. V.; Del Vecchio, R. Chromophoric DOM in the coastal environment. In *Biogeochemistry of marine dissolved organic matter*; Hansell, D. A., Carlson, C. A., Eds.; Academic Press: Amsterdam, **2003**.

(70) Helms, J. R.; Stubbins, A.; Ritchie, J. D.; Minor, E. C.; Kieber, D. J.; Mopper, K. Absorption spectral slopes and slope ratios as indicators of molecular weight, source, and photobleaching of chromophoric dissolved organic matter. *Limnol. Oceanogr.* **2008**, *53* (3), 955-969.
(71) Wilkinson, K. J.; Balnois, E.; Leppard, G. G.; Buffle, J. Characteristic features of the major components of freshwater colloidal organic matter revealed by transmission electron and atomic force microscopy. *Colloids Surf., A* **1999**, *155* (2-3), 287-310.
(72) Dominguez-Medina, S.; Blankenburg, J.; Olson, J.; Landes, C. F.; Link, S. Adsorption of a protein monolayer via hydrophobic interactions prevents nanoparticle aggregation under harsh environmental conditions. *ACS Sustainable Chem. Eng.* **2013**, *1* (7), 833-842.
(73) Golas, P. L.; Louie, S.; Lowry, G. V.; Matyjaszewski, K.; Tilton, R. D. Comparative Study of Polymeric Stabilizers for Magnetite Nanoparticles Using ATRP. *Langmuir* **2010**, *26* (22), 16890-16900.
(74) Roefs, S. P. F. M.; Scheutjens, J. M. H. M.; Leermakers, F. A. M. Adsorption Theory for Polydisperse Polymers. *Macromolecules* **1994**, *27* (17), 4810-4816.
(75) Thurman, E. M. *Organic geochemistry of natural waters*; Martinus Nijhoff/Dr W. Junk Publishsers: Dordrecht, **1985**.
(76) Thurman, E. M.; Malcolm, R. L. Preparative isolation of aquatic humic substances. *Environ. Sci. Technol.* **1981**, *15* (4), 463-466.
(77) IHSS. Source materials for IHSS samples. **2013**, http://www.humicsubstances.org/sources.html.
(78) Waples, J. S.; Nagy, K. L.; Aiken, G. R.; Ryan, J. N. Dissolution of cinnabar (HgS) in the presence of natural organic matter. *Geochim. Cosmochim. Acta* **2005**, *69* (6), 1575-1588.
(79) Khwaja, A. R.; Bloom, P. R.; Brezonik, P. L. Binding constants of divalent mercury (Hg2+) in soil humic acids and soil organic matter. *Environ. Sci. Technol.* **2006**, *40* (3), 844-849.
(80) Xia, K.; Weesner, F.; Bleam, W. F.; Bloom, P. R.; Skyllberg, U. L.; Helmke, P. A. XANES studies of oxidation states of sulfur in aquatic and soil humic substances. *Soil Sci. Soc. Am. J.* **1998**, *62* (5), 1240-1246.
(81) Karlsson, T.; Persson, P.; Skyllberg, U. Extended X-ray absorption fine structure spectroscopy evidence for the complexation of cadmium by reduced sulfur groups in natural organic matter. *Environ. Sci. Technol.* **2005**, *39* (9), 3048-3055.
(82) Manceau, A.; Nagy, K. L. Quantitative analysis of sulfur functional groups in natural organic matter by XANES spectroscopy. *Geochim. Cosmochim. Acta* **2012**, *99*, 206-223.
(83) Fimmen, R. L.; Cory, R. M.; Chin, Y. P.; Trouts, T. D.; McKnight, D. M. Probing the oxidation-reduction properties of terrestrially and microbially derived dissolved organic matter. *Geochim. Cosmochim. Acta* **2007**, *71* (12), 3003-3015.
(84) Stankus, D. P.; Lohse, S. E.; Hutchison, J. E.; Nason, J. A. Interactions between Natural Organic Matter and Gold Nanoparticles Stabilized with Different Organic Capping Agents. *Environmental Science & Technology* **2011**, *45* (8), 3238-3244.
(85) Liu, J. F.; Legros, S.; Von der Kammer, F.; Hofmann, T. Natural organic matter concentration and hydrochemistry influence aggregation kinetics of functionalized engineered nanoparticles. *Environ. Sci. Technol.* **2013**, *47* (9), 4113-4120.
(86) Ji, Z. X.; Jin, X.; George, S.; Xia, T. A.; Meng, H. A.; Wang, X.; Suarez, E.; Zhang, H. Y.; Hoek, E. M. V.; Godwin, H.; Nel, A. E.; Zink, J. I. Dispersion and stability optimization of TiO_2 nanoparticles in cell culture media. *Environ. Sci. Technol.* **2010**, *44* (19), 7309-7314.

(87) Aubouy, M.; Raphael, E. Scaling description of a colloidal particle clothed with polymers. *Macromolecules* **1998**, *31* (13), 4357-4363.
(88) Baker, J. A.; Berg, J. C. Investigation of the adsorption configuration of poly(ethylene oxide) and its copolymers with poly(propylene oxide) on model polystyrene latex dispersions. *Langmuir* **1988**, *4* (4), 1055-1061.
(89) Biver, C.; Hariharan, R.; Mays, J.; Russel, W. B. Neutral and charged polymer brushes: A model unifying curvature effects from micelles to flat surfaces. *Macromolecules* **1997**, *30* (6), 1787-1792.
(90) Daoud, M.; Cotton, J. P. Star shaped polymers - A model for the conformation and its concentration dependence. *J. Phys.* **1982**, *43* (3), 531-538.
(91) Garvey, M. J.; Tadros, T. F.; Vincent, B. Comparison of adsorbed layer thickness obtained by several techniques of various molecular weight fractions of poly(vinyl alcohol) on aqueous polystyrene latex particles. *J. Colloid Interface Sci.* **1976**, *55* (2), 440-453.
(92) Lundqvist, M.; Sethson, I.; Jonsson, B. H. Protein adsorption onto silica nanoparticles: Conformational changes depend on the particles' curvature and the protein stability. *Langmuir* **2004**, *20* (24), 10639-10647.
(93) Roach, P.; Farrar, D.; Perry, C. C. Surface tailoring for controlled protein adsorption: Effect of topography at the nanometer scale and chemistry. *J. Am. Chem. Soc.* **2006**, *128* (12), 3939-3945.
(94) Vertegel, A. A.; Siegel, R. W.; Dordick, J. S. Silica nanoparticle size influences the structure and enzymatic activity of adsorbed lysozyme. *Langmuir* **2004**, *20* (16), 6800-6807.
(95) Lau, B. L. T.; Hockaday, W. C.; Ikuma, K.; Furman, O.; Decho, A. W. A preliminary assessment of the interactions between the capping agents of silver nanoparticles and environmental organics. *Colloids Surf., A* **2013**, *435*, 22-27.
(96) Corrado, G.; Sanchez-Cortes, S.; Francioso, O.; Garcia-Ramos, J. V. Surface-enhanced Raman and fluorescence joint analysis of soil humic acids. *Anal. Chim. Acta* **2008**, *616* (1), 69-77.

Chapter 8. Summary of novel contributions and perspectives for future research

8.1 Summary of novel contributions

This dissertation has produced several contributions to improve our understanding of the fate and transport behavior of engineered nanoparticles. This knowledge will be useful to predict the distribution of these novel materials in the environment and to assess the risk of exposure of biological or ecological entities of interest. Novel contributions of this work from the two parts of this dissertation are summarized here.

8.1.1 Part I: Characterization of adsorbed layers on nanoparticles by soft particle electrokinetic modeling

1. Determined that parameter identifiability problems in soft particle electrokinetic modeling approaches limits the range of systems for which adsorbed layer properties can be estimated with good confidence. Since the development of soft particle electrokinetic models by Ohshima in 1995, various studies across the fields of colloid science, microbiology, and environmental engineering have applied electrokinetic modeling approaches to estimate adsorbed layer properties, including layer thickness, charge density, permeability, and homogeneity. Often, this approach is applied without a good understanding of the statistical limitations of this method. This dissertation presented a thorough assessment of parameter identifiability for both analytical and numerical solutions of the soft particle electrokinetic model and demonstrated that significant limitations in parameter identifiability exist. This result highlights the need for

uncertainty assessment when applying this method, which will improve the quality of future studies that employ these models. Importantly, it suggests that the characteristics of adsorbed natural organic matter may be determined with this method in many cases because the conditions favorable for its application occur with adsorbed organic matter.

2. Identified trends in parameter identifiability across a range of particle and adsorbed layer properties, and systematic biases likely to affect parameter estimates. By assessing a wide range of modeled particle charges and adsorbed layer properties, electrokinetic models were determined to be most useful to estimate layer thicknesses on more highly charged particles with thin, low-charge adsorbed layers. Trends in the identifiability of charge density and adsorbed layer permeability were also identified. The identifiability analysis also demonstrated that layer thicknesses were likely to be overestimated, particularly when using the analytical model. These findings will guide researchers in determining the appropriateness of this method to assess their systems of interest.

3. Identified simple parameters that can represent confidence in fitted parameters. Rigorous statistical analysis (i.e., by likelihood plots) can be daunting and unwieldy for typical users of the soft particle electrokinetic model. Here, easily computed sensitivity and collinearity parameters were determined to represent parameter identifiability well (albeit not perfectly). These analyses were demonstrated in this dissertation for experimental systems (in publications by Louie et al.[1] and Hotze et al.[2]) and can be feasible for researchers to apply in the future.

4. Determined scenarios where parameter reduction in the model will and will not be useful. The analysis of likelihood plots in this dissertation clearly identified cases where parameter reduction will provide significant improvement in the confidence in the fitted parameter of interest. However, it also demonstrated that parameter reduction cannot be assumed to solve all parameter identifiability problems. For example, layer thickness is always non-identifiable for some types of adsorbed layers, regardless of whether all other parameters of the model are known. This analysis will guide researchers in deciding the value of combining soft particle electrokinetic modeling with other methods to characterize adsorbed layers.

5. Demonstrated how limitations in characterization can hamper our understanding of the transport behavior of coated nanoparticles. Hotze et al. tested the hypothesis that adsorbed coatings could control the transport behavior of nanoparticles (i.e., cause different nanoparticles to exhibit the same transport behavior) on a seemingly straightforward system in which three types of nanoparticles were coated with the same macromolecules. However, the observed transport behavior was complex, and no apparent correlation was observed with measured properties of the coated particles (including layer thicknesses estimated from electrokinetic modeling). Part of the problem was attributed to the poor confidence in the layer thickness estimates for the coated particles used in this study, further emphasizing the need for statistical analysis when applying this method. More broadly, the results show that additional or improved characterization methods in general will be required to predict nanoparticle transport behavior. These needs are discussed in Section 8.2.

8.1.2 Part II: Properties of heterogeneous natural organic matter that control nanoparticle aggregation behavior

1. Distinguished the importance of the highest molecular weight components of NOM in steric stabilization of gold nanoparticles. The > 100,000 g/mol fraction of NOM was demonstrated to provide significantly better stability of gold nanoparticles than the smaller components of NOM. Characterization of the aromaticity of the fractions and the electrophoretic mobility of the nanoparticles coated with the different fractions suggested that molecular weight was the dominant factor in the stabilization, and that steric (rather than electrostatic) effects were likely responsible for the behavior. Furthermore, the presence or absence of small quantities of this high molecular weight material (e.g. 1 to 6 wt % of the total organic matter present) was shown to significantly affect nanoparticle aggregation behavior. These results emphasized the importance of characterizing the molecular weight distribution of NOM (rather than simply average molecular weights) to fully explain nanoparticle fate and transport in natural environments.

2. Observed evidence for interactions of different molecular weight components of NOM in the full mixture of NOM. Comparison of gold nanoparticle aggregation behavior in the unfractionated NOM versus its separated, constituent molecular weight fractions indicated that neither the filtrate or retentate fractions alone could replicate the effects of the mixture. That is, some interaction of the components occurs to impart better nanoparticle stability. This work implies that the use of pre-fractionated samples typically used in laboratories to represent NOM

may need to be questioned before extrapolation of results to real environments that contain complicated "supermixtures" of NOM.

3. Distinguished molecular weight and the exponential slope coefficient of the UV-vis spectrum of NOM as better explanatory parameters than specific UV absorbance (SUVA). A previous study found that average molecular weight and SUVA both showed good correlation with nanoparticle aggregation behavior in the presence of bulk (unfractionated) NOM.[3] In this study, the use of fractionated samples (where molecular weight and SUVA do not always co-vary) allowed for the novel finding that nanoparticle aggregation rates correlate better with molecular weight than SUVA across the samples tested here. These results suggest that molecular weight effects are dominant in producing the stabilizing effect of NOM (e.g., due to enhanced adsorption or thicker adsorbed layers, resulting in steric stabilization), whereas interactions with hydrophobic, aromatic functional groups play a less important role. Another novel finding was that the slope coefficient of the UV-vis spectrum correlated better with nanoparticle aggregation than absorbance at a single wavelength and thus may be a useful parameter to assess in future correlations.

4. Identified molecular weight as the best explanatory parameter for the effects of NOM on gold nanoparticle aggregation, while identifying the importance of other parameters as well. Overall, the aggregation rate of the citrate-stabilized gold nanoparticles and various properties of NOM correlated best with the weight-averaged molecular weight of the NOM. Furthermore, weighting of the average toward the highest molecular weight portion of the NOM was needed to distinguishing the differing effects of the unfractionated NOM and the < 100 kg/mol fraction on

nanoparticle aggregation. However, one NOM type (Pony Lake fulvic acid) did not follow this trend. The behavior was postulated to result from enhanced adsorption of this sample to the gold nanoparticles due to the high reduced sulfur content of this sample, while other properties (charge, aromaticity, and aliphatic content) could be discounted. Direct measurements of adsorbed mass or further assessment of other NOM samples with high reduced sulfur content are needed to test this hypothesis. These results support previous correlations determined for bulk NOM samples,[3,4] while highlighting the role of the highest molecular weight fraction and identifying potential parameters (e.g., sulfur content) that could improve future correlations. These results are also consistent with expectations from basic colloid and polymer science; no nano-specific effects could be distinguished for the system assessed in this thesis.

8.2 Perspectives for future research

The research presented in this dissertation informs broader perspectives on future research needs. These needs include improved characterization methods for coated nanoparticles and a deeper understanding of nanoparticle interactions and behavior with complex mixtures of natural macromolecules.

8.2.1 Characterization needs to enable development of correlations

Both parts of this dissertation have demonstrated the importance of thorough characterization of the macromolecules that are likely to coat nanoparticles, and the need for additional or improved characterization methods to explain the deposition or aggregation behavior of macromolecule-coated nanoparticles. A number of advanced characterization methods not assessed in this study are now available or being developed to characterize adsorbed

layers on colloids or nanoparticles. Promising methods include size separation based methods (e.g., flow field-flow fractionation and electrospray differential mobility analysis), spectroscopic methods (e.g., small angle neutron scattering and attenuated total reflectance – Fourier transform infrared spectroscopy), and force analysis methods (e.g., atomic force microscopy).

First, a comparison of methods and assessment of the strengths and limitations of each method would provide useful information for researchers to make decisions regarding the best method (or suite of methods) to characterize their coated nanoparticles of interest. Such comparisons have recently been made for sizing methods for uncoated nanoparticles;[5-7] these studies have already made a high impact in the field of environmental nanotechnology. Analogous research is now needed for coated nanoparticles.

Then, these characterization methods can be more broadly applied to nanoparticle effects studies in order to identify mechanisms by which adsorbed macromolecules affect nanoparticle fate and transport behavior. In particular, studies that prepare and assess a larger or more systematically varied set of coated nanoparticles will enable the development of correlations between adsorbed layer properties and nanoparticle aggregation and deposition behavior. These correlations will have a high impact for the development of models for nanoparticle fate and transport.

8.2.2 Assessment of coatings on nanoparticles challenged in realistic environmental scenarios

In the work of this dissertation and many other recent studies,[8-13] as well as the traditional colloid and polymer science literature, it is apparent that adsorbed macromolecules will significantly affect the fate and transport behavior, as well as the toxicity, of nanoparticles. Much of the mechanistic work to date on the effects of adsorbed macromolecules has been

performed in simple, well-controlled systems. However, nanoparticles released into complex environments will be exposed to conditions that challenge the stability or persistence of the macromolecular coating; that is, the coating is likely to be transformed. Transformations of the inorganic nanoparticle core (e.g. sulfidation) have been studied in realistic systems (e.g., pilot wastewater treatment plants, environmental mesocosms) and can have significant effects on their fate and toxicity.[14-18] Analogous studies on the transformations of organic coatings are needed.

Challenging environmental conditions include exposure to new macromolecules (e.g., in a wastewater treatment plant), interactions with organisms (e.g. bio-degradation), exposure to sunlight, and changing pH, ionic strength, or redox conditions as the nanoparticle moves among various environmental compartments. Under these conditions, an adsorbed coating can change conformation, be displaced by other adsorbing species, or be degraded (Figure 8.1).

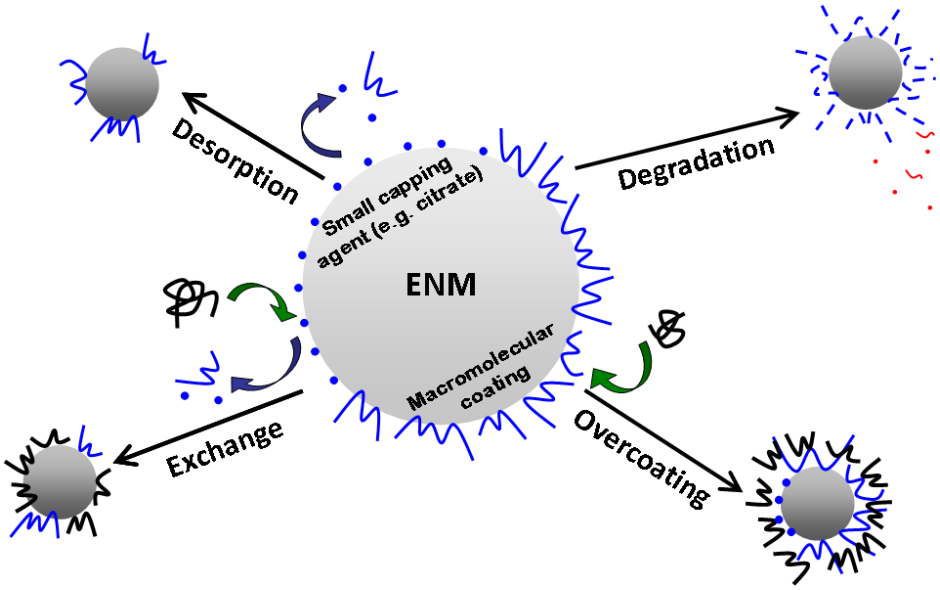

Figure 8.1. Possible transformations of the adsorbed coating on an engineered nanomaterial (ENM).

Some of these processes have now been well studied for protein adsorption and exchange in biological systems.[12,19,20] These processes are also beginning to be probed for synthetic coatings interacting with natural organic matter[21-25] or exposed to bacteria that can degrade the coating.[26] Although some studies of nanoparticles in complex systems have assessed one or more types of macromolecule coatings (e.g., poly(vinyl pyrrolidone)- and gum arabic-coated silver nanoparticles), to our knowledge, the properties of the adsorbed coatings on the end-products have not been assessed in these complex systems. These transformations will be very difficult to characterize, requiring the development of improved and innovative methods. However, for conserved nanoparticles (i.e., those where the nanoparticle core does not rapidly transform) of concern, these processes will be important to understand in order to predict their environmental fate and transport behavior.

Additional studies are needed that describe the kinetics of macromolecule adsorption or transformations processes on nanoparticles in an environmental context, i.e., compared to the rates of other environmental processes and the residence time of the nanoparticle in different environmental compartments. For example, even if higher molecular weight NOM is thermodynamically favored to adsorb to nanoparticles and will provide better electrosteric stabilization, it is possible that the kinetics of this process will be slower than the timescale of aggregation or heteroaggregation of nanoparticles that are initially uncoated or coated with other components. If the nanoparticles cannot be disaggregated, the stabilizing capability of the high MW NOM components may no longer be relevant. The ability of NOM to disaggregate nanoparticles has not been well characterized, although a recent study demonstrated the ability of NOM to disaggregate TiO_2 nanoparticles.[27] Reactions that transform the nanoparticle surface chemistry, such as oxidation or sulfidation, will also change the affinity of macromolecular

components; vice versa, adsorbed layers can change the rate of reaction of the nanoparticle. The NOM study presented here suggests that NOM will adsorb and change nanoparticle homoaggregation behavior within minutes at environmentally relevant NOM concentrations (~ 5 ppm as carbon), although adsorption kinetics may be slower at lower ionic strengths than used here (100 mM NaCl). The kinetics of heteroaggregation, deposition, or chemical transformation will depend on the concentration of suspended solids or reactants and the properties of the system (e.g., flowrate and ionic strength). Finally, a wide range of time scales (hours to years) and potentially drastic spatial or temporal changes in system conditions must be considered when assessing nanoparticle fate and transport across its lifetime in the environment, as it moves among different compartments of interest (e.g., wastewater treatment plants, soils, surface waters, groundwater and sediments, and estuaries).

Clearly, comparison of the kinetics of multiple transformation processes across multiple environmental compartments will be crucial to predict the likely sequence of nanoparticle transformations and improve predictions of nanoparticle behavior in realistic environments. The results presented in this thesis provide foundations for understanding nanoparticle interactions with complex NOM mixtures and suggest important properties of NOM (e.g., molecular weight distribution) that may be incorporated into models to predict nanoparticle fate and transport. However, future investigation of systems of greater complexity will be required to extend the results of this work to realistic natural systems.

References for Chapter 8

(1) Louie, S. M.; Phenrat, T.; Small, M. J.; Tilton, R. D.; Lowry, G. V. Parameter identifiability in application of soft particle electrokinetic theory to determine polymer and polyelectrolyte coating thicknesses on colloids. *Langmuir* **2012**, *28* (28), 10334-10347.

(2) Hotze, E. M.; Louie, S. M.; Lin, S.; Wiesner, M. R.; Lowry, G. V. Nanoparticle core properties affect attachment of macromolecule-coated nanoparticles to silica surfaces. *Environ. Chem.* **2014**, *11* (3), 257-267.

(3) Deonarine, A.; Lau, B. L. T.; Aiken, G. R.; Ryan, J. N.; Hsu-Kim, H. Effects of humic substances on precipitation and aggregation of zinc sulfide nanoparticles. *Environ. Sci. Technol.* **2011**, *45* (8), 3217-3223.

(4) Nason, J. A.; McDowell, S. A.; Callahan, T. W. Effects of natural organic matter type and concentration on the aggregation of citrate-stabilized gold nanoparticles. *J. Environ. Monit.* **2012**, *14* (7), 1885-1892.

(5) Dieckmann, Y.; Colfen, H.; Hofmann, H.; Petri-Fink, A. Particle size distribution measurements of manganese-doped ZnS nanoparticles. *Anal. Chem.* **2009**, *81* (10), 3889-3895.

(6) Domingos, R. F.; Baalousha, M. A.; Ju-Nam, Y.; Reid, M. M.; Tufenkji, N.; Lead, J. R.; Leppard, G. G.; Wilkinson, K. J. Characterizing manufactured nanoparticles in the environment: Multimethod determination of particle sizes. *Environ. Sci. Technol.* **2009**, *43* (19), 7277-7284.

(7) Mahl, D.; Diendorf, J.; Meyer-Zaika, W.; Epple, M. Possibilities and limitations of different analytical methods for the size determination of a bimodal dispersion of metallic nanoparticles. *Colloids Surfaces A* **2011**, *377* (1-3), 386-392.

(8) Christian, P.; Von der Kammer, F.; Baalousha, M.; Hofmann, T. Nanoparticles: Structure, properties, preparation and behaviour in environmental media. *Ecotoxicology* **2008**, *17* (5), 326-343.

(9) Ju-Nam, Y.; Lead, J. R. Manufactured nanoparticles: An overview of their chemistry, interactions and potential environmental implications. *Sci. Total Environ.* **2008**, *400* (1-3), 396-414.

(10) Klaine, S. J.; Alvarez, P. J. J.; Batley, G. E.; Fernandes, T. F.; Handy, R. D.; Lyon, D. Y.; Mahendra, S.; McLaughlin, M. J.; Lead, J. R. Nanomaterials in the environment: Behavior, fate, bioavailability, and effects. *Environ. Toxicol. Chem.* **2008**, *27* (9), 1825-1851.

(11) Lowry, G. V.; Gregory, K. B.; Apte, S. C.; Lead, J. R. Transformations of nanomaterials in the environment. *Environ. Sci. Technol.* **2012**, *46* (13), 6893-6899.

(12) Nel, A. E.; Madler, L.; Velegol, D.; Xia, T.; Hoek, E. M. V.; Somasundaran, P.; Klaessig, F.; Castranova, V.; Thompson, M. Understanding biophysicochemical interactions at the nano-bio interface. *Nat. Mater.* **2009**, *8* (7), 543-557.

(13) Nowack, B.; Ranville, J. F.; Diamond, S.; Gallego-Urrea, J. A.; Metcalfe, C.; Rose, J.; Horne, N.; Koelmans, A. A.; Klaine, S. J. Potential scenarios for nanomaterial release and subsequent alteration in the environment. *Environ. Toxicol. Chem.* **2012**, *31* (1), 50-59.

(14) Colman, B. P.; Arnaout, C. L.; Anciaux, S.; Gunsch, C. K.; Hochella, M. F.; Kim, B.; Lowry, G. V.; McGill, B. M.; Reinsch, B. C.; Richardson, C. J.; Unrine, J. M.; Wright, J. P.; Yin, L. Y.; Bernhardt, E. S. Low concentrations of silver nanoparticles in biosolids cause adverse ecosystem responses under realistic field scenario. *Plos One* **2013**, *8* (2).

(15) Colman, B. P.; Espinasse, B.; Richardson, C. J.; Matson, C. W.; Lowry, G. V.; Hunt, D. E.; Wiesner, M. R.; Bernhardt, E. S. Emerging contaminant or an old toxin in disguise? Silver nanoparticle impacts on ecosystems. *Environ. Sci. Technol.* **2014**, *48* (9), 5229-5236.
(16) Levard, C.; Hotze, E. M.; Lowry, G. V.; Brown, G. E. Environmental transformations of silver nanoparticles: Impact on stability and toxicity. *Environ. Sci. Technol.* **2012**, *46* (13), 6900-6914.
(17) Lowry, G. V.; Espinasse, B. P.; Badireddy, A. R.; Richardson, C. J.; Reinsch, B. C.; Bryant, L. D.; Bone, A. J.; Deonarine, A.; Chae, S.; Therezien, M.; Colman, B. P.; Hsu-Kim, H.; Bernhardt, E. S.; Matson, C. W.; Wiesner, M. R. Long-term transformation and fate of manufactured Ag nanoparticles in a simulated large scale freshwater emergent wetland. *Environ. Sci. Technol.* **2012**, *46* (13), 7027-7036.
(18) Ma, R.; Levard, C.; Judy, J. D.; Unrine, J. M.; Durenkamp, M.; Martin, B.; Jefferson, B.; Lowry, G. V. Fate of zinc oxide and silver nanoparticles in a pilot wastewater treatment plant and in processed biosolids. *Environ. Sci. Technol.* **2014**, *48* (1), 104-112.
(19) Monopoli, M. P.; Aberg, C.; Salvati, A.; Dawson, K. A. Biomolecular coronas provide the biological identity of nanosized materials. *Nat. Nanotechnol.* **2012**, *7* (12), 779-786.
(20) Eigenheer, R.; Castellanos, E. R.; Nakamoto, M. Y.; Gerner, K. T.; Lampe, A. M.; Wheeler, K. E. Silver nanoparticle protein corona composition compared across engineered particle properties and environmentally relevant reaction conditions. *Environ. Sci.: Nano* **2014**, *1* (3), 238-247.
(21) Liu, J. F.; Legros, S.; Von der Kammer, F.; Hofmann, T. Natural organic matter concentration and hydrochemistry influence aggregation kinetics of functionalized engineered nanoparticles. *Environ. Sci. Technol.* **2013**, *47* (9), 4113-4120.
(22) Stankus, D. P.; Lohse, S. E.; Hutchison, J. E.; Nason, J. A. Interactions between natural organic matter and gold nanoparticles stabilized with different organic capping agents. *Environ. Sci. Technol.* **2011**, *45* (8), 3238-3244.
(23) Bone, A. J.; Colman, B. P.; Gondikas, A. P.; Newton, K. M.; Harrold, K. H.; Cory, R. M.; Unrine, J. M.; Klaine, S. J.; Matson, C. W.; Di Giulio, R. T. Biotic and abiotic interactions in aquatic microcosms determine fate and toxicity of Ag nanoparticles: Part 2-Toxicity and Ag speciation. *Environ. Sci. Technol.* **2012**, *46* (13), 6925-6933.
(24) Unrine, J. M.; Colman, B. P.; Bone, A. J.; Gondikas, A. P.; Matson, C. W. Biotic and abiotic interactions in aquatic microcosms determine fate and toxicity of Ag nanoparticles: Part 1 - Aggregation and dissolution. *Environ. Sci. Technol.* **2012**, *46* (13), 6915-6924.
(25) Lau, B. L. T.; Hockaday, W. C.; Ikuma, K.; Furman, O.; Decho, A. W. A preliminary assessment of the interactions between the capping agents of silver nanoparticles and environmental organics. *Colloids Surfaces A* **2013**, *435*, 22-27.
(26) Kirschling, T. L.; Golas, P. L.; Unrine, J. M.; Matyjaszewski, K.; Gregory, K. B.; Lowry, G. V.; Tilton, R. D. Microbial bioavailability of covalently bound polymer coatings on model engineered nanomaterials. *Environ. Sci. Technol.* **2011**, *45* (12), 5253-5259.
(27) Loosli, F.; Le Coustumer, P.; Stoll, S. Effect of natural organic matter on the disagglomeration of manufactured TiO2 nanoparticles. *Environ. Sci.: Nano* **2014**, *1* (2), 154-160.

Appendix A: Supporting information for Chapter 3

A.1 Review of prior applications of soft particle electrokinetic modeling

A review of the literature for determination of adsorbed layer properties by soft particle electrokinetic modeling was performed. The types of systems and ranges of fitted parameters obtained are reported in Table A.1.

Table A.1. Layer properties previously obtained using soft particle electrokinetic models

System studied	Model used	Coating properties*		
		N/N_A (mol m^{-3})	$1/\lambda$ (nm)	d (nm)**
Bacteria surface[1]	Analytical[2], uncharged core	6 - 56	0.5 - 6.6	n/a
Bacteria surface[3]	Analytical[2], uncharged core	11-41	1.0-2.5	n/a
Bacteria with EPS[4]	Analytical[2], uncharged core	4-43	1.2-2.5	n/a
Bacteria with EPS[5]	Analytical[2], uncharged core	9-42	1.0-4.8	n/a
Zirconia colloids with PAA coating[6]	Analytical[2], uncharged core	1.1-8.1	6.5-19.1	n/a
Magnetite nanoparticles with PAA coating[7]	Analytical[2], uncharged core	0.7-14	4.7-24.3	n/a
NZVI with PSS,CMC,PAP coatings[8]	Analytical[2], charged core	0.13-0.37	9.2-55	7.2-198
Titanium dioxide, hematite, latex nanoparticles with various synthetic and NOM coatings[9]	Analytical[2], charged core	0.4-12.3	0.1-29	0.7-70
Natural rubber latex with protein/lipid coatings[10]	Analytical[2], uncharged core	20-200	0.7-0.9	n/a
pNIPAM microgels[11]	Analytical[2], uncharged core	1-24	1-4	n/a

System studied	Model used	Coating properties*		
		N/N_A (mol m^{-3})	$1/\lambda$ (nm)	d (nm)**
Gold nanoparticles with citrate, creatine, and human serum albumin coatings[12]	Comparison of analytical models[2,13,14], uncharged core	1.4-10.1	0.059-2	Measured (1 nm for citrate, 10 nm for creatine)
Magnetite nanoparticles with citrate and IGF coatings[15]	Analytical and numerical models[14], uncharged core	28.7-109.5	2-5	2.5-23
K. pneumoniae surface[16]	Numerical[14], uncharged core	2.8-180	0.75-3.85	Measured (2, 30, 160 nm for various strains)
Humic acid[17]	Numerical[14], no core	Estimated, pH dependent	0.25-0.55	Measured (<1 nm)
S. salivarius surface[18]	Numerical[14], uncharged core	Estimated, pH dependent	1.2-1.9	Literature/measured (23 nm wall, ~200 nm fibrils)
MS2 bacteriophage[19]	Numerical[14], uncharged core	Estimated	1-1.9	Literature (multilayer, 8.5+2.8+2.1 nm)
Red blood cells[20]	Numerical[14], uncharged core	50	0.6-1.9	Literature (3-15 nm)
Copolymer micelles with poly(styrene sulfonate) corona[21]	Numerical[22], uncharged core	From segment density (29, 2.6)†	3.3, 11.2	Measured (37, 77 nm)
PEO-coated polystyrene lattices[21]	Numerical[22], charged core	Uncharged	2.3-3.8‡	13.8-27.3‡

*Obtained by model fitting unless otherwise specified

**Layer thickness is listed as "n/a" where it does not appear as a variable in analytical equations for an uncharged core, taking the limit of either $d << a$ or $d >> a$ in $f(d/a)$

†Charge density was expressed in terms of λ during the model fitting, so only λ was fitted

‡Data on adsorbed mass and hydrodynamic layer thickness were used to provide additional fitting constraints

A.2 Sample calculations and computed values for sensitivity and collinearity indices

Identifiability measures for all 180 simulated cases using the numerical model (MPEK-0.02 software, provided by Dr. Reghan Hill)[22] are provided in Table A.2. For an experimental case, interpolation on the table can be used to roughly estimate sensitivity and collinearity indices for the system of interest. Sensitivity and collinearity indices can also be easily

computed for the least squares estimate. These indices can be compared to Figures 3.5, A.4, or A.5 to assess whether identifiability may be problematic for d, N, or λ^{-1}, respectively. For layer thickness, cases with $\delta_d^{msqr} \leq 0.009$ and $\delta_d^{msqr} \leq 0.005$ are expected to fall in Groups C and D, respectively. Exceptions are at very high N (e.g. 10^{25} mol/m^3), where identifiability can be better than suggested by δ_d^{msqr}. For N and λ^{-1}, both the sensitivity and collinearity indices must be computed.

Since consistency in the details of the computation are important when comparing sensitivity values to those provided in this study, a sample calculation of δ_d^{msqr} (based on equations published by Brun *et al.*[23]) is provided for Case 89:

Ionic strengths, $\boldsymbol{I}$: [5, 10, 15, 20, 30, 40, 50, 60, 70, 80] mM (n = ten points; indices i=1,2,…,n)

True parameter set, $\boldsymbol{\theta_{true}}$: [$d$ = 10 nm; $\lambda^{-1} = 0.5d$ = 5 nm; $N = 5\text{x}10^{24}$ m^{-3}] (parameter indices j)

Electrophoretic mobility at $\boldsymbol{\theta_{true}}$ for the 10 ionic strengths = $\boldsymbol{\eta(\theta_{true})}$

= [-2.39, -2.12, -1.99, -1.91, -1.82, -1.76, -1.72, -1.69, -1.66, -1.64] μm-cm/V-s

To compute sensitivity (Equations 11 and 12), $\Delta\theta_j$, SC_i, and a computation of the slope υ_{ij} at each ionic strength i for each parameter j are necessary. Here, the chosen values are as follows:

- $\Delta\theta_j$ = 1 mol/m^3 for N and 1 nm for d and λ^{-1}
- $SC_i = \left|\eta_i\left(\hat{\boldsymbol{\theta}}\right)\right|$ where $\hat{\boldsymbol{\theta}}$ is the true parameter set or the least squares estimate
- υ_{ij} is computed as a linear approximation between $\eta_i(\theta_{j,true})$ and $\eta_i(1.1\theta_{j,true})$ for each parameter, holding the other two parameters at their true value or least squares estimate

Sample calculations for sensitivity to d are as follows:

Electrophoretic mobility at d = 1.1*10 nm = 11 nm (holding λ^{-1} and N at their true values) = [-2.43, -2.17, -2.05, -1.98, -1.89, -1.84, -1.80, -1.77, -1.75, -1.73] μm-cm/V-s

υ_{1d} (slope at I=5 mM, varying d) = (-2.43 – -2.39) μm-cm/V-s /(11 – 10) nm = -0.041 (μm-cm/V-s)/nm

$\boldsymbol{\upsilon_d}$ (over all I) = [-0.041, -0.054, -0.064, -0.067, -0.072, -0.077, -0.077, -0.080, -0.082, -0.083] (μm-cm/V-s)/nm

$s_{1d} = \upsilon_{1d} * \Delta\theta_d / SC_{i=1}$ = -0.041 (μm-cm/V-s)/nm * 1 nm / |-2.43| μm-cm/V-s = -0.017

$\boldsymbol{s_d}$ (over all I) = [-0.017, -0.025, -0.032, -0.035, -0.040, -0.044, -0.045, -0.047, -0.049, -0.050]

From Equation 13:

$$\delta_d^{msqr} = \sqrt{\frac{1}{n}\sum_{i=1}^{n} s_{id}^2}\ , \qquad n = 10 \text{ ionic strengths; } i = 1, 2, \ldots, 10$$

$$= [1/10*(-0.017^2 + -0.025^2 + \ldots + -0.050^2)]^{(1/2)} = 0.040$$

Table A.2. Sensitivity (δ^{msqr}) and collinearity (γ_K) indices for 180 simulated cases

Case	True Parameters				Numerical model[22]						
					δ^{msqr} summaries			γ_K collinearity indices			
	σ_{surf} (C/m^2)	d (nm)	λ^{-1}/d	N (m^{-3})	δ_N^{msqr}	δ_d^{msqr}	$\delta_{1.\lambda}^{msqr}$	$\gamma_{N,d,1/\lambda}$	$\gamma_{N,d}$	$\gamma_{N,1/\lambda}$	$\gamma_{d,1/\lambda}$
1	-3E-04	5	0.2	1E+20	156.7	0.45	1.43	5.5	1.2	1.2	5.3
2	-3E-04	5	0.2	1E+22	6.0	0.40	1.37	8.0	4.5	7.8	5.0
3	-3E-04	5	0.2	1E+24	0.5	0.04	0.96	7.3	5.3	5.3	3.4
4	-3E-04	5	0.2	5E+24	0.1	0.01	0.93	5.9	1.2	4.9	1.4
5	-3E-04	5	0.2	1E+25	0.1	0.01	0.93	7.0	1.0	5.2	1.2
6	-3E-04	10	0.2	1E+20	266.3	0.21	1.06	4.9	1.5	1.7	4.3
7	-3E-04	10	0.2	1E+22	18.0	0.15	0.95	25.1	3.3	23.4	3.5
8	-3E-04	10	0.2	1E+24	0.6	0.004	0.72	18.6	1.3	7.4	1.1
9	-3E-04	10	0.2	5E+24	0.1	0.003	0.71	17.1	2.5	7.7	3.4
10	-3E-04	10	0.2	1E+25	0.1	0.004	0.71	51.8	1.9	13.0	2.2
11	-3E-04	20	0.2	1E+20	237.6	0.09	0.52	9.9	1.1	1.1	9.6
12	-3E-04	20	0.2	1E+22	36.1	0.04	0.47	23.5	3.6	16.2	4.2
13	-3E-04	20	0.2	1E+24	0.6	0.003	0.44	18.4	3.9	15.5	4.5
14	-3E-04	20	0.2	5E+24	0.1	0.004	0.43	86.0	5.3	27.8	6.5
15	-3E-04	20	0.2	1E+25	0.2	0.003	0.42	144.5	3.2	23.7	2.8
16	-3E-04	40	0.2	1E+20	402.9	0.04	0.26	33.4	2.0	2.0	32.3
17	-3E-04	40	0.2	1E+22	50.4	0.01	0.25	46.7	3.8	40.3	4.0
18	-3E-04	40	0.2	1E+24	0.6	0.002	0.25	94.5	5.7	53.0	6.3
19	-3E-04	40	0.2	5E+24	0.1	0.002	0.23	121.6	3.9	22.2	3.3
20	-3E-04	40	0.2	1E+25	0.5	0.002	0.21	121.1	1.4	12.7	1.6
21	-3E-04	5	0.5	1E+20	83.7	0.29	0.47	11.3	1.1	1.2	11.0
22	-3E-04	5	0.5	1E+22	4.0	0.27	0.46	13.5	5.9	9.0	9.8
23	-3E-04	5	0.5	1E+24	0.5	0.04	0.38	15.5	4.2	10.0	6.1
24	-3E-04	5	0.5	5E+24	0.1	0.08	0.37	23.0	10.0	9.1	22.3
25	-3E-04	5	0.5	1E+25	1.4	0.08	0.37	49.4	20.1	28.0	38.6
26	-3E-04	10	0.5	1E+20	178.1	0.15	0.30	14.6	1.5	1.6	12.7
27	-3E-04	10	0.5	1E+22	12.6	0.11	0.28	34.1	4.5	10.6	7.4
28	-3E-04	10	0.5	1E+24	0.6	0.05	0.24	62.6	9.9	21.1	17.3
29	-3E-04	10	0.5	5E+24	0.1	0.05	0.23	252.6	15.2	29.7	30.6
30	-3E-04	10	0.5	1E+25	0.4	0.05	0.23	389.9	22.7	56.5	16.3
31	-3E-04	20	0.5	1E+20	194.2	0.08	0.16	32.3	1.1	1.1	29.5

Case	True Parameters				Numerical model[22]						
					δ^{msqr} summaries			γ_K collinearity indices			
	σ_{surf_2} (C/m^2)	d (nm)	λ^{-1}/d	N (m^{-3})	δ_N^{msqr}	δ_d^{msqr}	$\delta_{1.\lambda}^{msqr}$	$\gamma_{N,d,1/\lambda}$	$\gamma_{N,d}$	$\gamma_{N,1/\lambda}$	$\gamma_{d,1/\lambda}$
32	-3E-04	20	0.5	1E+22	31.3	0.03	0.15	43.2	2.6	8.9	3.6
33	-3E-04	20	0.5	1E+24	0.6	0.03	0.13	76.9	29.2	70.1	34.6
34	-3E-04	20	0.5	5E+24	0.1	0.03	0.13	149.3	144.4	21.8	21.0
35	-3E-04	20	0.5	1E+25	0.4	0.02	0.11	304.5	5.7	16.9	8.5
36	-3E-04	40	0.5	1E+20	311.1	0.04	0.08	29.9	2.0	2.1	27.9
37	-3E-04	40	0.5	1E+22	49.5	0.005	0.08	81.9	2.2	20.0	2.0
38	-3E-04	40	0.5	1E+24	0.6	0.01	0.07	324.0	56.1	64.3	30.4
39	-3E-04	40	0.5	5E+24	0.1	0.01	0.06	133.2	10.0	4.8	9.1
40	-3E-04	40	0.5	1E+25	0.4	0.01	0.04	40.2	2.9	10.6	3.8
41	-3E-04	5	0.8	1E+20	9621.4	0.18	0.18	17.5	1.1	1.2	15.3
42	-3E-04	5	0.8	1E+22	483.2	0.16	0.18	13.3	1.2	1.2	11.9
43	-3E-04	5	0.8	1E+24	0.5	0.13	0.16	22.5	1.3	1.3	19.7
44	-3E-04	5	0.8	5E+24	0.1	0.17	0.15	63.8	1.2	1.2	58.5
45	-3E-04	5	0.8	1E+25	6.7	0.17	0.15	115.6	8.1	7.4	74.9
46	-3E-04	10	0.8	1E+20	109.6	0.10	0.11	19.9	1.1	1.1	18.5
47	-3E-04	10	0.8	1E+22	11.5	0.06	0.11	7.1	1.1	1.2	6.3
48	-3E-04	10	0.8	1E+24	0.6	0.10	0.09	35.2	1.3	1.2	32.7
49	-3E-04	10	0.8	5E+24	0.1	0.10	0.09	42.5	1.1	1.1	40.8
50	-3E-04	10	0.8	1E+25	0.6	0.10	0.09	144.9	8.8	6.2	21.2
51	-3E-04	20	0.8	1E+20	122.1	0.05	0.06	43.5	1.2	1.2	37.7
52	-3E-04	20	0.8	1E+22	30.0	0.01	0.06	45.1	1.1	8.2	1.0
53	-3E-04	20	0.8	1E+24	0.6	0.06	0.05	119.2	70.3	111.0	58.9
54	-3E-04	20	0.8	5E+24	0.1	0.05	0.05	341.4	23.9	12.2	24.8
55	-3E-04	20	0.8	1E+25	0.5	0.04	0.04	32.4	8.8	5.0	10.6
56	-3E-04	40	0.8	1E+20	257.1	0.03	0.03	28.8	2.5	2.6	23.6
57	-3E-04	40	0.8	1E+22	49.1	0.02	0.03	92.7	10.9	16.9	6.7
58	-3E-04	40	0.8	1E+24	0.6	0.03	0.03	388.0	128.2	32.2	42.1
59	-3E-04	40	0.8	5E+24	0.1	0.02	0.02	224.0	3.8	2.9	11.4
60	-3E-04	40	0.8	1E+25	0.02	0.01	0.01	72.7	1.2	1.0	5.1
61	-3E-03	5	0.2	1E+20	7.5	0.45	1.43	23.8	2.7	5.0	5.4
62	-3E-03	5	0.2	1E+22	1.5	0.44	1.42	5.5	1.3	1.4	5.2
63	-3E-03	5	0.2	1E+24	0.3	0.22	1.14	19.1	5.7	9.2	3.8
64	-3E-03	5	0.2	5E+24	0.1	0.08	0.99	19.9	6.2	6.4	3.3

Case	True Parameters				Numerical model[22]						
					δ^{msqr} summaries			γ_K collinearity indices			
	σ_{surf_2} (C/m^2)	d (nm)	λ^{-1}/d	N (m^{-3})	δ_N^{msqr}	δ_d^{msqr}	$\delta_{1.\lambda}^{msqr}$	$\gamma_{N,d,1/\lambda}$	$\gamma_{N,d}$	$\gamma_{N,1/\lambda}$	$\gamma_{d,1/\lambda}$
65	-3E-03	5	0.2	1E+25	0.1	0.04	0.96	17.7	5.0	6.7	3.0
66	-3E-03	10	0.2	1E+20	112.6	0.21	1.06	5.3	1.4	1.7	4.4
67	-3E-03	10	0.2	1E+22	2.8	0.20	1.04	4.2	1.7	1.8	4.2
68	-3E-03	10	0.2	1E+24	0.5	0.05	0.78	45.7	2.6	14.9	2.2
69	-3E-03	10	0.2	5E+24	0.1	0.01	0.73	50.3	1.9	9.2	1.6
70	-3E-03	10	0.2	1E+25	0.2	0.004	0.71	72.5	1.2	7.7	1.1
71	-3E-03	20	0.2	1E+20	106.3	0.09	0.53	9.9	1.0	1.0	9.5
72	-3E-03	20	0.2	1E+22	10.6	0.08	0.52	8.3	2.4	2.8	7.4
73	-3E-03	20	0.2	1E+24	0.6	0.004	0.44	52.0	1.7	21.5	1.6
74	-3E-03	20	0.2	5E+24	0.1	0.003	0.43	70.5	3.1	29.5	3.4
75	-3E-03	20	0.2	1E+25	0.2	0.003	0.42	29.4	3.9	8.9	2.8
76	-3E-03	40	0.2	1E+20	38.8	0.05	0.26	58.1	1.8	1.8	42.7
77	-3E-03	40	0.2	1E+22	23.5	0.03	0.25	18.0	2.7	3.8	8.2
78	-3E-03	40	0.2	1E+24	0.6	0.001	0.25	70.3	3.9	57.0	4.0
79	-3E-03	40	0.2	5E+24	0.1	0.002	0.23	78.4	5.1	24.6	4.3
80	-3E-03	40	0.2	1E+25	0.5	0.001	0.21	113.9	1.5	12.9	1.6
81	-3E-03	5	0.5	1E+20	4.2	0.29	2.62	36.3	2.6	3.1	14.5
82	-3E-03	5	0.5	1E+22	1.0	0.29	2.62	14.0	1.4	1.4	13.8
83	-3E-03	5	0.5	1E+24	0.2	0.14	2.45	28.9	6.1	26.4	5.6
84	-3E-03	5	0.5	5E+24	0.1	0.02	2.30	38.8	1.1	17.5	1.1
85	-3E-03	5	0.5	1E+25	1.2	0.042	0.38	57.3	5.4	17.9	4.2
86	-3E-03	10	0.5	1E+20	74.0	0.16	0.30	15.5	1.5	1.6	13.4
87	-3E-03	10	0.5	1E+22	1.4	0.15	0.30	11.9	1.9	2.0	11.4
88	-3E-03	10	0.5	1E+24	0.4	0.02	0.25	64.6	1.1	35.3	1.2
89	-3E-03	10	0.5	5E+24	0.1	0.04	0.24	133.0	7.4	77.0	8.0
90	-3E-03	10	0.5	1E+25	0.4	0.045	0.23	304.1	14.7	49.8	11.4
91	-3E-03	20	0.5	1E+20	102.0	0.08	0.16	32.3	1.2	1.2	29.7
92	-3E-03	20	0.5	1E+22	7.3	0.07	0.16	18.2	2.0	2.1	16.1
93	-3E-03	20	0.5	1E+24	0.5	0.02	0.13	130.8	8.6	59.0	7.6
94	-3E-03	20	0.5	5E+24	0.1	0.03	0.13	93.5	81.3	19.7	17.6
95	-3E-03	20	0.5	1E+25	0.4	0.022	0.11	227.6	5.9	16.7	9.0
96	-3E-03	40	0.5	1E+20	34.7	0.04	0.08	53.3	1.8	1.9	38.0
97	-3E-03	40	0.5	1E+22	20.9	0.02	0.08	23.8	2.7	4.2	6.9

Case	True Parameters				Numerical model[22]						
					δ^{msqr} summaries			γ_K collinearity indices			
	σ_{surf_2} (C/m^2)	d (nm)	λ^{-1}/d	N (m^{-3})	δ_N^{msqr}	δ_d^{msqr}	$\delta_{1.\lambda}^{msqr}$	$\gamma_{N,d,1/\lambda}$	$\gamma_{N,d}$	$\gamma_{N,1/\lambda}$	$\gamma_{d,1/\lambda}$
98	-3E-03	40	0.5	1E+24	0.6	0.01	0.07	334.0	37.3	52.6	22.0
99	-3E-03	40	0.5	5E+24	0.1	0.01	0.06	164.5	9.3	4.8	9.9
100	-3E-03	40	0.5	1E+25	0.4	0.006	0.04	41.1	2.9	10.5	3.9
101	-3E-03	5	0.8	1E+20	2.6	0.18	0.18	37.8	2.6	3.1	15.8
102	-3E-03	5	0.8	1E+22	0.7	0.18	0.18	15.4	1.6	1.7	14.8
103	-3E-03	5	0.8	1E+24	0.2	0.05	0.17	36.2	2.6	36.2	2.6
104	-3E-03	5	0.8	5E+24	0.1	0.09	0.16	62.4	6.7	29.6	8.3
105	-3E-03	5	0.8	1E+25	5.9	0.128	0.15	56.6	14.7	7.0	12.8
106	-3E-03	10	0.8	1E+20	43.4	0.10	0.11	23.0	1.4	1.5	20.5
107	-3E-03	10	0.8	1E+22	1.4	0.10	0.11	17.9	1.4	1.4	17.5
108	-3E-03	10	0.8	1E+24	0.4	0.05	0.10	84.3	4.8	21.5	4.0
109	-3E-03	10	0.8	5E+24	0.1	0.09	0.09	289.1	22.7	66.1	17.0
110	-3E-03	10	0.8	1E+25	0.5	0.090	0.09	222.6	9.4	6.2	17.6
111	-3E-03	20	0.8	1E+20	65.1	0.06	0.06	44.6	1.2	1.2	40.2
112	-3E-03	20	0.8	1E+22	6.3	0.04	0.06	19.4	2.6	2.9	14.6
113	-3E-03	20	0.8	1E+24	0.5	0.05	0.05	145.0	28.4	35.5	16.1
114	-3E-03	20	0.8	5E+24	0.1	0.05	0.05	169.8	21.8	11.4	23.4
115	-3E-03	20	0.8	1E+25	0.5	0.040	0.04	37.5	8.8	5.1	11.2
116	-3E-03	40	0.8	1E+20	31.3	0.03	0.03	54.5	2.1	2.2	37.7
117	-3E-03	40	0.8	1E+22	19.9	0.01	0.03	24.2	2.2	4.7	3.9
118	-3E-03	40	0.8	1E+24	0.6	0.02	0.03	254.7	150.4	28.7	33.9
119	-3E-03	40	0.8	5E+24	0.1	0.02	0.02	268.5	3.7	2.9	12.1
120	-3E-03	40	0.8	1E+25	0.02	0.010	0.01	69.3	1.2	1.0	5.2
121	-9E-03	5	0.2	1E+20	13.8	0.45	1.43	6.1	1.0	1.0	5.3
122	-9E-03	5	0.2	1E+22	1.8	0.44	1.42	7.3	1.0	1.1	5.3
123	-9E-03	5	0.2	1E+24	0.1	0.33	1.27	17.1	5.9	12.7	4.6
124	-9E-03	5	0.2	5E+24	0.1	0.16	1.08	63.2	4.6	14.6	3.5
125	-9E-03	5	0.2	1E+25	0.04	0.101	1.02	57.2	5.7	9.1	3.5
126	-9E-03	10	0.2	1E+20	53.2	0.21	1.06	4.3	1.1	1.1	4.3
127	-9E-03	10	0.2	1E+22	2.2	0.21	1.05	4.6	1.9	2.2	4.3
128	-9E-03	10	0.2	1E+24	0.3	0.09	0.85	25.2	2.9	24.4	2.8
129	-9E-03	10	0.2	5E+24	0.1	0.03	0.75	91.8	2.6	13.3	2.2
130	-9E-03	10	0.2	1E+25	0.3	0.011	0.72	21.1	2.6	6.8	2.0

Case	True Parameters				Numerical model[22]						
					δ^{msqr} summaries			γ_K collinearity indices			
	σ_{surf_2} (C/m^2)	d (nm)	λ^{-1}/d	N (m^{-3})	δ_N^{msqr}	δ_d^{msqr}	$\delta_{1.\lambda}^{msqr}$	$\gamma_{N,d,1/\lambda}$	$\gamma_{N,d}$	$\gamma_{N,1/\lambda}$	$\gamma_{d,1/\lambda}$
131	-9E-03	20	0.2	1E+20	172.3	0.09	0.52	9.7	1.2	1.2	9.5
132	-9E-03	20	0.2	1E+22	3.2	0.09	0.52	10.4	2.6	3.0	8.6
133	-9E-03	20	0.2	1E+24	0.5	0.01	0.45	42.8	3.5	26.3	3.1
134	-9E-03	20	0.2	5E+24	0.1	0.001	0.43	64.5	1.2	35.4	1.3
135	-9E-03	20	0.2	1E+25	0.1	0.002	0.42	8.4	5.8	3.1	2.3
136	-9E-03	40	0.2	1E+20	211.9	0.05	0.26	61.1	1.2	1.2	50.3
137	-9E-03	40	0.2	1E+22	12.3	0.04	0.25	25.1	2.9	3.3	17.9
138	-9E-03	40	0.2	1E+24	0.6	0.001	0.25	87.7	1.1	63.0	1.1
139	-9E-03	40	0.2	5E+24	0.1	0.002	0.23	50.7	6.0	24.2	4.9
140	-9E-03	40	0.2	1E+25	0.5	0.001	0.21	108.9	1.5	13.0	1.7
141	-9E-03	5	0.5	1E+20	1.7	0.29	0.47	17.3	2.4	2.9	10.9
142	-9E-03	5	0.5	1E+22	0.8	0.29	0.47	13.2	1.0	1.0	11.1
143	-9E-03	5	0.5	1E+24	0.1	0.22	0.45	20.5	8.4	20.5	8.3
144	-9E-03	5	0.5	5E+24	0.1	0.09	0.41	52.7	3.7	49.1	3.8
145	-9E-03	5	0.5	1E+25	1.0	0.032	0.39	147.0	1.7	12.8	1.9
146	-9E-03	10	0.5	1E+20	67.2	0.15	0.30	14.4	1.3	1.4	13.8
147	-9E-03	10	0.5	1E+22	3.0	0.15	0.29	13.4	1.6	1.7	12.5
148	-9E-03	10	0.5	1E+24	0.3	0.06	0.27	30.4	3.1	13.2	3.8
149	-9E-03	10	0.5	5E+24	0.1	0.02	0.24	186.0	2.7	40.6	2.5
150	-9E-03	10	0.5	1E+25	0.4	0.034	0.23	184.7	7.9	42.1	6.7
151	-9E-03	20	0.5	1E+20	124.8	0.08	0.16	28.6	1.2	1.2	26.0
152	-9E-03	20	0.5	1E+22	3.1	0.08	0.16	30.3	2.9	3.2	21.6
153	-9E-03	20	0.5	1E+24	0.5	0.01	0.14	79.0	2.0	22.8	1.8
154	-9E-03	20	0.5	5E+24	0.1	0.02	0.13	90.4	82.3	17.1	15.8
155	-9E-03	20	0.5	1E+25	0.4	0.021	0.11	454.9	6.3	16.6	10.1
156	-9E-03	40	0.5	1E+20	186.2	0.04	0.08	51.0	1.2	1.2	49.2
157	-9E-03	40	0.5	1E+22	11.1	0.03	0.08	28.3	2.8	3.2	17.1
158	-9E-03	40	0.5	1E+24	0.6	0.01	0.07	230.8	17.3	39.3	12.1
159	-9E-03	40	0.5	5E+24	0.1	0.01	0.06	98.8	8.6	4.8	10.8
160	-9E-03	40	0.5	1E+25	0.4	0.006	0.04	42.4	3.0	10.3	4.0
161	-9E-03	5	0.8	1E+20	1.0	0.18	0.18	19.9	2.3	2.6	14.8
162	-9E-03	5	0.8	1E+22	0.5	0.18	0.18	17.9	1.0	1.0	15.3
163	-9E-03	5	0.8	1E+24	0.1	0.12	0.17	38.7	6.3	24.1	7.8

Case	True Parameters				Numerical model[22]						
					δ^{msqr} summaries			γ_K collinearity indices			
	σ_{surf_2} (C/m^2)	d (nm)	λ^{-1}/d	N (m^{-3})	δ_N^{msqr}	δ_d^{msqr}	$\delta_{1.\lambda}^{msqr}$	$\gamma_{N,d,1/\lambda}$	$\gamma_{N,d}$	$\gamma_{N,1/\lambda}$	$\gamma_{d,1/\lambda}$
164	-9E-03	5	0.8	5E+24	0.1	0.02	0.16	81.8	1.2	27.9	1.2
165	-9E-03	5	0.8	1E+25	4.7	0.066	0.16	48.3	15.9	6.9	4.9
166	-9E-03	10	0.8	1E+20	21.6	0.10	0.11	20.9	1.0	1.0	20.8
167	-9E-03	10	0.8	1E+22	2.0	0.10	0.11	18.6	1.7	1.8	17.1
168	-9E-03	10	0.8	1E+24	0.3	0.02	0.10	43.7	1.2	10.9	1.3
169	-9E-03	10	0.8	5E+24	0.1	0.07	0.09	108.7	16.5	19.4	9.0
170	-9E-03	10	0.8	1E+25	0.5	0.078	0.09	121.0	11.1	6.3	14.4
171	-9E-03	20	0.8	1E+20	88.5	0.06	0.06	37.2	1.1	1.1	32.9
172	-9E-03	20	0.8	1E+22	2.6	0.05	0.06	44.5	3.4	3.9	24.1
173	-9E-03	20	0.8	1E+24	0.5	0.03	0.05	122.5	11.6	17.7	7.1
174	-9E-03	20	0.8	5E+24	0.1	0.05	0.05	141.9	17.8	10.4	24.7
175	-9E-03	20	0.8	1E+25	0.5	0.039	0.04	44.1	8.7	5.3	12.8
176	-9E-03	40	0.8	1E+20	128.3	0.03	0.03	55.2	1.2	1.2	53.3
177	-9E-03	40	0.8	1E+22	9.9	0.02	0.03	26.6	3.0	3.8	12.7
178	-9E-03	40	0.8	1E+24	0.5	0.02	0.03	158.4	157.9	23.6	23.3
179	-9E-03	40	0.8	5E+24	0.1	0.02	0.02	173.6	3.6	2.9	13.3
180	-9E-03	40	0.8	1E+25	0.02	0.010	0.01	60.6	1.1	1.0	5.4

A.3 Additional likelihood plots for1/λ vs. N for theoretical cases

Conditional and profile likelihood plots for $1/\lambda$ vs. N are shown in Figure A.1 below for the four representative cases used in Figure 3.4.

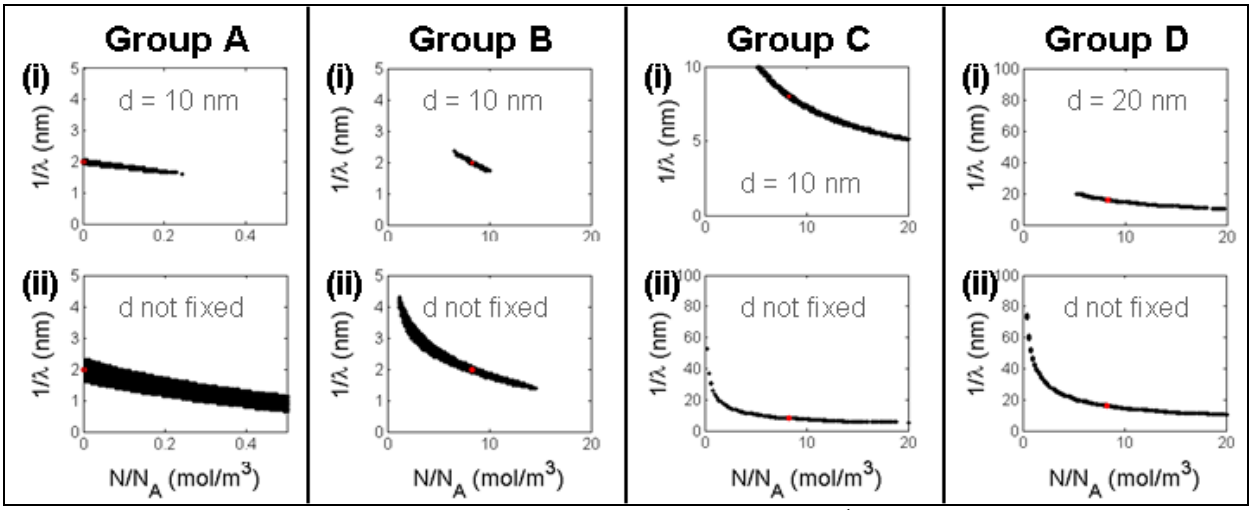

Figure A.1. (i) Conditional and (ii) profile likelihood plots for λ^{-1} vs. N for Group A, B, C, and D cases used in Figure 3.4.

Comparison of analytical[2] *and numerical*[22] *models*

Additional comparison plots are provided in Figures A.2 and A.3 for σ_{surf}=3x10^{-3} and 9x10^{-3} C/m^2, respectively. These plots are analogous to Figure 3.9 (for σ_{surf}=3x10^{-4}). Improved sensitivity to d is observed for the numerical model at high N and λ^{-1}. In addition, sensitivity is better for higher σ_{surf}.

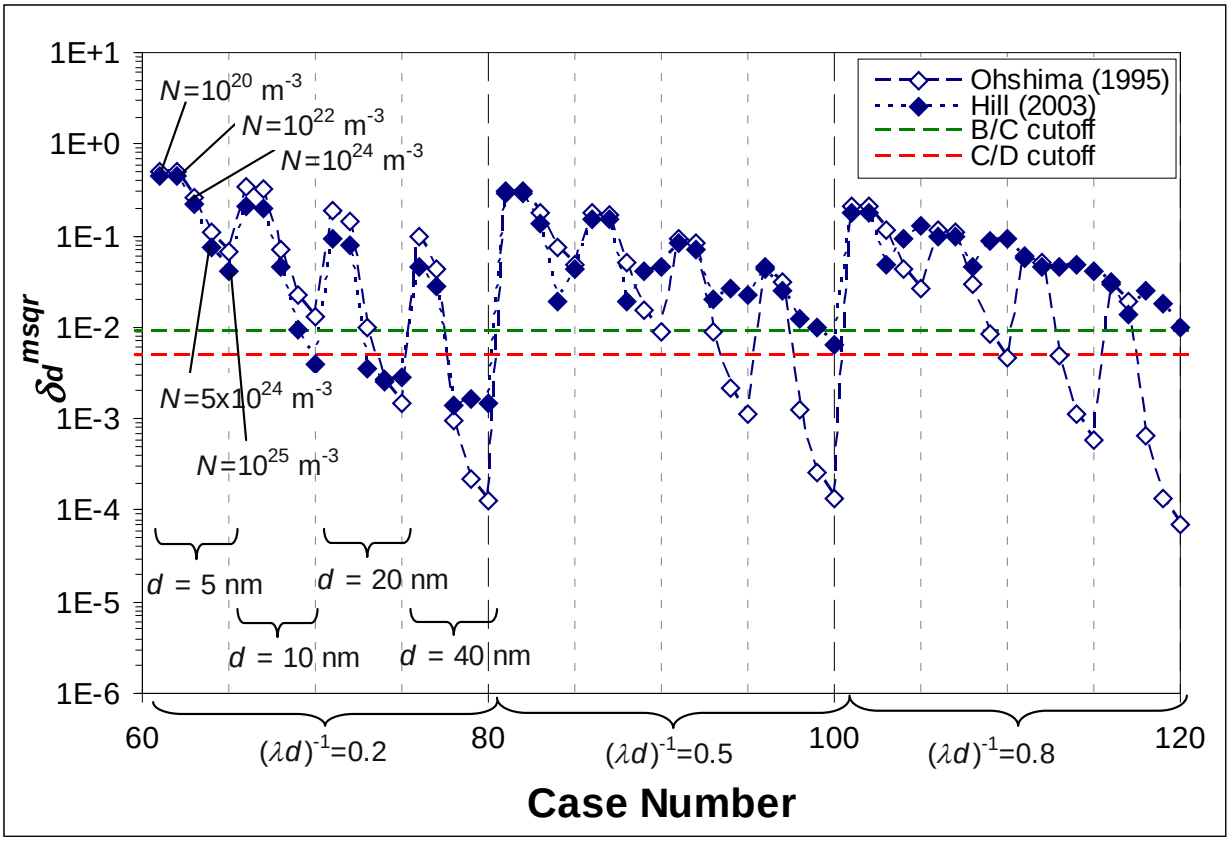

Figure A.2. Sensitivity to d (δ_d^{msqr}) for the analytical[2] and numerical[22] models for σ_{surf}= 3x10^{-3} C/m^2.

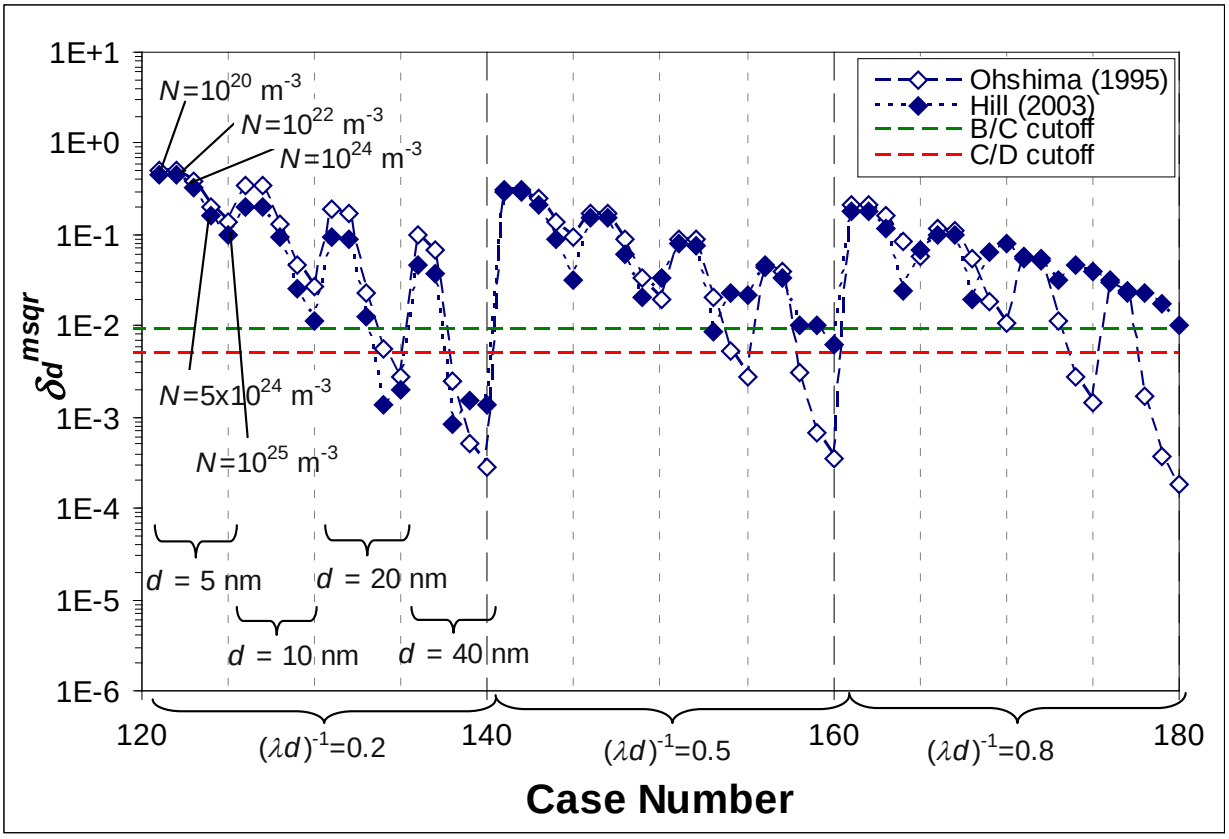

Figure A.3. Sensitivity to d (δ_d^{msqr}) for the analytical[2] and numerical[22] models for σ_{surf}=9x10^{-3} C/m^2.

A.4 Identifiability analysis of layer charge density and permeability

Plots analogous to Figure 3.5 are provided for N and λ^{-1} in Figures A.4 and A.5, respectively. Unlike identifiability of d, which could be determined solely by model sensitivity, both sensitivity and collinearity are important for identifiability of N or λ^{-1}. Since N and λ^{-1} are of the fitted parameters of interest in many studies, this plot can be useful to determine whether these parameters are always identifiable (Group A), only identifiable if d is measured with confidence (Group B), or only identifiable if only one parameter (either N or λ^{-1}) is fitted (Group C). The model is sensitive enough to N and λ^{-1} individually that no Group D cases are observed in the simulated range used here. The constraint $d \geq \lambda^{-1}$ was maintained, so λ^{-1} is always identifiable within the range 0 to d if d is known. Here, Group C is instead labeled "Group C*" and denotes cases where the likelihood region in λ^{-1} extends to the constraint $d \geq \lambda^{-1}$ instead of an arbitrary, large value (e.g. 100 nm).

Groups A to D were determined unambiguously for the analytical model; then, collinearity and sensitivity indices for the numerical model are plotted for comparison. These plots indicate that identifiability should be significantly improved in the numerical model, although several cases are expected to fall in Groups B or C. Since the parameter subset (N, λ^{-1}) is not always identifiable, statistical confidence should be acknowledged when applying the model to fit these parameters together. It is also noted that "identifiability" for N is arbitrarily defined within the range 0 to 50 mM. One should consider what confidence range is deemed acceptable for their particular application.

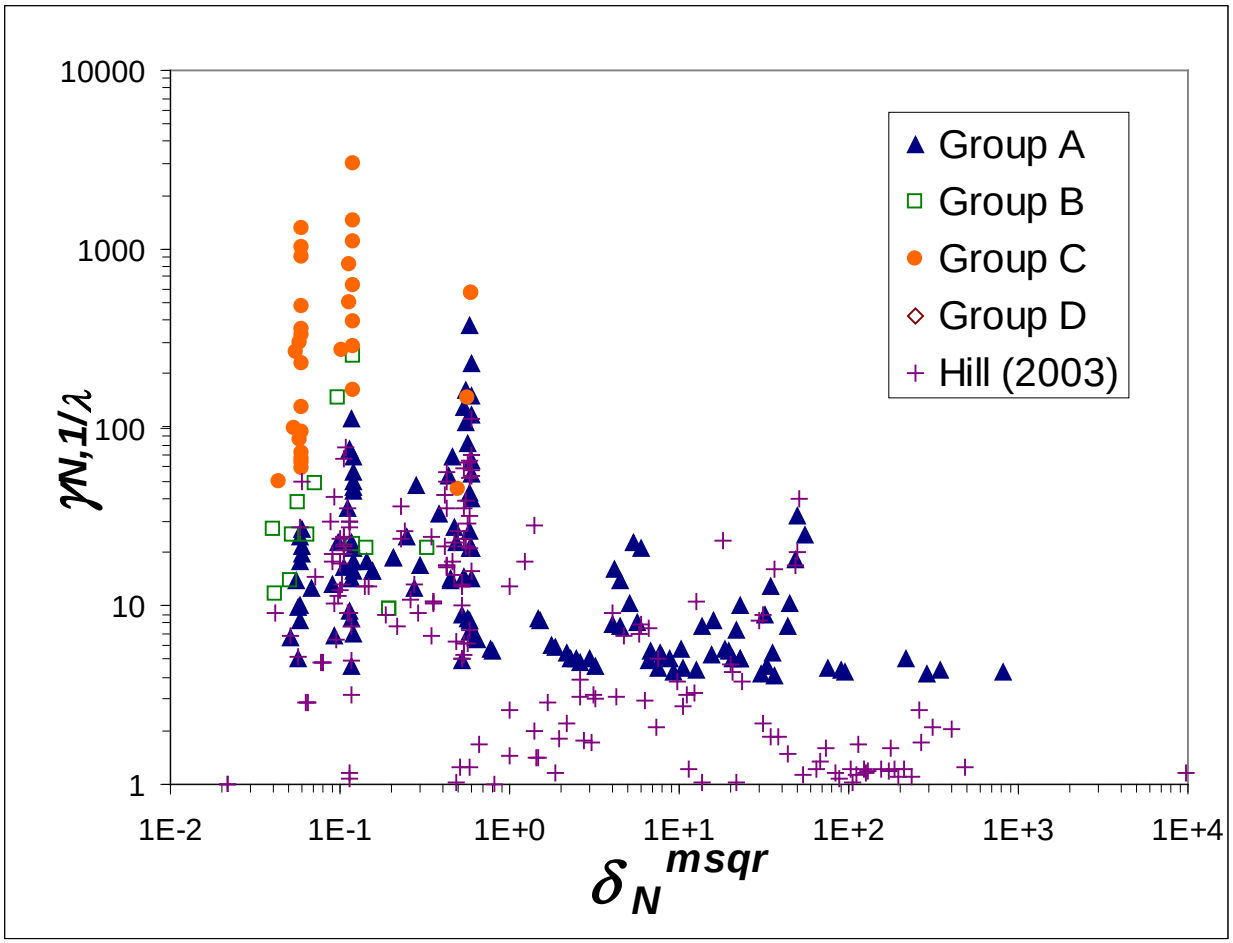

Figure A.4. Sensitivity to N and collinearity indices for the subset (N,λ^{-1}) for the 180 simulated cases using the analytical model[2] and the numerical model[22]. Parameter identifiability is grouped from good (Group A) to poor (Group D) by analysis of likelihood plots, analogous to the analysis for d. The upper limit to define identifiability is arbitrarily taken as N/N_A = 50 mM. Identifiability of N using the analytical model shows some correlation to the collinearity and sensitivity indices. Collinearity between parameters is lesser in the numerical model, so identifiability in the numerical model is expected to improve in comparison to the analytical model.

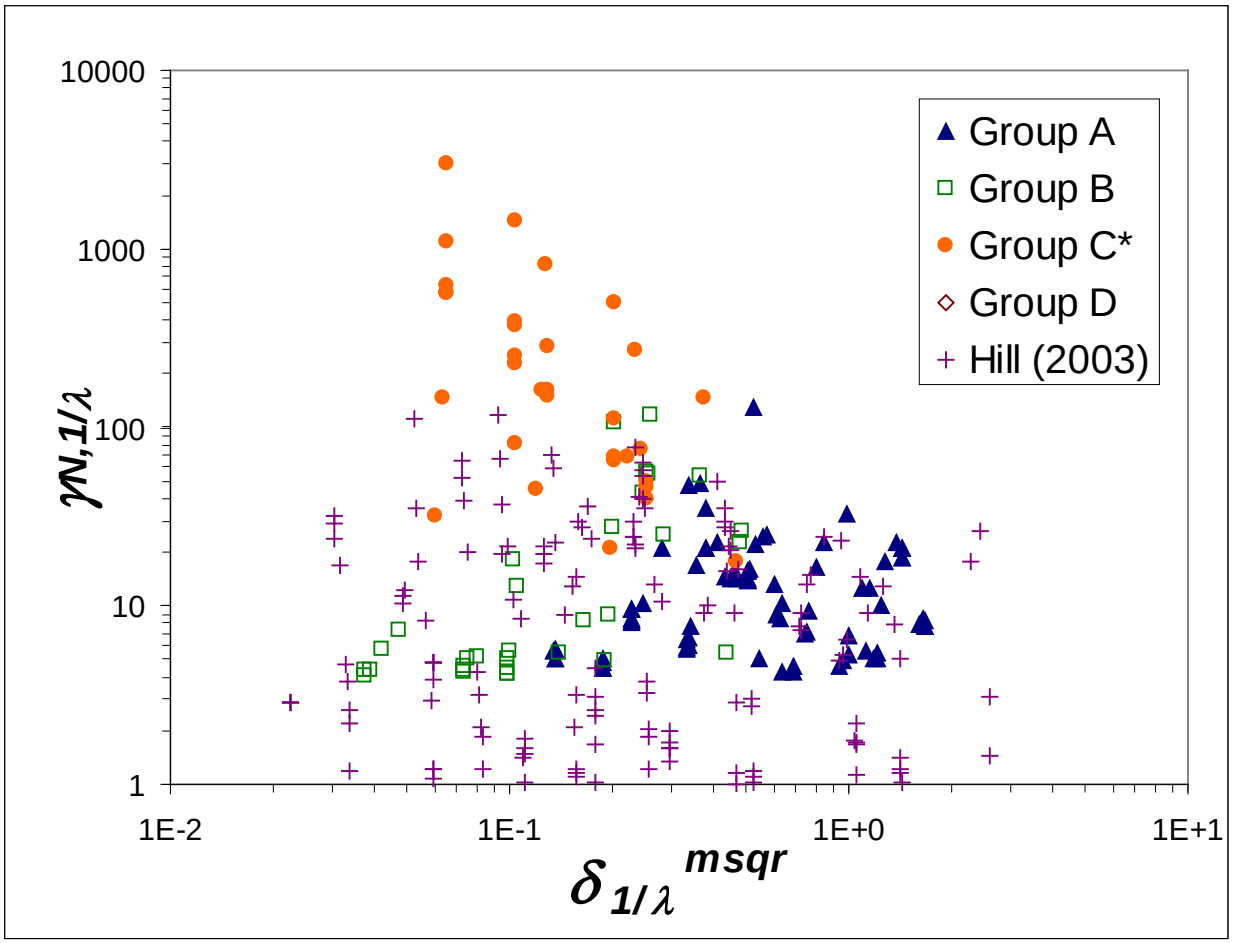

Figure A.5. Sensitivity to λ^{-1} and collinearity indices for the subset (N,λ^{-1}) for the 180 simulated cases. Parameter identifiability is grouped from good (Group A) to poor (Group D), with Groups defined analogously to those for d. The upper limit chosen to define identifiability for λ^{-1} is 100 nm, except when d is fixed: here, since the constraint $\lambda^{-1} \leq d$ is applied, Group C* is defined such that the likelihood region extends to d_{true}. Identifiability of λ^{-1} using the analytical model correlates well to the sensitivity and collinearity indices. Collinearity is generally lower for the numerical model, so identifiability should be improved; however, some cases are expected to fall in Groups B or C*, where λ^{-1} is only identifiable if one or both of the other parameters (d, N) are fixed, respectively.

A.5 Methods and data for Section 3.5.5 (Parameter identifiability of select systems)

Experimental samples or data sets were assessed in conjunction with the uncertainty analysis to confirm the results for the theoretical cases. Three types of coated nanoparticles were tested: poly(ethylene glycol) (PEG)-coated gold (Au) nanoparticles, poly(acrylic acid) (PAA)-coated magnetite (Fe_3O_4) nanoparticles, and poly(styrene sulfonate) (PSS)-coated reactive nano-iron particles (RNIP).

PEG-coated Au particles were prepared and measured for this study. Citrate-reduced Au nanoparticles (~13 ± 1.3 nm primary particle diameter by TEM (unpublished data from Stella Marinakos); 28 nm intensity-weighted diameter, polydispersity index (PdI) 0.17, by dynamic light scattering (Malvern Instruments, Westborough, MA)) were provided in suspension by Stella Marinakos (Duke University, Durham, NC) and were synthesized by sodium citrate reduction of hydrogen tetrachloroaurate in water at reflux. Poly(ethylene glycol) methyl ether thiol, average M_n 1000, was purchased from Sigma Aldrich. PEG stock solution was prepared by dissolving solid PEG in DI water overnight. PEG surface modification of the Au nanoparticles was performed at pH 8.3 in 1 mM NaHCO3, by adding PEG stock solution to the Au-citrate stock suspension for a final concentration of 176 ppm Au-citrate and 0.1 g/L PEG. The sample was mixed on an end-over-end rotator at room temperature for 41 hours. Prior to measuring u_e, Au samples were washed two to three times of excess citrate and polymer by centrifuging at 57,000 g (~22,000 rpm) for 3 hr 20 min, removing the supernatant, and resuspending in DI water.

PAA-coated Fe_3O_4 samples used were prepared and described previously.[24] The primary particle diameter is ~20-30 nm (PdI 0.26); the DLS intensity-weighted diameter is 170 nm. The PAA was synthesized by ATRP with average molecular weight ~14,400. The general procedure

for adsorption of polymer to the nanoparticles was performed similarly to above, but with 1-2 g/L polymer and 6 g/L particle concentrations, at pH 9-10, mixing end-over-end for 18-24 hr, and washing twice at 42,275 g (27,500 rpm) for 1 hr 20 min, then 40 min.

Electrophoretic mobility (u_e) data for PSS-coated RNIP were published previously,[8] with no additional data taken for this study. The primary particle diameter is ~40 nm, and the PSS molecular weight was ~70,000.

For u_e measurements, samples were diluted to 10 and 30 ppm for the PEG-coated Au and PAA-coated Fe_3O_4 samples, respectively. Ionic strength adjustments were made using NaCl. Six samples ranging from 2 to 20 mM, and six samples ranging from 5 to 80 mM NaCl, were prepared for PEG-Au and PAA-Fe_3O_4, respectively. Ionic strengths higher than 20 mM were unusable for PEG-Au due to extensive aggregation and settling of particles. (Sensitivity indices recomputed for the 180 simulated cases using six data from 2 to 20 mM or from 5 to 80 mM are not different enough from those using ten data from 5 to 80 mM to change conclusions drawn on identifiability.) pH was adjusted by HCl/NaOH addition to 8.3 and 8.5 for PEG-Au and PAA-Fe_3O_4, respectively. Samples were equilibrated overnight and pH readjusted if necessary, immediately prior to measurement. Electrophoretic mobility was measured on a Malvern Zetasizer 3000 instrument. The average and standard deviation of the mean u_e was taken over at least six repeat measurements. Data and best fits are shown in Figure A.6. The weighted sum of squared errors, normalized by the number of data, are similar for all fits (0.33, 0.19, and 0.15 for PEG-Au, PAA-Fe_3O_4, and PSS-RNIP, respectively). Therefore, better identifiability of layer thickness for PEG-Au can be attributed to model sensitivity, not differences in goodness of fit.

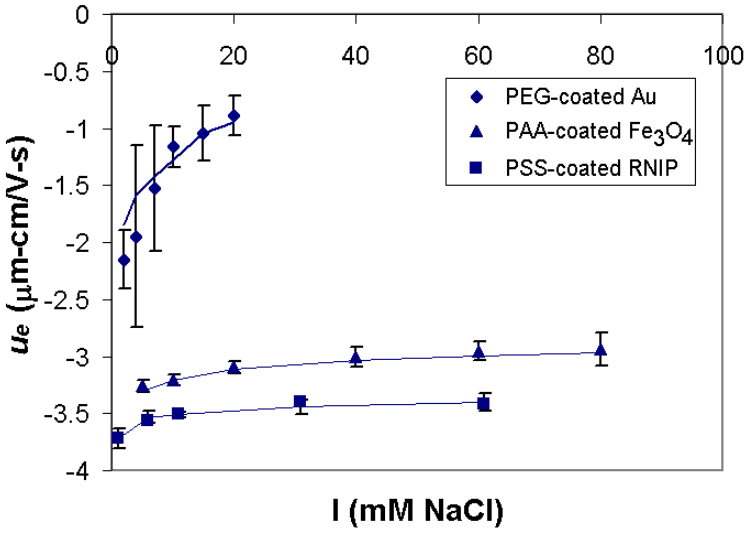

Figure A.6. Data (filled symbols) and weighted least square model fits (lines) for experimental cases. Error bars represent standard deviation in experimental measurements.

A.6 Attachment efficiency expressions for nanoparticle transport in packed columns

Expressions used to compute attachment efficiency in a packed column from experimental data, α_{exp}, and the single-collector collision efficiency, η_0,[25] are presented below.

$$\alpha_{\exp} = -\ln\left(\frac{C}{C_0}\right)\frac{4a_c}{3(1-\varepsilon)\eta_0 L} \tag{A.1}$$

where a_c is the radius of glass beads, ε is the packed bed porosity, η_o is the predicted single-collector contact efficiency in the absence of repulsive interactions, L is the length of the column, and C_o and C are the influent and effluent particle concentrations, respectively.

$$\eta_0 = 2.4A_s^{1/3}N_R^{-0.081}N_{Pe}^{-0.715}N_{vdW}^{0.052} + 0.55A_sN_R^{1.675}N_A^{0.125} + 0.22N_R^{-0.24}N_G^{1.11}N_{vdW}^{0.053} \tag{A.2}$$

where A_s is a porosity-dependent parameter, N_R is the aspect ratio, N_{Pe} is the Peclet number, N_{vdW} is the van der Waals number, N_A is the attraction number, and N_G is the gravity number. The reader is referred to the work by Tufenkji and Elimelech for definitions of these dimensionless parameters.[25]

A.7 Semi-empirical correlation of attachment efficiency

A semi-empirical correlation developed by Phenrat et al.[9] was assessed in the study of coated nanoparticle deposition by Hotze, Louie, et al.[26] for its accuracy in predicting the measured attachment efficiencies from the measured particle and adsorbed layer properties. Phenrat et al. derived dimensionless parameters for the correlation by using the Buckingham-Π approach based on an analysis of several sets of attachment efficiency data for coated nanoparticles. One of these parameters N_{LEK}, includes physical layer properties that contribute to steric repulsion forces and decreased frictional forces that arise when coatings are on the surface of a particle:[9]

$$N_{LEK} = \frac{d_p d_M^2 u_s \Gamma N_a \rho_p}{\mu M_W} \tag{A.3}$$

where d_p is the particle diameter, d_M is the adsorbed layer thickness, u_s is the porewater velocity in the column, Γ is the surface concentration of adsorbed macromolecule, N_a is Avagadro's number, ρ_p is coating density, μ is viscosity, and M_W is the coating molecular weight. The overall semi-empirical correlation equation including this dimensionless number gives the predicted attachment value, α_{pre}:[9]

$$\alpha_{pre} = 10^{-1.35} N_{LO}^{0.39} N_{E1}^{-1.17} N_{LEK}^{-0.10} \quad \text{(A.4)}$$

The predicted and experimental attachment efficiencies are shown in Figure A.7. For all coated nanoparticles, the attachment efficiency is under-predicted by an order of magnitude using the semi-empirical correlation.

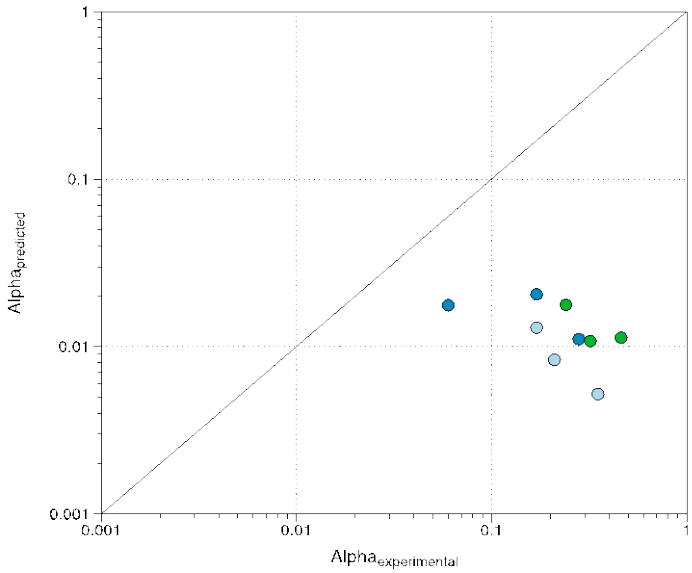

Figure A.7. Attachment efficiencies predicted from a semi-empirical correlation ($Alpha_{predicted}$) versus those experimentally determined in column experiments ($Alpha_{experimental}$). Colors represent bare (white), humic acid- (light blue), PAA- (dark blue), and BSA-coated (green) particles.

A.8 Reassessment of transport correlations for the deposition of coated nanoparticles

The numerical solution to the soft particle electrokinetic model was employed to reassess the set of electrophoretic mobility data used by Phenrat et al.[9] for development of a semi-empirical correlation to predict the deposition of coated nanoparticles in porous media. For the previously published correlation, adsorbed layer thicknesses were estimated using Ohshima's analytical solutions[2] to the soft particle electrokinetic model. In this study, the electrophoretic

mobility data are reanalyzed using Hill's numerical solution,[22] which is expected to provide more accurate estimates of layer thickness, as previously discussed.

The materials included in this study are polystyrene latex (PSL), hematite (Fe_2O_3), and titanium dioxide (TiO_2) nanoparticles coated with humic and fulvic acids (HA and FA), poly(styrene sulfonate) (PSS), polyaspartate (PAP), and carboxymethylcellulose (CMC). The electrophoretic mobility data and nanoparticle deposition data were collected by Phenrat et al.,[9] Amirbahman and Olson,[27,28] and Franchi and O'Melia.[29] For the original correlation, Ohshima's analytical solution to the electrokinetic model[2] was used to estimate layer thicknesses. Here, layer thickness estimates are revised using Hill's numerical solution.[22] The attachment efficiency correlation was then revised by Tanapon Phenrat using the Buckingham-Π approach, as described previously.[9] The ability of the modified correlation to capture the observed deposition data was compared to the original model. Revised layer thickness estimates are reported in Table A.3.

Table A.3. Layer thickness estimates using the analytical and numerical electrokinetic models for coated particles assessed by Phenrat et al.[9]

Particle	Coating	Layer thickness (nm)	
		Analytical model[2]	**Numerical model[22]**
Polystyrene latex[29]	Suwannee River Humic Acid (SRHA)	3	4
Polystyrene latex[28]	Pahokee Peat Humic Acid (PHA)	2	8
Polystyrene latex[28]	Georgetown Fulvic Acid (GFA)	0.7	6
Hematite[27]	Pahokee Peak Fulvic Acid (PFA)	4	14
Hematite[27]	Georgetown Fulvic Acid (GFA)	4.2	4
Hematite[27]	Pahokee Peat Humic Acid (PHA)	7	11
Hematite[9]	Polystyrene sulfonate (PSS)	70	**8**
Hematite[9]	Polyaspartic acid (PAP)	52	**7**
Hematite[9]	Carboxymethyl cellulose (CMC)	32	**14**
Titanium dioxide[9]	Polystyrene sulfonate (PSS)	70	**16**
Titanium dioxide[9]	Polyaspartic acid (PAP)	54	**4**
Titanium dioxide[9]	Carboxymethyl cellulose (CMC)	36	**4**

The most significant difference in layer thickness estimates between the two models is observed for the macromolecules with the highest molecular weights (polystyrene sulfonate, polyaspartic acid, and carboxymethyl cellulose), whereas the layer thickness estimates for fulvic and humic acids agree within 10 nm for the two models. These results are consistent with expectations, considering the poorer accuracy and sensitivity of the analytical model for thicker and more highly charged layers, as would be expected for the synthetic polyelectrolytes and carboxymethyl cellulose. The results suggest that these layer thicknesses were overestimated using the analytical model, consistent with the conclusions drawn from the likelihood plots (Section 3.5.1).

The implications of the overestimation of layer thickness in predicting the attachment efficiency or deposition of coated nanoparticles are considered. It is expected that the overestimated layer thicknesses would result in lower predicted attachment efficiencies from the correlation (α_{pre}) compared to the experimentally measured attachment efficiencies (α_{exp}). To investigate this hypothesis, the correlation was revised using the improved layer thickness estimates. The original[9] and revised correlation equations are given in Equations A.5 and A.6, respectively. N_{LO}, N_{E1}, $N_{DL,}$ and N_{LEK} are the London number, a dimensionless electrokinetic parameter, a double layer force parameter, and the layer electrokinetic parameter, respectively.[9]

Original correlation[9]: $$\alpha_{pre} = 10^{-1.35} N_{LO}^{0.39} N_{E1}^{-1.17} N_{LEK}^{-0.10} \quad \text{(A.5)}$$

Revised correlation: $$\alpha_{pre} = 10^{-2.58} N_{LO}^{-0.401} N_{E1}^{-0.613} N_{DL}^{-0.457} N_{LEK}^{-0.416} \quad \text{(A.6)}$$

The data in the original correlation by Phenrat et al.[9] that correspond to the nanoparticles coated with high molecular weight polymers are highlighted (filled symbols) in Figure A.8(a). Some deviation is observed in the ability of the overall correlation to predict these polymer-coated nanoparticles compared to from the humic- and fulvic-coated nanoparticles.

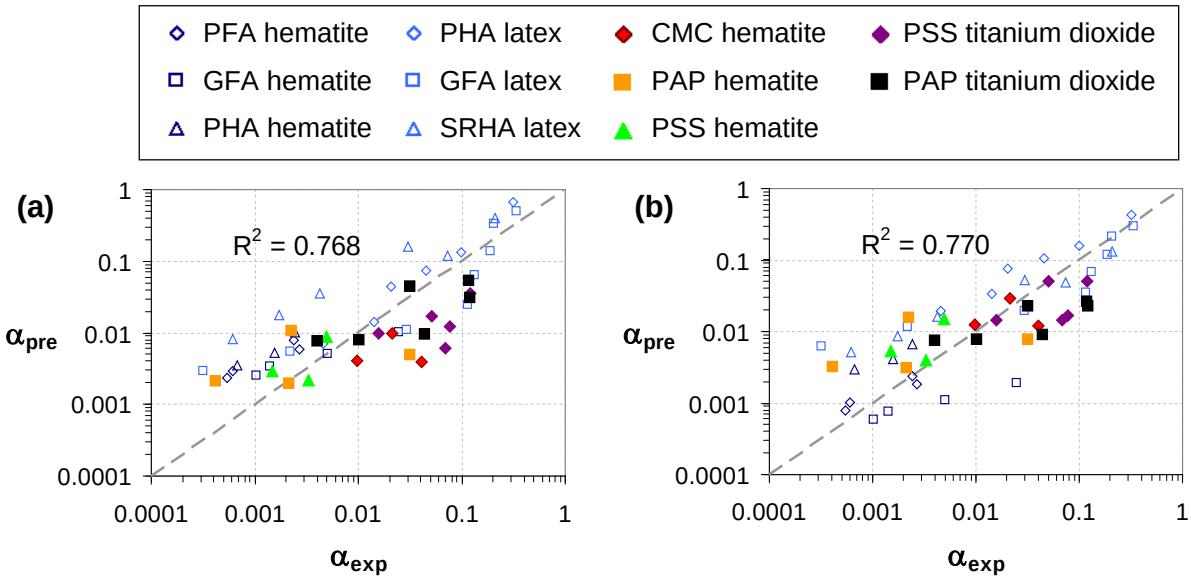

Figure A.8. Comparison of correlations for the attachment efficiency of coated nanoparticles, developed with layer properties estimated using analytical[9] (a) or numerical[22] (b) solutions to the soft particle electrokinetic model. Layer thickness estimates from the numerical model were lower than those from the analytical model, resulting in small improvements in the correlation for the polymer-coated nanoparticles (filled symbols) with $\alpha_{exp} > 0.05$. However, the correlations have similar goodness of fit overall. Both correlations were produced by T. Phenrat; adsorbed layer properties for the revised correlation were provided by S. Louie.

The revised correlation is shown in Figure A.8(b). In the revised correlation, some improvement is observed for the nanoparticles coated with high molecular weight polymers where $\alpha_{exp} > 0.05$. However, the coefficient of determination (R^2) for the correlation across all samples is similar in the original and revised correlations. These results suggest that, while minor improvement to the prediction of nanoparticle deposition is possible for the polymer-coated nanoparticles when more accurate layer thicknesses are provided, additional properties of the coated nanoparticles or the system are needed to better explain the variance in the data. Furthermore, considering the insignificant change in the coefficient of determination given the lower layer thicknesses for all of the polymer-coated nanoparticles (representing 40% of the data

used to develop the correlations), further improvement in the accuracy of the layer thickness estimate (e.g., within ~ 10 nm) is not expected to further improve the correlation for the data set used here.

A.9 Possible route for parameter reduction

Expressions can be written (Equations A.7, A.11, and A.13) relating the layer thickness, charge density, and permeability to a single fitted parameter, i.e. the volume fraction of polymer in the adsorbed layer, ϕ (assuming uniform segment density), and properties that can be measured externally (adsorbed mass by solution depletion methods, number of charges per macromolecule or monomer from titration methods) or estimated (number of charges from known polyelectrolyte structure, segment radius or volume). These expressions are presented below. Expressions for the Brinkman screening length were presented by Hill et al. and Doane et al.[22,30]

Layer thickness (d)

$$V_{shell} = 4/3(\pi)[(a+d)^3-a^3] \tag{A.7}$$

$$d = \left(\frac{3}{4\pi}V_{shell} + a^3\right)^{1/3} - a \tag{A.8}$$

$$\text{where} \quad V_{shell} = \frac{V_{poly}}{\phi} \tag{A.9}$$

$$V_{poly} = \frac{\Gamma A_{NP}}{MW_{segment}}V_{segment} \tag{A.10}$$

$$\boxed{d = \left(\frac{3}{4\pi}\frac{\Gamma A_{NP}V_{segment}}{MW_{segment}\phi} + a^3\right)^{1/3} - a} \tag{A.11}$$

Charge density (N)

$$N = \frac{n_{charge}}{V_{shell}} = r_{charge} n_{segment} \tag{A.12}$$

$$\boxed{N = r_{charge} \frac{\phi}{V_{segment}}} \tag{A.13}$$

Permeability or Brinkman screening length (λ^{-1} or l_b)

$$l_b^{-2} = 6\pi n_{segment} a_{segment} F(\phi) \tag{A.14}$$

$$\text{where} \quad F(\phi) = \frac{1 + 3(\phi/2)^{1/2} + (135/64)\phi \ln\phi + 16.456\phi}{1 + 0.681\phi - 8.48\phi^2 + 8.16\phi^3} \approx 1 + 3(\phi/2)^{1/2} \tag{A.15}$$

$$n_{segment} = \frac{3\phi}{4\pi\left(a_{segment}\right)^3} \quad \text{or} \quad n_{segment} = \frac{\phi}{V_{segment}} \tag{A.16}$$

$$\boxed{l_b^{-2} = 6\pi \frac{\phi}{V_{segment}} a_{segment} \left(1 + 3(\phi/2)^{1/2}\right)} \tag{A.17}$$

Variable definitions

m_{poly} = total mass adsorbed per particle

A_{NP} = surface area of particle

$\Gamma = m_{poly} / A_{NP}$ = adsorbed mass

a = radius of particle

V_{shell} = volume of adsorbed layer

V_{poly} = total volume of polymer per particle

ϕ = volume fraction of polymer in adlayer

$MW_{segment}$ = molecular weight of monomer

$V_{segment}$ = volume of monomer

n_{charge} = total number of charges per particle

r_{charge} = charge-to-segment ratio

$n_{segment}$ = number density of segments

$a_{segment}$ = segment radius

References for Appendix A

(1) Kiers, P. J. M.; Bos, R.; van der Mei, H. C.; Busscher, H. J. The electrophoretic softness of the surface of Staphylococcus epidermidis cells grown in a liquid medium and on a solid agar. *Microbiol.-UK* **2001**, *147*, 757-762.
(2) Ohshima, H. Electrophoresis of soft particles. *Adv. Colloid Interface Sci.* **1995**, *62* (2-3), 189-235.
(3) Rodriguez, V. V.; Busscher, H. J.; Norde, W.; van der Mei, H. C. Softness of the bacterial cell wall of Streptococcus mitis as probed by microelectrophoresis. *Electrophoresis* **2002**, *23* (13), 2007-2011.
(4) Tsuneda, S.; Jung, J.; Hayashi, H.; Aikawa, H.; Hirata, A.; Sasaki, H. Influence of extracellular polymers on electrokinetic properties of heterotrophic bacterial cells examined by soft particle electrophoresis theory. *Colloids Surf., B* **2003**, *29* (2-3), 181-188.
(5) Tsuneda, S.; Aikawa, H.; Hayashi, H.; Hirata, A. Significance of cell electrokinetic properties determined by soft-particle analysis in bacterial adhesion onto a solid surface. *J. Colloid Interface Sci.* **2004**, *279* (2), 410-417.
(6) Viota, J. L.; de Vicente, J.; Ramos-Tejada, M. M.; Duran, J. D. G. Electrical double layer and rheological properties of yttria-stabilized zirconia suspensions in solutions of high molecular weight polyacrylic acid polymers. *Rheol. Acta* **2004**, *43* (6), 645-656.
(7) Viota, J. L.; de Vicente, J.; Duran, J. D. G.; Delgado, A. Stabilization of magnetorheological suspensions by polyacrylic acid polymers. *J. Colloid Interface Sci.* **2005**, *284* (2), 527-541.
(8) Phenrat, T.; Saleh, N.; Sirk, K.; Kim, H. J.; Tilton, R. D.; Lowry, G. V. Stabilization of aqueous nanoscale zerovalent iron dispersions by anionic polyelectrolytes: adsorbed anionic polyelectrolyte layer properties and their effect on aggregation and sedimentation. *J. Nanopart. Res.* **2008**, *10* (5), 795-814.
(9) Phenrat, T.; Song, J. E.; Cisneros, C. M.; Schoenfelder, D. P.; Tilton, R. D.; Lowry, G. V. Estimating attachment of nano- and submicrometer-particles coated with organic macromolecules in porous media: Development of an empirical model. *Environ. Sci. Technol.* **2010**, *44* (12), 4531-4538.
(10) Ho, C. C.; Kondo, T.; Muramatsu, N.; Ohshima, H. Surface structure of natural rubber latex particles from electrophoretic mobility data. *J. Colloid Interface Sci.* **1996**, *178* (2), 442-445.
(11) Lopez-Leon, T.; Ortega-Vinuesa, J. L.; Bastos-Gonzalez, D.; Elaissari, A. Cationic and anionic poly(N-isopropylacrylamide) based submicron gel particles: Electrokinetic properties and colloidal stability. *J. Phys. Chem. B* **2006**, *110* (10), 4629-4636.
(12) Lopez-Viota, J.; Mandal, S.; Delgado, A. V.; Toca-Herrera, J. L.; Moller, M.; Zanuttin, F.; Balestrino, M.; Krol, S. Electrophoretic characterization of gold nanoparticles functionalized with human serum albumin (HSA) and creatine. *J. Colloid Interface Sci.* **2009**, *332* (1), 215-223.
(13) Ohshima, H. Electrophoresis of soft particles: Analytic approximations. *Electrophoresis* **2006**, *27* (3), 526-533.
(14) Duval, J. F. L.; Ohshima, H. Electrophoresis of diffuse soft particles. *Langmuir* **2006**, *22* (8), 3533-3546.

(15) Viota, J. L.; Rudzka, K.; Trueba, A.; Torres-Aleman, I.; Delgado, A. V. Electrophoretic Characterization of Insulin Growth Factor (IGF-1) Functionalized Magnetic Nanoparticles. *Langmuir* **2011**, *27* (10), 6426-6432.
(16) Clements, A.; Gaboriaud, F.; Duval, J. F. L.; Farn, J. L.; Jenney, A. W.; Lithgow, T.; Wijburg, O. L. C.; Hartland, E. L.; Strugnell, R. A. The Major Surface-Associated Saccharides of Klebsiella pneumoniae Contribute to Host Cell Association. *PLoS One* **2008**, *3* (11).
(17) Duval, J. F. L.; Wilkinson, K. J.; Van Leeuwen, H. P.; Buffle, J. Humic substances are soft and permeable: Evidence from their electrophoretic mobilities. *Environ. Sci. Technol.* **2005**, *39* (17), 6435-6445.
(18) Duval, J. F. L.; Busscher, H. J.; van de Belt-Gritter, B.; van der Mei, H. C.; Norde, W. Analysis of the interfacial properties of fibrillated and nonfibrillated oral streptococcal strains from electrophoretic mobility and titration measurements: Evidence for the shortcomings of the 'classical soft-particle approach'. *Langmuir* **2005**, *21* (24), 11268-11282.
(19) Langlet, J.; Gaboriaud, F.; Gantzer, C.; Duval, J. F. L. Impact of chemical and structural anisotropy on the electrophoretic mobility of spherical soft multilayer particles: The case of bacteriophage MS2. *Biophys. J.* **2008**, *94* (8), 3293-3312.
(20) Hyono, A.; Gaboriaud, F.; Mazda, T.; Takata, Y.; Ohshima, H.; Duval, J. F. L. Impacts of Papain and Neuraminidase Enzyme Treatment on Electrohydrodynamics and IgG-Mediated Agglutination of Type A Red Blood Cells. *Langmuir* **2009**, *25* (18), 10873-10885.
(21) Hill, R. J.; Saville, D. A. 'Exact' solutions of the full electrokinetic model for soft spherical colloids: Electrophoretic mobility. *Colloids Surf., A* **2005**, *267* (1-3), 31-49.
(22) Hill, R. J.; Saville, D. A.; Russel, W. B. Electrophoresis of spherical polymer-coated colloidal particles. *J. Colloid Interface Sci.* **2003**, *258* (1), 56-74.
(23) Brun, R.; Reichert, P.; Kunsch, H. R. Practical identifiability analysis of large environmental simulation models. *Water Resour. Res.* **2001**, *37* (4), 1015-1030.
(24) Golas, P. L.; Louie, S.; Lowry, G. V.; Matyjaszewski, K.; Tilton, R. D. Comparative Study of Polymeric Stabilizers for Magnetite Nanoparticles Using ATRP. *Langmuir* **2010**, *26* (22), 16890-16900.
(25) Tufenkji, N.; Elimelech, M. Correlation equation for predicting single-collector efficiency in physicochemical filtration in saturated porous media. *Environmental Science & Technology* **2004**, *38* (2), 529-536.
(26) Hotze, E. M.; Louie, S. M.; Lin, S.; Wiesner, M. R.; Lowry, G. V. Nanoparticle core properties affect attachment of macromolecule-coated nanoparticles to silica surfaces. *Environ. Chem.* **2014**, *11* (3), 257-267.
(27) Amirbahman, A.; Olson, T. M. Transport of humic matter-coated hematite in packed-beds. *Environ. Sci. Technol.* **1993**, *27* (13), 2807-2813.
(28) Amirbahman, A.; Olson, T. M. The role of surface conformations in the deposition kinetics of humic matter-coated colloids in porous-media. *Colloids Surfaces A* **1995**, *95* (2-3), 249-259.
(29) Franchi, A.; O'Melia, C. R. Effects of natural organic matter and solution chemistry on the deposition and reentrainment of colloids in porous media. *Environ. Sci. Technol.* **2003**, *37* (6), 1122-1129.
(30) Doane, T. L.; Chuang, C. H.; Hill, R. J.; Burda, C. Nanoparticle zeta-Potentials. *Accounts Chem. Res.* **2012**, *45* (3), 317-326.

Appendix B: Supporting information for Chapters 5, 6, and 7

B.1 Additional methods and characterization of natural organic matter (NOM) samples (Chapters 5 and 6)

Detailed methods and additional characterization of the NOM samples (Pahokee Peat humic acid (PPHA), Suwannee River humic acid (SRHA), Suwannee River natural organic matter (SRNOM), Elliott Soil fulvic acid (ESFA), Pony Lake fulvic acid (PLFA) and Pacific Ocean fulvic acid (POFA)) are reported here.

B.1.1 Fluorescence EEM: Correction for inner filter effect

To correct for the inner filter effect, UV absorbance spectra were collected on the same samples used for the fluorescence measurements, using a Cary 300 Bio UV-Vis spectrophotometer (Agilent Inc.) and a 1 cm quartz cuvette. Assuming the fluorescence emission is measured from the center of the cell, the pathlengths are 0.5 cm for both the excitation and emission light. The corrected fluorescence intensities, I_{corr}, were calculated from the observed fluorescence intensities, I_{obs}, using Equation B.1:[1]

$$I_{corr} = I_{obs}\,\text{antilog}\left(\frac{A_{ex} + A_{em}}{2}\right) \tag{B.1}$$

where A_{ex} and A_{em} are the absorbances for a 1 cm pathlength at the excitation and emission wavelengths, respectively.

B.1.2 SEC-MALS chromatograms for filtrate and retentate fractions of all NOM samples

The chromatograms for the filtrate and retentate fractions are shown in Figure B.1 (with the chromatograms for the whole samples shown again for comparison). Good removal of the > 100,000 g/mol portion in the filtrate and the < 100,000 g/mol portion in the retentate is observed.

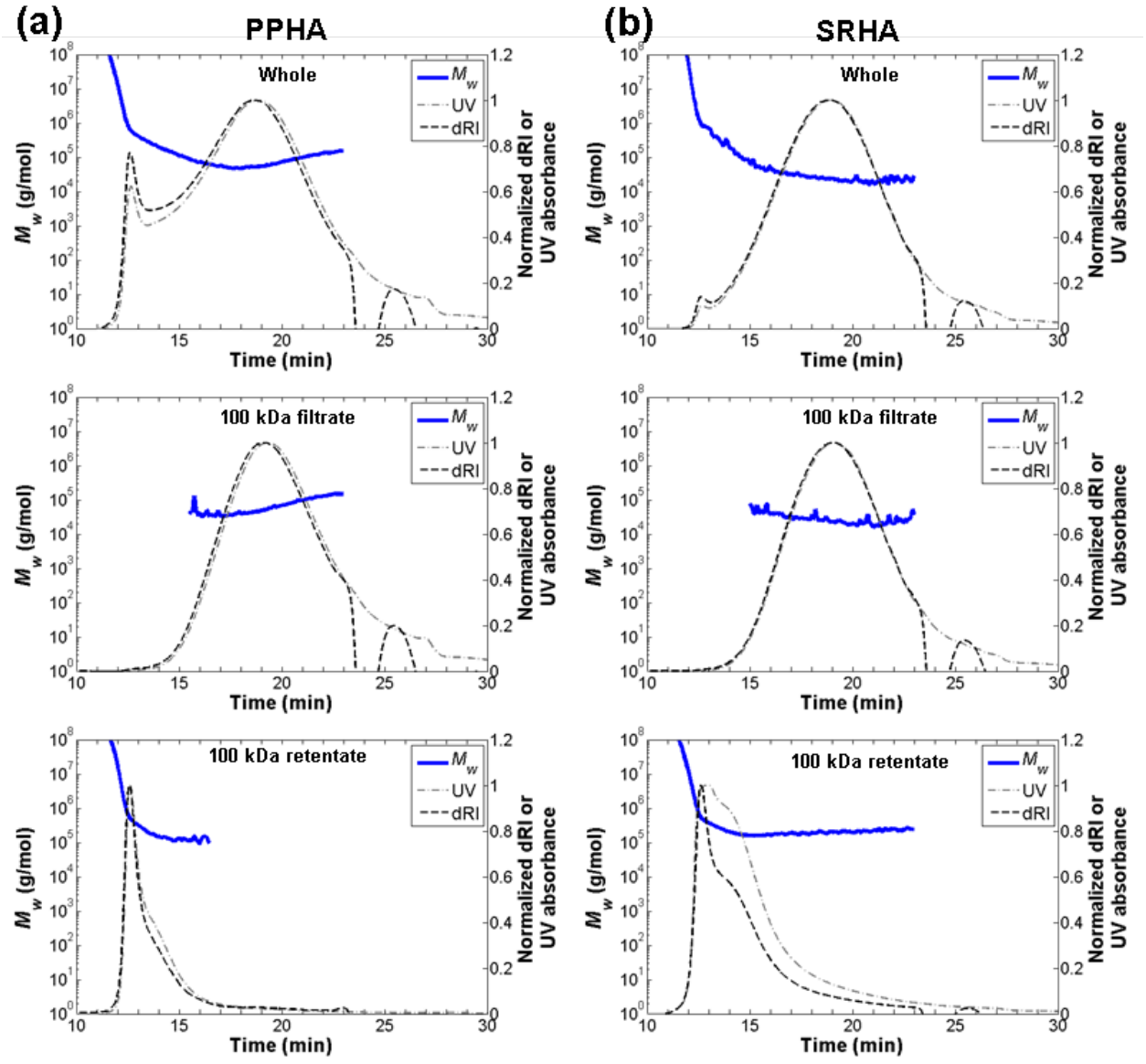

Figure B.1 ***(continued on next page)***

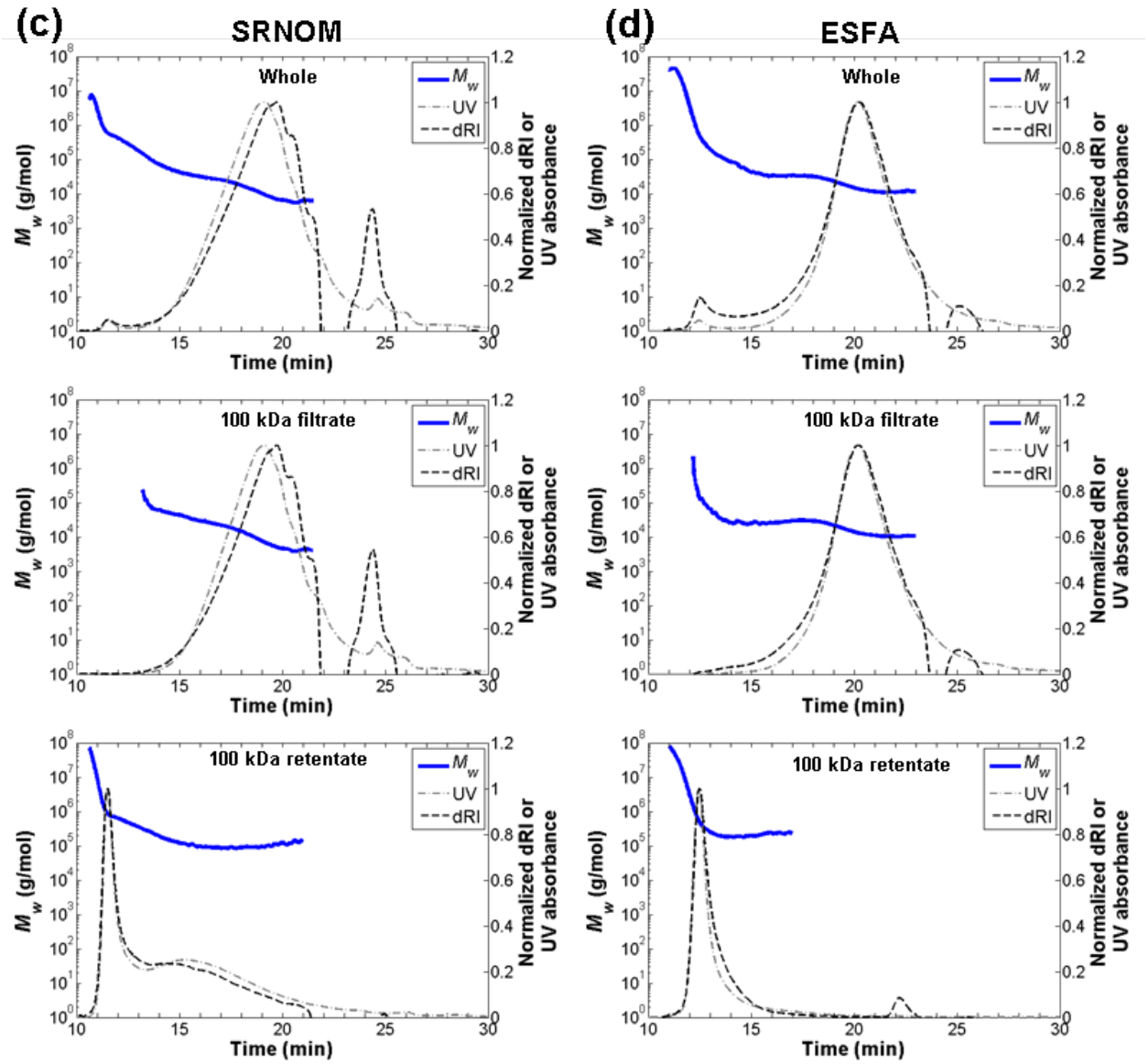

Figure B.1 ***(continued on next page)***

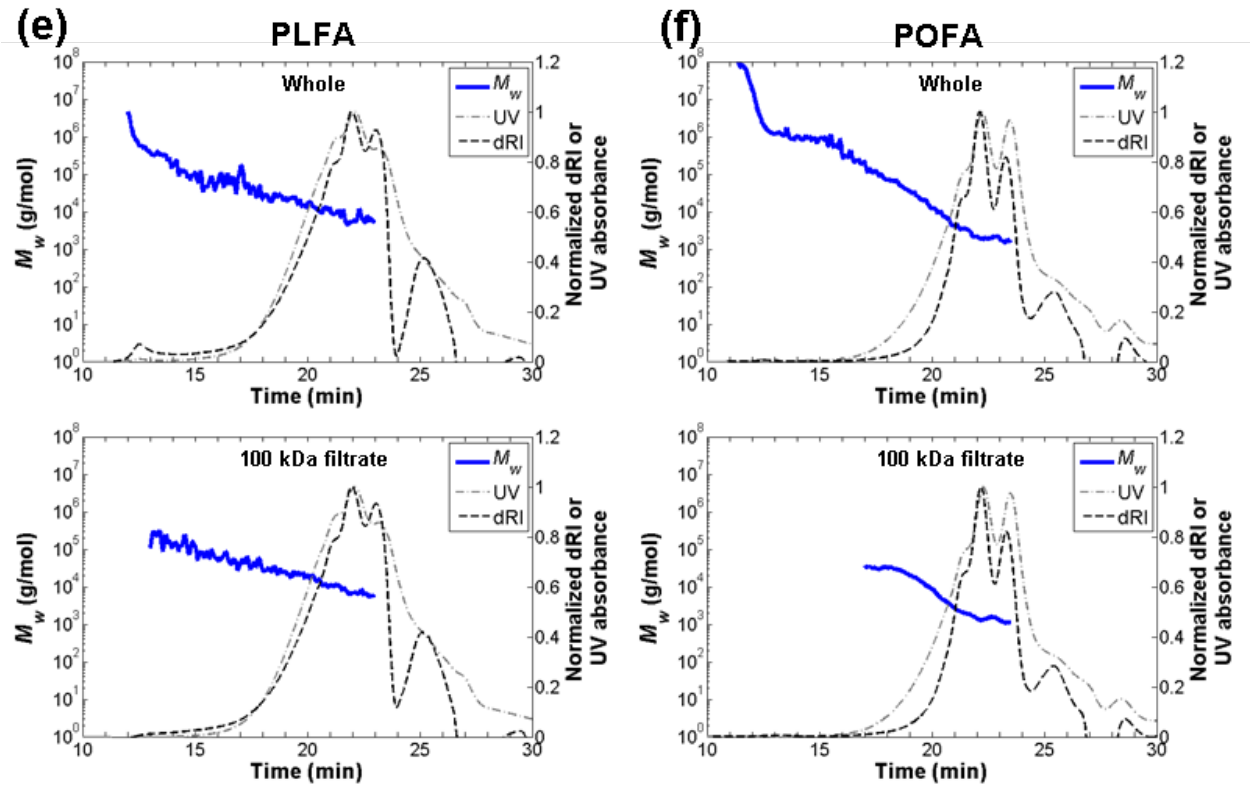

Figure B.1. SEC-MALS chromatograms for the whole, filtrate, and retentate fractions for PPHA (a), SRHA (b), SRNOM (c), ESFA (d), PLFA (e), and POFA (f). Blue lines shown the weight-average molecular weight determined by MALS (using the RI detector for concentration determination). Dark gray dashed lines and light gray dash-dotted lines represent the dRI and UV absorbance (normalized to the peak height), respectively. Insufficient retentate for PLFA or POFA was collected for this analysis.

B.1.3 Molecular weight determination from MALS software (ASTRA 5.3.4, Wyatt Technology)

The analysis of the MALS data to obtain the "unadjusted" molecular weights is described in this section. All calculations and processing are performed in the ASTRA 5.3.4 software (Wyatt Technology). The raw data collected by the instruments include the UV and dRI signal and the light-scattering signal (intensity) at 16 scattering angles. For all samples, the dRI signal was used to determine the eluting concentration, and the first-order Zimm model (the default

method in the ASTRA 5.3.4 software) was used to fit the light scattering data to obtain the weight-averaged molecular weight (M_w) at each measurement along the chromatogram. Data from the two detectors at the lowest angles (28° and 32°), and depending on the noise in the signal, from additional low angle detectors up to 50°, were not included in the Zimm analysis. The signal at these low scattering angles (i.e., forward scattering) is sensitive to shedding of large particles from the SEC column, resulting in high noise compared to the signal due to the NOM. (Typically, exclusion of these data does not change the overall MALS results, but simply results in a smoother line for M_w versus elution time.) For a detailed discussion of accuracy in MALS measurements, the reader is referred to the work of Andersson et al.[2]

Prior to each set of NOM runs on SEC-MALS, a bovine serum albumin (BSA) or ribonuclease A (RnA) standard was run. These standards were prepared at 2 g/L in DI water. The RnA peak or the monomer peak of BSA was used to perform detector alignment, band broadening corrections, and normalization. Monodisperse molecules with radius of gyration less than 10 nm are required for these operations. Detector alignment shifts the UV, MALS, and dRI chromatograms along elution time to align the peak in the detector signals, thus correcting for the delay between detectors due to the tubing volume. Band broadening correction adjusts the signals for diffusion or dispersion from the first online detector (UV) to the subsequent detectors (MALS, followed by dRI). Normalization is performed for each of the 16 independent light scattering detectors (located at 16 scattering angles), where the intensity measured by each detector is normalized against that of the 90° detector, assuming isotropic (equal) scattering for a small molecule.

The alignment, band broadening, and normalization values are then applied to the NOM samples that are subsequently analyzed. The weight-averaged molecular weight across the selected peak of the SEC-MALS chromatogram is calculated in ASTRA 5.3.4 as follows:

$$M_w = \frac{\sum (c_i M_i)}{\sum c_i} \tag{B.2}$$

where c_i and M_i are the concentration and molecular weight determined at each point along the chromatrogram. It is noted that this formula differs from the typical expression for weight-averaged molecular weight because each M_i already represents a weight-averaged molecular weight of the NOM eluting at each point.

Number-averaged molecular weights (M_n) can also be computed from M_w and the concentration. M_n will not be accurate for these NOM samples because perfect separation is not achieved in the SEC column; however, these values are reported in Section B.1.4 for comparison. The formula used in ASTRA 5.3.4 is as follows:

$$M_n = \frac{\sum c_i}{\sum \left(\frac{c_i}{M_i} \right)} \tag{B.3}$$

B.1.4 Fitting of SEC-MALS molecular weight distributions

The late-eluting portion of the NOM samples could not be analyzed by MALS because of the low signal to noise ratio (due to the small size or molecular weight) or overlap with the RI signal for the solvent peak. The mass fraction of the sample that was analyzed, *n*, was first

determined by dividing the mass of NOM in the portion of the dRI peak that was analyzed by the total mass of NOM injected into the SEC column. The un-analyzed fraction ($1 - n$) was assumed to have lower molecular weight than the NOM that was analyzed. The cumulative weight fraction computed directly by MALS (ASTRA 5.3.4 software, Wyatt Technology), $F_x(x)$, was then adjusted by Equation B.4 to account for the un-analyzed fraction, giving the corrected cumulative weight fraction, $F_x(x)_{,corr}$:

$$F_x(x)_{,corr} = (1\text{-}n) + n\, F_x(x) \tag{B.4}$$

where x is the weight-averaged molecular weight obtained from each MALS measurement along the SEC chromatogram.

The molecular weight distribution of NOM has previously been shown to fit well to a lognormal distribution.[3] The cumulative distribution function for the lognormal distribution is given by Equation B.5:

$$F_x(x) = \frac{1}{2}\mathrm{erfc}\left(-\frac{\log_{10} x - \mu}{\sigma\sqrt{2}}\right) \tag{B.5}$$

The mean of the lognormal distribution, μ, and standard deviation of the lognormal distribution, σ, were fitted to minimize the sum of squared errors between the modeled $F_x(x)$ from Equation B.5 and $F_x(x)_{,corr}$ from Equation B.4.

All fitted cumulative distribution functions are shown in Figure B.2. The fitted distributions generally capture the location of the peak well, although the high molecular weight

tail is typically not fully represented; therefore, the mean of the distribution can be underestimated using this fitting method.

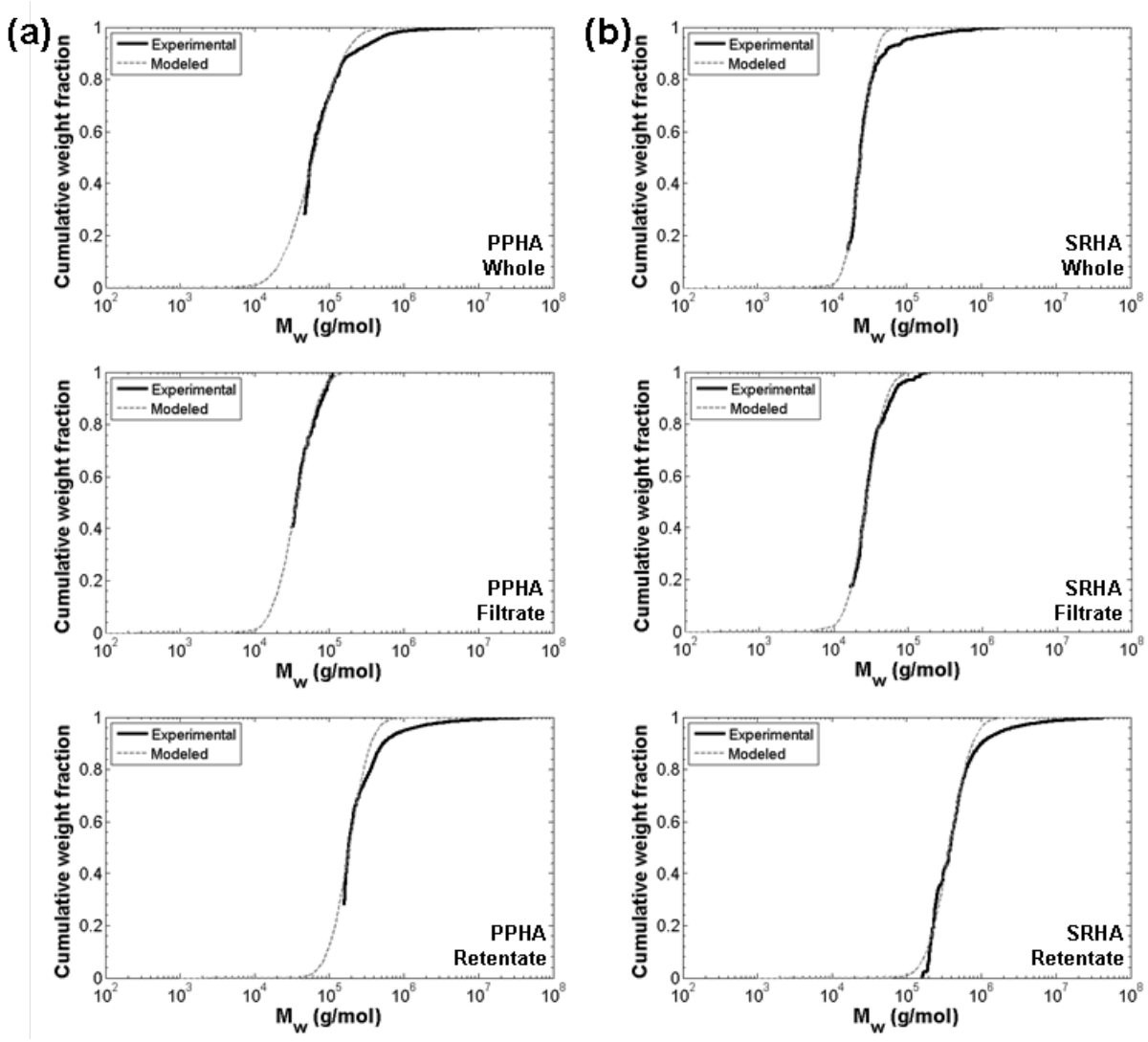

Figure B.2. ***(continued on next page)***

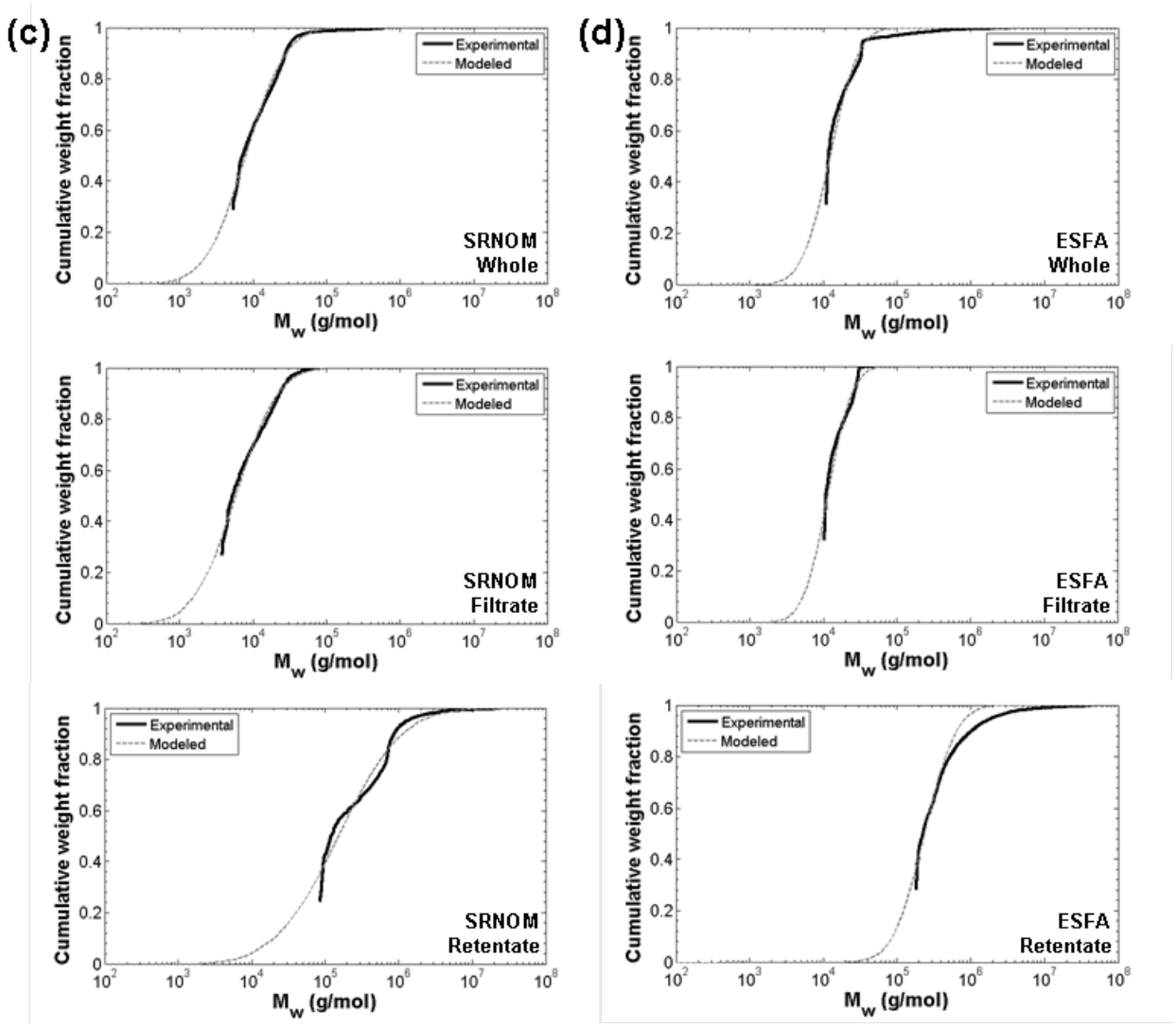

Figure B.2. ***(continued on next page)***

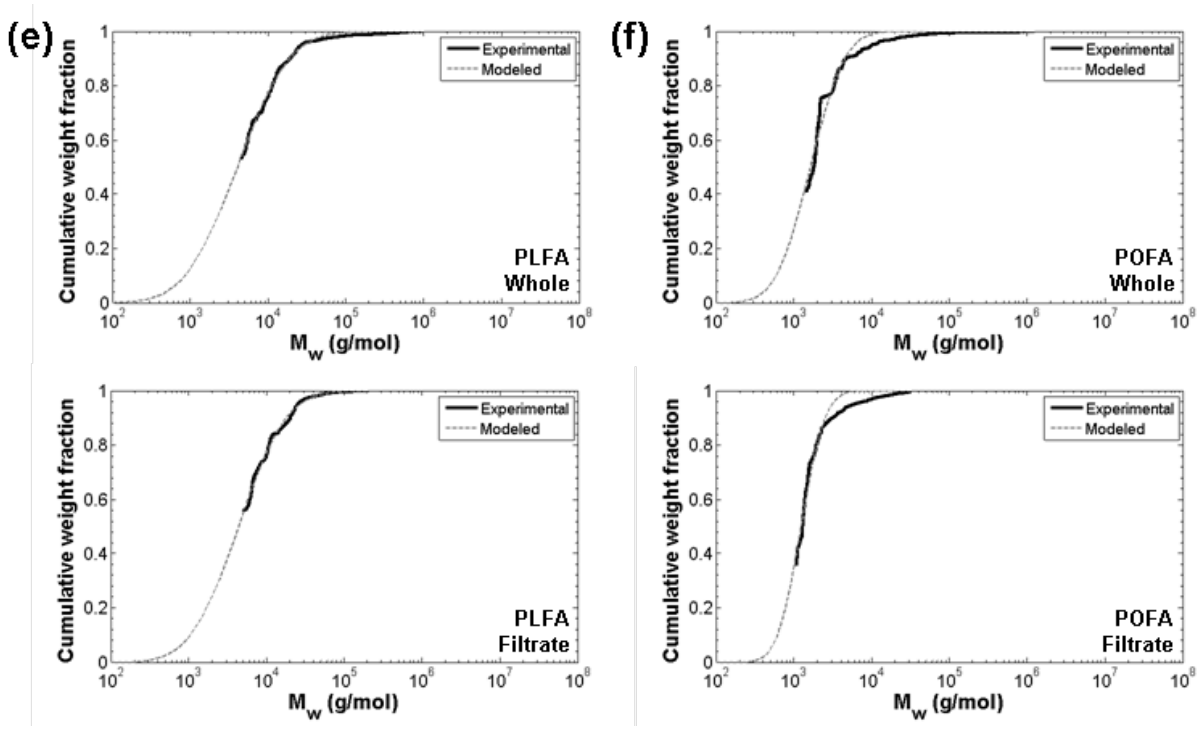

Figure B.2. Experimental and modeled cumulative distribution functions for unfractionated samples and 100 kDa filtrate, and 100 kDa retentate fractions of (a) PPHA, (b) SRHA, (c) SRNOM, (d) ESFA, (e) PLFA, and (e) POFA. The black lines show the corrected experimental distribution functions, $F_{corr}(x)$, and the gray dotted lines show the fitted lognormal distributions. Insufficient retentate for PLFA and POFA was collected for SEC-MALS measurements.

The cumulative distribution functions for all six unfractionated samples are compared together in Figure B.3 below:

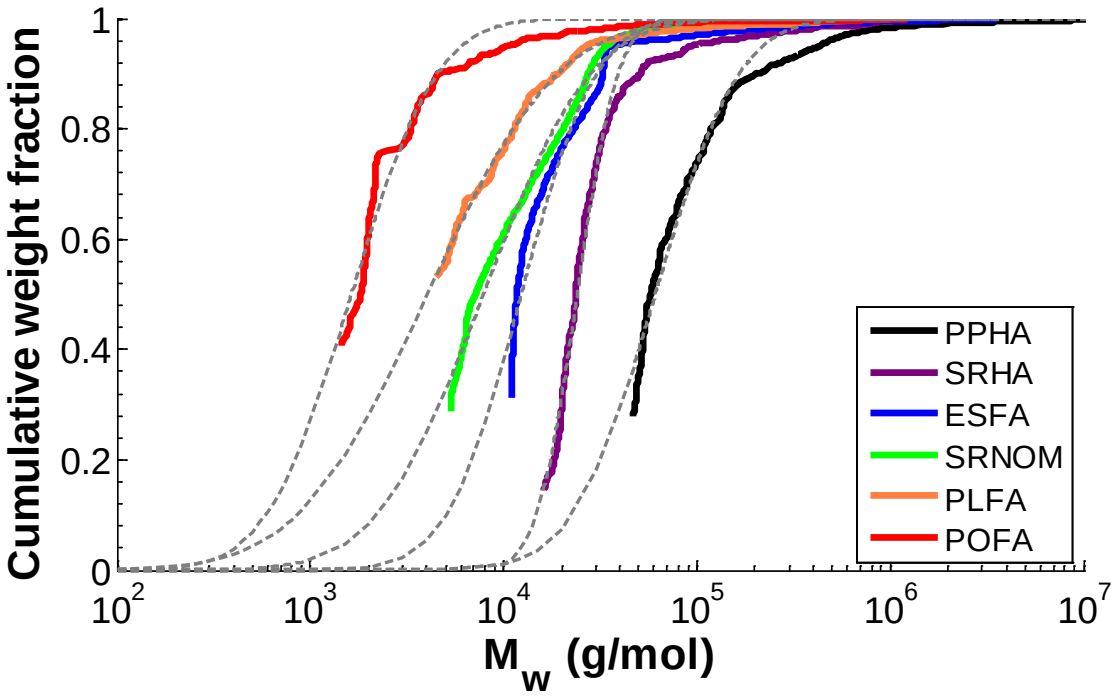

Figure B.3. Cumulative distribution functions for unfractionated PPHA, SRHA, ESFA, SRNOM, PLFA, and POFA. The solid lines represent the corrected experimental distribution functions, $F_{corr}(x)$ and $f_{corr}(x)$, and the gray dotted lines represent the modeled lognormal distributions.

The geometric mean of the weight-average molecular weight distribution (M_g) was computed from the fitted mean of the lognormal distribution (base 10) by the following equation:

$$M_g = 10^{\mu} \tag{B.6}$$

M_g, μ, and σ (Equation B.5) are reported in Table B.1, along with the unadjusted weight-average molecular weight (M_w), number-average molecular weight (M_n), and polydispersity (i.e., M_w/M_n) reported directly by the MALS software (ASTRA 5.3.4, Wyatt Technology).

Table B.1. Mean molecular weights and polydispersity or standard deviation, unadjusted or fitted from a lognormal distribution model

NOM type	NOM fraction	Unadjusted			Fitted (Equations B.5 and B.6)		
		M_w (kg/mol)	M_n (kg/mol)	Poly-dispersity	M_g (kg/mol)	μ (log g/mol)	σ (log g/mol)
PPHA	Whole	307	80	3.9	61	4.79	0.34
	Filtrate	67	54	1.2	36	4.56	0.24
	Retentate	857	242	3.5	185	5.27	0.23
SRHA	Whole	114	27	4.3	24	4.38	0.17
	Filtrate	27	25	1.1	27	4.44	0.21
	Retentate	980	346	2.8	372	5.57	0.24
SRNOM	Whole	23	10.4	2.2	7.9	3.90	0.43
	Filtrate	13	7.4	1.7	5.8	3.76	0.45
	Retentate	691	185	3.7	151	5.18	0.68
ESFA	Whole	85	16	5.2	12.3	4.09	0.3
	Filtrate	17	14	1.2	12.0	4.06	0.26
	Retentate	1030	318	3.2	231	5.37	0.34
PLFA	Whole	38	9.5	4.1	4.0	3.61	0.53
	Filtrate	16	10.0	1.6	4.4	3.64	0.49
	Retentate	n.d.	n.d.	n.d.	n.d.	n.d.	n.d.
POFA	Whole	4.2	2.5	1.7	1.6	3.21	0.35
	Filtrate	2.9	1.7	1.7	1.3	3.10	0.24

n.d.: not determined (insufficient sample collected for this analysis)

As discussed above and in Chapter 5, none of these measures is perfectly accurate. The advantages and disadvantages of each measure are listed in Table B.2.

Table B.2. Advantages and disadvantages of the molecular weight descriptors obtained from the unadjusted or fitted distributions

Descriptor	Advantages	Disadvantages
Unadjusted M_w	Only uses directly measured MALS data	Does not include late-eluting portion of NOM Highly sensitive to selection of peak at low elution time (where very high molecular weights are obtained)
Unadjusted M_n	Less sensitive to peak selection than M_w	Does not include late-eluting portion of NOM Not accurate for MALS when eluting fractions are not monodisperse
Unadjusted polydispersity	Accounts for presence of small amounts of very high molecular weight NOM	Same as those for the unadjusted M_w and M_n
Fitted μ and M_g (Equations B.5 and B.6)	Accounts for late-eluting portion of NOM	Assumes all late-eluting NOM has lower molecular weight than those measured Typically does not capture the high molecular weight tail of the distribution
Fitted σ (Equation B.5)	Less sensitive to peak selection than the unadjusted polydispersity (M_w/M_n)	Typically does not capture the high molecular weight tail of the distribution

Despite the differences in the methods, the mean molecular weights in Table B.1 tend to correlate with each other (Figure B.4). However, the unadjusted M_w more clearly distinguishes the whole NOM from the filtrate fraction for some samples (circled on Figure B.4), compared to the unadjusted M_n or the fitted M_w.

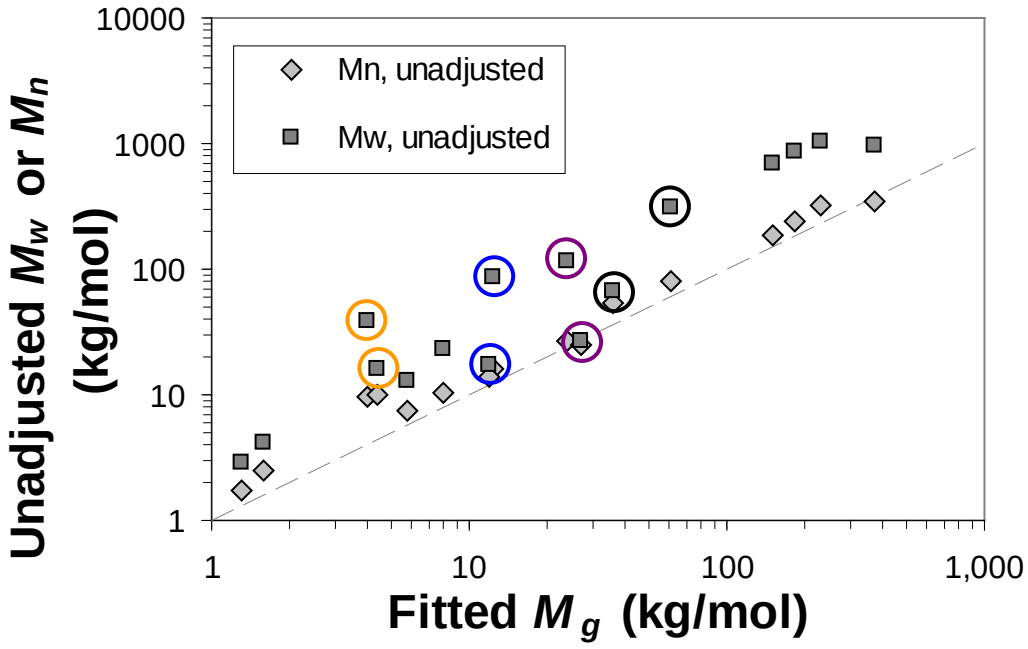

Figure B.4. Comparison of the geometric mean, M_g, of the fitted lognormal distribution of weight-averaged molecular weights (*x*-axis) with the weight- and number-average molecular weights (M_w and M_n) directly measured by MALS (*y*-axis). Molecular weights from either method tend to correlate. However, the unadjusted M_w is always higher than the geometric mean, M_g, obtained from fitting. Notably, the higher M_w of the unfractionated NOM compared to the fractionated NOM for PLFA (circled in orange), ESFA (blue), SRHA (purple), and PPHA (dark gray) is most clearly distinguished in the unadjusted M_w. The dashed line represents a 1:1 correlation.

B.2. Additional characterization and aggregation data for SRNOM (Chapter 5)

B.2.1 SRNOM (Chapter 5): SEC-MALS in 2 mM phosphate buffer

SEC-MALS analysis was conducted for the Suwannee River natural organic matter 0.2 μm filtrate (NOM_1), the < 100,000 g/mol filtrate (NOM_f), and the > 100,000 g/mol retentate (NOM_r) using 2 mM phosphate buffer at pH 7 (Figures B.5 and B.6). At this lower ionic strength, most of the sample elutes before the DI water solvent, allowing a more complete

analysis of the sample. However, poor resolution of the void and main peaks is obtained. Faster elution could be due to reduced adsorption at lower ionic strength, or swelling of NOM molecules or aggregates due to decreased electrostatic screening. Weight-average molecular weights, M_w, are reported in Table B.3. M_w for each sample was within 10% of that obtained using 4 mM phosphate buffer.

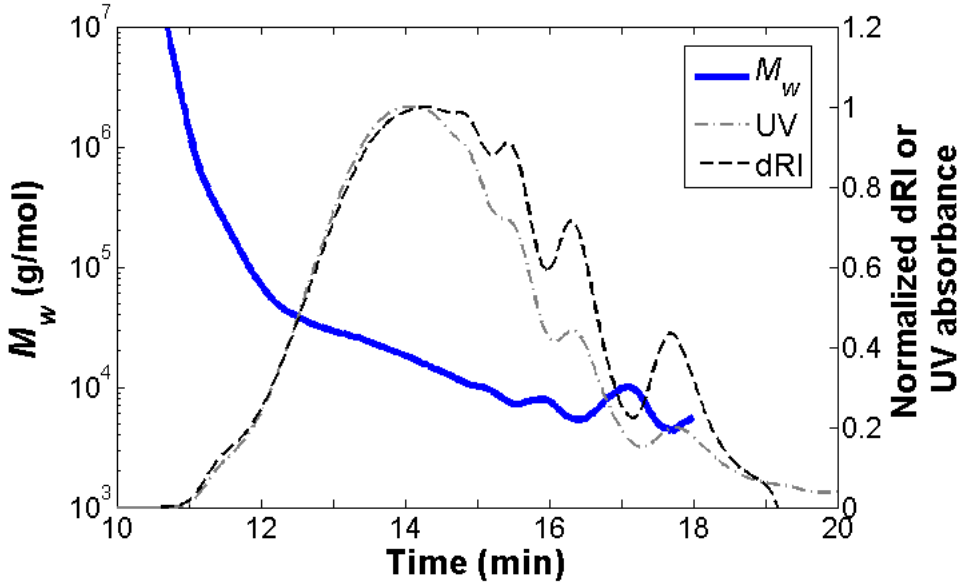

Figure B.5. SEC-MALS results for NOM_1 in 2 mM phosphate buffer, pH 7.

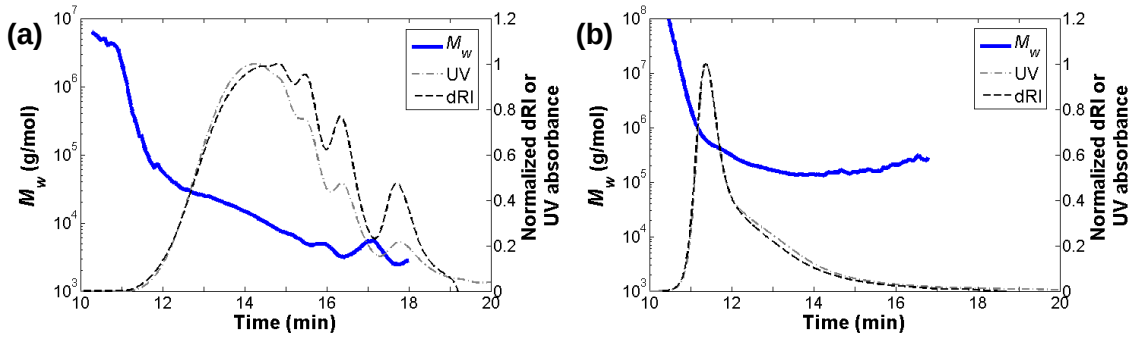

Figure B.6. SEC-MALS results for (a) NOM_f and (b) NOM_r in 2 mM phosphate buffer, pH 7. Molecular weights are similar to those determined in higher ionic strength buffer (4 mM phosphate with 25 mM NaCl, pH 7).

Table B.3. M_w for NOM_1, NOM_f, and NOM_r in 2 mM phosphate buffer (not adjusted for unanalyzed portion at elution times > 18 min)

Eluent	Fraction	Peak selection (min)	M_w (kg/mol)
2 mM phosphate, pH 7	NOM_1 (entire sample)	10-18	23.9
	NOM_r	10-18	665
	NOM_f	10-18	13.9

B.2.2 SRNOM (Chapter 5): DLS and SEC-MALS in NP aggregation solution conditions

DLS and SEC-MALS were performed on NOM samples without NPs in the solution conditions used for the aggregation experiments, 100 mM NaCl with 1 mM $NaHCO_3$, pH 8.3. DLS measurements were performed on the highest concentrations of NOM used (560 ppm NOM_1, 550 ppm NOM_f, and 10 ppm NOM_r) before and after addition of NaCl; no significant light scattering was observed for any sample. SEC-MALS performed on the NOM_1 sample showed a similar range of molecular weights but smaller void peak area (Figure B.7(a)), which may be attributable to conformational changes or additional adsorption to the column packing (ionic strength is higher than that of the 4 mM phosphate + 25 mM NaCl (pH 7) eluent). Comparison of the cumulative molecular weight distribution in the two eluents (Figure B.7(b)) indicates that approximately the same amount of > 100 kg/mol material is present (1.4 to 1.9 wt%) using either eluent; some disaggregation of < 30 kg/mol NOM may occur in 100 mM NaCl with 1 mM $NaHCO_3$ at pH 8.3 (M_w of the main peak is 14.1 kg/mol, in contrast to 15.6 kg/mol in the phosphate/NaCl eluent).

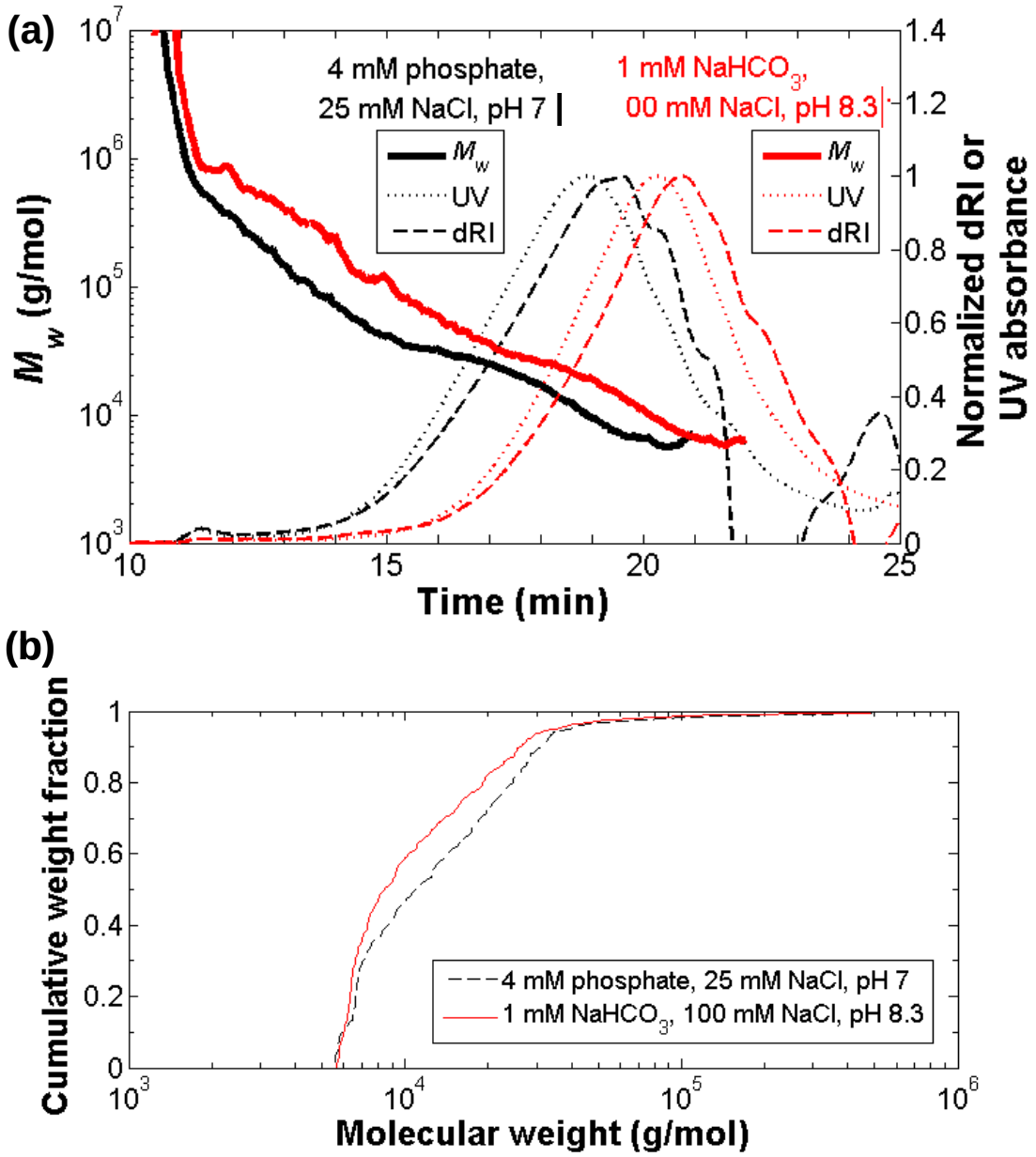

Figure B.7. SEC-MALS results (a) and unadjusted cumulative distribution of weight-averaged molecular weights (b) for NOM_1 (whole SRNOM) in NP aggregation solution conditions. Compared to the eluent used for characterization (4 mM phosphate, 25 mM NaCl, pH 7), minimal change in the shapes of the plots or the range of molecular weights is observed in 1 mM $NaHCO_3$ with 100 mM NaCl (pH 8.3), although some disaggregation of < 30 kg/mol NOM may occur. Cumulative weight fractions were not adjusted for the unanalyzed portion

B.2.3 SRNOM (Chapter 5): ^{1}H NMR spectra

The ^{1}H NMR spectra are shown in Figure B.8 for NOM_1 and NOM_f. Insufficient mass of NOM_r was available for ^{1}H NMR. Spectra were collected on a Bruker Avance 500 NMR instrument. NOM_1 and NOM_f sample preparation was similar to that described by Thorn *et al.*[4] Briefly, dissolved samples (~2 g/L) were adjusted to pH 8.5 with NaOH, then lyophilized and resuspended in D_2O twice. For the last resuspension, 27 mg of lyophilized sample was suspended into 0.6 mL D_2O. No significant differences were observed in the NOM_1 and NOM_f spectra.

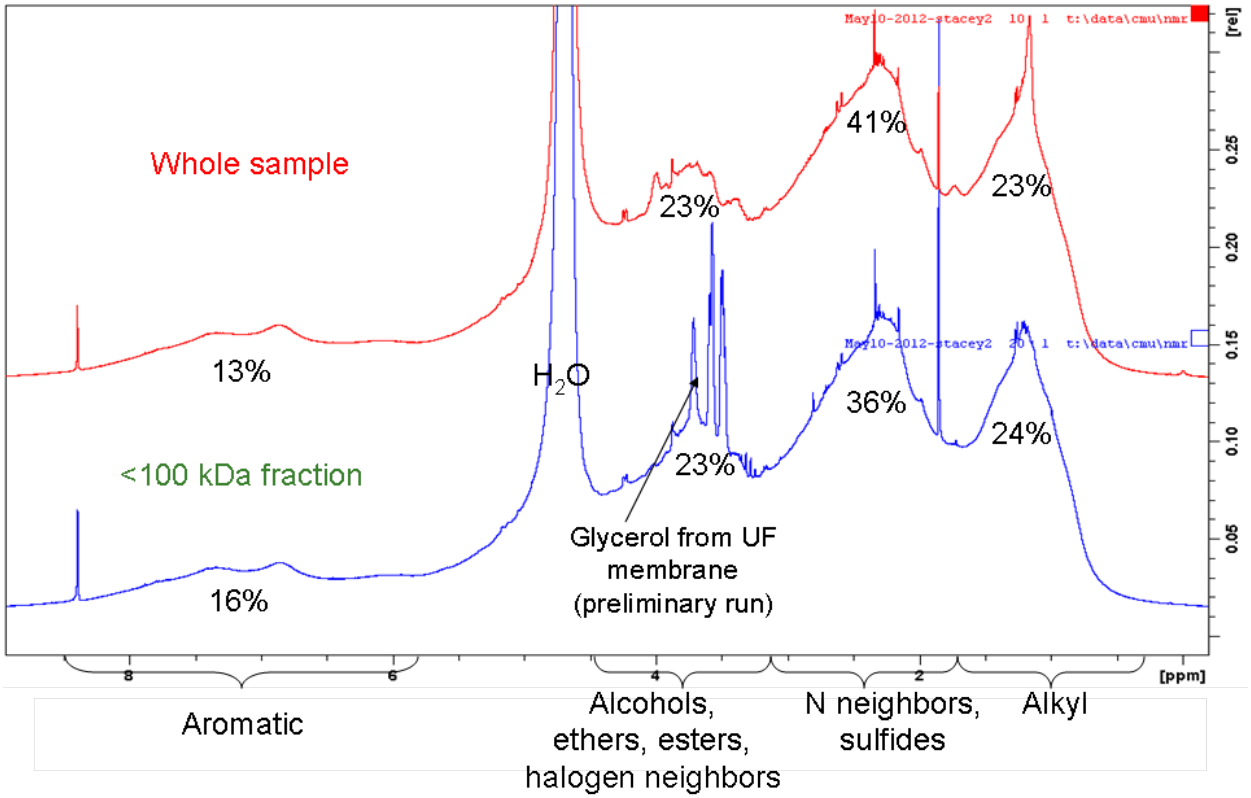

Figure B.8. ^{1}H NMR spectra for NOM_1 and NOM_f for SRNOM. Insufficient mass of NOM_r was collected for this analysis. No significant differences are apparent in the peaks present or relative peak areas. A portion of the filtrate was collected from a preliminary ultrafiltration (UF) performed without rinsing the Amicon membrane. Additional peaks in the filtrate spectrum are likely glycerol residue from the membrane. The membranes were rinsed for all other experiments to remove glycerol.

B.2.4 Aggregation of citrate-stabilized Au NPs without NOM

The aggregation of the citrate-stabilized gold nanoparticles (Au NPs) was first tested without NOM, varying the concentration of NaCl (Figure B.9). Aggregation increases with ionic strength as expected, due to charge screening of the citrate surface coating and hence reduced electrostatic repulsion. In 5 to 20 mM NaCl, minimal size increases are observed, and the size remains stable over time. Aggregation occurs in 50 mM NaCl, and rapid aggregation is observed in 100 mM NaCl.

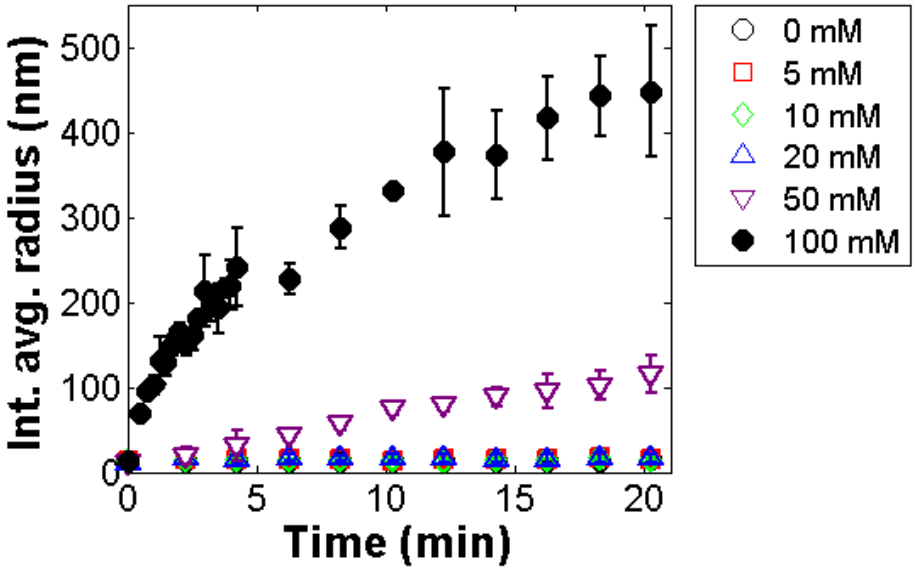

Figure B.9. Time-resolved intensity average radius by DLS for citrate-stabilized Au NPs in 0 to 100 mM NaCl. All samples are in 1 mM $NaHCO_3$ at pH 8.3. Rapid aggregation of the NPs is observed in 50 and 100 mM NaCl.

B.2.5 SRNOM (Chapter 5): Aggregation of Au NPs in 50 mM NaCl with 10 mM NOM_f or NOM_r

Because the particles are stable against rapid aggregation in up to 20 mM NaCl, higher ionic strengths were used for the SRNOM experiments to better observe possible differences in NOM effects. Aggregation behavior in 50 mM NaCl with 10 ppm of NOM_f or NOM_r is shown

in Figure B.10. Both fractions stabilize the NPs against aggregation similarly well at this ionic strength, so 100 mM NaCl was used for all following experiments to further challenge the system. Steric effects are more evident at this relatively high salt concentration, where electrostatic repulsion is screened.

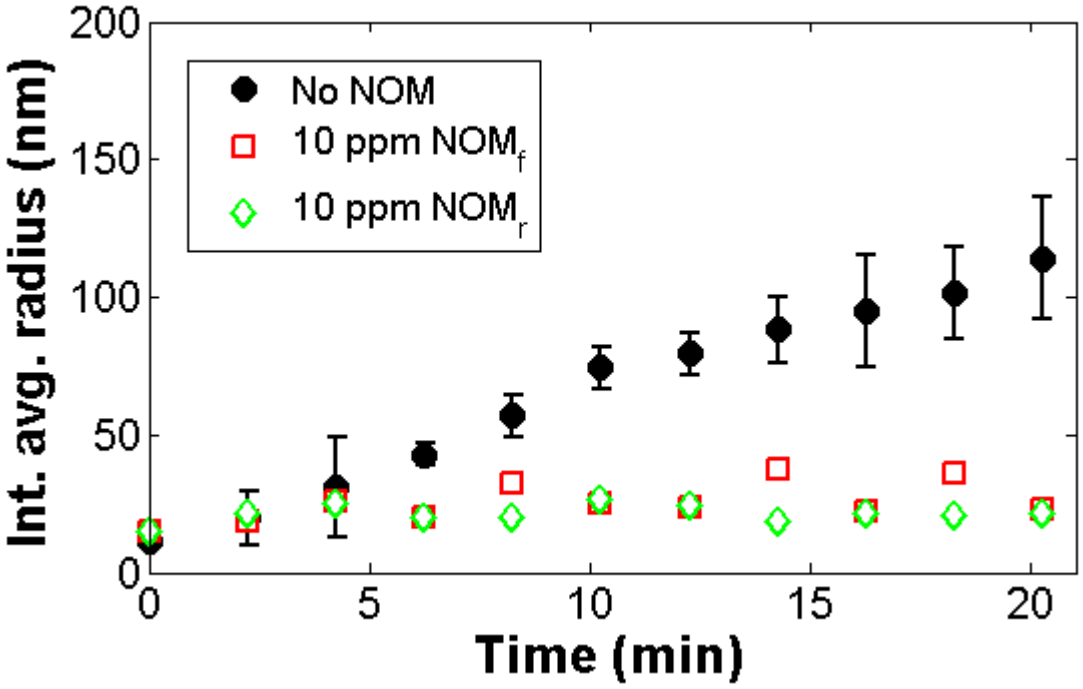

Figure B.10. Time-resolved DLS intensity average radius for citrate-stabilized Au NPs in 50 mM NaCl (with 1 mM $NaHCO_3$, pH 8.3) without NOM and in the presence of 10 ppm NOM_f or NOM_r. Both NOM fractions provide similarly good stability at this ionic strength.

B.2.6 SRNOM (Chapter 5): Aggregation of Au NPs in 100 mM NaCl, varying NOM_r concentrations

The effect of NOM_r concentration (from 0.18 to 10 ppm) is shown in Figure B.11. No stabilization is provided at 0.18 or 0.36 ppm NOM_r, but increasingly better NP stability is obtained as the NOM_r concentration is increased from 1 to 10 ppm.

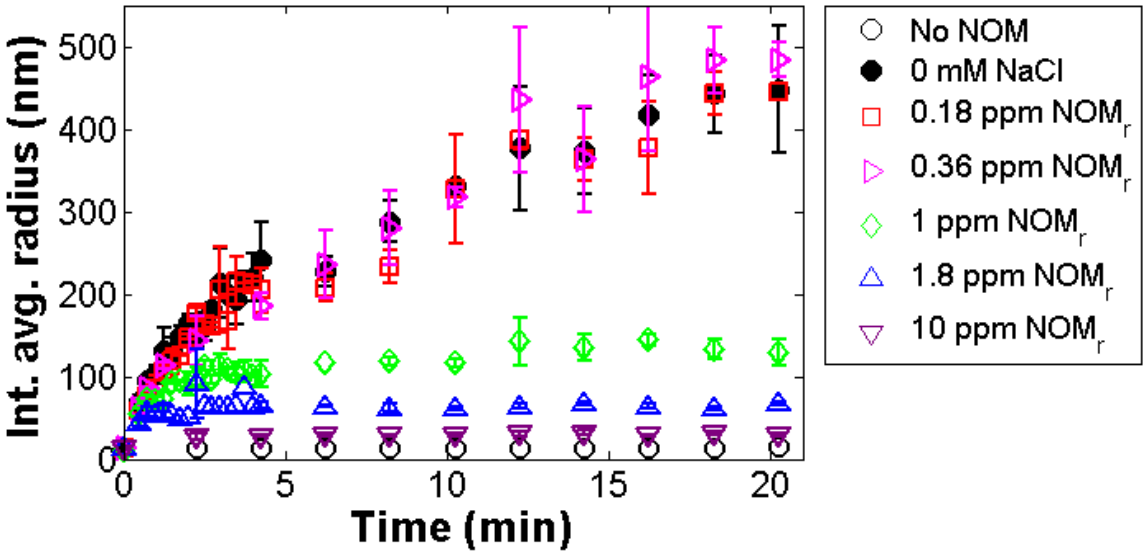

Figure B.11. Time-resolved DLS intensity average radius of citrate-stabilized Au NPs with 0.18, 0.36, 1, 1.8, and 10 ppm of NOM_r.

B.2.7 SRNOM (Chapter 5): TEM images for citrate-stabilized Au NPs in the presence of NOM_f

TEM micrographs for citrate-stabilized Au NPs with NOM_f coatings are shown in Figure B.12. The procedure was the same as that used for NOM_r in the main text (drop deposition of a suspension of 20 ppm Au NPs with 10 ppm NOM_f adjusted to pH 8.3 with NaOH). No coating is visible by TEM.

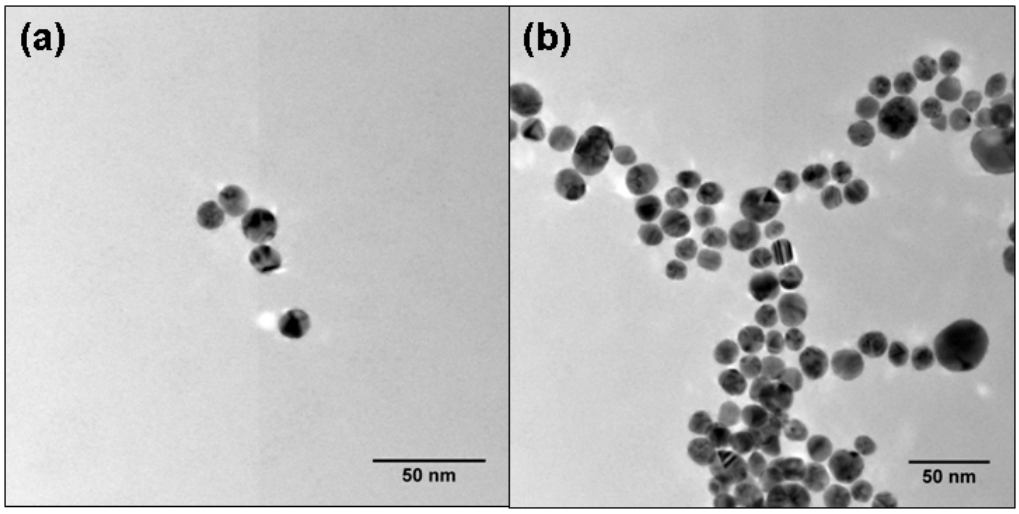

Figure B.12. TEM images of citrate-stabilized Au NPs in the presence of 10 ppm NOM_f.

B.3. Additional characterization and aggregation data across all NOM types (Chapter 6)

B.3.1 Mass recovery in the ultrafiltration process

A mass balance was performed on the 100 kDa ultrafiltration process for each NOM sample, using the inputted volume and TOC concentration and the collected volumes and concentrations of filtrate and retentate fractions. The mass recovered and lost are reported in Table B.4.

Table B.4. Mass recovery and loss in the 100 kDa centrifugal ultrafiltration units

NOM type	Wt % recovered in filtrate	Wt % recovered in retentate	Wt % lost onto filter or in rinse liquid
PPHA	59 %	27 %	13 %
SRHA	89 %	1.1 %	10 %
SRNOM	91 %	1.1 %	8 %
ESFA	97 %	3.3 %	3 %
PLFA	86 %	0.6 %	13 %
POFA	96 %	not collected	< 4 %

B.3.2 UV-vis absorbance spectra compared across NOM types

The UV-vis spectra shown in Figure 6.3 are replotted in Figure B.13 to better demonstrate trends across the six different types of NOM. Generally, the UV absorbance at 280 nm trends with the average molecular weight of the NOM, except for the retentate fractions. $SUVA_{280}$, $SUVA_{254}$, the exponential slope coefficient, and the average of aromaticities estimated from three correlations[5-7] are provided in Table B.5.

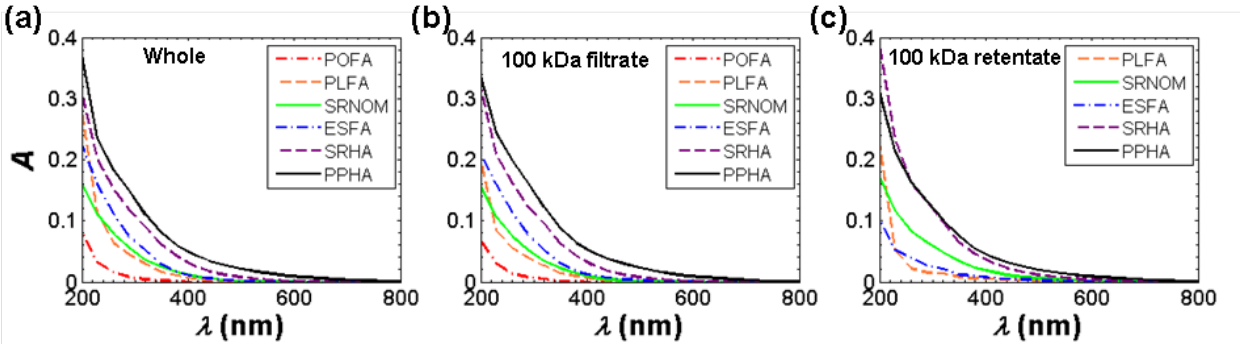

Figure B.13. UV absorbance of the whole NOM (a) and the filtrate (b) and retentate (c) fractions of NOM. Samples were prepared at 5 ppm in DI water.

Table B.5. UV-vis absorbance properties and estimated aromaticities for NOM fractions

NOM type	NOM fraction	$SUVA_{280}$ (L mg-1 cm-1)	$SUVA_{254}$ (L mg-1 cm-1)	Aromaticity (%)[5-7]	Slope coefficient
PPHA	whole	0.065	0.076	51	0.0087
	filtrate	0.07	0.082	55	0.0088
	retentate	0.058	0.069	46	0.0084
SRHA	whole	0.059	0.072	48	0.0125
	filtrate	0.062	0.075	49	0.0127
	retentate	0.065	0.076	51	0.0106
SRNOM	whole	0.036	0.048	33	0.014
	filtrate	0.033	0.046	31	0.0146
	retentate	0.041	0.05	35	0.0105
ESFA	whole	0.04	0.054	36	0.016
	filtrate	0.041	0.055	36	0.0147
	retentate	0.014	0.018	17	0.0101
PLFA	whole	0.024	0.031	24	0.0166
	filtrate	0.02	0.025	21	0.0153
	retentate	0.009	0.011	13	0.0109
POFA	whole	0.004	0.007	10	0.0246
	filtrate	0.033	0.005	9	0.0227

B.3.3 Electrophoretic mobility of unwashed gold nanoparticles in 10 ppm NOM

Electrophoretic mobilities (EPM) of the gold NPs in 10 ppm NOM were also measured without removing excess NOM, in 20 mM NaCl, 1 mM $NaHCO_3$, pH 8.3 (Figure B.14). This procedure minimizes aggregation that can occur when separating the NPs and dissolved NOM (by centrifugation), as well as desorption of NOM that can occur when resuspending into NOM-free medium. Similar results are obtained as for the washed particles (Figure 6.5): no trend is observed between EPM and M_w for the samples (where the NOM sources are ordered from highest to lowest M_w from left to right in Figure B.14); however, the retentate NOM tends to produce lower EPM than the filtrate NOM from the same source.

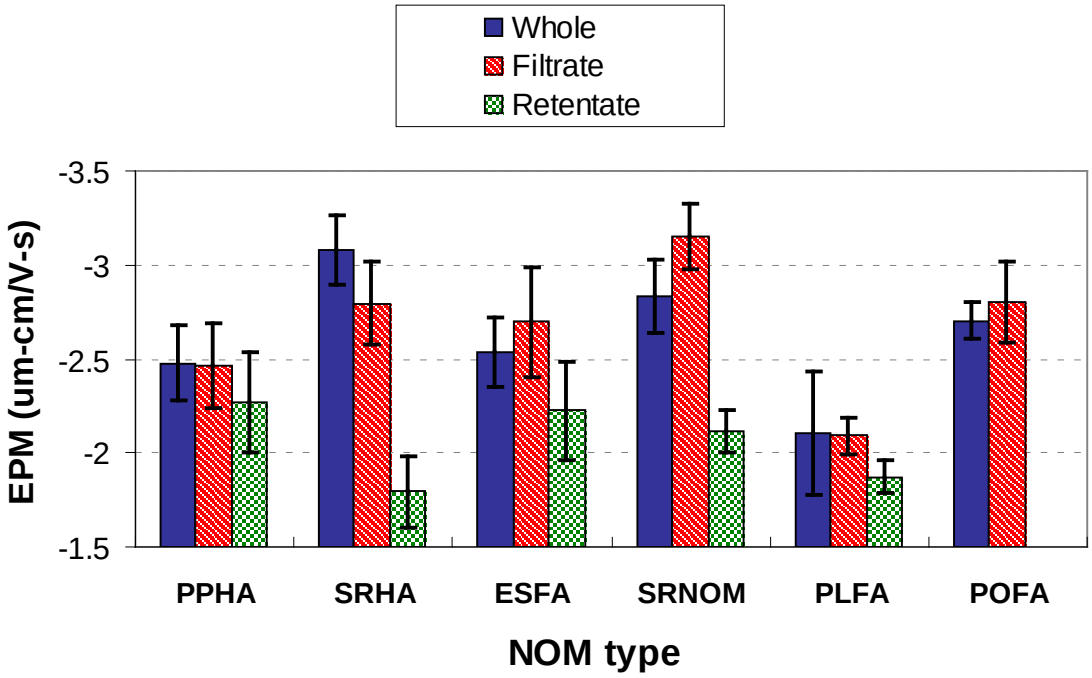

Figure B.14. EPM measured for unwashed citrate-stabilized gold NPs with 10 ppm of NOM in 20 mM NaCl, 1 mM $NaHCO_3$, pH 8.3. The NOM types are ordered from highest M_w (PPHA) to lowest M_w (POFA). No trend with M_w is observed across the six NOM types, although the retentate fraction tends to produce a less negative EPM than the filtrate fraction within each NOM type.

B.3.4 Aggregation of gold nanoparticles in 1 ppm NOM

Aggregation was also measured in 1 ppm of the unfractionated and fractionated NOM, in 100 mM NaCl, 1 mM $NaHCO_3$, pH 8.3 (Figure B.15). At this concentration, differences between molecular weight fractions are more apparent in some samples (SRHA, PLFA, ESFA) than at 10 ppm NOM concentrations. Qualitative trends are generally the same for 1 ppm and 10 ppm of NOM.

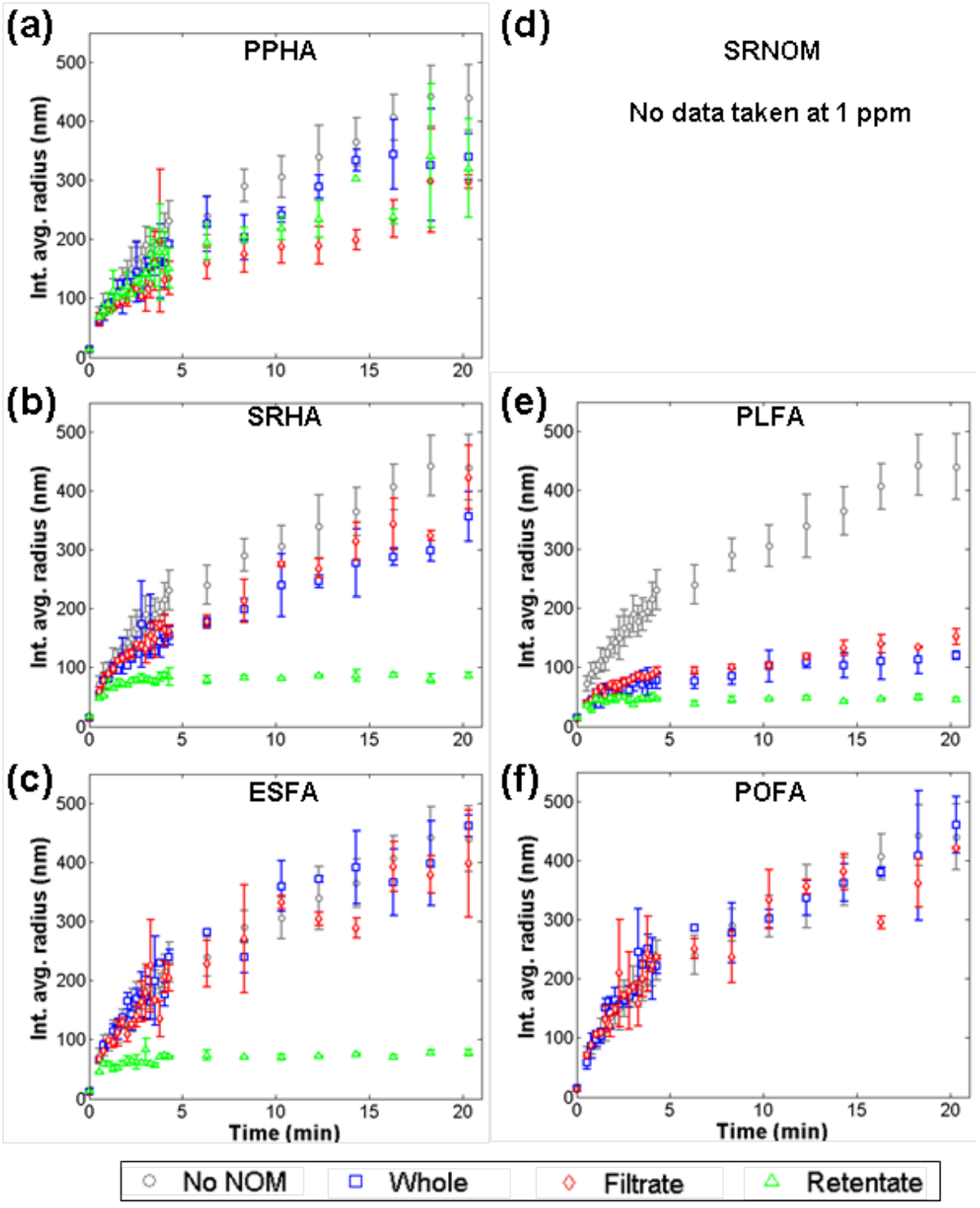

Figure B.15. Hydrodynamic radius measured by time-resolved DLS for 20 ppm citrate-stabilized gold NPs in the presence of 1 ppm of PPHA (a), SRHA (b), ESFA (c), SRNOM (d), PLFA (e), and POFA (f) in 100 mM NaCl, in 1 mM $NaHCO_3$ at pH 8.3. NOM types are ordered from highest to lowest M_w (a to f) of the unfractionated NOM. Error bars represent the standard deviation for two or more runs. SRNOM was assessed in the initial study (Chapter 5), and additional data were not taken at this concentration.

B.3.5 Aggregation of gold nanoparticles with recombined fractions of NOM

The filtrate (< 100 kg/mol) and retentate (> 100 kg/mol) fractions of NOM were recombined in their estimated proportions from the SEC-MALS analysis (see Figure 6.2) to obtain a final concentration of 10 ppm NOM. They were also compared separately at these concentrations. Both the whole NOM and the recombined fractions typically provide better NP stability against aggregation than the separated fractions (Figure B.16).

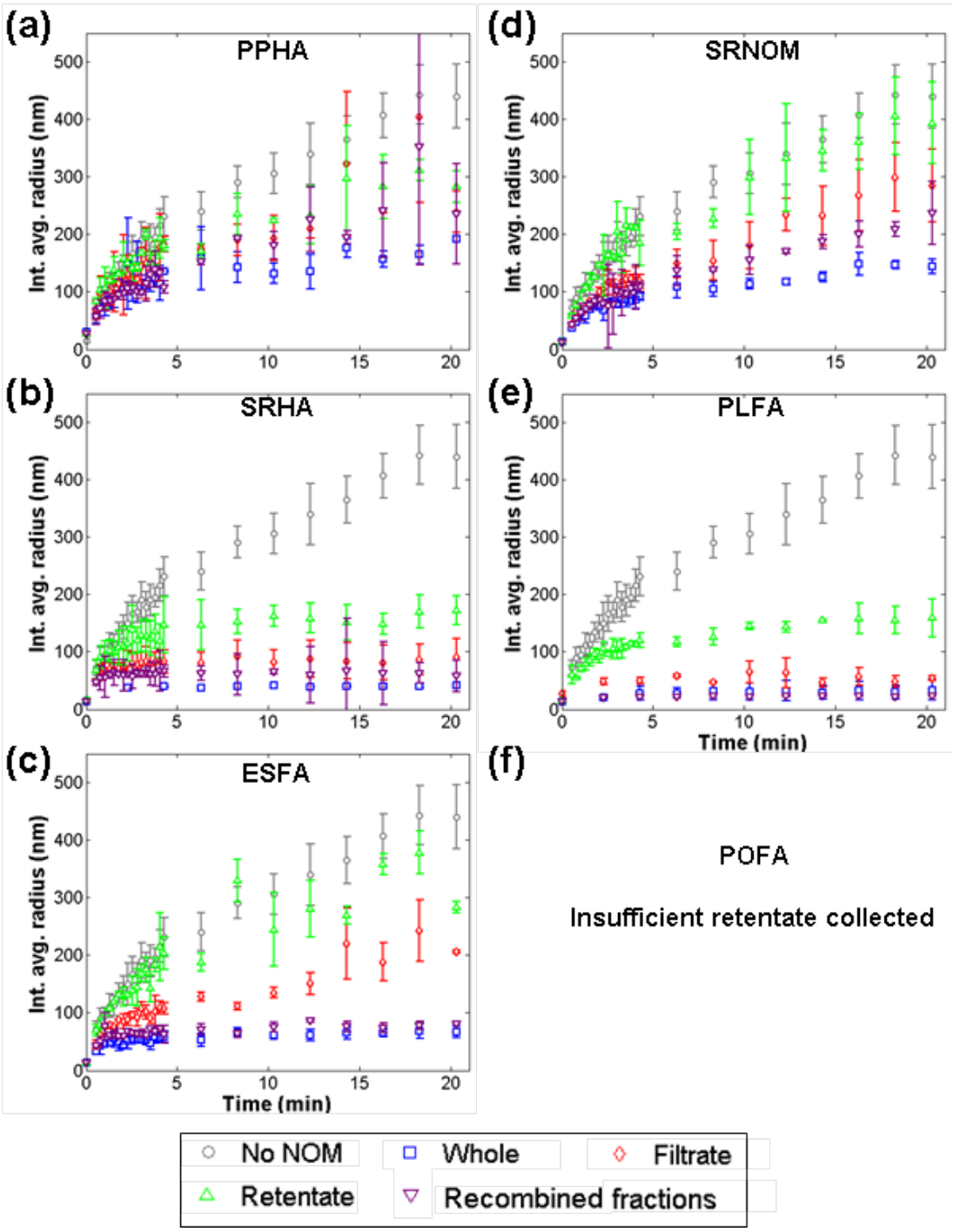

Figure B.16. Effect of NOM mixture or degree of heterogeneity on gold NP aggregation for PPHA (a), SRHA (b), ESFA (c), SRNOM (d), PLFA (e), and POFA (f) in 100 mM NaCl, 1 mM $NaHCO_3$ at pH 8.3. Mixtures or recombined fractions (at 10 ppm total concentration) typically provide better NP stability than the separated fractions. NOM types are ordered from highest to lowest M_w (a to f) of the unfractionated NOM. Error bars represent the standard deviation for two or more runs. Insufficient quantities of POFA retentate were collected for these experiments.

B.3.6 Aggregation of nanoparticles compared across NOM sources

Data from Figure 6.4 are re-organized in Figure B.17 to more clearly show trends in aggregation with the NOM source.

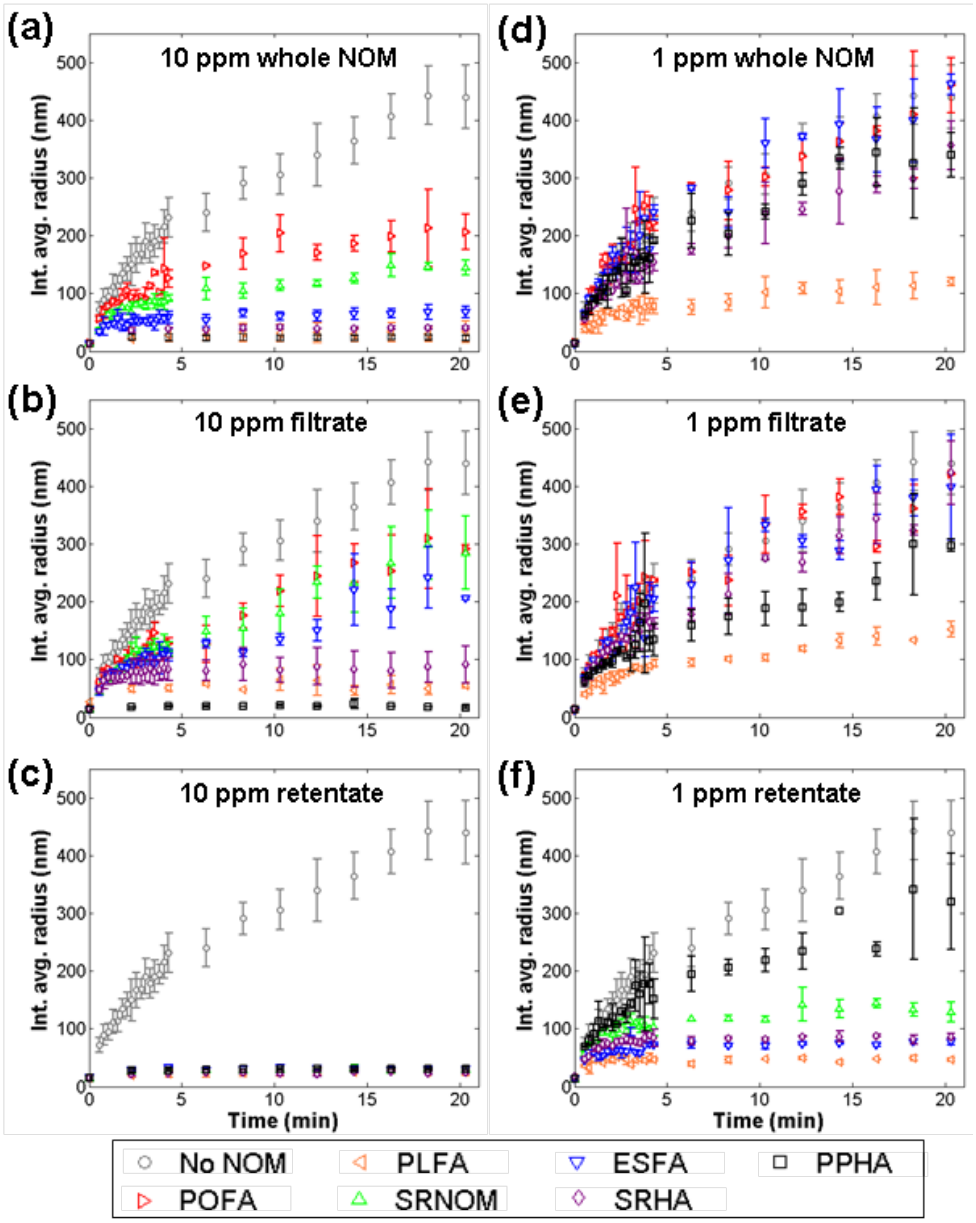

Figure B.17. Gold NP aggregation in the whole (unfractionated) NOM and filtrate and retentate fractions at 10 ppm (a-c) and 1 ppm (d-f) concentrations. Legend is organized from the lowest M_w (POFA) to the highest M_w (PPHA) of the unfractionated NOM. Aggregation behavior typically correlates with M_w except for PLFA (all plots) and PPHA retentate (f).

B.3.7 Computation of initial aggregation rates

In this study, aggregation was typically too rapid to obtain data during the initial doublet formation (i.e., until the hydrodynamic radius, R_h, reaches 1.3 times the initial R_h), so the rate was estimated between the initial size and the first measurement. Some uncertainty is introduced from the delay (approximately 15 to 20 s) between addition of NaCl solution and the first measurement. Furthermore, samples that did not aggregate rapidly were only measured every two minutes (instead of 15 s), so the initial rate may be higher than that estimated here (i.e., by dividing by 135 seconds, assuming a 15 s delay); however, calculations using a shorter time (35 s) did not change the general conclusions of this study.

In spite of the uncertainties involved, these rates generally correlate with the hydrodynamic radius, R_h, at later times, e.g., from 3.5-4 minutes (Figure B.18(a)), or at 20 minutes (Figure B.18(b)). Sedimentation may contribute to the poorer correlation at 20 minutes. The initial aggregation rate for citrate-stabilized gold NPs without NOM (in 100 mM NaCl, 1 mM $NaHCO_3$, pH 8.3) was 1.64 nm/s (not included in Figure B.18).

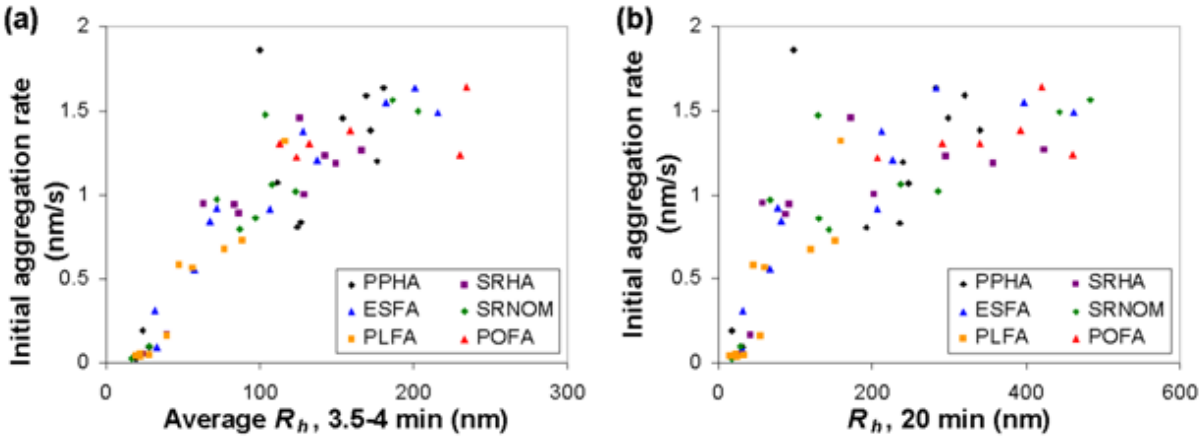

Figure B.18. Correlation of the initial aggregation rate with R_h of the gold NPs after 3.5-4 min (a) or 20 min (b) in 100 mM NaCl, 1 mM $NaHCO_3$, pH 8.3.

B.3.8 Correlation for gold nanoparticle aggregation in 1 ppm NOM

A correlation was attempted using the data collected with 1 ppm NOM. However, most aggregation rates were near that of the uncoated NPs, and no correlation was observed (Figure B.19).

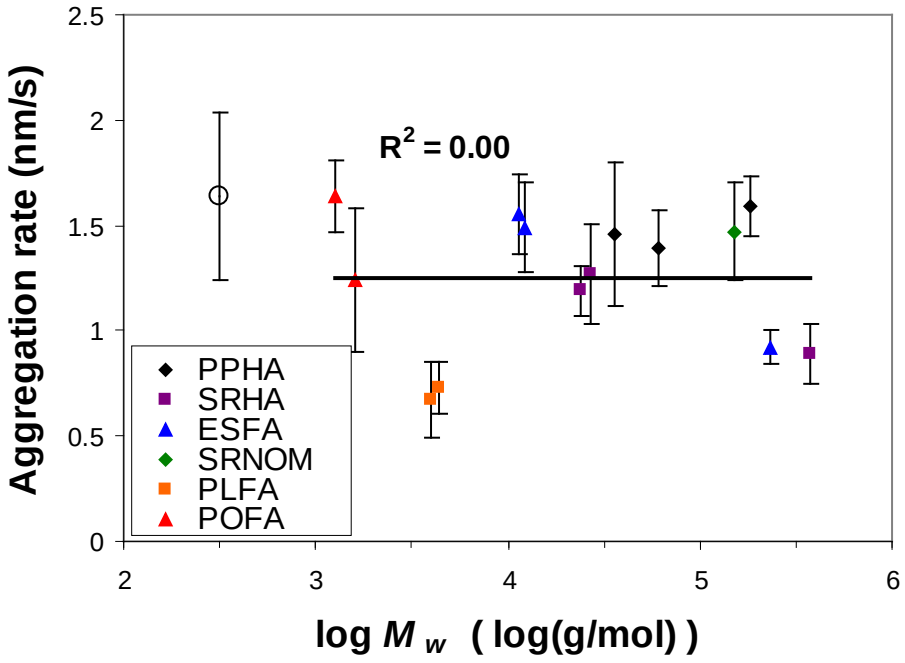

Figure B.19. Aggregation rates in 1 ppm NOM show no correlation with M_w. The empty circle represents the aggregation rate of the citrate-stabilized gold NPs without NOM (plotted at an arbitrary location on the x-axis).

B.3.9 Correlation for gold nanoparticle aggregation using log-log models

Correlations were assessed for a log-log model between initial aggregation rate, k_{agg}, and molecular weight (either M_g or $M_{w,unadjusted}$). The form of the model is given by Equation B.7:

$$k_{agg} = aM^b \qquad \text{(B.7)}$$

The linearized form, Equation B.8, is fitted to minimize the sum of squared errors.

$$\log k_{agg} = \log a + b \log M \qquad \text{(B.8)}$$

The advantage of this form compared to those presented in Chapter 6 is that negative values of k_{agg} are precluded. However, the log-log models show a lower R^2 value, shown in Figure B.20:

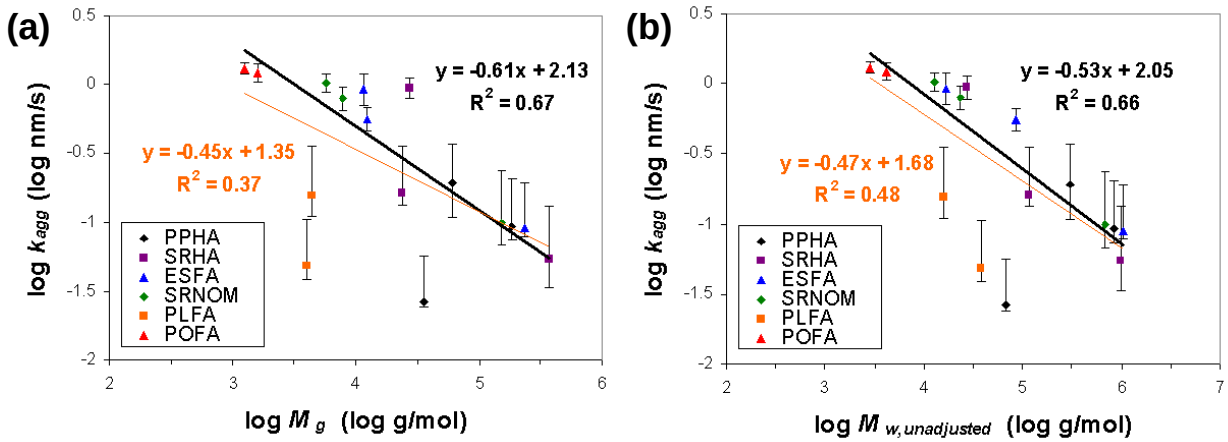

Figure B.20. Correlation of aggregation rate with molecular weight using a log-log model, with molecular weights determined from two methods: the geometric mean, M_g, for a fitted lognormal distribution of weight-averaged molecular weights (a), or $M_{w,unadjusted}$ directly measured by MALS (b). Lower R^2 values are obtained than for correlations in Chapter 6 (linear in k_{agg}).

B.3.10 Correlation between gold nanoparticle aggregation and absorbance ratios

UV-vis absorbance ratios are often used to characterize NOM. Commonly used absorbance ratios include E4/E6 (defined as A_{436}/A_{665}),[8] A_{254}/A_{203}, A_{254}/A_{436}, A_{250}/A_{365}.[9] The latter two absorbance ratios were assessed here because they avoid regions of very low absorbance at high wavelengths (e.g., 665 nm) and regions with a high likelihood for uncertainty, e.g. due to

absorbance of salt species, at low wavelengths (e.g., 203 nm). The correlations for A_{254}/A_{436} and A_{250}/A_{365} are shown in Figure B.21. The former provides similar goodness of fit compared to the exponential slope coefficient, whereas the latter provides poorer goodness of fit.

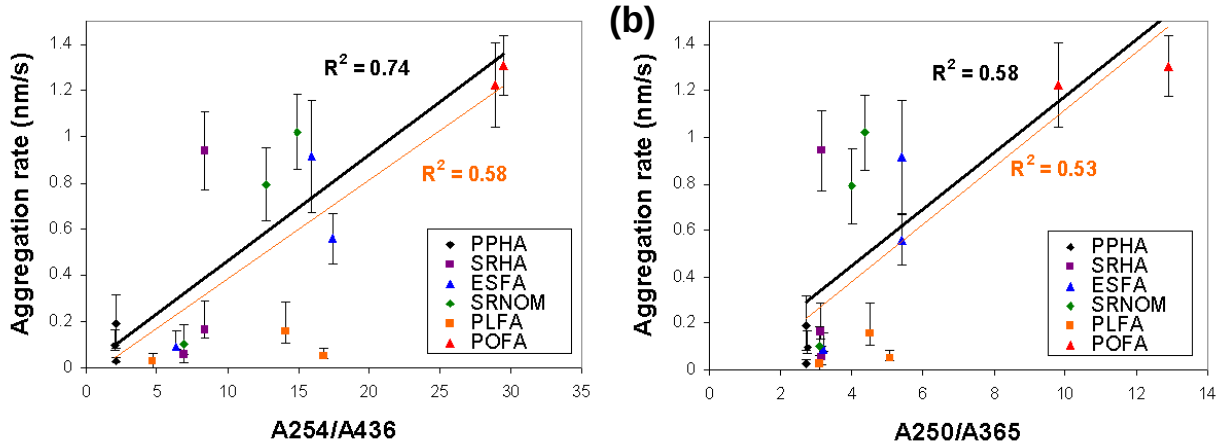

Figure B.21. Correlation of aggregation rate with A_{254}/A_{436} (a) and A_{250}/A_{365} (b) from UV-vis absorbance measurements on NOM. Correlations are shown either excluding or including the PLFA results (black or orange lines, respectively).

B.3.11 Akaike Information Criteria for one- and two-parameter correlations

Two- and three-parameter linear models (both purely empirical) were compared for the correlation of NP aggregation rates in NOM. The forms of the two models are shown in Equations B.9 and B.10:

Two-parameter correlation: $k_{agg} = a_1 \log(M_w) + b_1$ (B.9)

Three-parameter correlation: $k_{agg} = a_2 \log(M_w) + b_2(x_s) + c_2$ (B.10)

Best fit parameters were determined, either including or excluding the PLFA data. These parameters are presented in Table B.6. The Akaike Information Criterion (AIC) is given by Equation B.11:

$$AIC = 2m + n\left[\ln\left(\frac{2\pi RSS}{n}\right) + 1\right] \tag{B.11}$$

where m is the number of parameters in the model, n is the sample size (16 including PLFA; 14 excluding PLFA), and RSS is the residual sum of squares between the modeled and observed k_{agg}. The AIC values are reported in Table B.6. A lower AIC is desirable. The results indicate that reduced S content provides sufficient improvement in goodness of fit to justify including in the correlation if PLFA is considered; however, it does not significantly improve the correlation if PLFA is not included.

Table B.6. Fitted parameters and AIC for the models assessed

Model	**Fitted parameters**		**AIC**	
	All data	**Excluding PLFA**	**All data**	**Excluding PLFA**
Eqn. B.7	a_1 = -0.42 * b_1 = 2.3 † RSS = 1.8 ‡	a_1 = -0.55 * b_1 = 3.0 † RSS = 0.64 ‡	14.3	0.6
Eqn. B.8	a_2 = -0.50 * b_2 = -0.53 † c_2 = 2.9 † RSS = 0.64 ‡	a_2 = -0.51 * b_2 = -0.35 † c_2 = 2.9 † RSS = 0.63 ‡	-0.1	2.3

* units of nm s^{-1} $(\log g/mol)^{-1}$
† units of nm/s
‡ units of $(nm/s)^2$

References for Appendix B

(1) Lakowicz, J. R., Ed. *Principles of fluorescence spectroscopy*; Plenum Press: New York, 1983.
(2) Andersson, M.; Wittgren, B.; Wahlund, K. G. Accuracy in multiangle light scattering measurements for molar mass and radius estimations. Model calculations and experiments. *Anal. Chem.* **2003**, *75* (16), 4279-4291.
(3) Cabaniss, S. E.; Zhou, Q. H.; Maurice, P. A.; Chin, Y. P.; Aiken, G. R. A log-normal distribution model for the molecular weight of aquatic fulvic acids. *Environ. Sci. Technol.* **2000**, *34* (6), 1103-1109.
(4) Thorn, K. A.; Folan, D. W.; MacCarthy, P. *Characterization of the International Humic Substances Society standard and reference fulvic and humic acids by solution state carbon-13 (^{13}C) and hydrogen-1 (^{1}H) nuclear magnetic resonance spectrometry*; Water-Resources Investigation Report 89-4196; U. S. Geological Survey: Denver, 1989.
(5) Abbt-Braun, G.; Lankes, U.; Frimmel, F. H. Structural characterization of aquatic humic substances - The need for a multiple method approach. *Aquat. Sci.* **2004**, *66* (2), 151-170.
(6) Chin, Y. P.; Aiken, G.; Oloughlin, E. Molecular-weight, polydispersity, and spectroscopic properties of aquatic humic substances. *Environ. Sci. Technol.* **1994**, *28* (11), 1853-1858.
(7) Traina, S. J.; Novak, J.; Smeck, N. E. An ultraviolet absorbance method of estimating the percent aromatic carbon content of humic acids. *J. Environ. Qual.* **1990**, *19* (1), 151-153.
(8) Thurman, E. M. *Organic geochemistry of natural waters*; Martinus Nijhoff/Dr W. Junk Publishsers: Dordrecht, **1985**.
(9) Matilainen, A.; Gjessing, E. T.; Lahtinen, T.; Hed, L.; Bhatnagar, A.; Sillanpaa, M. An overview of the methods used in the characterisation of natural organic matter (NOM) in relation to drinking water treatment. *Chemosphere* **2011**, *83* (11), 1431-1442.